



The University of
Nottingham

UNITED KINGDOM • CHINA • MALAYSIA

Mapping Fluid Flow in Porous Biomaterials for Tissue Engineering

By Catherine Taylor, MEng

Thesis Submitted to the University of Nottingham for the
degree of Doctor of Philosophy, September 2021

Abstract

Tissue engineering strategies seek to regenerate cartilage tissue *in vitro* using a combination of cells, scaffolds and cell stimulation via means including bioreactors, as an alternative treatment option to cartilage defects and injuries. There is great interest in capitalising on perfusion and the associated fluid induced forces as a means of providing mechanical stimulation to cells, to ultimately influence desired tissue formation. The use of perfusion bioreactors to introduce such mechanical stimulation has been shown to effectively encourage cartilage regeneration when applied to cells in 3D porous scaffolds. In tissue engineering, cell scaffold constructs are often matured *in vitro* for extended periods prior to *in vivo* use so it is vital that the culture environment facilitated by bioreactors enhances tissue formation. Nonetheless, application of excessive perfusion rates can be detrimental to cell attachment, and cause non-desirable changes to differentiation pathways. Therefore, it is imperative that perfusion flow is closely controlled to ensure it provides appropriate levels of mechanical stimulation to cells. However, the relationship between fluid flow and the cellular response to fluid flow in culture, in addition to how far these two influence one another over time needs to be elucidated.

To investigate the effectiveness of perfusion bioreactors, research currently relies predominantly on computational models to predict behaviour, and post analysis of scaffolds after perfusion. Experimental real time data to understand how not only does a dynamic culture system change with culture time, but also how the porous architecture influences the fluid pathway would provide a great insight into how scaffold design and subsequent cell proliferation and differentiation effect the flow velocity and fluid induced forces. The optimisation of dynamic culture experiments, bioreactor design and scaffold porous architecture could all benefit from this level of insight.

In this thesis, a technique for mapping fluid velocity in porous scaffolds using NMR and MRI is presented. This technique utilises the spin properties of nuclei in proton dense liquids to provide spatially resolved information about the location and physical properties of atom nuclei, and is able to distinguish between atoms with different physical properties, including those atoms experiencing different translational diffusion. All of this information can be obtained non-invasively and in real time making it an ideal tool to study perfusion in porous biomaterial scaffolds for tissue engineering. However, to date there has been very limited use of this technique with respect to tissue engineering, such that the studies in this will seek to validate NMR and MRI techniques in this field and further explore the extent of how it can be used.

The impact of obtaining flow velocity profiles within porous scaffolds will undoubtedly inform decisions on scaffold design, bioreactor design and flow conditions. Small variations in flow distributions and velocities could impact cell responses in regards to proliferation, migration and differentiation. Small and unexpected variations in cell behaviour could lead to undesired and inhomogeneous tissue formation. Therefore understanding how variations in flow occur in culture and affect overall cell behaviour and tissue formation can be used to both mitigate for these factors, but also optimise experiments to ensure flow conditions constantly facilitate an environment desirable for tissue regeneration.

Firstly, to examine the effects of scaffold porous architectures on fluid flow regimes, 3D printing techniques were used to fabricate cell free scaffolds with varied pore characteristics. 3D printing and computer aided design allow for a high level of control over pore architecture, which dependent on desired flow patterns, can be altered to facilitate such flow patterns. Results demonstrated the effects scaffold architecture has on flow can be mapped using NMR and MRI velocimetry.

Secondly, this project further utilised the capabilities of MRI to investigate porous scaffold, which had in this instance been seeded with ihMSC cells. MR imaging was

successful in visualisation of both cells that had been labelled with iron oxide nanoparticles, and unlabelled cells within the porous polymer matrix. This imaging method was non-destructive to the scaffold, and therefore could be used to monitor changes in cell densities and migration during cell culture. Finally, this project combined both velocimetry and cell visualisation techniques to link cell location and fluid field patterns. When compared with cell free scaffolds there was significant differences in velocity of fluid in cell-seeded scaffolds, which in some scenarios could be directly linked with cell location.

Table of Contents

1	Introduction	1
1.1	Project Overview	4
2	Literature Review	5
2.1	Cartilage Tissue Engineering	5
2.1.1	Cell based approaches	7
2.1.2	Scaffold strategies	9
2.1.2.1	Solid Porous Scaffolds	10
2.1.2.2	Hydrogel Scaffolds	11
2.1.3	Scaffold Fabrication	11
2.1.3.1	Conventional methods of scaffold fabrication	12
2.1.3.2	3D printing	13
2.1.4	Scaffold Materials	16
2.1.4.1	Natural Materials	16
2.1.4.2	Synthetic Materials	18
2.2	Dynamic Cell Culture	20
2.2.1	Bioreactors	20
2.2.2	Porous Architecture	22
2.2.2.1	Cell Response	23
2.2.2.2	Mechanical Properties	24
2.2.2.3	Pore size and distribution	25
2.2.2.4	Pore Geometry	27
2.2.2.5	Interconnectivity and permeability	29
2.2.2.6	Scaffold Surface Chemistry	30
2.2.3	Role of flow	31
2.2.4	Cellular response to flow	31

2.2.4.1	Shear stresses	31
2.2.4.2	Flow Distributions	32
2.2.4.3	Effects of structural design on flow	37
2.2.5	Current methods of mapping flow	38
2.2.5.1	Computational Fluid Dynamics	38
2.2.5.2	Optical methods	40
2.3	NMR and MRI	41
2.3.1	Basic principles	42
2.3.1.1	NMR Physics	42
2.3.1.2	Velocity encoding and flow imaging	45
2.3.2	MRI for Flow Imaging	46
2.3.3	Application of NMR in porous materials	47
2.3.4	Potential applications in Tissue Engineering	48
2.3.5	Use of Magnetic Nanoparticles in MRI	49
2.4	Summary	50
3	Methodology	52
3.1	Scaffold Design and Fabrication	52
3.2	Cell Culture	52
3.2.1	Immortalised Human Mesenchymal Stem Cells	52
3.3	Cell Characterisation	53
3.3.1	Pico Green Assay	53
3.3.2	Dimethylmethylene Blue Assay	53
3.4	Compressive Testing	53
3.5	Scanning Electron Microscopy	54
3.6	Micro Computed Tomography	54

3.7	Osmium Tetroxide Staining	54
3.8	MRI and NMR Velocimetry	55
3.8.1	Flow Chamber and system	55
3.8.2	NMR and MRI Velocity Measurements	55
3.8.3	Data Processing	56
3.9	Magnetic Nano Particles labelling	56
3.9.1	Cell Labelling with Magnetic Nano Particles	56
3.9.2	Prussian Blue Assay	56
3.9.3	Alamar Blue Assay	57
3.9.4	MSME Imaging of Labelled Cells	57
3.10	Statistical Analysis	58
4	<i>NMR and MRI Velocimetry for Distinct Cell Free Scaffold Architecture</i>	59
4.1	Introduction	59
4.2	Methodology	63
4.2.1	Scaffold Design and Fabrication	63
4.2.2	Flow Chamber and System	65
4.2.2.1	NMR and MRI Velocity Measurements	67
4.2.3	Compressive Testing	69
4.2.4	Scanning Electron Microscopy	69
4.2.5	Micro Computed Tomography	70
4.2.6	Statistical Analysis	70
4.3	Results and Discussion	71
4.3.1	Printing Optimisation	71
4.3.2	Scaffold Characterisation	73
4.3.3	Mechanical Characterisation	76
4.3.4	Fluid Velocity Measurements	78

4.3.4.1	Pore Size	86
4.3.4.2	Pore Geometry	91
4.3.4.3	Leak Area	97
4.4	Conclusion	103
5	<i>Magnetic Nanoparticle Cell labelling Study for Locating Cells in 3D</i>	
	<i>Porous Scaffolds</i>	105
5.1	Introduction	105
5.2	Methodology	109
5.2.1	Scaffold Design and Fabrication	109
5.2.2	Cell Culture and Scaffold Seeding	109
5.2.2.1	Cell labelling	109
5.2.2.2	Static culture	110
5.2.2.3	Dynamic Culture	110
5.2.3	Cell Culture Analysis	111
5.2.4	Prussian Blue Staining	111
5.2.5	Scaffold preparation for MR imaging	112
5.2.6	Gel Formation	112
5.2.7	MR Imaging for Cell Seeded Scaffolds	113
5.3	Results and Discussion	114
5.3.1	Prussian Blue	114
5.3.2	Cell Viability	115
5.3.3	Static cell culture	117
5.3.4	Dynamic Cell Culture	120
5.3.5	MR Imaging	122
5.3.5.1	Sample Preparation	122
5.3.5.2	Imaging labelled cells	125
5.3.5.3	Imaging cell seeded scaffolds	141

5.4	Conclusion	155
6	<i>The Relationship between Cell Seeded 3D porous Scaffolds and Perfusion</i>	157
6.1	Introduction	157
6.2	Methodology	160
6.2.1	Scaffold Design and Fabrication	160
6.2.2	Cell culture and scaffold seeding	161
6.2.2.1	Static Culture	161
6.2.2.2	Dynamic Culture	161
6.2.3	Flow chamber and System	162
6.2.4	NMR and MRI velocity Measurements	163
6.2.5	MR Imaging of Cell seeded scaffolds	163
6.2.6	Cell viability and Chondrogenic differentiation analysis	164
6.2.7	Osmium Tetroxide staining	164
6.2.8	Micro-computed Tomography	164
6.3	Results and Discussion	166
6.3.1	Static cell culture	166
6.3.1.1	Cell Seeding efficiency and proliferation	166
6.3.1.2	MSC Chondrogenic differentiation	169
6.3.2	Dynamic Cell Culture	170
6.3.2.1	Cell seeding efficiency and growth	170
6.3.2.2	MSC Chondrogenic Differentiation	173
6.3.3	Fluid Velocity Measurements	174
6.4	Conclusion	204
7	<i>Conclusions and Future Work</i>	205
7.1	Conclusions	205

7.2	Future Work	206
8	References	208

Table of Figures

<i>Figure 2-1 Layered structure of both chondrocyte cells and collagen fibrils in articular cartilage [24].....</i>	<i>6</i>
<i>Figure 2-2 Tissue engineering paradigm consisting of cells, signals and scaffolds displaying where scaffold free techniques would fit in this paradigm. Image from GD DuRaine et al. [42].</i>	<i>9</i>
<i>Figure 2-3 Schematic examples of extrusion based 3D printing technologies. Image modified from [75]</i>	<i>15</i>
<i>Figure 2-4 Schematic showing basic principles of Perfusion bioreactor</i>	<i>21</i>
<i>Figure 2-5 Examples of bioreactors A) Spinner flask bioreactor B) Flow perfusion bioreactor and C) rotating wall bioreactor. Adapted image from [117].</i>	<i>22</i>
<i>Figure 2-6 Comparison of CFD results against micro PIV results inside porous scaffold from Campos Marin [16]</i>	<i>41</i>
<i>Figure 2-7 Magnetic field causing the nucleus to precess at the Larmor frequency.....</i>	<i>43</i>
<i>Figure 2-8 Application of RF pulse tips magnetisation in to transverse plane</i>	<i>44</i>
<i>Figure 2-9 Schematic of spin echo inversion recovery pulse sequence</i>	<i>45</i>
<i>Figure 2-10 Schematic showing 90° pulse rotating M into xy plane, the spins lose phase coherence and the 180° flips the spins. Spins refocus to form an echo. Phase shifts are acquired for spins associated with flow. P is positive flow, S is stationary flow and N is negative flow.</i>	<i>46</i>
<i>Figure 4-1 RegenHu Biodiscovery 3D printer used for FDM scaffold</i>	<i>64</i>
<i>Figure 4-2 A) CAD drawings of flow chamber displaying the blown out assembly of individual parts and the complete assembly. B) Images of the manufactured parts and its assembly, of the flow chamber used. C) Schematic representation of the closed loop flow system.</i>	<i>66</i>
<i>Figure 4-3 Schematic representation of pulse sequence for spin echo velocimetry imaging....</i>	<i>68</i>
<i>Figure 4-4 Schematic of axial slices from a side view, 3D visualisation of scaffold from micro CT reconstruction, and example of axial slice MRI image from scaffold.</i>	<i>69</i>

*Figure 4-5 A) Graph showing how increasing speed of print head speed effected the diameter of struts printed, sizes determined using analyses of SEM images. B) Graph shows how increasing the size of nozzle used for printing effects the pore size of scaffolds, pore size also determined using SEM images. C) Increasing extrusion rate shows increasing strut diameter. D) Increasing pre-programmed spacing between struts resulted in increasing pore size. *P 0.026 **P 0.09 ***P < 0.001 ****P< 0.0001. Values are reported as mean ± standard deviation, n=3 71*

Figure 4-6 SEM Images of the porous structure of FDM printed scaffolds, A-D pore size samples from top view (PCL-90-150, PCL-90-300, PCL-90-450, PCL-90-800), E-G Pore geometry samples all from top view with average pore length and pore width measurements (PCL-0-90, PCL-0-45, PCL-0-15)..... 73

*Figure 4-7 A) Compressive modulus mean values with ± standard deviation of scaffolds with varied geometry (n=3) and B) the representative associated stress-strain curves. C) Compressive moduli mean values with ± standard deviation of scaffolds with different pore sizes (n=3) and D) their representative stress-strain curves E) Stress-strain curve for PCL-0-90 indicating 10% linear region from which the modulus was calculated. *P 0.026 **P 0.09 ***P < 0.001 76*

Figure 4-8 Example of pore velocity profiles, taken across a group of pores (above) and the profile of one single pore (below). Distance indicates location across the axial slice of a scaffold..... 80

Figure 4-9 Flow chamber design before alterations, consisting of inlets that were not tapered that resulted in a high degree of bubble formation. Image of individual parts that make up chamber (left) and schematic of how parts fit together [241]..... 81

Figure 4-10 MSME imaging used to show how bubble formation in scaffolds, which appear as dark areas void of signal. Images taken as axial slices from top to bottom of scaffold. 81

Figure 4-11 Sagittal projections slicing from left to right in the scaffold showing the formation of bubbles, appearing as larger round dark areas, particularly at the top region of the scaffold closest to the outlet..... 82

Figure 4-12 Redesigned flow chamber with inlets that sit either side of scaffold holder, the internal diameter of inlets has been greatly increased to avoid bubble formation. Image of individual components (top) and schematic of parts assembled (below)..... 83

Figure 4-13 Resultant velocity map (top) in which colour scale indicates recorded velocities as mm/s. MSME images (bottom) from changing the design of flow chamber inserts to avoid bubble formation Images taken from 3 sliced locations in the axial and sagittal directions.. Velocity map shows a inhomogeneous pattern of velocity. MR imaging shows bubbles were successfully removed..... 85

Figure 4-14 Mapped velocity in porous scaffolds using NMR and MRI. Signal is recorded from proton dense fluid water in individual pores travelling in the z direction. Areas around the scaffold made up of plastic represent areas of noise..... 86

*Figure 4-15 (A-D) Relative frequency of velocities measured in scaffolds with varied pore sizes shown in histograms. E) Box Plots showing distribution and amount of variation of velocity and F) comparison of average velocity of flow through scaffolds with varying pore sizes. Significance difference (***) $p < 0.001$ between all group comparisons for mean velocity measurements for pore size groups (n=3)..... 87*

Figure 4-16 Relative frequency distribution of three sliced images taken from different locations within the same scaffold. Boxplot to visualise how the spread of data compares and a bar chart to show the average velocity and standard deviation of each slice (n=3)..... 92

*Figure 4-17 A) Mapped velocity in porous scaffold using NMR and MRI displaying the flow distribution in different pore geometries. B) 7 Histograms displaying relative frequency of velocity within each geometry. C-D) Distribution box plots and average velocity measure \pm standard deviation in porous scaffold with distinct pore geometry *** $P < 0.001$ (n=3). 94*

Figure 4-18 Examples of curve fitting of velocity profiles for individual pores for each scaffold geometry..... 96

Figure 4-19 Image showing a scaffold within flow chamber insert that encases it during flow experiments compared with the flow map produced from this. Highlighted are the gaps formed when the scaffold is enclosed in the chamber and the corresponding effects in velocity mapping. 97

Figure 4-20 Velocity profiles of PCL-0-90, PCL -0-45 and PCL-0-15 geometry porous scaffolds repeated three times on separate scaffolds under the same flow conditions and relative frequency distribution graphs for each sample..... 98

*Figure 4-21 A) Box plot diagrams displaying the distribution of velocities recorded for each scaffold with in pore geometry groups. B) Average velocities \pm standard deviation for each sample within each geometry group *P 0.03 ***P <0.001 (n=3). 99*

Figure 4-22 A) The total area of the leak area (scaffold where the seal to bioreactor is not flush and allows to flow through) plotted against the standard deviation of velocity within a scaffold where R^2 value shows 26% of standard deviation is accounted for by the Leak area. B) The overall average velocity plotted against the leak area, where R^2 value shows 22% of Average velocity is accounted for by the leak area..... 100

Figure 4-23 A) Velocity maps for each pore architecture highlighting a region of interest from which velocities were extracted B) Boxplots comparing the degree of variation between velocities recorded for a whole scaffold area and an area of ROI C) Average velocities for each measurements \pm standard deviation (n=3). 102

Figure 5-1 Schematic diagram of components of dynamic culture experiments (left), and image of set up in cell culture incubator [241] 111

Figure 5-2 Prussian blue staining of ihMSC's fed with A) 0 $\mu\text{g/ml}$ B) 25 $\mu\text{g/ml}$ C) 50 $\mu\text{g/ml}$ D) 100 $\mu\text{g/ml}$ of magnetic nanoparticles. Monolayer of PFA fixed culture was stained with Prussian blue after being left overnight in media containing nanoparticles. 114

Figure 5-3 Prussian Blue staining of cells seeded on 3D PCL scaffolds using static seeding with different pore geometry 3 hours after seeding scaffolds with labelled cells using a concentration of 50 $\mu\text{g/ml}$. Scaffold geometry used were laydown patters 0/15(A) 0/45(B) and 0/90(C). Prior to staining scaffolds were fixed using PFA. For imaging scaffolds were sectioned and images taken from internal regions of scaffold. 115

Figure 5-4 Alamar blue reduction (A) and DNA quantification (B) of ihMSC cells cultured with MNP's for seven days using 6 well culture plates. Cells were labelled with magnetic nanoparticles, seeded using static seeding and then cultured in growth media for up to 7 days under static conditions (n=3). 116

*Figure 5-5 DNA content of scaffolds grown with labelled cells in static conditions, and DNA relative to Day 0. Scaffolds used had 0-90 strut orientation and pore size of approximately 270µm. 1x10⁶ ihMSC cells were seeded per scaffold, n=3 for each time point. *p<0.0332 **p<0.0021 117*

Figure 5-6 Cell seeding efficiency measured using DNA content of cell suspension of 1x10⁶ ihMSCs compared to DNA content of scaffold after initial seeding and attachment (n=3) presented as a percentage..... 117

Figure 5-7 DNA content of scaffolds grown with labelled cells in dynamic perfusion conditions, and DNA relative to Day 0. Scaffolds were pre seeded with 1x10⁶ ihMSCs before being grown under perfusion flow of 1mL/min for up to 14 Days. 121

Figure 5-8 MR Images showing different methods of sample preparation for unseeded cell free scaffolds, in an attempt to remove artefacts caused by bubble formation; A) No preparation to keep porous structure filled with water B) Scaffold manually filled by immersing in fluid C) Scaffold placed under vacuum and then immersed D) Pores were vacuumed, filled with degassed water and then entire scaffold encapsulated in kappa carrageenan gel..... 122

Figure 5-9 A) and B) Showing parts of system to vacuum air out of pores of blank cell free scaffolds C) Chamber used to house scaffold for imaging D) Schematic of process to encapsulate scaffold in kappa carrageenan gel after scaffold had been removed from vacuum. 125

Figure 5-10 Signal intensity images of labelled cells dispersed through 2ml of Pluronic F-127 gel in a 10mm NMR tube imaged. A) Gradient echo imaging acquisition method. Images left to right are acquired in series with 4ms echo time between each image. Images were acquired as a 2 mm thick sagittal slice in a 128x128 pixel array. TE 4 ms, TR 1000 ms. B) Spin echo of same slice of gel. Images acquired every echo, using parameter TE 5.1 ms and TR 1000 ms..... 126

Figure 5-11 A) Blank gel not containing cells in 10 mm NMR tube. Signal intensity images acquired in 2 mm slices using gradient echo pulse sequence to give images with increasing echo time from left to right by 4 ms with each echo image B) Spin echo images of identical slices of blank gel using MR imaging parameters TE 5.1 ms and TR 1000 ms. 127

Figure 5-12 Images of gel containing cells dispersed throughout the gel compared to a blank gel. Both images represent the third echo image, in which signal has had 12 ms to decay. The presence of iron oxide nanoparticles causes the gel containing cells to lose signal at a much quicker rate confirming they can be detected within Pluronic F-127 gel using this MR imaging method..... 128

Figure 5-13 Images showing NMR tube containing a mix of blank gel and Pluronic gel that has labelled cell dispersed throughout. First and last echo images show over time the amount of signal present in the gel containing cells decreases much quicker. The blank gel maintains similar levels of signal intensity between images. 130

Figure 5-14 MR images showing signal intensity. 10 mm NMR tube (left) containing both Plurionic F-127 gel dispersed with 1×10^6 cells (bottom section of gel in tube) and gel only (top section of gel in tube). Gradient echo images acquired every 2 ms from a 2 mm thick sagittal orientated slice. Six Echoes are acquired with a 128x128 pixel array. Each echo image shows decay in signal over time, quicker decay indicates the presence of iron labelled cells. 131

Figure 5-15 Two gel types imaged in 10mm NMR tube. One gel free of cells, the other containing iron oxide labelled cells. Axial 2 mm slice echo images every 5 ms showing differences in signal intensity between blank gel and gel containing iron oxide labelled cells. 128x128 pixel images acquired using gradient echo pulse sequences, and imaging parameters TE 5 ms, TR 1000 ms. 132

Figure 5-16 Axial projection of NMR tube containing both types of gel. In the time between the first and last echo image the signal in the gel containing iron labelled cell decreases a great deal more than the contrasting blank gel..... 132

Figure 5-17 T2 relaxation map, separated into two regions of interest, of an NMR tube containing two parts corresponding with each region of interest; a gel mixed with iron labelled cells (left) and a blank gel [241]. Associated histograms show the distribution of T2* relaxation times for both material types..... 133*

Figure 5-18 First and last echo image acquired with 8 ms between each image, showing how over time the scaffold containing iron labelled cells loses signal at a much more substantial rate than the scaffold containing gel only. 135

Figure 5-19 Two Scaffolds with 600 μm pores, stacked upon one another and imaged using MRI. One scaffold is filled with gel containing labelled cells (top) and one filled with a blank gel (bottom), to visualise cells within a polymer network. Gradient Echo imaging of two sagittal 0.5 mm sliced locations, 4 echo images acquired per slice, each 2ms apart. 136

Figure 5-20 MR signal intensity images. Axial slices of stacked scaffolds, containing either gel with dispersed labelled cells or blank gels. Images acquired as a 0.5 mm slice every 2 ms. Slice 1 and slice 2 are axial 0.5 mm slices taken from different locations in stacked scaffolds, one from scaffold with gel/cells mixture (Slice 1) and one from scaffold with blank gel (slice 2). 137

Figure 5-21 Slice of each scaffold acquired as gradient echo images. First echo at 2ms (left) and Fourth echo image [241] after 8 ms shows that in the scaffold containing cells there is a greater degree of reduction in signal intensity over the same time period compared to the scaffold containing the blank gel only. 138

Figure 5-22 Regions of interest bounding each gel filled scaffold, cell free (left) and with labelled cells [241] taken from axial T2 relaxation maps. Corresponding histograms show the frequency and distribution of T2* relaxation times. Cell free scaffolds filled with 20 w/v% Pluronic F-127 gel. Scaffold containing cells, has pores filled with Pluronic F-127 gel that has been seeded with 1x10⁶ magnetic labelled ihMSCs. Axial images of stacked scaffolds were used to generate T2* maps. 139*

Figure 5-23 Regions of interest bounding each gel filled scaffold, cell free (left) and with labelled cells [241] taken from sagittal T2 relaxation maps. Corresponding histograms show the frequency and distribution of T2* relaxation times. . Cell free scaffolds filled with 20 w/v% Pluronic F-127 gel. Scaffold containing cells, has pores filled with Pluronic F-127 gel that has been seeded with 1x10⁶ magnetic labelled ihMSCs. Sagittal projection of stacked scaffolds. 140*

Figure 5-24 Axial images acquired using spin echo pulse sequence. Slice 1 shows scaffold filled with cell seeded gel, cells having been labelled with iron containing nanoparticles. Slice 2 shows porous scaffold filled with gel only. Images were acquired using parameters TE 5.1 ms, TR 1000 ms to produce 128x128 pixel images. 141

Figure 5-25 Spin echo images of sagittal 0.5 mm slices showing spin echo images acquired every 5.1 ms of stacked scaffolds with labelled and blank gels. Lower scaffold contains gel

only, and upper scaffold contains labelled cells dispersed throughout gel. Slices acquired from two different sagittal planar locations. Imaging acquisition parameters TE 5.1 ms, TR 1000 ms, 128x128 pixels..... 141

Figure 5-26 A) MR signal intensity images of Gradient echo pulse sequence to acquire 1mm axial slices throughout 300um pore scaffold seeded with ihMSCs labelled prior to seeding. Scaffold had been seeded using manual droplet of 1×10^6 cells suspended in 100 μ l of media and cultured for a subsequent 14 days in expansion media. B) Spin echo images of identical slices from the same scaffold. C) Micro CT reconstruction of scaffold, and images of cell seeded scaffold showing clustering of labelled cells on surfaces. 144

Figure 5-27 Images of cell seeded scaffold, after 14 days in culture, seeded with labelled cells (left) compared against MR gradient echo sequenced images of the corresponding scaffold surface [241]. Highlighted are examples of some corresponding areas of cells between actual and MR imaged scaffold surface..... 145

Figure 5-28 MR signal intensity images acquiring twelve 0.5mm axial slices of A) gradient echo sequenced images and B) spin echo sequenced images of a scaffold seeded with labelled cells and grown under static conditions for 14 days. Both MR acquisition sequences were used to produce 512x512 pixel images. Showing 12 slices from second echo for both image sets..... 146

Figure 5-29 MR signal intensity images of twenty 0.5 mm sagittal sliced A) gradient echo images acquired every 2ms and B) spin echo images acquired every 5.1 ms in a pixel of 256x256. Scaffold seeded with magnetic nanoparticle labelled cells and grown in static conditions for 14 days. Large areas of signal voids in both image sets correspond with location of cells. 149

Figure 5-30 Comparison between gradient echo (left) and spin echo [241] of identical sagittal sliced images taken from a scaffold seeded with cells post labelling with iron oxide nanoparticles. Areas of signal void show location of cells, spin echo sequenced images more accurately portray the size of cells or groups of cells..... 150

Figure 5-31 Comparison of (A) scaffold seeded with labelled cells and static cultured for 14 days against a completely cell free scaffold (B) both filled with Pluronic F-127 gel. Both sets of images were acquired using a gradient echo pulse sequence using parameters TE 2 ms and TR

1000 ms to produce 256x256 pixel array images. Large areas void of signal indicate presence and location of cells that are not present in the blank scaffold. 151

Figure 5-32 Slice from same axial location in a cell seeded scaffold (left) and a blank scaffold [241]. Highlighted area shows large loss of signal, indicating the presence of cells, labelled with iron oxide nanoparticles to act as a negative contrast agent. 152

Figure 6-1 Dynamic perfusion culture set-up in incubator, cell culture chamber image and schematic images showing chamber design. 162

Figure 6-2 DNA content measured over 28 days for 3D cell seeded PCL scaffolds, seeded and grown under static conditions in chondrogenic media containing TGF- β . A) DNA content average content \pm standard deviation (n=3) and B) Relative DNA content normalised to day 0. C) cell seeding efficiency measured using DNA content of cell suspension compared to scaffold after initial seeding and attachment (n=3). ****p<0.0001 166

Figure 6-3 Micro-CT reconstructions of cell seeded scaffolds and grown under static conditions in chondrogenic growth media at Day 0, 14 and 28 post staining with osmium tetroxide. ... 168

Figure 6-4 Chondrogenic differentiation of MSCs in 3D printed scaffolds quantified using DMMB assay (to measure sGAG content), and measured over 28 days in static culture (n=3) (left). sGAG content relative to total DNA content normalised to day 0 (n=3) [241]. ***p<0.0002 169

Figure 6-5 Results for cell seeded scaffolds grown under perfusion dynamic culture at 1mL/min for up to 28 days in chondrogenic media, showing DNA content [241] quantified using Pico Green Assay (n=3), and sGAG content (left) measured using DMMB assay (n=3). ***p<0.0002 170

Figure 6-6 Velocity bulk measurements mapped as velocimetry images of scaffolds, showing a cell free blank scaffold (top) and a cell seeded scaffold that has been cultured in growth media for 14 days under static conditions (bottom). 176

Figure 6-7 Histograms showing the relative frequency distributions recorded from peak velocity values within each pore for a blank cell free scaffold (left) and for a scaffold that has been cell seeded and cultured in static conditions for 14 days. 177

*Figure 6-8 Box Plots showing distribution of velocity and average velocity of flow through scaffolds without cells, and cultured with cells for up to 14 days under static conditions in growth media. ****p<0.0001 (n=1)..... 177*

Figure 6-9 Velocimetry map of cell seeded scaffold grown in static culture for 14 days, and MR images of the same scaffold. Highlighted on the velocimetry map (left) is the largest impediment of flow, represented as a large area where velocity is 0 mm/s. MR images [241] acquired with a spin echo pulse sequence show the sagittal and axial projections of slices that show dense areas of cells that correspond with the location of the area of no flow. 178

Figure 6-10 As displayed in the previous chapter, cell seeded scaffold that cells have been pre labelled with magnetic nanoparticles, seeded at 1×10^6 per scaffold and then cultured for 14 days in static conditions. A) Gradient echo 1mm sliced images and B) spin echo 1 mm sliced images to visualise labelled cell location within scaffolds. C) Schematic of scaffold and images showing clustering of labelled cells on outer surfaces of scaffold. 181

Figure 6-11 Signal intensity MR images from cell seeded scaffold cultured for 14 days in growth media under static conditions imaged using different MR image acquisition methods A) Gradient echo image acquisition and B) spin echo image acquisition of sagittal slices showing locations of labelled cells on scaffold from which velocity was mapped. 183

*Figure 6-12 Cell seeding efficiency of cells labelled with magnetic nanoparticles compared to unlabelled cells seeded with the same seeding method onto identical scaffolds. Scaffolds were seeded and left for 3 hours to attach before cells were harvested, and DNA was quantified and compared with DNA content of total cell suspension. **p<0.002 (n=3)..... 185*

Figure 6-13 Bulk measurements of velocity to produce velocimetry maps showing distribution of flow velocity through scaffolds without cells (top), and cultured with cells for up to 28 days with chondrogenic media (bottom). Velocity was measured using NMR and MRI velocimetry methodology. 187

*Figure 6-14 Box Plots showing distribution of velocity and average velocity \pm standard deviation of flow through scaffolds without cells, and cultured with cells for 28 days with chondrogenic media. ****p<0.0001 (n=3). 188*

Figure 6-15 Relative frequency of peak pore velocities measured in scaffolds. The blank scaffold shows peak recorded velocities for a cell free scaffold. Day 28 shows peak recorded velocities for a scaffold that has been cultured under static conditions for 28 days in chondrogenic media..... 188

Figure 6-16 Blank scaffold and scaffold cultured for 14 days in static conditions using growth media. Histograms show the distribution of velocities taken from all pixel in velocity map, including peak pore velocities and velocities at pore walls..... 190

Figure 6-17 Blank scaffold and scaffold cultured for 28 days in static conditions using chondrogenic media including TGF- β 1 growth factors. Histograms show the distribution of velocities taken from all pixel in velocity map, including peak pore velocities and velocities at pore walls..... 191

Figure 6-18 Velocities extracted from each pixel in gap regions between scaffold wall and chamber wall, comparing range of velocities between blank scaffold and 14 day cell seeded scaffold cultured under static conditions in growth media..... 192

Figure 6-19 Velocities extracted from each pixel in gap regions between scaffold wall and chamber wall, comparing range of velocities between blank scaffold and 28 day cell seeded scaffold grown under static conditions in chondrogenic media..... 193

Figure 6-20 Sagittal sliced spin echo images acquired from cell seeded scaffold, cultured for 28 days in chondrogenic media. Images acquired every 0.5 mm as slices with a 14 ms echo time and 512x512 pixel array..... 194

Figure 6-21 Axial sliced spin echo images acquired from cell seeded scaffold, cultured for 28 days in chondrogenic media. Images acquired every 0.5 mm as slices with a 14 ms echo time and 512x512 pixel array..... 195

Figure 6-22 Sagittal slices selected from Figure 6-20 to more clearly show brighter areas in highlighted regions which indicate the presence of cellular material. Images acquired using spin echo method to produce 0.5 mm slices with a 14 ms echo time. 196

Figure 6-23 MSME images of both blank and cell seeded scaffolds grown for 28 under static conditions in chondrogenic media to compare regions of cells against those without. 198

Figure 6-24 Individual MR images of axial slices taken from a scaffold cultured for 28 days in static conditions using chondrogenic media. Slices show profiles of highlighted pores in relation to signal intensity to demonstrate increased signal in presence of cells compared to other areas..... 199

Table of Tables

<i>Table 2-1 Table summarising literature based on studies into the effect of perfusion flow for bone and cartilage tissue engineering applications.....</i>	<i>36</i>
<i>Table 4-1 Printing settings for scaffold designs including the programmed layer height, print head speed and the chosen needle tip diameter</i>	<i>64</i>
<i>Table 4-3 Scaffold Characteristics measured from SEM top view images. Table A lists measurements of pore size, strut size and porosity for pore size samples. Table B is the scaffold measurements for scaffolds with varied pore geometry. Geometry values are recorded as mean values \pm standard deviation taken from samples n=3.</i>	<i>74</i>

List of Abbreviations

μ -CT Micro Computed Tomography

μ -PIV Micro Particle Image Velocimetry

2D Two Dimensional

3D Three Dimensional

ADC Apparent Diffusion Coefficient

CAD Computer Aided Design

CFD Computational Fluid Dynamics

DEF Diethyl Fumarate

DMMB Dimethyl methylene Blue

DOCT Doppler Optical Coherence Tomography

ECM Extra Cellular Matrix

EDTA Ethylene Diamine Tetraacetic Acid

ER Extrusion Rate

FBS Foetal Bovine Serum

FDA Food and Drug Administration (US)

FDM Fused Deposition Modelling

FID Free Induction Decay

FLASH Fast Low-Angle Shot

FOV Field Of View

HA Hydroxyapatite

HMDS Hexamethyldisilazane

ihMSC immortalised human Mesenchymal Stem Cells

K-CG Kappa Carrageenan

MNP Magnetic Nanoparticle

MSME Multi Slice Multi Echo

OCT Optical Coherence Tomography

PBS Phosphate Buffered Saline

PBT Polybutylene Terephthalate

PCL Polycaprolactone

PEEK Polyether Ether Ketone

PETG Polyethylene Terephthalate Glycol

PET Polyethylene Terephthalate

PFA Perfluoroalkoxy Alkane

PGA Polyglycolic Acid

PLA Polylactide Acid

PPF Poly(propylene fumarate)

PVA Polyvinyl Alcohol

RF Radio Frequency

ROI Region of Interest

SEM Scanning Electron Microscopy

sGAG sulphated Glycosaminoglycan

SLA Stereolithography

SLS Selective Laser Sintering

SPION Superparamagnetic Iron Oxide Nanoparticles

TE Echo Time

TGF Transforming Growth Factor

TPMS Triply-Periodic Minimal Surfaces

TR Repetition Time

UV Ultra Violet

Acknowledgements

Firstly, I would like to thank my supervisors Dr Jing Yang, Dr Galina Pavlovskaya and Dr Joel Segal for the opportunity to undertake this research and for their continued support and guidance throughout my PhD.

I would also like to extend my gratitude to friends and colleagues, and staff in both the BDI RMCT group and SPMIC for all of the advice and help, both in and out of the lab.

Thanks to my family for their continued support to pursue my PhD, and thanks to my friends for always providing much needed relief in the form of beer and silliness.

Finally, I would like to acknowledge the funding support and research opportunities provided throughout my postgraduate studies by the Regenerative Medicine and tissue engineering CDT and the EPSRC.

1 Introduction

Tissue engineering is a multi-disciplinary field combining engineering and biological principles to resolve problems in medicine. Generally, tissue-engineering constructs are made using tissue forming cells, alongside a scaffold supporting structure and regulatory signals including mechanical stimuli and growth factors [1]. Tissues can be matured *in vitro* using either static culture methods, or employing bioreactors to culture tissue dynamically. Understanding the relationship between tissue regeneration in perfusion culture bioreactors and the physical design of porous scaffolds is crucial for understanding the biological responses to the environment cells experience. There are well documented benefits to culturing cells in a perfusion bioreactor, including increased mass transport for better diffusion of nutrients and gasses [2], the introduction of shear stresses to illicit certain cell differentiation responses [3, 4] and increased homogenous distribution of cells or extra cellular matrix [5]. In particular, the use of Mesenchymal stem cells (MSC) in bioreactors to differentiate to cartilage or bone has benefited from the aforementioned properties of dynamic culture. However, if these systems are not optimised for the desired tissue formation the results can be less successful. Examples of this include hypertrophic tissue formation [6] in cartilage tissue engineering, and high levels of cell detachment [7] or cell death from increased shear stresses [8]. Therefore, effectively characterising the interactions between the physical properties of the system and the biological response will go a long way to optimising the culture process and maximise tissue regeneration.

This thesis has taken an integrated approach, combining tissue engineering, additive manufacturing and magnetic resonance techniques to study the relationship between scaffold design and cellular response in the presence of perfusion flow. In particular, attention is focused on the culture of MSC in perfusion flow when seeded onto 3D printed scaffolds. 3D printing in recent years has become a popular method of scaffold fabrication, offering design process capable of more precise and complex porous

structures compared to more traditional examples of scaffold fabrication. Complex porous architectures are beneficial if they can ultimately be tailored to promote optimal cellular responses. Examples of this include introducing unique pore geometries [9] or pore gradients across a scaffold [10]. Interest in how 3D printing and design can be used to optimise scaffold performance has extended to considering scaffold properties in relation to dynamic culture and the use of bioreactors.

Bioreactors introduce the movement of culture media through scaffolds, the velocity and forces associated with this hydrodynamic environment are in part influenced by the shape and size of pores. Pore size has been shown to be inversely proportional to cell detachment [7], whilst non uniform distributions of pore sizes has resulted in almost three fold variation in shear rates across a scaffold [11]. Equally, varying pore geometry has a distinct influence on characterising optimal flow rates [12].

Furthermore, considerations must be made for how far the size and shape of pores change with cell proliferation and ECM deposition, and the resulting differences in shear stresses [13, 14]. Pore characteristics also play a role in the dynamic seeding efficiency of cells. Varying the architecture of pores but maintaining all other variables saw a seven fold increase in cell seeding efficiency for one study [15]. All of these factors compound the need for a comprehensive understanding of the relationship between scaffold properties and the fluid dynamic environment cells experience as a result.

Most experimental studies into dynamic flow environments in tissue engineering involve running cell culture experiments alongside computational fluid dynamic predictions to assess the final outcome of cell response. This data is limited to the assumption that the cell culture system is behaving in line with modelling predictions with no real way to assess how far this is true. Some studies have included the use of particle tracers [16] and optical imaging [17] to give more insight into fluid movement through a scaffold, however the invasive nature, and limitations in the extent of materials that can be probed do not make either the most ideal solution.

In this thesis, an alternative method is proposed in the form of NMR and MRI as a technique able to effectively probe opaque materials non-invasively to produce velocimetry maps. NMR velocimetry and MR Imaging can be used to obtain images containing information on velocity and acceleration of liquids. It is useful for measurements in porous materials as NMR is able to distinguish between chemically different substances, and distinguish between moving and stationary phases in a system. Firstly, this approach was used to assess a range of scaffold architectures under the same flow conditions and produce velocity maps. From this, data could quantify how far flow conditions varied by scaffold design, and also variability between scaffolds of the same porous architecture. This information is important for quantifying initial parameters in a perfusion culture experiment, however as the system is dynamic and the pore characteristics are likely to change in time with tissue formation, quantifying the effect of this is an important consideration.

Fluid velocity measurements using NMR approach was used for cell seeded scaffolds. Cell ingrowth into pores over the *in vitro* culture period is one of the most challenging elements of cell culture to monitor and assess the effects this has in the hydrodynamic environment. Measuring how far the velocity of fluid changes over a long culture time, in conjunction with traditional cell culture techniques to assess cell growth and ECM production to identify relationships between cellular response and changes in fluid velocity. MR imaging holds the ability to produce high-resolution images using non-invasive and non-destructive techniques, evident in its popular use in clinical imaging. Low sensitivity can be one drawback, but this usually overcome with the inclusion of contrast agents. Emerging magnetic nanoparticle technology in recent years is one such contrast agent that in particular is of great interest to cellular applications.

Monitoring cell migration and infiltration into scaffolds, especially when seeding and culturing is dynamic is important for ensuring homogenous growth, cell-cell interactions and good cell attachment. Seeding into the architecture of scaffolds is more difficult when compared to monolayer cultures, and the interconnectivity and

complexity of the porous structure have to be considered. Visualising cell locations over time in culture using MRI as a non invasive technique would be a useful tool to establish how cells migrate into scaffolds, and how much this can be improved by the use of perfusion culture. The inclusion of magnetic nanoparticles is necessary to provide adequate contrast to locate cells within the porous matrix. Throughout this project MR imaging and NMR techniques have been used to aid the dynamic tissue culture process for 3D printed scaffolds in order to try and provide unique insights into how that culture system changes with time and how cellular response is guided by the physical interactions with flow.

1.1 Project Overview

This thesis draws upon additive manufacturing, tissue engineering, fluid mechanics and NMR/MRI techniques for interdisciplinary study into the relationship between fluid hydrodynamic environments and *in vitro* cell responses. The initial part of the thesis (Chapter 1) introduces background for tissue engineering and scaffold fabrication, specifically covering research aimed towards cartilage tissue regeneration. Further to this, literature on bioreactors and dynamic culture is explored with a focus on how porous architecture has been studied currently in relation to fluid culture environments. Chapter 1 also introduces the basic principles of NMR/MRI, before extending more specifically into its use in velocimetry measurements. Chapter 2 covers methodologies used across the duration of the project. The first experimental chapter (Chapter 3) presents NMR and MRI velocimetry studies to produce velocity maps for cell-free scaffolds manufactured with a variety of pore geometries and pore sizes. The next chapter (Chapter 4) expands the use of MRI to imaging cell seeded scaffolds, in which cells have been labelled with magnetic nanoparticles, in order to image cell infiltration and migration into scaffolds under dynamic culture conditions. In chapter 5, NMR and MRI velocimetry methods have been combined with cell seeded scaffolds to assess changes in the hydrodynamic environment in relation to cell proliferation and ECM production. This thesis ends with an overview of the results and discussions that arose

from this research, and covers any future research progression possibilities (Chapter 6).

2 Literature Review

2.1 Cartilage Tissue Engineering

Tissue engineering seeks to provide methods to assist the regeneration of tissues, which, for a variety of reasons, are not being suitably repaired by the body itself. Commonplace in tissue engineering is the use of scaffolds to act as a replacement extracellular matrix (ECM) onto which cells can organise into a three dimensional architecture. The requirements of the scaffold will vary depending on the intended tissue to be regenerated, but with respect to articular cartilage the mechanical strength of the structure must be able withstand the forces the native tissue undergoes [18]. Alongside this, the scaffold must exhibit good biocompatibility, a degradation rate in line with the growth of the natural tissue, and provide a porous environment. Such environments can facilitate cell migration, proliferation and adhesion in addition to the passage for mass transfer of nutrients and waste products [19]. Designing a scaffold that fulfils all this criteria, and provides optimum tissue growth is key to the success of tissue engineering and regenerative medicine.

Articular cartilage is a well organised structure, made up predominantly of extra cellular matrix, consisting largely of collagen and proteoglycans, and a small number of chondrocyte cells making up less than 10% of the tissue wet weight [20]. The ECM is arranged in such a way that the mechanical properties and cell morphology varies with the depth of the tissue [21]. These variations have been defined by four distinct zones; the superficial zone, the middle zone, the deep zone and the calcified zone. Water decreases as it the progresses from the superficial to deep zones. Flow of water through the tissue and across the articular surface is important for lubrication

and the distribution of nutrients. Water also plays a crucial role in the tissues ability to withstand loads, resulting from a combination of frictional resistance of the matrix to the flow of water due to low permeability, and the pressurisation of water [22]. In osteoarthritic joint the amount of water present increases to around 90% [23], which serves to disrupt the surrounding matrix and increase the tissues permeability. This causes a decrease in the elastic modulus and therefore the ability of cartilage to load bear [23].

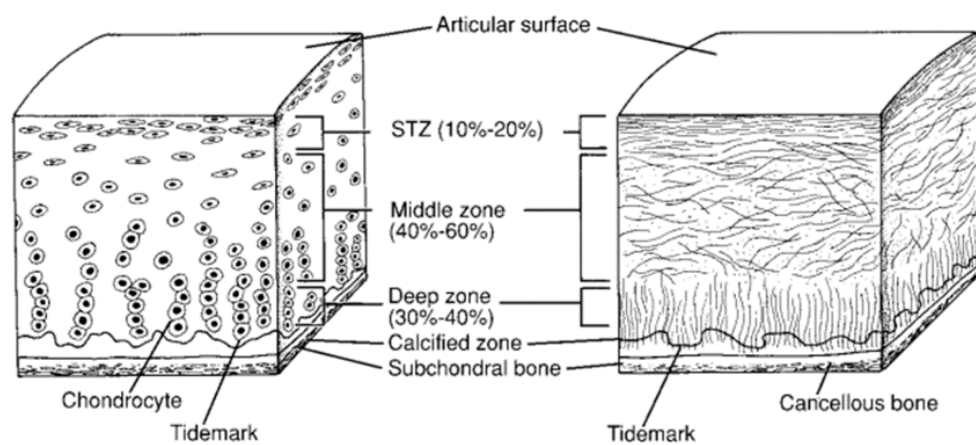


Figure 2-1 Layered structure of both chondrocyte cells and collagen fibrils in articular cartilage [24]

Cartilage can be understood as a biphasic model, consisting of a fluid and solid component when considering the tissue in compression. Fluid moves through the porous solid matrix, and when cartilage is compressed there is a pressure gradient created, causing fluid to flow through, or even out of the permeable tissue. The flow created causes frictional resistance, and it is this resistance that gives rise to frictional dissipation which contributes mostly to the viscoelastic properties of cartilage [25, 26]. There are three forces that act in unison to actively balance externally applied forces; the stress in the deforming collagen matrix, the pressure within the fluid phase and the frictional resistance between the solid and fluid phase created [25].

Cartilage is described as an avascular tissue, such that it has a very poor blood supply meaning that any subsequent wound healing response is often an insufficient one, and any repairs that can be carried out by chondrocytes are often incomplete [27]. The low numbers of chondrocytes present in cartilage is coupled with a dense extracellular matrix, which limits the ability of chondrocytes to migrate. Cartilage also lacks neural and lymphatic systems, as well as local progenitor cells which have the ability to differentiate into chondrocytes [28] and have been successfully isolated from chondrocytes [29]. The tissue has also been described as having high number of protease inhibitors which can inhibit efficient tissue repair [30]. A combination of all these factors indicate why it is so challenging to restore full tissue function without intervention.

2.1.1 Cell based approaches

There are two main cell sources used in cell-based approaches, the resident cartilage cell chondrocytes, and mesenchymal stem cells which are mainly isolated from bone marrow or adipose tissue. Adult chondrocytes are found in very low numbers and therefore can be more difficult to source. Early attempts to expand chondrocytes *in vitro* using a monolayer culture resulted in the cells dedifferentiating, losing their phenotype to consist primarily of collagen type I [31]. This expression of collagen I is more associated with that of a fibroblast phenotype. Cell differentiation however is not unidirectional and is reversible. Culturing in a 3D environment has been found to be influential in chondrocytes regaining their phenotype compared to 2D environments [32].

An often-researched alternative source is mesenchymal stem cells (MSC). Isolation from their respective tissues is simpler than chondrocytes, and they can be expanded in monoculture, with a much higher proliferation rate than chondrocytes [33]. *In vitro* studies have shown that with the addition of growth factors, MSC's will undergo chondrogenesis, showing increased ECM and collagen type II production in addition to

down regulation of collagen type I gene expression [34-36]. Often the resulting tissue although technically cartilage, differs from that of natural articular cartilage, often having much lower collagen contents than that required to bear weight [37]. Another limitation surrounding the use of MSC's is their tendency to differentiate into hypertrophic chondrocytes, which is indicative of endochondral bone formation as opposed to cartilage [38]. Therefore, in order to meet their potential the conditions for the proper differentiation of MSC's into suitable cartilage tissue needs to be developed.

Scaffold free approaches either rely on the self-organisation or self-assembly processes. Self-organisation involves an external energy or force to create order in a system, as opposed to self-assembly which spontaneously forms from disorder without any requirement for external stimuli or force [39]. For tissue engineered cartilage the predominantly used methods are self-organisation via cell sheet engineering [40], and aggregate engineering [41], and then the self-assembling process [42]. Scaffold free cell based approaches can circumvent some issues surrounding the use of scaffolds, such as their degradation profiles, cells are not exposed to any harsh processing techniques that could limit their viability, in addition to their high cellularity benefiting integration when implanted. From a mechanical point of view, the mechanotransduction forces being applied directly to the scaffold free structure, eliminates stress shielding that can occur in scaffolds [39].

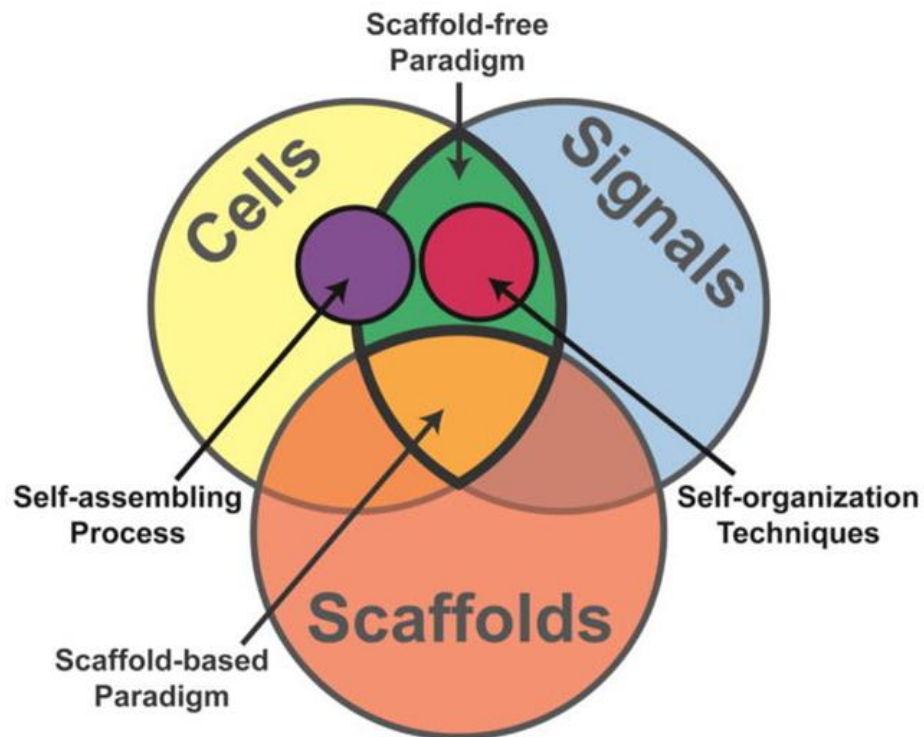


Figure 2-2 Tissue engineering paradigm consisting of cells, signals and scaffolds displaying where scaffold free techniques would fit in this paradigm. Image from GD DuRaine et al. [42].

2.1.2 Scaffold strategies

The more popular approach in tissue engineering is to incorporate a scaffold with cells to enhance tissue formation. The role of a scaffold should be to provide adequate structural strength to support tissue growth in its natural environment, be biocompatible with surrounding tissues, degrade at a rate that is consistent with the rate of formation of the new tissue, and provide suitable porosity and interconnectivity to allow appropriate cell migration and efficient nutrient exchange [28]. Scaffolds are fabricated via a variety of techniques from synthetic or natural materials. The vast options of material and fabrication methods, allows for properties such as mechanical, and chemical composition to be altered according to desired tissue. The major benefits of incorporating a scaffold is the provision of a 3D structure, which can be

beneficial to the differentiation of chondrocytes and maintenance of their phenotype, the initial mechanical strength that is required *in vivo*, and enhancement of cell retention.

2.1.2.1 Solid Porous Scaffolds

Solid scaffolds are a popular choice for cartilage and bone tissue engineering due to superior mechanical properties compared to semi-solid hydrogel methods. Methods of fabrication for solid scaffold facilitate the design and fabrication of internal pore architectures. Synthetic polymers to produce scaffolds for cartilage tissue engineering benefit from including a range of FDA approved materials that allow for material properties to be tuned to specific purposes. For example 3D printing Polycaprolactone (PCL) scaffolds, tuning the mechanical properties was achieved by lowering the molecular weight of PCL and pore architecture [43], altering the macro and micro porosity [44], and altering the orientation of filaments from linear to sinusoidal [45]. However, the use of synthetic polymers for solid scaffold formation can be limited by a lack of affinity for cell adhesion, such that methods to alter surface properties have been researched to improve cell surface attachment. For instance, the hydrophobicity of PCL limits cells ability to adhere, preferring to adhere to hydrophilic materials. Co-polymers creating from blending PCL with other more hydrophilic materials, including other synthetic polymers [46], and natural materials such as chitosan [47] and collagen [48]. Further to this, scaffolds can be fabricated entirely from natural materials, including decellularized cartilage to promote cell adhesion [49] as it better mimics the natural environment cells would experience *in vivo*.

2.1.2.2 *Hydrogel Scaffolds*

Hydrogels are best described as a network of hydrophilic polymers, which are either physically or covalently cross-linked. Hydrogels have gained popularity in the field of tissue engineering due to their unique compositional and structural similarities to living tissues, in particular the extracellular matrix [50]. The viscoelastic properties of hydrogels can further make them an attractive prospect for cartilage regeneration, a tissue that displays this property naturally. However concerns over mechanical strength being inferior to native cartilage [51] could hinder the use of hydrogels for a weight bearing tissue, such that additional reinforcement maybe required [52]. Recent advancements in hydrogel design and manufacture have shown scope to increase the overall stiffness and strength including multi-material scaffolds and nanocomposite hydrogels, Multi-material scaffolds utilise chemical crosslinkers to improve linkages between single polymeric components and the overall characteristics [53].

Nanocomposite hydrogels, which use additional nanoparticles to change the physical properties of scaffolds using the chemical functionality of the nanoparticles to act as cross linkers between polymer chains [54]. Therefore, there is scope to improver and modulate mechanical properties to levels deemed more appropriate for load bearing applications.

2.1.3 Scaffold Fabrication

Given a 3D culture is able to provide a more physiologically relevant environment that is used to guide cell fate and improve their function much effort has been put into to the development and fabrication of scaffolds to adequately facilitate this. In cell aggregates there are issues surrounding cell death through lack of mass transfer [55], and issue which can be negated with the use of a scaffold. Porous scaffolds are designed with a number of important considerations in mind. The scaffold must provide an adequate volume of surface area to provide cell adhesion sites, whilst simultaneously providing enough pore space to allow the free flow of liquids, gases

and nutrients to reach all cells whilst supporting the structural shape of a tissue [56]. A number of methods have been employed to fabricate scaffolds in the field to achieve these criteria, some of which are discussed below.

2.1.3.1 Conventional methods of scaffold fabrication

Solvent casting and particulate leaching work in combination to firstly cast a polymer solution leaving behind a polymer matrix with salt particles throughout once the solvent has dissolved. These particulates are then leached out by immersing the structure in water to form the pores [57]. However the use of salts to act as a porogen limits the viable wall thickness to a maximum of 2 mm to facilitate porogen removal, such that porogens can become trapped and achieve non-uniform distribution limiting control over and reproducibility of the porous structure [58].

Another fabrication technique uses a foaming agent added to a polymer phase to generate an inert gas. The porous structure is then created by removing the dispersed gas phase from the continuous polymer phase, resulting in the nucleation and growth of gas bubbles in the polymer [59]. Gas foaming does not require the addition of any solvents which can benefit its biocompatibility. However there are difficulties surrounding controlling the interconnectivity, as often during fabrication large closed pores sometimes form in the structure [60].

In a further technique, phase separation, scaffolds are formed using a thermally induced reaction to produce a liquid-liquid phase, one phase polymer rich and one phase polymer poor. Solvent is then removed, and the spaces left behind by the solvent become pores [57]. Although a porous structure is formed, this method can be limited in tissue engineering largely by having a small range of possible pore sizes, usually below 200 μm which would limit applications in some applications, particularly bone tissue engineering which tends to use larger pore sizes. This is combined with difficulties in controlling the macro and micro structures of the scaffold [60].

2.1.3.2 3D printing

Conventional scaffold fabrication methods are process dependent and limited by a lack of control over precise architectures, the variety of pore structures that can be formed, and are often labour and time intensive with multiple steps required [58]. It is the lack of control over architecture that can be most detrimental to the success of the scaffold, potentially leading to inadequate migration of cells into the scaffold, and appropriate levels of nutrient exchange [61]. This hinders the overall progression of 3D tissue formation. 3D printing offers an option to circumvent these issues, a design dependent process, it offers much greater control over scaffold design. Thus, reproducibility and potential complexity of design can both be increased [62].

2.1.3.2.1 Selective Laser Sintering

Selective laser sintering (SLS) is a fabrication technique that dispenses a layer of powder, after which the powder particles are sintered together in the desired design using a laser beam. Once the first layer has been deposited on a surface, the process is repeated, to build up a layer by layer design on top of the pre-existing layers [63]. Post processing of the scaffold can include dissolving any unsintered polymer particles [64]. Commonly used polymers in SLS manufacture of biocompatible scaffolds include polyetheretherketone (PEEK), polycaprolactone (PCL), poly vinyl alcohol (PVA) and poly(lactic acid) (PLA) [65]. SLS technique has the ability to sinter polymers with bioactive ceramics such as hydroxyapatite and tri-calcium phosphate making it an attractive option for bone tissue engineering [63, 66, 67]. Parameters of scaffolds can be changed by altering the laser scanning speed, which in turn alters the density of the construct. Sufficiently high energy promotes better melting of powders and can therefore produce a high density structure. Producing a higher density material can improve the mechanical properties of the scaffold but this can at the expense of accurate dimensions [68]. Williams et al. processed bone scaffolds using SLS to try and accurately control pore size and porosity, but found that the actual

fabricated scaffold porosity differed from that of the design of the scaffold, with actual scaffold porosity 30-40% lower than designed scaffold [63]. In another study the effects of SLS parameters on the pore morphology of scaffolds and established that layer thickness had the greatest effect on the average pore size, and the number of pores that are properly able to facilitate bone regeneration [69].

2.1.3.2.2 *Fused Deposition Modelling*

Fused deposition modelling (FDM) is a printing technique reliant on the rheological properties of thermoplastic polymers. Melted material is extruded through a nozzle and deposited onto a stage, with new layers of material fusing with the previously deposited material in order to generate a 3D structure layer-by-layer [70]. FDM has the ability to change the orientation of material struts for each deposited layer, in addition to the spacing between struts, which in turn allows high control over the pore morphology and interconnectivity of the structures being designed [58]. FDM has been successfully employed to produce porous scaffolds that have both appropriate mechanical strengths and provide an appropriate environment for tissue in-growth [9, 70]. The effects of altering the pore structure using extrusion based methods on cell proliferation has also been studied to indicate the control given by this method can be used to improve regeneration capabilities [10]. This high control can however be restricted by the conditions under which they are processed, FDM is often associated with high temperatures, pressure and shear rates during extrusion [71]. These conditions may affect the final geometry and composition of the material. A number of process parameters can be altered in an attempt to optimise aspects such as dimensional accuracy and surface roughness, including layer height, extrusion pressure, and angles but the actual attainable range of these parameters can limit FDM designs [72]. That said the level of control that FDM does possess means it has the capabilities to form physical gradients in all directions within the scaffold [73]. This has been utilised to create scaffolds for osteochondral regeneration, with a varied pore

size which seeks to more accurately represent the structural variations in the natural tissue [74].

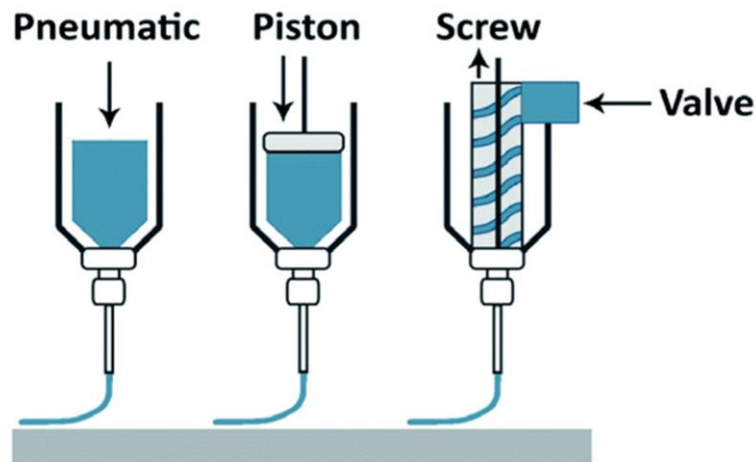


Figure 2-3 Schematic examples of extrusion based 3D printing technologies. Image modified from [75]

2.1.3.2.3 Stereolithography

Stereolithography (SLA) utilises photopolymer resins and exposes them to a single laser beam in order to crosslink or polymerise the material. The liquid photopolymer resin is scanned over by the light beam layer by layer forming cross-linked polymer structures [62]. A post curing treatment is carried out using UV light to ensure the total conversion of reactive groups is complete which often improves the mechanical properties [76]. The kinetics of the curing reaction can determine the thickness of each layer, and the cure depth is determined by the energy of the light the resin is exposed to. Various parameters can be changed to control this energy and fine tune the kinetics including the light source, scanning speed, and exposure time [76].

Traditionally SLA is a bottom up approach, with the bottom layer created first and the structure built up from there, but there has been increasing interest in top down approaches which involves every newly fabricated layer is formed beneath previous

layers and photo induced polymerisations occurs from irradiation beneath. This approach has a lot of potential as it requires less resin, produces a smoother surface finish [73]. However, as the fresh layer of resin is always in contact with the oxygen in the air as opposed to immersed in the vat of resin, it can result in inhibited photopolymerization resulting in incomplete surface curing [77]. A limitation associated with SLA is the few commercially available biocompatible materials that can be used [76]. Tissue engineering constructs using SLA have been fabricated however using poly(propylene fumarate) [78], polycaprolactone [79] and poly (D,L-lactide) [80]. SLA does benefit from a very high resolution of up to 1.2 μm [81], which can be valuable when creating complex structures however the specificity of this resolution is limited to only the z-direction [73].

2.1.4 Scaffold Materials

Biomaterials for use in scaffold fabrication have some basic requirements including biocompatibility, appropriate surface properties that allow for cell attachment, proliferation and differentiation [57]. Biomaterials are derived from either natural or synthetic sources. For the purpose of 3D printing, polymers come in a variety of forms, filaments for FDM, powder beads for SLS and liquid solution for SLA, each requiring different characteristics for their application [82].

2.1.4.1 *Natural Materials*

Materials derived from natural sources are an attractive option largely due to their innate biological functions providing benefits for cellular processes. For example using a polymer that is naturally occurring in the ECM of a tissue is likely to result in more cell attachment, and better mimic the natural ECM [65]. Natural polymers are classified into one of three groups, polysaccharides made up from sugars, polyamides made up from proteins and polynucleotides made up of chains of nucleotides [83]. Natural polymers are more widely used to form 3D hydrogel scaffolds using printing

technologies. Hyaluronic acid (HA) is a naturally occurring glycosaminoglycan that is a major component in intracellular regions of connective tissues, which makes it an attractive material for scaffold fabrication [84]. Many recent advances have been made to use HA for 3D printing of hydrogels for applications including neural and bone regeneration studies [85, 86]. Suri et al. [85] demonstrated that by photo-crosslinking HA could produce 3D scaffold structures with distinct geometries, by varying pore size, shape and controlled degradability.

Gelatin is a polymer of natural origin, and is derived from collagen hydrolysis [87]. Gelatin has a thermo-reversible quality such that it is in a liquid state above 30°C but forms a gel at below 20°C, which garners interest with 3D printing techniques [88]. Landers et al. [89] utilised the thermo-reversible properties of gelatin to manufacture hydrogel scaffolds with controlled pore structures, such that an appropriate surface coating and pore formation were able to facilitate cell adhesion and growth. This study however did not investigate the mechanical properties of the scaffold, which is always an important design parameter.

Alginate is a polysaccharide made up from repeating monomers of α -D-mannuronic acid and β -D-guluronic acid and is derived from algae [83]. Alginate has been used in rapid prototyping techniques to produce scaffolds with stable heterogeneous architecture, and with encapsulated different cell types was able exhibit ECM formation in the osteochondral graft [90]. Stereolithographic fabrication methods have also used alginate to create a scaffold with tuneable mechanical and degradation properties, in addition to facilitating the spatial organisation of multiple cell types. SLA was able to afford control over the spatial distribution and adhesion of both hippocampus neurons and skeletal muscle myoblast cells [91]. Methods of bio-printing have shown that collagen type II, one of the major components located in the ECM, used in conjunction with chondrocytes increased ECM production and successfully created a biomimetic cell density gradient [92]. The mechanical stability of printing with collagen II has been demonstrated using high-density collagen hydrogels, displaying a

modulus of 30kPa and successfully supporting cell growth [93]. Human cartilage has been found to possess a compressive modulus in the range of 0.44-20.4 MPa dependent on location [94], which is considerably higher indicating more may need to be done to make the aforementioned hydrogels more suited to regeneration of a weight bearing tissue like cartilage. A study comparing a number of natural materials for 3D printing demonstrated that alginate and agarose best supported the development hyaline cartilage and supported MSC viability [95] although this study was not all encompassing of all the aforementioned materials.

2.1.4.2 *Synthetic Materials*

The overriding benefit of synthetic materials is the ability to tune mechanical and degradation properties by altering the aspects such as molecular weights, degradation linkages and cross-linkers, instead of relying on inherent material properties. The control over physical properties and material chemistry also serves as a benefit in respect to reproducibility [96]. The most well researched synthetic polymers are those biodegradable ones that already have Food and Drug Administration (FDA) approval; polylactic acid (PLA), polyglycolic acid [97] polyfumarates, polyorthoesters, polycaprolactone (PCL) and polycarbonates [57]. Poly(lactic) acid (PLA) is an established choice of biomaterial for 3D printing, and has been used to successfully produce high resolution 3D structures [98]. A popular thermoplastic choice for FDM due to its melt temperature of around 175°C and processing temperatures in excess of 190°C, it is ideal for extrusion based methods [99]. Additionally PLA is cheap, biocompatible, and biodegradable [83]. PLA has also been shown to have good mechanical properties as a polymer, but has a lower compressive strength than that of bone, which considering its common use in bone tissue engineering applications serves as a limitation [82]. Attempts to overcome this are being made via the

incorporation of ceramics, dispersing high modulus inorganic particles of material like hydroxyapatite within the PLA matrix to increase mechanical properties [100].

Poly(propylene) fumerate (PPF) is a photo cross-linkable polymer used in solution with diethyl fumarate (DEF) has been studied extensively for use in stereolithography. Mechanical properties and viscosity of the material are dependent on the ratio of DEF to PPF, DEF decreases viscosity but increases the mechanical strength of the material [101]. One study optimised this ratio as 60:40 weight ratio PPF/DEF, in addition to optimising the laser parameters, in order to successfully print 3D structures with controlled architecture [102]. As a biomaterial PPF has potential as it is simply degraded by hydrolysis of its ester bonds in to non-toxic products [103]. To assess the biocompatibility Fisher [104] investigated the tissue response to photo cross-linked PPF scaffolds in cranial defects in a rabbit model. Results showed only a mild tissue response in both soft and hard tissues indicating its suitability as a biomaterial. The superior rheological and viscoelastic properties of PCL under heating compare to many other resorbable polymers, coupled with its low melting point and thermal stability means it has attracted a great deal of interest in heat extrusion based methods of 3D printing [105]. PCL is degraded by hydrolysis, but has a much longer degradation rate than other polymers, and can take up to 24 months to complete the process [83] which could limit the variety of tissues types PCL scaffolds could be used for. Hutmacher used FDM technique to print 3D scaffolds, and display not only that they possessed good mechanical properties but also excellent biocompatibility when cultured with human fibroblasts and periosteal cells [9]. A more recent study showed that MSC's were able to adhere to and proliferate on PCL scaffolds, although in this study cell viability was lower than that of the control group [106]. Modulating the mechanical behaviour of 3D printed PCL scaffolds was achieved by not only altering the pore geometric configurations, but also the molecular weight of PCL. PCL with a molecular weight of 45,000 g/mol demonstrated feasibility to print non-brittle scaffolds with an appropriate compressive modulus to produce flexible, visco-elastic load bearing scaffolds ideal for cartilage tissue engineering [43].

2.2 Dynamic Cell Culture

2.2.1 Bioreactors

Bioreactors have become a popular tool in cell culture to increase the delivery of nutrients, mass transport and mechanical stimuli to cells in order to influence proliferation, differentiation and ultimately tissue formation. Examples of bioreactors used in cell culture experiments for cartilage tissue engineering include perfusion bioreactors [107], spinner flask [108], and rotating wall bioreactors [109]. The success of static culture is often limited by poor mass transport as diffusion is the only mechanism by which nutrients are delivered to cells, and waste products removed [110]. Perfusion bioreactors work to create microcirculation to better simulate *in vivo* environments than spinner flask or rocking bioreactors [110, 111]. Perfusion bioreactors have been used successfully in conjunction with MSC's for both osteogenic [5, 112, 113] and chondrogenic [3, 114] differentiation showing the potential benefits over static culture. However, the rate at which fluid is perfused through cell laden scaffolds and the resultant forces has to be properly understood and quantified. In some cases, for chondrogenic differentiation of MSCs, flow perfusion was seen to increase hypertrophic matrix components and reduce GAG release [6]. In this study the hypertrophic marker, osteocalcin was significantly elevated when MSC's were exposed to flow perfusion for 10 days compared to static culture, which could indicate a move towards osteogenic differentiation. Reduced chondrogenic potential was also evident when comparing the levels of GAG released, levels were lower in samples exposed to flow compared to static culture. Additionally, research has shown that dynamic culture can suppress chondrogenic differentiation when the oxygen tension was not lowered within the bioreactor [114]. Similarly, cell seeding efficiency and the rate of cell detachment is influenced by the rate of perfusion, and can be optimised by increased understanding of the physical properties of flow and cells within the internal scaffold environment. Koch et al was able to show how initial cell seeding and attachment were influenced by fluid velocity and the

number of cycles used in their oscillating perfusion system, and achieve uniform distribution and attachment a minimum fluid velocity had to be exceeded [115].

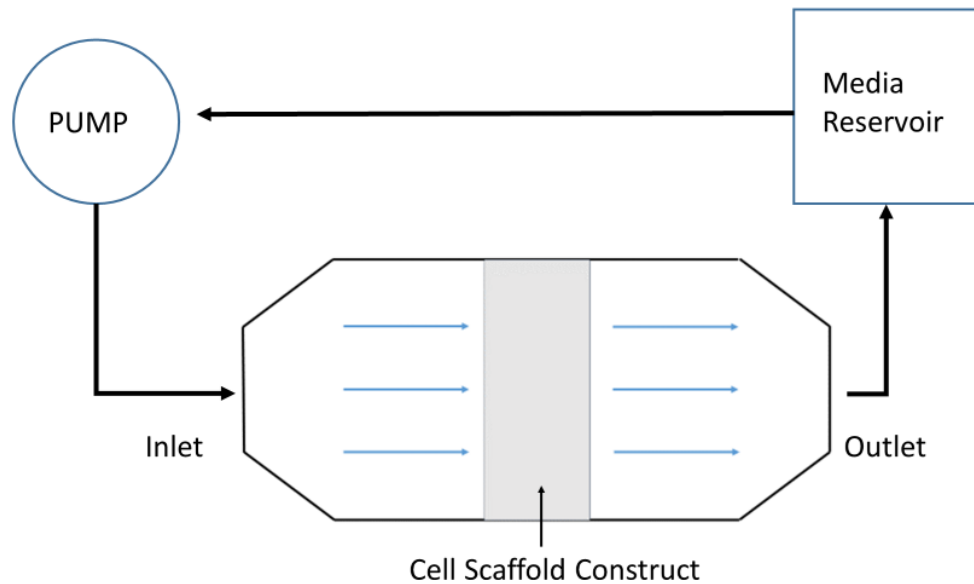


Figure 2-4 Schematic showing basic principles of Perfusion bioreactor

Real time experimental investigations to quantify cell adhesion inside scaffolds in perfusion systems is difficult. Alternative numerical modelling methods have been used and been able to show that increasing perfusion and the associated pressure, leads to a shorter contact time between cell and substrate and higher hydrodynamic forces increasing the chances of adhesion failure [116]. McCoy et al. studied cell behaviour under perfusion in conjunction with the effects of the scaffold pore size in which cell detachment was proportional to increasing flow rate, but inversely proportional to the scaffold pore size [7]. In order to optimise bioreactor function the operating conditions, the behaviour of cells and the design of scaffolds all need to be understood individually and how they interact with each other to determine the overall success of the system.

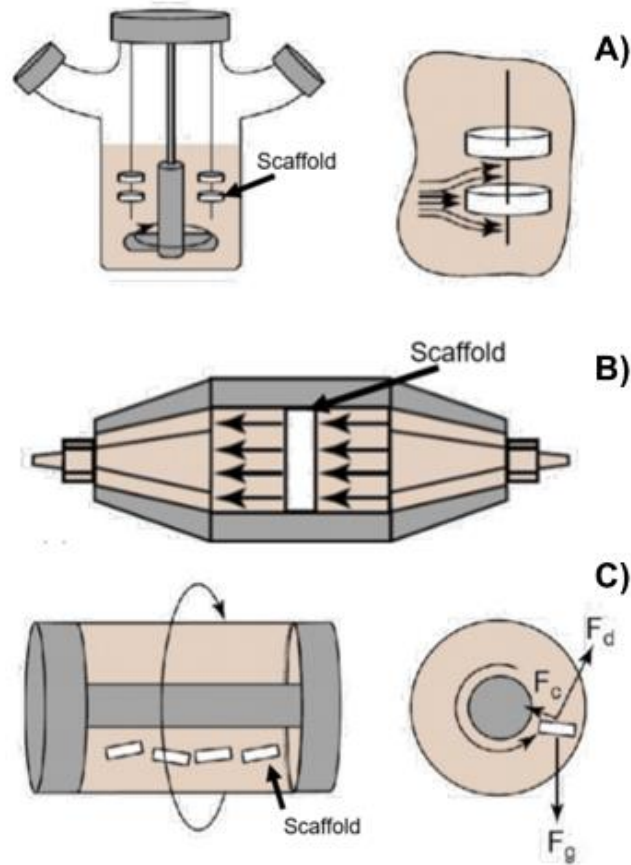


Figure 2-5 Examples of bioreactors A) Spinner flask bioreactor B) Flow perfusion bioreactor and C) rotating wall bioreactor. Adapted image from [117].

2.2.2 Porous Architecture

The fabrication of 3D scaffolds are designed with porous architectures in an attempt to provide the optimal microenvironment for optimal cell growth, mass transport and function. Since the development and introduction of 3D printing, which allows a much higher degree of control over the pore structure than traditional methods, increased interest has arisen in how this architecture affects the overall regeneration of tissues.

2.2.2.1 Cell Response

Despite extensive research, there are still limitations to scaffold design that hinder success. The homogeneous distribution of cells adequately throughout a porous scaffold and then to ensure that these cells, even at the very core of the matrix have an adequate supply of oxygen and nutrients remains a challenge. The scaffolds needs to provide an environment that is characterised with appropriate structural properties to influence cell behaviour [118]. Both static and dynamic culture can be limited by insufficient cell penetration, implying there are more factors at play than just culture conditions. One study showed scaffolds cultured *in vitro* using spinner flasks tended to have much higher cell densities at the periphery compared to the centre of the structure creating an oxygen gradient [119]. Conversely to this another study using static culture methods also showed limited homogeneous distribution when osteoblasts cultured onto polymer foams only reached a penetration depth 240µm [120] regardless of the variation in pore size. In addition to adequate cell penetration and mass transport of nutrients, a highly porous interconnected structure is also vital for the removal of waste products [121]. Despite the requirement of interconnected pores large enough to facilitate this mass transport and the migration of cells, there still needs to be adequate material surface area to allow proper cell adhesion, such that a balance between the two needs to be found. Significant differences are found in cell attachment when cells cultured with scaffolds of different mean pore sizes, with results indicating a strong correlation between increasing surface area and increased cell attachment [122]. In the case of tissue engineering models that include the use of MSCs, how the cell differentiation response differs in respect to changes in the pore architecture has also been studied. One study showed increasing pore size from 94 µm to 300 µm significantly increased cell proliferation and chondrogenic gene expression [123]. This study was carried out in static culture conditions, indicating that changes to scaffold porous architecture alone is enough to influence cell differentiation response. Similarly, increased expression of chondrogenic genes has also been shown through altering the pore geometry for 3D printed scaffolds [124]. Therefore,

with advances in 3D printing and design driven scaffolds, to optimise these designs for cell responses, a number of factors relating to the pore architecture are up for consideration.

2.2.2.2 *Mechanical Properties*

Not only does the internal porous structure play an important role in cell penetration and migration, it also influences the physical properties of the structure, therefore in designing a scaffold both the mechanical properties and cellular interactions have to be considered in unison. The total porosity, the pore size and distribution, and the pore geometry are all key parameters, which need to be finely balanced for optimal biological and physical characteristics [125]. It is commonly demonstrated that an increase in porosity tends to decrease the overall mechanical properties of scaffolds [126]. With the introduction of 3D printing, much more complex architectures can be fabricated and as a result, there are more parameters, which could affect mechanical properties. Pore morphology can be altered by varying strut morphology for instance Lee et al. evaluated the difference between lattice, staggered and diagonal struts. It was found that lattice had the lowest compressive strength whilst diagonal had the highest [127]. Additive manufacturing allows for many parameters to be changed in unison, for instance one study varied pores size by changing strut diameter, spacing between struts and the strut orientation [128]. Results of dynamic compression displayed evidence that by changing these parameters, the resulting increase in overall porosity subsequently decreased the dynamic stiffness of the scaffolds. Porous architecture can also be varied by introducing gradients to structural designs. Porosity gradients have been achieved using distinct strut space models 0.7, 1.0 and 1.4 mm stacked on top of one another [129]. Compared with uniform porosity the gradient scaffolds displayed similar compressive modulus to those with large (900 μm) and medium (500 μm) pore sizes but significantly lower than uniform small pores (200 μm). Therefore, particularly for tissues associated with load bearing, in which more focus is put upon the mechanical characteristics, efforts to optimise pore architectures for cell

behaviours should not be done at the expense of the overall mechanical properties. In fact, it is also important to recognise that the structural properties of scaffold can also effect cell response. Increasing scaffold stiffness has been linked with different effects on cell differentiation and proliferation [130].

2.2.2.3 Pore size and distribution

Pore size is a key design parameter for scaffold fabrication, should the pores be too small then cell migration becomes limited causing them to dominate the periphery of the scaffold, which can in turn effect mass transport and waste removal. Equally, pores which are too large mean there is less surface area available and therefore limits cell attachment [131, 132]. Currently there are many contradictory studies on what optimal pore size should be defined as, for instance for cartilage regeneration some studies have stated the optimal pore size for chondrocyte proliferation and ECM production pore size should be between 90 and 250 μm [133-135]. However, other studies state that much larger pores of 400 μm are more beneficial for ECM production than the smaller pores [136, 137]. Interestingly, a study by Stenhamre et al [138] found that chondrocytes subjected to chondrogenic and osteogenic induction in scaffolds with larger pore sizes of 300-500 μm tended to differentiate into the osteogenic pathway. It is important to keep in mind fabrication techniques however when considering the effects of pore size. Scaffolds fabricated via methods like freeze-thaw [123, 139] do not afford the same level of control and repeatability over scaffold architecture as scaffolds fabricated via 3D printing [135].

Disagreements in what the optimum pore size would also suggest that it is not the only variable effecting cell fate, and many other variables could be involved including, material properties, pore geometry and pore interconnectivity. Indeed pore size varies as well depending on the tissue type, one study compared chondrocytes, osteoblasts

and fibroblasts with a variety of pore sizes. Results indicated that chondrocytes and osteoblasts both showed better cell growth in the largest pore size of 380-405 μm , but fibroblasts preferred smaller pore sizes 186-200 μm [140]. The way in which pore size is measured and characterised between studies is also important to consider. 3D printed scaffolds with homogeneous square pores, the pore size is most commonly characterised using cross sectional images taken from the top view of the scaffold, and measured as the distance between two struts in the X-Y plane [141]. However this is less straightforward when the pore shape becomes more complex and taking singular cross sectional measurements could vary wildly within a single pore depending on where the measurement was taken [142].

There is a degree of compromise between pore size and the mechanical properties of a scaffold. Therefore, any porous structure must be assessed accordingly. As pore size increases creating more open space in the construct the overall strength decreases [143]. In an ideal scenario, the scaffold displaying the best mechanical properties will also be the most favoured porous structure for cells. This was the case for Zhang et al. who found that the scaffold with the smallest pore size of 215 μm significantly improved cell proliferation and ECM production, but this coincided with results showing the scaffolds possessed the greatest compressive and tensile moduli as well [135]. The trade off in pore size and available surface area for cell attachment is also an important factor to be considered. Murphy et al. showed that an increased surface area did indeed improve initial cell attachment. However, by day 7 it was actually the scaffold with the largest pores that displayed the highest cell number. This indicated the ability of cells to migrate through the larger pores outweighed the initial high cell attachment in the scaffolds with a greater surface area [131]. The suitability of mechanical properties of scaffolds are often considered in terms of the mechanical properties of intended tissue for regeneration. Such that modulating the pore size and overall porosity of scaffolds using additive manufacturing techniques can be used to control and create scaffolds that possess similar properties to articular cartilage [144]. Many materials that have been used to produce scaffolds of appropriate mechanical

strength has been done so at the expense of retaining a high porosity, such that despite *in vitro* success, *in vivo* the scaffolds failed due to lack of vascularisation [121]. Other methods however can still be used to improve the vascularisation of scaffolds including the addition of angiogenic factors to increase vascularisation but this is still dependant on the scaffold structure allowing ingrowth into the entire construct. *In vitro* pre vascularisation can also increase vascularisation, this is achieved by adding endothelial cells to aid the formation a pre-vascular network [145].

2.2.2.4 Pore Geometry

Scaffold design is critical to how it will perform *in vitro* and when implanted *in vivo* due to the interactions with the physiological environment it has been implanted in, therefore the geometry of pores can also impact the success of a design [146]. Pore geometry is dictated by the size, spacing and orientation of fibres or strands within the scaffold, in addition to the space between said struts. The effects of altering these parameters on the overall mechanical performance of the scaffold has been studied. Moroni et al. [128] varied pore shape by decreasing fibre diameter, spacing and orientation in order to increase overall porosity. This resulted in decreased elasticity but an increase in the viscous properties of the scaffold, showing that pore geometry can be used to modulate the viscoelastic properties of scaffolds, something which is important in the regeneration of tissues like cartilage. A more recent study modulating strand size, spacing and orientation found similar results, but that it is the size and spacing, not orientation which significantly affect the overall porosity of the scaffold. This increase in porosity inversely affected the mechanical properties including the compressive and tensile moduli, but increased the viscoelasticity of the scaffold [43]. A study by Woodfield et al. found that scaffolds with reduced fibre spacing and therefore lower porosity had higher dynamic stiffness [147].

The same group went on to mimic the natural structure of cartilage ECM using fibre spacing, to try and improve cellular response. To do this they used heterogeneous

gradient fibre spacing which resulted in an anisotropic distribution of cells and GAG's [148]. Many other studies have sought to understand how pore geometry might affect cell behaviour. Two chitosan scaffolds with either defined geometry or undefined random geometry showed that proteoglycan and collagen type II production was improved in the scaffold with random and undefined geometry [149]. Contrary to this other studies comparing salt leached scaffold with 3D printed scaffolds, found that the more ordered architecture in the 3D printed scaffolds, provided a better environment for cells to expand, and better permeability and cell penetration [150, 151]. The overall shape of the pore geometry could also prove important to cell fate. Cubic and cylindrical pores have been directly compared in 3D printed scaffolds seeded with MSC's. Results showed that the cubic pores significantly increased the gene expression of MSC's undergoing chondrogenesis suggesting this was a better internal environment for the cells [124]. A comprehensive study by Souness et al. [146] investigated printed PLA scaffolds, with distinctive laydown patterns of 0/90°, 45/135° and 60/120°. The scaffold designs were compared based on their mechanical performance, swell ability, diffusivity, compressive strength, and metabolic activity with MC3T3-E1 cells. Scaffold with 0/90° had the highest degree of swelling, which can be important for ensuring nutrients are transported into the matrix. These scaffolds also exhibited the highest levels of diffusivity. In addition, like as in aforementioned studies, the scaffolds with the lowest porosity had the highest compressive yield strengths. The parameters under which the scaffolds were tested were weighted on importance, and the scaffolds were scored accordingly, and it was deemed that the pore geometry of 0/90° performed the best overall in accordance with the study criteria. It is evident that there is much more agreement in how pore geometry effects mechanical properties then there is in how cells are affected; therefore, an optimum design is still yet to be defined.

2.2.2.5 Interconnectivity and permeability

The ability of a scaffold to support cell attachment, differentiation and proliferation can also be influenced by the interconnectivity of the internal pore structure.

Interconnectivity can be described as the mean size of the opening between two neighbouring pores, although it is often considered in a more binary way, in which either the pores are connected or they are not [152]. Scaffolds with insufficient pore interconnectivity can hinder chondrogenesis and matrix deposition, whilst those with larger interconnected pores and a more accessible pore volume are better able to facilitate GAG deposition [153]. Control over the pore interconnectivity can be well achieved with 3D printing processes and has been demonstrated to improve cartilage tissue like formation. Malda et al. compared salt leached and 3D fibre deposition printed scaffolds, in which the porosity was comparable for both scaffolds but the interconnectivity was varied. The 3D fibre deposited scaffold with larger interconnecting pores showed a significant increase in GAG and DNA content [154]. The results of this study are supported by another making similar comparisons varying the interconnectivity of pores [155]. This latter *in vivo* study showed that the larger interconnecting pores were able to improve cartilage repair in skeletally mature rabbit models.

Scaffold permeability is described as combination of porosity, pore size and distribution, pore interconnectivity, pore interconnection size and distribution, and pore orientation [132]. O'Brien et al. assessed the permeability of scaffolds as a function of pore size and found that with increasing pore size permeability increased. However as compressive strength was increased the permeability of the scaffold decreased [132], highlighting again how an optimum between an environment beneficial for cells and the mechanical properties needs to be closely considered. Scaffold permeability can influence cell fate differently depending on the cell type in question. For instance decreased permeability has been shown to increase chondrocyte matrix production on the one hand, but a scaffold with 5 fold higher porosity and therefore increased

permeability showed that for bone marrow derived stem cells the larger pore structure facilitated their differentiation towards a chondrocyte lineage [156]. This shows that there are a number of variables that play a role in determining tissue regeneration, and there still remains a challenge in defining the most optimal internal architecture.

Pores can also be arranged in size dependent gradients, such that the size is not homogeneous throughout. Although evidence from one study has shown that the homogeneous scaffolds had superior static and dynamic mechanical properties, the scaffolds which possessed a gradient structure improved cell seeding efficiency [10]. The pore gradient was created using varied pore sizes from 100µm to 750µm and the internal pore architecture appeared to be better suited to penetration of cells during seeding and subsequently a homogeneous distribution of cells. This further reinforces the idea that there exists a need to compromise between the biological and physical performances in order to progress scaffold design.

2.2.2.6 Scaffold Surface Chemistry

Another important aspect of scaffold design is the role the biomaterial plays in the success of the seeded construct. The surface chemistry of the scaffold is integral for how easily and readily cells are able to attach to the scaffold, good cell-material affinity is even more important when working alongside the additional forces imparted by dynamic flow culture. Surface functionalisation can be used when designing biomaterials that have the ability to promote cell adhesion, growth and repair of the intended tissue. To achieve this biomaterials can be modified by radiation, chemically or physically [157]. Surface graft polymerisation is one method to chemically alter the surface by grafting a suitable monomer or protein to the surface to tailor specific properties. This process usually involves a surface activation process to create reactive sites, which can be done using methods like UV, plasma and radiation [158].

Plasma coatings can be used for hydrophobic materials to help improve cell adhesion. PCL is an example of a hydrophobic material that can be treated with plasma surface modification. Results from one study showed that plasma treated PCL samples displayed increased metabolic activity and showed a marked increase in cell proliferation compared to PCL alone [159].

2.2.3 Role of flow

The effect of fluid flow on tissue regeneration is necessary to be understood fully, as not only does fluid flow enhance nutrient transfer and waste removal, it may also provide important mechanical cues such as shear stress to cells which is important for their growth [160]. There has been an increased interest in dynamic culture, since in static culture nutrient gradients develop, whereby a situation occurs in which cells at the surface receive adequate nutrients, but this nutrient concentration decreases approaching the core [161]. Dynamic culture using flow is seen as a way to overcome this, but naturally, flow introduces a range of forces onto cells and scaffold alike which need to be fully understood in order to progress and optimise the regeneration of tissues. The porous architecture of scaffolds is an important variable in influencing the levels of shear stresses introduced to a system, and how they are distributed and therefore needs to be investigated in unison with how flow effects cells. The need to understand this is further compounded by the changes seen within the architecture, as tissue begins to regenerate and fill pores and the scaffold begins to degrade, and how this will change flow patterns in real time.

2.2.4 Cellular response to flow

2.2.4.1 *Shear stresses*

Shear stress is defined as mechanical load generated by fluid flow. Shear stress can act as a stimulus for chondrocytes to increase ECM production and their ability to

express a chondritic phenotype [162]. As a method of applying shear stress, there has been increasing interest in the use of perfusion bioreactors. Other tested bioreactors systems such as free floating, or rotating wall are limited because they have unknown or unregulated fluid flows [163], limiting the information that can be reliably acquired from these systems. When compared with static culture, using a perfusion bioreactor to introduce shear stress into the culture system has been, with seeded scaffolds shown a 118% increase in DNA content and 184% increase in GAG content over static culture [163]. The exact action of shear response on chondrocytes is unclear on how exactly it influences cell behaviour. Shear could influence the physical activation of growth factors [164], it could simply be the action of increased mass transport of nutrients [165] or the loading influencing cell maturation through transduction of fluid shear stress across cell membranes [166]. Therefore, in order to better understand the action of fluid induced shear stress there exists a need to develop a method to quantify fluid flow on cell seeded porous scaffolds and how it progresses over time.

2.2.4.2 Flow Distributions

In standard static seeding and culture methods, the distribution of cells throughout the scaffold is driven by diffusion. However it has been shown that the diffusion process in tissue is limited to a distance of approximately 200 μm , such that there is an insufficient supply of vital nutrients to cells at the centre of the scaffold [167]. Therefore, flow distribution throughout the scaffold is important to enhance the mass transfer of nutrients throughout a scaffold to ensure a homogeneous supply. The homogeneous distribution of cells is important for a homogeneous tissue growth and fluid flow during seeding can help to achieve that [168]. Cell seeding could also be enhanced by being carried out in a dynamic environment. Cell seeding efficiency has been seen to be near 100% in PLLA scaffolds under a flow rate of 1.1 mL/cm^2 compared to an efficiency of just 50% in static culture. Microscopic observations also confirmed a uniform distribution over the entirety of the scaffold [169]. Interestingly in this study, cell seeding efficiency decreased with increasing flow rate, suggesting too

high flow rates could cause cell attachment. This was indeed found to the case in a study by McCoy et al. [7] that cell detachment proportional to the flow rate. However, the porous architecture was also demonstrated to play an important role, with cell detachment inversely proportional to pore size. These studies demonstrate that while the influence of flow has its benefits, there is a limit to this, and that needs to be understood in order to optimise culture conditions.

Author	Cell Type	Tissue	Scaffold	Flow input	Shear rate	Results
Zhao [12]	n/a	Bone	CFD – Pore geometry	0.5-5 mL/min	1.47 – 30 mPa	CFD for wss in square and circle pores. Porosity of scaffold biggest influence over wss
Bancroft [170]	MSC & Osteoblast	Bone	Non-woven Titanium fibre mesh	0.3, 1, 3 mL/min	n/a	Dynamic flow increased osteogenic differentiation Increasing flow rate increased Ca content
Li [171]	hMSC	Bone	Porous Tricalcium phosphate scaffold	3 mL/min	0.0005-0.015 Pa Dextran added to media to change viscosity of fluid	Homogenous ECM mineralisation Increased shear stress accelerated osteogenic differentiation
Sikavitsas [5]	Rat MSC	Bone	3D porous titanium fibre mesh Sealed scaffold in bioreactor in cassette	0.3 mL/min 0,3 or 6% dextran added to alter viscosity	0.01 to 0.03 Pa	increased expression of osteoblastic phenotype Increased homogeneously distributed ECM
Vetsch [172]	hMSC	Bone	3D porous freeze dried Silk Fibroin Enclosed perfusion bioreactor	0.001 and 0.061 m/s	0.56-34.20 mPa	4 fold change in osteogenic differentiation at high velocity Greater DNA quantity at low velocity, high velocity inhibited proliferation
Cartmell [8]	MC3T3	Bone	Human Trabecular bone scaffolds	0.01, 0.1, 0.2 and 1 mL/min	n/a	High velocity increased cell death compared to increased viable cells at low flow Increased proliferation at 0.01mL/min Osteogenic markers upregulated at 0.2mL/min

Zhao [173]	hMSC	Bone	PET non-woven matrices 3 scaffolds per perfusion chamber	0.1 and 1.5 mL/min	0.00001-0.0001 Pa	Low flow increased proliferation 1.4 fold at day 20 High flow upregulated osteogenic differentiation
McCoy [7]	MC3T3	Bone	Porous Collagen-GAG	0.05, 1, 5 mL/min	0.0009 - 0.879 Pa	Cell detachment proportional to flow rate and inversely proportional to pore size
Grayson [112]	hMSC	Bone	Decellularised trabecular Bone Scaffolds	0.1 and 0.4 mm/s	0.0007 Pa – 0.01 Pa	Increasing perfusion rate significantly increased proliferation bone related proteins increased but not significantly
Porter [174]	hMSC	Bone	PCL + Collagen (FDM) – varied thickness 3 to 9mm Axial perfusion bioreactor	0.2 mL/min	n/a	50 fold greater mineral deposition in dynamic culture Mineralisation greater at core than at periphery due to bioreactor
Raimondi [175]	Chondrocyte	Cartilage	Polyester urethane foam	0.5 mL/min	4.6 – 56 mPa	sGAG/DNA ratio decreased for increasing shear levels
Raimondi [176]	Chondrocyte	Cartilage	Polyurethane foam – scaffold enclosed at edges, culture media above and below	0.005, 0.023, 0.045 mL/min	0.05, 0.23, 0.45 mPa	Cell detachment minimised at 0.023mL/min and 0.23mPa 9 fold increase in flow rate caused 3 fold increase in cell detachment
Zhu [177]	Chondrocyte	Cartilage	10 ⁶ cells/cm ² high density monolayer	2 mL/min	0.1 mPa	-Hydrostatic pressure and perfusion improved chondrocyte differentiation -Increased COL2A1 and decreased

						COL1A1 expression
Cioffi [178]	Chondrocyte	Cartilage	PEGT/PBT foam disc enclosed in bioreactor, scaffold secured at periphery	0.03 and 0.3 mL/min	0.256 and 2.56 mPa	Low flow rate (0.03mL/min) resulted in anoxic (>1% O ₂) conditions at scaffold periphery near the outlet
Gharravi [179]	Chondrocyte	Cartilage	Alginate beads containing cells seeded in alginate hydrogel scaffolds	2 mL/min	0.0048 Pa max wss	Evidence of sulphated GAG production and accumulation of cartilage like matrix
Carmona-Moran [180]	hMSC	Cartilage	PCL salt leaching	0.1 mL/min	n/a	Cell layer and collagen II deposition formed closest to inlet this layer penetrated scaffold in direction of flow Even distribution of Collagen II
Davisson [181]	Chondrocyte	Cartilage	Polyglycolic acid mesh	0.05 and 0.8 mL/min	n/a	-Up to day 3 perfusion increased DNA content 35% -Perfusion at 0.05ml/min at day 9 increased DNA content 45% compare to 85% for 0.8mL/min

Table 2-1 Table summarising literature based on studies into the effect of perfusion flow for bone and cartilage tissue engineering applications

2.2.4.3 Effects of structural design on flow

Scaffold microarchitecture designs can also strongly influence flow patterns, distribution velocities and shear stresses, and in turn how flow interacts with cells. In order to best mimic the mechanical environment a cell naturally experiences and better understand cell responses *in vitro* and *in vivo* to applied forces, it is important to model flow rates in a 3D scaffold [182]. The effect of the microarchitecture on flow can be parameter dependent. For instance increased interconnectivity and permeability in scaffolds that have been dynamically seeded, induced a more homogeneous distribution of cells, implying that there was increased flow to all areas of the scaffold negating issues where cells only grow on the scaffold periphery [151]. This however is an assumption and does not identify exactly how the architecture effected the flow and in turn the related forces that a cell would be exposed too. Bartnikowski et al. [183] varied pore geometry in four 3D printed scaffolds, by altering the lay down angle of struts and introducing an offset between layers. The wall shear stresses induced by perfusion flow was modelled computationally. It was demonstrated that as the lay down angle decreased, and the offset was introduced, the pore size and permeability was reduced and in turn the wall shear stresses increased as the flow path becomes more restricted. Printing a pore architecture, designed using computer aided models, is easier to model flow compared to other more random scaffold pore orientations. The introduction of rapid prototyping techniques has increased control of architectures making it also possible to introduce features such as gradient architectures. In one study, Melchels et al. [11] using SLA created two structures, one with isotropic pores and a constant porosity, whilst the other scaffold was designed with a porosity gradient in the radial direction by introducing an offset between layers. Unsurprisingly the isotropic pores saw a uniform distribution of flow velocities, whilst the other scaffold saw a gradient distribution. This also led to gradients in cell densities, as it was found that the highest number of cells were found in the regions where velocities and shear were highest. This can be explained by the fact that cells follow the flow pattern dictated by the scaffold and higher velocity of the cell suspension at the wall

surfaces increases the number of cells that are likely to contact the surface and adhere. Therefore, flow patterns could be used to tailor cell seeding densities throughout a scaffold. These studies indicate that mapping the flow through porous media can give insight into how architecture parameters can be used to manipulate flow and in turn manipulate the induced mechanical forces and cell response.

2.2.5 Current methods of mapping flow

Given a dynamic culture environment can be enhanced by more efficient oxygen and nutrient delivery [165] and introduce the mechanical forces necessary to stimulate cells and tissue maturation [163], it is necessary to develop a clear understanding on the flow regimes and shear stresses and how they are applied. During the process of tissue growth, the increases in cell proliferation will fill pore spaces and increase the shear stresses [184] so real time evaluation to monitor changes in the system is vital. Therefore the hydrodynamic characteristics of a system should be quantified, characterised and well correlated with experimental data [185]. Computational and optical methods have received the most attention as a means to understand complete 3D flow profiles through porous structures.

2.2.5.1 *Computational Fluid Dynamics*

Computational fluid dynamics (CFD) is a method to mathematically model and analyse fluid flow, and interactions with solids or gases to provide numerical solutions depending upon the input parameters. CFD in tissue engineering serves as a time and cost efficient technique to measure and fully characterise 3D flow fields through porous media. This allows bioreactors, scaffolds and their respective flow rates and patterns to be theoretically investigated before they have even been fabricated. Parameters like the inlet velocities and shear stresses can also be varied and evaluated to predict their effects and influence on tissue growth [186]. Using CFD the influence of a number of variables like oxygen tension, velocity, stress and strain [187]

can all be investigated. CFD is a powerful tool with benefits that include the ability to integrate mass and momentum transfer, identifying and analysing any problems that may arise in the system, and configuring bioreactor parameters, whilst rather importantly reducing the cost and time of experiments required [187]. There are four steps to CFD that must be carried out in order to accurately and effectively evaluate the system; set up the correct geometry, divide the whole system into a number of elements at which the numerical calculations are performed, chose a the best representative mathematical model and finally apply appropriate boundary conditions [187].

One aspect CFD has been used to measure in the tissue engineering is the flow rates used in perfusion bioreactors. The behaviour of human MSCs has been studied under multiple flow rates in 3D culture. One study found that decreasing the flow rate from 0.061 m/s to 0.001 m/s resulted in the cells ability to form bone matrix being inhibited compared to the higher velocity, indicating the dependency of cells on perfusion induced stresses [172]. This is supported by other studies which have found increasing flow rates to better stimulate cells [170]. CFD has also been successfully utilised to map wall shear stresses. Zetterman et al. [182] successfully used to CFD to compare the wall shear stresses of irregular and regular internal architectures. This study provided evidence that flow in the irregular silk fibroin scaffold had a linearly increasing wall shear stress as fluid progressed through the scaffold in a homogeneous pattern, compared to the regular geometry of the PCL scaffold which saw a peak and plateau in shear stresses.

CFD offers a cost and time effective method to investigate flow in hydrodynamic tissue engineering systems, it is however not without its limitations. The biggest challenge facing this method is that the nature of gathering data computationally relies on a series of assumptions and therefore the model needs to be validated experimentally to prove its relevance. The results obtained need to be validated to show that the simulation correctly predicts the behaviour that would be seen experimentally [187].

Some studies evaluating the effects of flow on cells will use cell culture methods to quantitatively validate models [188] but this is often carried out post experiment using means that require the destruction of scaffolds. This highlights that there still exists a need for a method that can facilitate real time non-destructive measurements of localised flow patterns and shear stress.

2.2.5.2 *Optical methods*

The alternative to CFD, although sometimes also used as a method of experimental validation, are optical methods. Micro-Particle Imaging Velocimetry (μ -PIV) has been applied to visualise flow fields in cell seeded scaffolds, and establish that changes in flow fields relate significantly to changes in cell density [189]. This technique has also been applied velocity profiles within a 3D porous scaffold as a CFD validation method. However there is some disagreement in this study when compared to the CFD modelling, close to scaffold walls which has been attributed noise caused by scaffold brightness [16]. Micro-PIV can be limited as a fluid mapping technique because it requires optical access to the internal regions of interest such that scaffolds need to be transparent [16], not only that it also requires the addition of tracer particles, which have been associated with causing errors in algorithms and limitations in the visibility of the tracer particles [190].

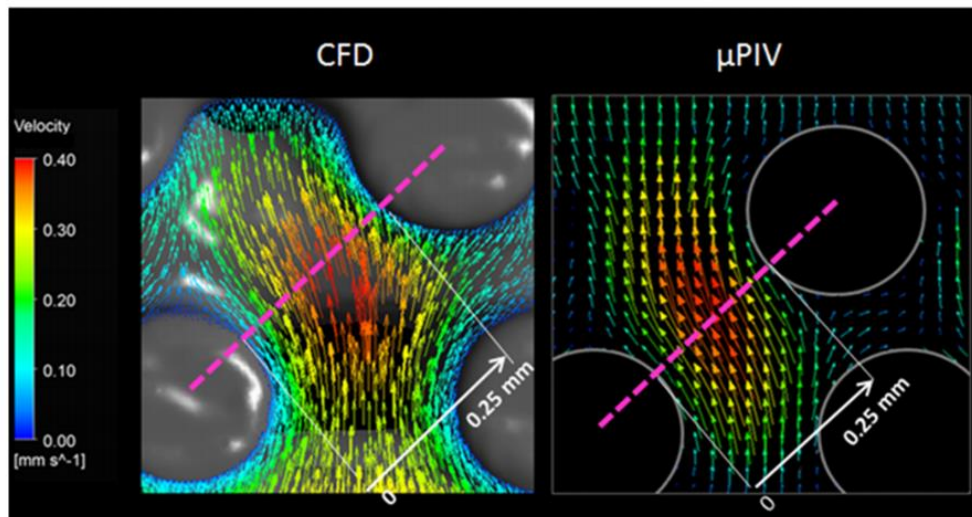


Figure 2-6 Comparison of CFD results against micro PIV results inside porous scaffold from Campos Marin [16]

A different optical method that has been implemented without the use of tracer particles is Doppler Optical Coherence Topography (DOCT) which works by combining structural images gathered using OCT, and flow images based on a Doppler frequency shift that can be obtained from moving objects, and correlating this data together to draw conclusions on parameters like interconnectivity [17]. As with other optical methods DOCT is limited by its dependence on an optical transparency. Therefore an experimental method that can probe opaque materials and doesn't require an additional tracer particles could offer an ideal solution to non-invasive flow measurement limitations.

2.3 NMR and MRI

Nuclear magnetic resonance (NMR) is a popular technique in physics, chemistry and biology, due to its ability to probe various molecular motions in solids and liquids, and detailed chemical information about molecules [191]. NMR has been combined with spatial imaging to produce magnetic resonance images [192], an imaging technique

regularly used in the field of medicine, including to measure flow within the body but has many other applications outside this field, where flow measurements can be applied. The appeal of MRI methods is that highly accurate measurements can be taken on samples with displacement of less than $1\mu\text{m}$ and velocities of as small as $10\mu\text{ms}^{-1}$, in addition to its ability to be used to probe opaque systems [191].

2.3.1 Basic principles

2.3.1.1 *NMR Physics*

MRI is an NMR technique that utilises spin properties of atomic nuclei to obtain spatially resolved information about a given structure and the dynamics inside [191]. A spinning nucleus possesses angular momentum and charge, which give rise to an associated magnetic moment μ . NMR relies upon the detection of nuclear spins precessing in a magnetic field, of which the frequency that the nuclei precess at is directly proportional to the strength of the magnetic field. NMR has the ability to detect and record the averages of an ensemble of precessing nuclei, known as the Larmor frequency [193]. Larmor frequency is defined as the rate of precession of the magnetic moment of protons about the external magnetic field. The Larmor frequency ω is directly proportional to the magnetic field strength β_0 times the constant magnetogyric ratio γ , which is essentially how strongly magnetic the nucleus is.

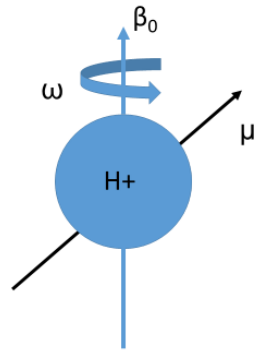


Figure 2-7 Magnetic field causing the nucleus to precess at the Larmor frequency

Magnetisation of nuclei develops parallel to the magnetic field, but this is not measured in equilibrium alignment, instead when magnetisation is rotated away from the field using a radio frequency (RF) magnetic field pulse that is the same as the Larmor frequency. The largest NMR signal produced occur when the magnetisation is rotated by 90° away from the magnetic field causing the nuclear magnetisation to lie in the transverse plane [193]. This is the most favoured angle for maximum signal. After the applied RF, precessing nuclei return to their equilibrium position parallel to the magnetic field. This process is called relaxation and consists of two independent processes. Longitudinal relaxation is time it takes for spins to return to equilibrium in the longitudinal axis (T1), whilst transverse relaxation the process by the decay of the Free Induction Decay (FID) signal that is received, and is characterised by time (T2) [191].

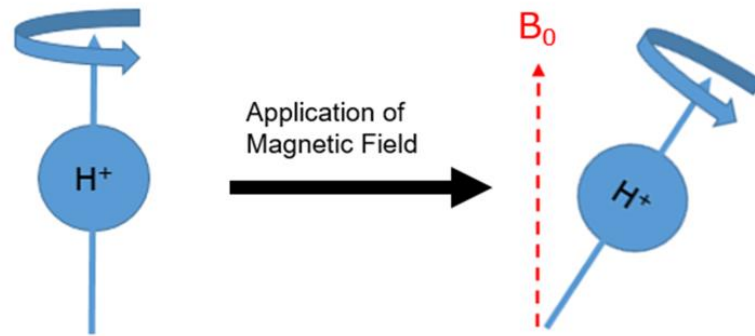


Figure 2-8 Application of RF pulse tips magnetisation in to transverse plane

In imaging, spatial gradients can be applied to create Larmor frequencies that are dependent upon position of the spin. If a system is made up of several little objects, each will have its own signal, associated with its own frequency and position characteristic. Fourier transform on the detected FID signal is used to give the spectrum in terms of the frequency domain, in which the width of spectrum relates to length of decay of the signal [193]. Inhomogeneous magnetic fields produce a more rapid decay and broader spectrum, this is because the Larmor frequencies are not the same throughout, and nuclei are precessing at different frequencies, such that they are not in phase. Altering magnetic field gradients can improve homogeneity, creating better signal resolution using a technique called spin echo [194]. Spin echo uses to opposing pulses of firstly 90° and then 180° to flip spins, causing them to re-phase and maximising signal.

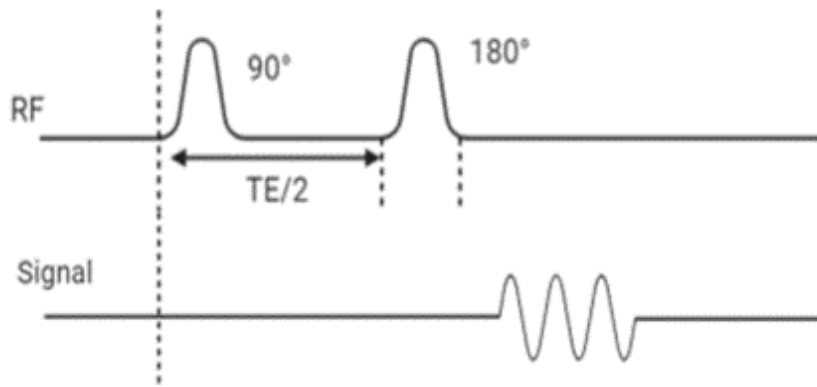


Figure 2-9 Schematic of spin echo inversion recovery pulse sequence

2.3.1.2 Velocity encoding and flow imaging

MRI is capable of measuring phase shifts Φ , which is essentially the spins losing coherence with each other, no longer precessing in phase. This is used for position encoding, because when magnetic field gradients are applied, there is a phase shift. It is the transverse component of magnetisation that can acquire phase shift, so this is first induced with a RF pulse before flow sensitive gradients can be applied [195]. Velocity encoding uses two opposing gradient pulses in the imaging sequence of pulses. Spins moving along a magnetic field gradient acquire a phase shift [195]. For static objects or in the case of no flow the stationary spins experience the gradients at equal but opposite magnitude such that they cancel each other out, and there is zero net phase accumulation. However if there is motion between the two applied pulses, then the nuclei that have moved will experience different pulses and the phase cancellation is incomplete. This leads to a residual phase which is proportional to velocity along the gradients direction [196]. Two scans are acquired together and subtracted from each other to remove any errors and give a velocity map. Stationary materials show zero-value pixels (grey) whilst velocities show positive pixels (brighter) and negative pixels (darker) with an accurate linear relationship to velocity [196].

Phase shifts are measured in degrees, between positive and negative 180° , therefore the peak velocity expected in the system should correspond with a phase shift of

+180°, which requires some prior knowledge of the flow system being investigated [195]. Velocity encoding is inversely proportional to the area of flow encoding gradients, therefore smaller velocities require stronger gradient amplitudes if imaging time is to remain unchanged [195].

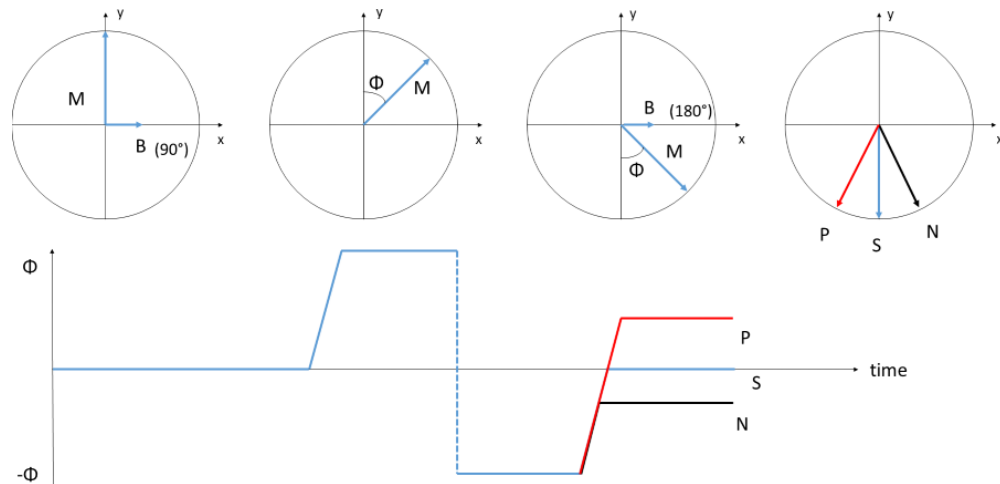


Figure 2-10 Schematic showing 90° pulse rotating M into xy plane, the spins lose phase coherence and the 180° flips the spins. Spins refocus to form an echo. Phase shifts are acquired for spins associated with flow. P is positive flow, S is stationary flow and N is negative flow.

2.3.2 MRI for Flow Imaging

Using phase contrast MRI in clinical applications has seen the technique become well established for clinical evaluation of cardiovascular diseases. 2D phase contrast MRI has been used traditionally since the 1980's for the assessment of blood flow in the heart and blood vessels. But more recently velocity encoding techniques along all 3 flow axis and 3D anatomic coverage has been used to evaluate haemo-dynamics in multiple regions of the body (termed 4D flow MRI) [197]. As a developing technique, it has a number of interesting potential applications. Liver cirrhosis treatment could benefit from the assessment of blood flow, for instance one small study has shown that in patients with advanced cirrhosis there was increased inward blood flow but decreased outward blood flow in the liver [198]. 4D flow MRI has additionally been

used to assess wall shear stresses in the aortic walls of patients with bicuspid aortic valves and [199] and to measure flow through the heart [200]. Outside of clinical applications MRI has been used to measure flow including sedimentation [201], in rheometers [202] and fluid/particulate mixtures for aseptic treatment of food [203].

2.3.3 Application of NMR in porous materials

A porous media consisting of a solid matrix phase, and a non-solid phase occupying the void space within the matrix can also be studied using NMR and MRI to establish flow velocity throughout the porous structure. Magnetic resonance measurements have been central to the understanding of a number of flow processes outside of a clinical setting, especially those involving porous media. Environmental scientists and engineers have employed NMR techniques to investigate solute transport, infiltration and diffusion processes in soil [204]. Further to this MRI has been a valuable tool for monitoring oil recovery from sedimentary rocks [205] and as a static measurements of fluids in rock cores [206].

Hydrogels have potential applications as biomaterials in industries including food and pharmaceutical, and the diffusion rate within these gels has also been investigated using MRI techniques [207, 208]. Although neither study was aimed at tissue engineered scaffolds, it still demonstrates that for hydrogel scaffold development, NMR could prove to be a powerful tool for the internal transport and the potential deformation that might occur as a result of hydrodynamic forces [207]. NMR has been used elsewhere to investigate biomaterials in the form of bioresorbable films [209]. This study found that NMR could be successfully used as a non-invasive method to investigate the pore size distribution in a soft porous biomaterial. The natural porous network of Cartilage ECM of full thickness cartilage samples, was placed under dynamic loading [97]. The results of this study demonstrated the influence of hydrostatic pressure in interstitial fluids can strongly influence deformation in the pore network. Thus, potential changes in the pore network and fluid transport properties

under compression is dependent not only on the instantaneous strain but also on the hydrostatic forces associated with interstitial fluid.

These aforementioned studies show the diverse application of NMR and MRI techniques with respect to flow in porous structures, and that there has been some interest in biomaterial and tissue properties and porous structures.

2.3.4 Potential applications in Tissue Engineering

The ability of NMR to map flow in porous structure could prove to advance the fabrication of porous scaffolds in tissue engineering. As a non-invasive experimental technique, it presents an opportunity to obtain real time raw data that will allow conclusions to be drawn on the relationship between the fluid mechanics of a system and cell behaviour. The overriding focus of research has been directed towards using CFD and optical methods in the past, such that there has been limited use of NMR and MRI with respect to tissue engineering scaffold architecture. From the currently limited research, Swider et al. [210] was able to develop an MRI methodology for the non-invasive and non-destructive measurement of fluid velocity, shear stresses and permeability of a porous hydroxyapatite commercially available material. The study focused primarily on the heterogeneous fluid flow in the axial direction and was also used to compute the local porosity. Fluid shear stresses were found to be highest at solid-fluid interfaces.

For investigating manufactured tissue engineering scaffolds, one group processed PCL scaffolds using a porogen leaching method, and hydrogel matrices from Matrigel and collagen for the investigation of the hydrodynamic properties of these scaffolds using NMR velocimetry [211]. The porous PCL scaffold exhibited heterogeneous flow. The permeability of the scaffold could be calculated at a local level, such that changes variations in permeability could be highlighted in particular locations that otherwise wouldn't be in bulk measurements. In the hydrogel samples, flow generally followed

the horizontal direction that was applied through the structure. However, under an increased flow rate of 100 $\mu\text{l}/\text{min}$, the increased hydrodynamic forces resulted in the deformation and collapse of the structure. Although this may have shown the hydrogel to be susceptible to damage when subjected to flow, it highlighted the benefit of using MRI, in that the structural deformation was seen in real time during the experiment. The real time evaluation evidenced by this study offers a real alternative to computer modelling, and offer insights that otherwise experimentally are difficult to see.

The same group has applied this MRI technique elsewhere to firstly examine the topology of micro-fluid channels in porous scaffolds and used MRI to validate an algorithm to control shear stress distributions through the optimisation of the topology [212]. The MRI method was also employed in the design of a multi-channel bioreactor, focusing on how mechanical forces could be tailored and achieve spatiotemporal control within the scaffold by feedback control. Shear rate maps derived using NMR velocity measurements were used to demonstrate how changes in multiple inlet velocities effected mechanical forces, with a view to controlling mechanical forces by inlet parameters [213].

There exists scope for the introduction of MRI as an important technique in regenerative medicine to experimentally evaluate flow in porous scaffolds. However this is yet to be studied extensively, in particular in scaffolds manufactured using 3D printing techniques.

2.3.5 Use of Magnetic Nanoparticles in MRI

The ability to effectively monitor and evaluate the distribution and migration of cells following scaffold seeding is important for improving the feasibility of scaffolds for clinical applications. A lack of homogenous cell distribution can impede uniform tissue formation and a low seeding efficiency may not be sufficient to sustain an appropriate rate of tissue formation [214]. Labelling cells with magnetic nanoparticles (MNP) prior

to seeding allows the location of iron containing cells to be detected by MRI. This therefore can be used as way of facilitating non-invasive assessment of distribution of cells within porous scaffolds. MNP's shorten the nuclear magnetic relaxation time T2, and appear as hypo-intense areas in T2 weighted gradient echo images [215, 216]. Labelled cells create a magnetic susceptibility artefact of T2* weighted images and appear as an area void of signal due to a loss in signal intensity that can be seen in iron sensitive T2 weighted MR images [217]. Labelling Stem cells with iron based nanoparticles to act as a negative contrast agent for MRI has been shown to effectively track cells in both *in vitro* and *in vivo* [217, 218]. Visualising cells within scaffolds using a non-invasive technique in combination with velocity profiles taken from the same scaffolds under perfusion would allow for a better understanding of the relationship between flow and cells. The ingrowth of cells into pores would in theory change velocity profiles but the extent of this is not simple to predict or model. However, a direct link between the location of cells and changes in velocity profiles could allow for a much clearer understanding of this relationship. In addition to this, the overall distribution of cells during initial seeding and the following migration during dynamic culture could be important for monitoring changes in distribution at several intervals in a culture period and determining how this is effected, if at all, by different flow conditions and porous architectures.

2.4 Summary

The benefits of precise control over porous architecture has been elucidated by many studies which have shown pore architecture plays a role in defining the mechanical properties and influencing cellular behaviour. Therefore, the opportunity to tailor the precise architecture of scaffolds using 3D printing techniques could be utilised to enhance tissue formation. In particular, the high level of control via fused deposition modelling in all axis directions, and on each layer of the structure [58, 73]. The effects that flow through a porous scaffold have also been highlighted in the literature, including enhancing mass transfer and facilitating the mechanical stimulation required

by some cell types. Understanding the relationship between flow and the porous architecture experimentally is vital. How far the microarchitecture influences the flow patterns, distribution velocities and shear stresses, all of which cells are exposed to is sought to be better understood. Therefore, optimisation over the architecture to positively influence cell behaviour is key to scaffold development and design. Further to this, reinforced by the popularity of CFD, is the need for real time experimental evaluations of flow to substantiate the models. In a dynamic cell culture environment, cells migrate, proliferate and secrete extracellular matrix, all of which can alter the internal environment of the scaffold and in turn flow patterns. Mapping these changes to flow patterns over the *in vitro* culture time can determine the parameter changes in the scaffold, and therefore can be used to guide improved design of scaffolds. MRI offers a method to do this experimentally, and used in combination with the high control fabrication method of FDM there exists a real opportunity to optimise scaffold porous architecture designs to facilitate optimal tissue culture conditions as a direct consequence of quantifying flow velocity within cell seeded porous biomaterial scaffolds.

3 Methodology

This chapter give a brief overview of methods used throughout the thesis. More detailed methodologies are given in the individual results chapters.

3.1 Scaffold Design and Fabrication

Scaffolds were designed with the software BioCAD which generates code to be used by a thermal extrusion based 3D printer (RegenHU, Switzerland) to fabricate a scaffolds. Polycaprolactone (PCL) pellets ($M_n=45,000$ g mol⁻¹ Sigma Aldrich UK) were extruded through a 330 μ m nozzle at a temperature of 74°C and a pressure of 4 bar, whilst the air temperature was maintained at 26°C using a hood to enclose the printer. Within the enclosed environment a fan set to 1000 rpm was used to aid the cooling of the struts upon deposition to the platform. Print head speed, extrusion rates and layer height were altered dependent on scaffold design.

3.2 Cell Culture

3.2.1 Immortalised Human Mesenchymal Stem Cells

Human mesenchymal stem cells (MSCs) were isolated according to previously published protocol [219] and was cultured in expansion medium (Dulbecco's modified eagle's medium with 10% FBS, 1% L-Glutamine and 1% antibiotic/antimycotic solution). Cells were cultured to approximately 80% confluence in expansion media using T75 flasks, passaged at a ratio of 1:3 to new culture flasks. Passage numbers for the cells were kept below 20. Detailed cell seeding methods can be found within each chapter.

3.3 Cell Characterisation

3.3.1 Pico Green Assay

Cells seeded scaffolds were washed with PBS and individually digested with 800 μ L of papain digestion solution (280 μ g/mL papain, 50 mM EDTA, and 5 mM L-cysteine in Duplecco's PBS at pH 6.5) at 37°C for 3 days. The supernatant of the digested samples were analysed using a Pico Green assay to quantify DNA with a Quant-iT Picogreen Kit (Invitogen). Fluorescence intensity was measured using a TECAN plate reader (Tecan, Switzerland) at an excitation of 480 nm and emission of 560 nm and DNA concentrations were deduced using a standard curve.

3.3.2 Dimethylmethylene Blue Assay

Cells seeded scaffolds were washed with PBS and individually digested with 800 μ L of papain digestion solution (280 μ g/mL papain, 50 mM EDTA, and 5 mM L-cysteine in Duplecco's PBS at pH 6.5) at 37°C for 3 days. sGAG content was quantified using 1,9-dimethylmethylene blue (DMMB, Sigam-Aldrich) from the digested supernatant.

3.4 Compressive Testing

To test the compressive modulus of the scaffolds a universal texture analyser was used (TA-HD plus, Stable Micro-Systems). Samples were compressed in the z-direction at a speed of 0.5 mm/s to a strain of 50%. The linear regions of computed stress-strain curves obtained, where stress is proportional to strain, for each sample were analysed to calculate the overall compressive modulus.

3.5 Scanning Electron Microscopy

The morphology of scaffolds were investigated using scanning electron microscopy (SEM JEOL JSM-6060LV). In order to prepare samples for SEM they were first mounted to stubs using carbon cement and then gold sputter coated (Leica EM SCD005). Specific scaffold characteristics were measured from the obtained images using randomly selected struts in image analysis software (Image J, National Institutes of Health). Osmium stained cell seeded scaffolds, were also visualised with SEM to assess cell morphology and differentiation.

3.6 Micro Computed Tomography

For characterisation, scaffolds were analysed using an x-ray μ -CT scanner (Skyscanner 1174) with a voxel resolution of 7.7 μm , x-ray source current 800 μA and voltage 50kV. X-ray images were obtained every 0.4° rotation in a full 360° revolution of the stage which samples were mounted to. N-Recon software reconstructs the obtained transmission images to 2-dimensional slices. CTAn software uses the reconstructed slices to create 3D models to visualise pore interconnectivity and carry out morphometric analysis of the scaffolds including calculating overall bulk porosity. Cell seeded scaffolds that have been fixed using osmium tetroxide staining can be imaged using this method to show the distribution of cells. Distribution of cells can be segmented from the structure of the scaffold by using thresholding.

3.7 Osmium Tetroxide Staining

Cell seeded scaffold were also fixed for image analysis using 2.5% glutaraldehyde overnight before being washed with PBS. Fixed scaffold were prepared for SEM and

micro-CT scanning by further fixation with 1% osmium tetroxide, before dehydration in an ethanol series (30%, 50%, 70%, 90% and 100% ethanol). Before being imaged the scaffold must be completely dry, so hexamethyldisilazane (HMDS) is added to samples, which are left to dry over-night in a fume hood.

3.8 MRI and NMR Velocimetry

3.8.1 Flow Chamber and system

The flow chamber was designed to fit a 25 mm bore in the appropriate probe for the MRI scanner. Brass inlet and outlets were fixed to either ends of the acrylic chamber, with a channel diameter of 3 mm also, allowing the chamber to be fixed (Swagelok) to silicone tubing ensuring a tight leak free system. A peristaltic pump (Watson Marlow) circulated continuous flow of deionised water. The circular flow system was completed with a reservoir to provide and collect deionised water for the flow system. The pump flow rate was set according to experiment requirements.

3.8.2 NMR and MRI Velocity Measurements

NMR velocity measurements of flow in the Z-direction through the porous architecture of the scaffolds were obtained with an NMR system consisting of a 9.4T 400 MHz Bruker instrument and a 25 mm imaging probe within which the flow chamber was placed vertically. 3D acquisition is required for this method, where by spatial encoding is performed in two planes and in the third plane the flow encoding gradient is applied. In this experiment the flow encoding gradient was applied in the Z direction, to produce velocity mapped image sizes of 256x256 pixels. Experiment times and parameters are dependent of flow conditions, and are defined within each experimental chapter.

3.8.3 Data Processing

Data processing and velocity calculations were carried out using Prospa software (Magritek, Wellington), whilst subsequent analysis was done using IGOR pro (Wavemetrics, USA).

3.9 Magnetic Nano Particles labelling

3.9.1 Cell Labelling with Magnetic Nano Particles

Commercially available Nanomag-D (Micromod, Germany) 250 nm particles with COOH surface functionality were used to label cells. Immortalised human MSCs were seeded in a T75 flask were allowed to reach 80% confluency in FBS containing expansion media before the expansion media was replaced with an appropriate volume magnetic nanoparticles diluted in expansion media. Cells were incubated overnight (24hrs) at 37°C and 5% CO₂ giving time for the particles to be internalised by the cells. Cells were then washed (3x) to remove any non-internalised particles ready for fixation and Prussian blue staining.

3.9.2 Prussian Blue Assay

Prussian blue is an iron based stain that can be used to identify the presence of Magnetic Nanoparticles. Monolayers of cells fixed in well plate with 4%PFA for 15-20 minutes at room temperature before equal volumes of 20% Hydrochloric Acid solution and 10% Potassium Ferrocyanide were added immediately to the cells. In order to effectively stain cells this mixture was applied to the monolayer culture for 5 minutes at room temperature. Images were taken using a Nikon Eclipse TS100 with blue regions indicating the presence of MNP's.

3.9.3 Alamar Blue Assay

For assessment of cell health, metabolic assay Alamar blue was carried out according to the manufacturers instructions. Briefly, cells seeded in a 24 well plate with a seeding density of 40,000 cells per well, were labelled with expansion media containing MNP's at concentrations 25, 50 and 100 µg/ml. Cells were assessed before labelling (Day 0) and then at Day 1 and Day 7 post labelling and compared with untreated controls for metabolic activity.

3.9.4 MSME Imaging of Labelled Cells

Confluent immortalised human Mesenchymal Stem cells (ihMSC) were treated with 50 ug/ml nanoparticle containing expansion media (Dulbecco's modified eagle's medium with 10% FBS, 1% L-Glutamine and 1% antibiotic/antimycotic solution) and allowed to internalise the particles overnight (24hrs) during incubation at 37°C and 5% CO₂. Cells were then manually seeded with 1 x 10⁶ labelled cells in 100 µl of FBS containing expansion media. Supernatant containing cells was manually reseeded onto scaffolds every 30 minutes for 3 hours to ensure good cell seeding efficiency. Cells were then fixed to scaffolds with 4% PFA for 8 hours at 4°C before 3x washes with PBS ready for imaging.

MR imaging of the cell seeded scaffolds were obtained with an NMR system consisting of a 9.4T 400 MHz Bruker instrument and a 25mm imaging probe. A gradient echo imaging method (ParaVision 6.0, Bruker BioSpin MRI GmbH, Germany) was used to obtain axial, sagittal and coronal slice images.

3.10 Statistical Analysis

Statistical analysis unless otherwise stated was carried out using Prism version 8.0 (GraphPad Software). Statistical significance was determined using one way and two way ANOVA testing.

4 NMR and MRI Velocimetry for Distinct Cell Free Scaffold Architecture

4.1 Introduction

An important element in regenerative medicine is the application of three-dimensional scaffolds to mimic a biological environment that allow cells to proliferate and differentiate in order to regenerate functional tissue both *in vitro* and *in vivo*. Therefore a key element of scaffold fabrication is the internal porous architecture which must provide an environment with appropriate structural shape for the intended tissue, provide adequate cell adhesions sites, allow the transportation of oxygen and nutrients, and the removal of waste products [57]. Diffusion of nutrients into scaffolds is limited in static culture, and in many cases nutrient gradients develop resulting in poor tissue growth at the core of scaffolds [161]. As cells proliferate and produce extra cellular matrix, the need for nutrient delivery and waste removal becomes greater, and diffusion is not sufficient for nutrients to reach the full depth of a scaffold [220], inevitably causing tissue growth to be limited to the periphery of scaffolds [8]. In some case scaffolds of up to 3mm thickness only sustained viable tissue growth to a depth of 500um [221]. Further to this, proliferation of cells can also cause cells to occlude pores and further impede transport of nutrients to the centre of scaffolds particularly in scaffolds with smaller pore sizes and reduced porosity [222]. This has prompted an increased interest in perfusion bioreactors, to create a dynamic environment to facilitate homogenous cell seeding [168, 223], increase mass transport of oxygen [224]. Fluid flow may also be crucial in providing important mechanical cues to cells via associated forces including shear stresses to better resemble *in vivo* environments [160]. Increased shear stresses in perfusion bioreactors have been associated with upregulation of chondrogenic [175, 177] and osteogenic factors [5, 170]. However, the degree to which shear stresses are applied can vary depending on the desired outcome as multi-shear perfusion devices have demonstrated [225, 226].

Current understanding of flow profiles within 3D porous scaffolds has largely been established by computational flow dynamics (CFD) modelling techniques. CFD can theoretically model scaffold geometries, bioreactor conditions and their relative flow fields. Parameters like inlet velocities and shear stresses can be easily varied and evaluated to predict the influence on tissue growth [186]. Given a dynamic culture environment can be enhanced by more efficient oxygen and nutrient delivery [165] and introduce the mechanical forces necessary to stimulate cells and tissue maturation [163] a clear understanding of these mechanisms has been sought through modelling. However, with any theoretical modelling approach there will always be a need to experimentally validate the results so models can be better developed and optimised and their assumptions can be tested [186].

Fluid flow through porous materials ultimately means that the interconnectivity of pores in internal architecture is a key element influencing the optimal flow regimes for homogeneous cell seeding. Scaffolds can be fabricated with varying pore size, geometry, distribution and overall interconnectivity and permeability. The contribution of each parameter towards the resulting flow velocity, distribution, and mechanical stimulation is difficult to characterise but important for understanding how to optimise scaffold design to maximise tissue regeneration. CFD has been used to show that the distribution of perfusion induced forces is very dependent on the distribution of pores throughout the scaffold and that the shape of pores can be used to allow better accessibility of fluid, important for homogeneous cell seeding and mass transport [227].

The introduction of 3D printing techniques offer the opportunity to fabricate more complex and customisable architectures using CAD/CAM in an attempt to better guide tissue regeneration [128]. In particular Fused Deposition Modelling (FDM), an extrusion based printing method has the ability to change the orientation between struts for each deposited layer, in addition to spacing between struts, allowing high control over pore morphology and overall interconnectivity [58]. Porous scaffolds have

been successfully produced via FDM to have both appropriate mechanical strength [70] and provide an environment for cell proliferation and ECM production [9].

Given the importance of scaffold design, many tissue engineering studies have investigated the effects of internal porous architecture with a lot of focus on the implications pore size has on the biological and mechanical functionality of scaffolds [148, 228]. Pore size has been shown to effect MSC chondrogenic [123, 229] and osteogenic differentiation [230-232]. Pore shape has also been shown to play a key role in the fate of engineered tissues, and is varied by altering the size, spacing and orientation of scaffold struts. Changes in pore geometry have been used to modulate mechanical properties of scaffolds to try and closely match those of the native tissue [43, 128]. The influence of pore geometry, in terms of cell proliferation and attachment has also been investigated [233, 234] and shown that in particular the deposition angle strongly affects the seeding efficiency and viability of cells in static culture. Despite substantial research no real consensus for gold standard of scaffold design, perhaps due to the complexity and number of variables involved in successful tissue regeneration, has been achieved.

One such variable is the use of bioreactors to create a dynamic growth system to increase mass transport of oxygen and nutrients, and mimic forces experienced by cells in the native tissue environment. Outside of theoretical CFD studies there is limited experimental analysis exploring the relationship between architecture and flow conditions. Cell culture studies post experiment under modelled conditions can be used to show cell behaviour [188] but this does not account for how nutrient supply and shear stresses may change with the pore ingrowth of cells during culture. Experimentally micro-particle imaging velocimetry (μ -PIV) has had some degree of success validating a CFD model, but was limited by significant differences between theoretical and experimental models at points where the scaffold brightness was too high [16]. Other optical methods have been limited by the requirement for transparent scaffolds and the addition of particle tracers [16, 190].

Mapping fluid velocity patterns in opaque porous materials without using invasive techniques is achievable using Nuclear Magnetic Resonance (NMR) and Magnetic Resonance Imaging [192] velocimetry methods [193, 194]. Although the NMR velocimetry has been more widely investigated in other disciplines such as environmental science [204-206], chemical engineering [235, 236] and medical applications [237, 238], there is limited research into its application for porous biomaterial scaffolds in regenerative medicine [210-213]. Mostly, the current research is limited to scaffolds fabricated with a random geometry. Youssef and co-workers [213] sought to use the flow data gathered as feedback for bioreactor design to allow greater control over fluid fields with multiple inlets. However, there is little evidence for how controlling and altering pore architecture, achieved with 3D printing could be used to influence flow fields, based on feedback from experimental NMR flow data. NMR is sensitive to proton dense liquids and capable of distinguishing nuclei of atoms with different physical properties, including atoms experiencing different translational diffusion [193], in addition to having the capability to alter temporal and spatial scales to gain motional data as a function of averaging [193], making it an ideal tool to study flow in a porous medium.

The aim of this study is to compare scaffolds with distinct pore geometries and pore sizes under flow conditions to decipher the effect of internal scaffold architecture on the fluid velocity and distribution of flow for efficient cell seeding and tissue regeneration.

4.2 Methodology

4.2.1 Scaffold Design and Fabrication

Scaffolds were designed with the software BioCAD which generates code to be used by a thermal extrusion based 3D printer (RegenHU, Switzerland) to fabricate a scaffold of the dimensions 10 mm x 10 mm x 5 mm (length x width x height). Distinct scaffold structures with varied pore geometry were designed by altering the laydown angle of struts, 0/15°, 0/45° and 0/90°. Scaffolds with differing pore size were created by varying distance between struts. Polycaprolactone (PCL) pellets ($M_n=45,000$ g mol⁻¹ Sigma Aldrich UK) were extruded through nozzle diameters ranging from 100 μm to 330 μm at a temperature of 74°C and a pressure of 4 bar, whilst the air temperature was maintained at 26°C using a hood to enclose the printer. Within the enclosed environment, a fan set to 1000 rpm was used to aid the cooling of the struts upon deposition to the platform. Print head speed was set to between 15 mm s⁻¹ and 30 mm s⁻¹ and the extrusion rate of the material was set to 15 revolutions per metre travelled by the print head. The height of each printed layer was set to between 0.14 mm and 0.20 mm for the scaffold (Table 4-1).



Figure 4-1 RegenHu Biodiscovery 3D printer used for FDM scaffold

Sample name	Laydown angle (°)	Needle dia (µm)	Layer Height (µm)	Print Head Speed (mm s ⁻¹)
PCL-90-150	0/90	100	140	30
PCL-90-300	0/90	150	160	30
PCL-90-450	0/90	330	200	20
PCL-90-800	0/90	330	200	15
PCL-0-90	0/90	150	160	30
PCL-0-45	0/45	150	160	30
PCL-0-15	0/15	150	160	30

Table 4-1 Printing settings for scaffold designs including the programmed layer height, print head speed and the chosen needle tip diameter

4.2.2 Flow Chamber and System

The flow chamber (Figure 4-2) was designed to fit a 25 mm proton clear bore volume resonator of 9.4T Bruker Avance III vertical bore MRI scanner. The chamber body was manufactured out of acrylic, containing a further three acrylic inserts. One to hold scaffolds with the dimensions of 10 mm x 10 mm x 5 mm (L x W x H) in the central region of the chamber and then two further acrylic inserts of 27.5 mm length, tapered at an angle of 7.25° on both walls to sit either side of the central scaffold containing insert. The tapered inserts created a channel that started at 3mm diameter at the inlet and outlet, and had a 10mm diameter nearest the scaffold, to allow fluid flow through the chamber without sudden changes in pressure. Brass inlet and outlets were fixed to either ends of the acrylic chamber, with a channel diameter of 3 mm also, allowing the chamber to be fixed (Swagelok) to silicone tubing ensuring a tight leak free system. A peristaltic pump (Watson Marlow) circulated continuous flow. The pump used silicone manifold (Elkay labs) tubing with an inner diameter of 2.29 mm which connected to Masterflex Tygon E-food (B-44-4x) tubing with an inner diameter 1.6 mm and made up the tubing network outside of the peristaltic pump. The circular flow system was completed with a reservoir to provide and collect water for the flow system. The pump flow rate was set to 50 rpm, which was calculated to be a mass flow rate of 5mL/min.

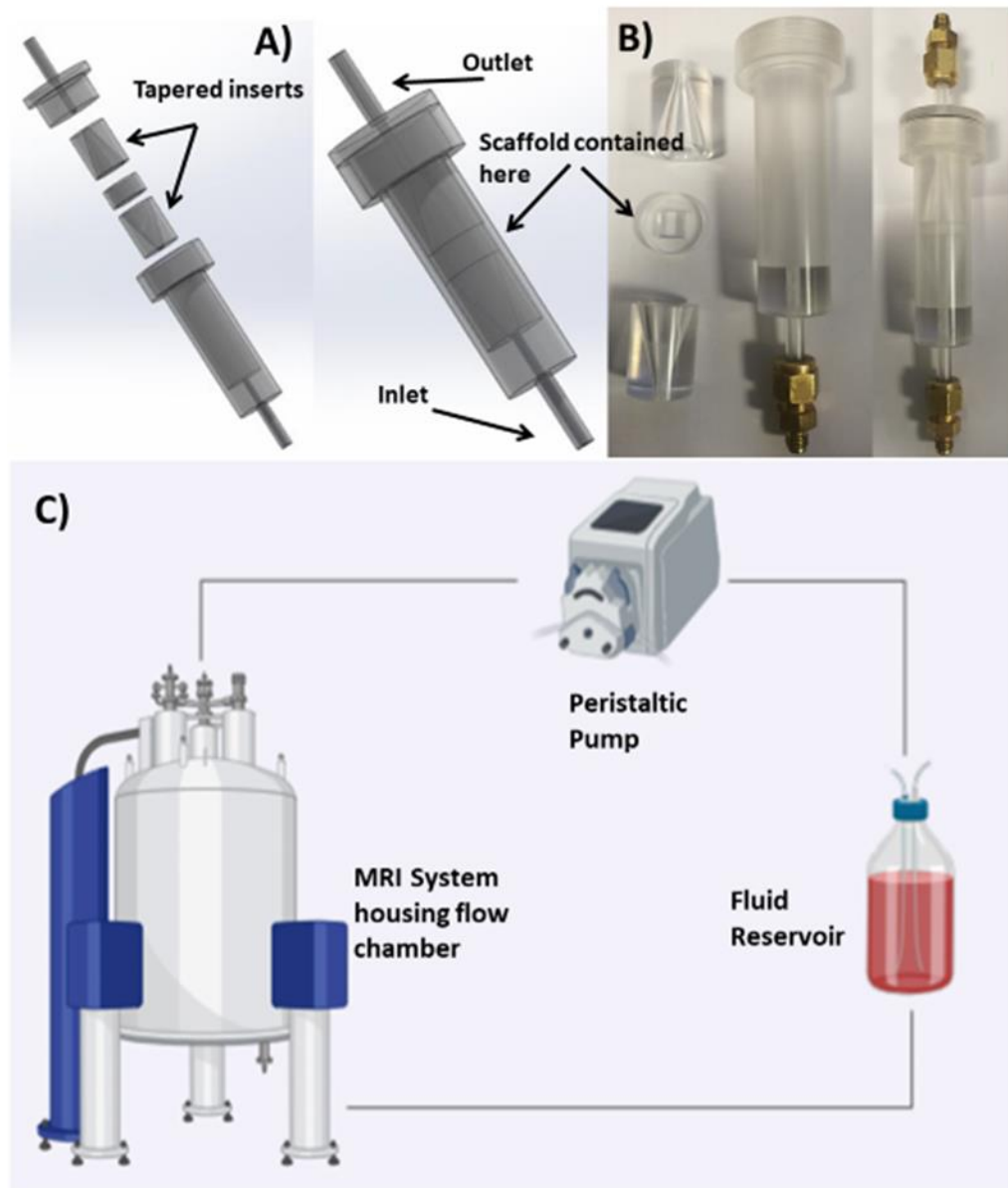


Figure 4-2 A) CAD drawings of flow chamber displaying the blown out assembly of individual parts and the complete assembly. B) Images of the manufactured parts and its assembly, of the flow chamber used. C) Schematic representation of the closed loop flow system.

4.2.2.1 NMR and MRI Velocity Measurements

MRI is an NMR technique that utilises spin properties of atomic nuclei to obtain spatially resolved information about a given structure and the dynamics inside [191]. NMR relies on the ability to detect averages of frequencies of spins precessing about a magnetic field, known as Larmor frequencies. When a substance with a high proton density, like water, is placed in a static magnetic field, bulk magnetisation parallel to this field develops, which is proportional to the spin density and strength of the field. The measurable signal is at its largest when the application of a 90° radio frequency magnetic field pulse rotates the magnetisation into the transverse plane [193].

Slice selective velocity measurements of flow in the Z-direction through the porous architecture of the scaffolds with a slice thickness of 1 mm were obtained with an NMR system consisting of a 9.4T Bruker instrument and a 25 mm imaging probe within which the flow chamber was placed vertically. Imaging flow velocity using NMR and MRI methods is carried out using a phase encoding technique [194] in which the absolute phase of nuclei spins relating to specific location is measured and motion is proportional to phase differences [239]. Between Slice selection and imaging a matched pair of phase encoding field gradients of different polarity, with strength g and duration δ , is applied in the Z plane in addition to a radio frequency (RF) pulse which is required to excite magnetisation into the transverse plane, where they can then acquire motion induced phase shifts. The strength of the pair of field gradients are chosen to be large enough to encode the highest expected flow velocity, as this avoids unwanted aliasing effects. The first 90° pulse gradient induces a phase shift, which is then inverted by the second 180° gradient pulse. During the time (Δ) between gradient pulses, moving magnetic moments (spins) acquire phase shift (Φ) which is proportional to the velocity of spins. In the case of no flow, stationary spins are compensated for by the bipolar gradient such that the phase they accumulate from the first gradient is equal and opposite to that of the second gradient. Therefore total phase accumulation is equal to zero for stationary spins. The phase difference that

remains for moving spins after the application of the matched pair of pulse gradients, is used for calculating velocity in each voxel and combined with standard MR imaging techniques [194] to form velocity maps [195].

To obtain velocity measurements at specific locations in the scaffold rather than bulk flow information in the whole scaffold an additional slice selective gradient is added to the pulse sequence which linearly varies resonance frequencies in the direction perpendicular to the plane to be imaged. Simultaneously, an RF pulse is applied that excites a narrow selection of matched frequency components such that only protons within a selected slice are excited (Figure 4-3). Slice selective gradient varies the frequency as a function of position, and matched frequency RF pulses use this to select specific locations with a finite slice width.

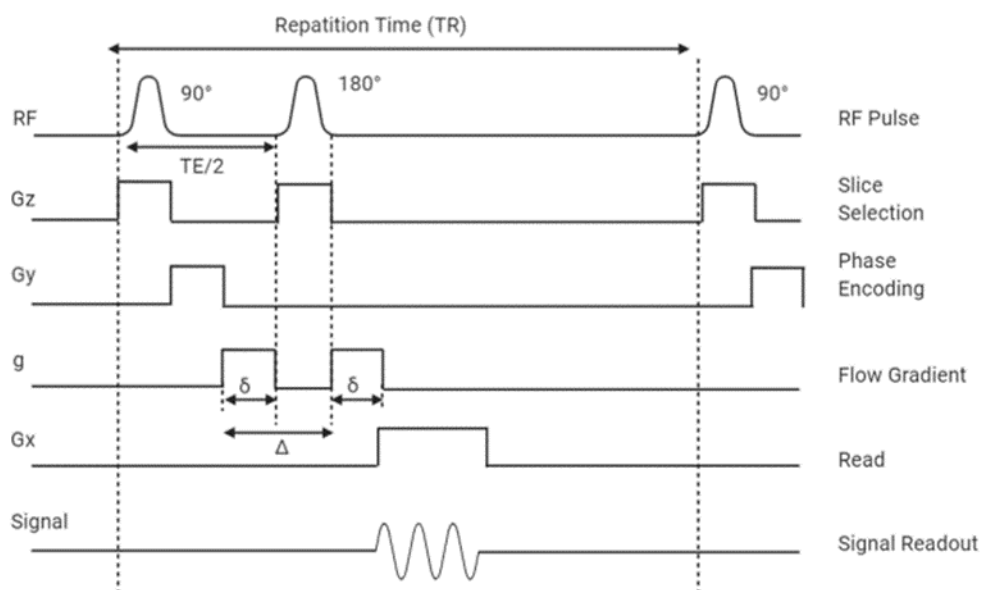


Figure 4-3 Schematic representation of pulse sequence for spin echo velocimetry imaging

3D acquisition is required for this method, where by spatial encoding is performed in two planes and in the third plane the flow encoding gradient is applied. In this experiment the flow encoding gradient was applied in the Z direction, to produce image sizes of 256x256 pixels. Imaging slice thickness was set at 1.2 mm and

positioned in the centre of the scaffold. Imaging parameters were TE=30 ms, TD=1 s, FOV=15 mmx15 mm. Data processing and velocity calculations were carried out using Prospa software (Magritek, Wellington), whilst subsequent analysis was done using IGOR pro 7.08 (Wavemetrics, USA).

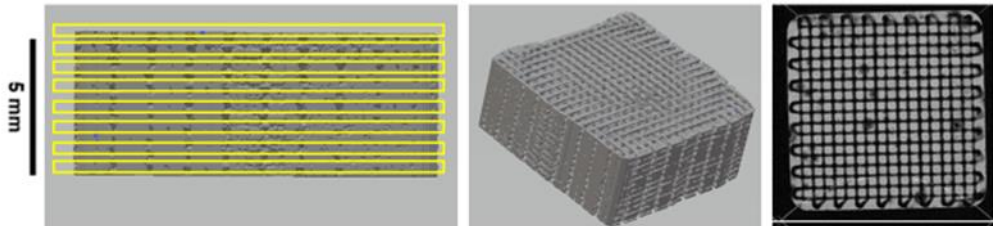


Figure 4-4 Schematic of axial slices from a side view, 3D visualisation of scaffold from micro CT reconstruction, and example of axial slice MRI image from scaffold.

4.2.3 Compressive Testing

To test the compressive modulus of the scaffolds a universal texture analyser was used (TA-HD plus, Stable Micro-Systems). Samples were compressed in the z-direction at a speed of 0.5 mm/s to a strain of 50%. Each scaffold was tested with 3 repeats. The linear regions of computed stress-strain curves obtained, where stress is proportional to strain, for each sample were analysed to calculate the overall compressive modulus.

4.2.4 Scanning Electron Microscopy

The morphology of scaffolds were investigated using scanning electron microscopy (SEM JEOL JSM-6060LV). In order to prepare samples for SEM they were first mounted to stubs using carbon cement and then gold sputter coated (Leica EM

SCD005). The distance between strut edges and the thickness of struts were measured from the obtained images using randomly selected struts in image analysis software (Image J, National Institutes of Health).

4.2.5 Micro Computed Tomography

For characterisation, scaffolds were analysed using an x-ray μ -CT scanner (Skyscanner 1174) with a voxel resolution of 7.7 μm , x-ray source current 800 μA and voltage 50 kV. X-ray images were obtained every 0.4° rotation in a full 360° revolution of the stage which samples were mounted to. N-Recon software reconstructs the obtained transmission images to 2-dimensional slices. CTAn software uses the reconstructed slices to create 3D models to visualise pore interconnectivity and carry out morphometric analysis of the scaffolds including calculating overall bulk porosity.

4.2.6 Statistical Analysis

Statistical analysis unless otherwise stated was carried out using Prism version 8.0 (GraphPad Software). Statistical significance was determined using one way and two way ANOVA testing, and using Tukeys multiple comparison.

4.3 Results and Discussion

4.3.1 Printing Optimisation

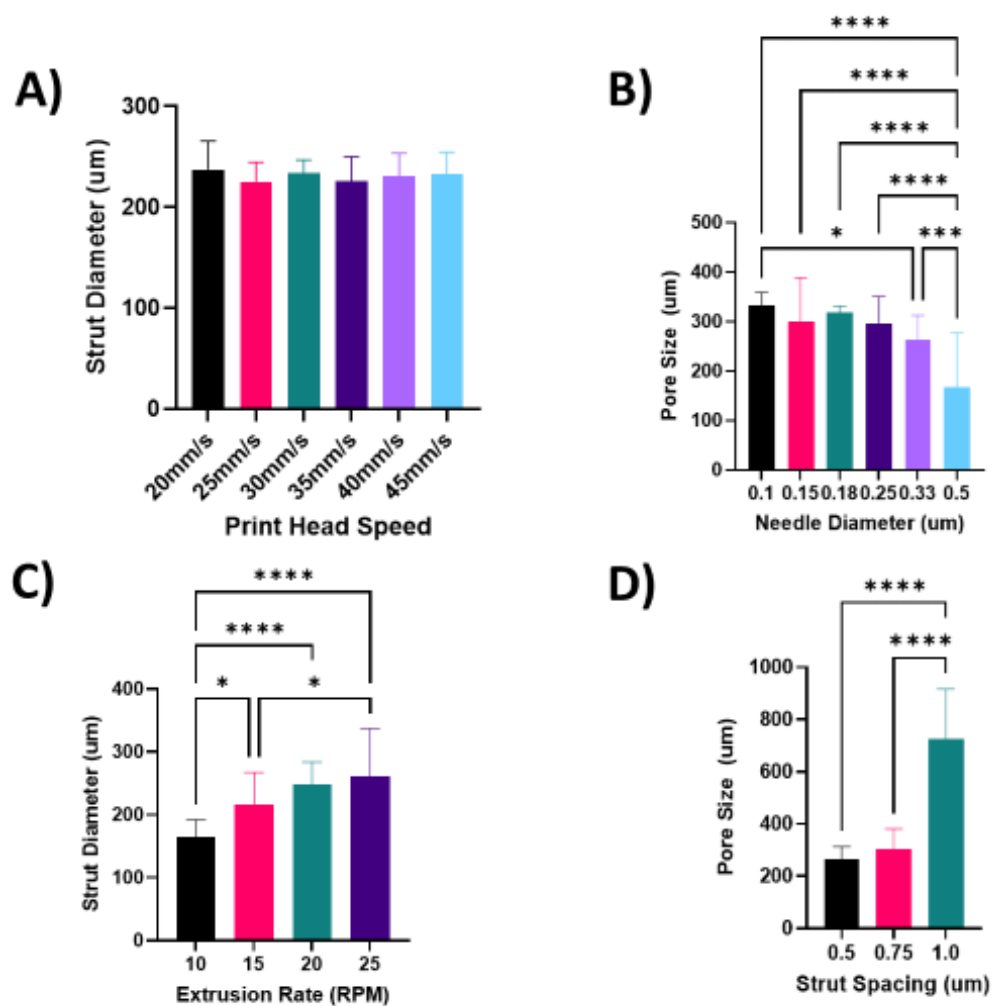


Figure 4-5 A) Graph showing how increasing speed of print head speed effected the diameter of struts printed, sizes determined using analyses of SEM images. B) Graph shows how increasing the size of nozzle used for printing effects the pore size of scaffolds, pore size also determined using SEM images. C) Increasing extrusion rate shows increasing strut diameter.

D) Increasing pre-programmed spacing between struts resulted in increasing pore size. *P 0.026 **P 0.09 ***P < 0.001 ****P < 0.0001. Values are reported as mean ± standard deviation, n=3

Prior to running experiments, 3D printing characteristics needed to be optimised such that parameters were varied and scaffolds were evaluated on their quality. There are a number of different parameters that are controlled by the user, including layer height, strut orientation, melting temperature, needle diameter and strut spacing. All of these parameters influence outputs like the overall porosity, pore size and mechanical strength. In order to assess overall quality of scaffolds, a combination of scanning electron microscopy [188] and Micro-CT volumetric analysis. Scaffolds should have a good degree of controlled reproducibility so variation characteristics should be kept to minimum. It was found that the primary reason for high strut size variation was for a high extrusion rate coupled with low printing speeds often led to thicker and non-uniform struts, although changing only the printing head speed and keeping other variables constant did not affect strut size (Figure 4-5). Strut spacing and layer height was very dependent on the needle diameter. Larger needle diameters decreased pore size (Figure 4-5) and as a result required increased strut spacing to accommodate the increased width of extruded material, to avoid fusion of struts together. Layer height also had to be increased to avoid struts being flattened and further widened under the deposition of layers on top of one another. The printing temperature was found to be most optimal at 74°C, temperatures below this led to needles becoming clogged with semi-molten material, and anything higher than this temperature was too high for layers to cool quickly enough to provide a solid surface for the next layer to be deposited on.

Overall, from imaging and CT acquisitions, the parameters which produced the least inter scaffold variability for a number of scaffolds using differing pore geometry and sizes were selected on an individual basis (Table 4-1) and carried forward for the experiments used in this thesis.

4.3.2 Scaffold Characterisation

The representative SEM images of the scaffolds with varied pore size and geometry are shown in. Table 4-2 summarises the measured geometries of the various scaffolds.

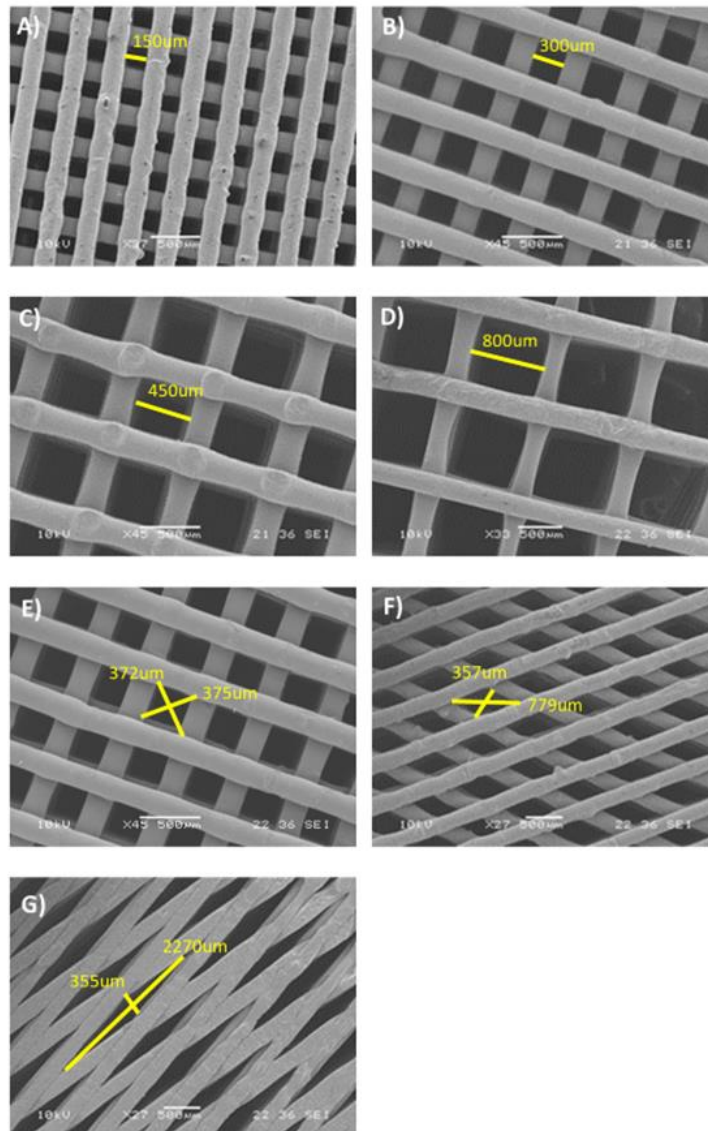


Figure 4-6 SEM Images of the porous structure of FDM printed scaffolds, A-D pore size samples from top view (PCL-90-150, PCL-90-300, PCL-90-450, PCL-90-800), E-G Pore geometry samples all from top view with average pore length and pore width measurements (PCL-0-90, PCL-0-45, PCL-0-15)

A)

Sample name	Laydown	Pore Size(μm)	Strut Size (μm)	Porosity
PCL-90-150	0/90°	171 \pm 22	196 \pm 5	60%
PCL-90-300	0/90°	267 \pm 20	197 \pm 11	68%
PCL-90-450	0/90°	431 \pm 25	218 \pm 20	75%
PCL-90-800	0/90°	828 \pm 45	210 \pm 19	81%

B)

Sample Name	Laydown	Pore Length (μm)	Pore Width (μm)	Strut Size (μm)	Porosity
PCL-0-90	0/90°	375 \pm 28	372 \pm 35	197 \pm 11	68%
PCL-0-45	0/45°	779 \pm 45	357 \pm 23	216 \pm 10	68%
PCL-0-15	0/15°	2270 \pm 210	355 \pm 41	199 \pm 17	67%

Table 4-2 Scaffold Characteristics measured from SEM top view images. Table A lists measurements of pore size, strut size and porosity for pore size samples. Table B is the scaffold measurements for scaffolds with varied pore geometry. Geometry values are recorded as mean values \pm standard deviation taken from samples n=3.

Scaffolds with large pores in the region of 500 μm to 850 μm have been shown to induce an increased osteogenic response in MSC's in addition to much faster fluid permeation [232]. Comparatively, chondrogenic differentiation of MSC's in scaffolds with smaller pore sizes ranging from 300 μm to 90 μm [123, 134, 135]. For each scaffold with varying pore size, all parameters excluding the distance between struts, were kept constant. SEM and μ -CT were used to characterise the size of the struts,

the size of the pores and the overall porosity (by μ -CT) of the scaffolds. In this instance pore size is quantified as the distance from edge to edge between struts. Strut size is measured as the diameter of the struts from cross sectional SEM images, and overall bulk porosity is calculated using micro CT. Bulk porosity increases with increased pore size as porosity is measured as the proportion of the volume of interest that is not occupied by solid objects.

Each scaffold design with varied pore geometry was also characterised using μ -CT and SEM to assess the pore size, strut spacing, strut size and overall porosity. The width of the pore is measured as the shortest distance corner to corner within pores and was kept as close to 360 μm as possible such that only the pore shape from altering the laydown angle was the over-riding variable. This variable is given as the pore length, which in this study is quantified as the longest diagonal from corner to corner within a single pore from SEM top down view images, given that this is the parameter that varies most between scaffold architectures. Micro-CT models show that the structures maintain interconnected pores for each design reflecting the controlled fabrication of FDM printing techniques. Porosity, calculated as the volume of void space using μ -CT reconstructions, across all three structures is shown to be relatively consistent, again to ensure the only variable effecting the functionality of the scaffold would be the shape of pores. Although there is no gold standard pore structure for cartilage regeneration, similar pore sizes, levels of porosity and amount of interconnectivity of the values used in this study have all been linked to good cartilage regeneration capabilities, supporting proliferation and differentiation towards chondrocyte lineage [139, 153, 156].

4.3.3 Mechanical Characterisation

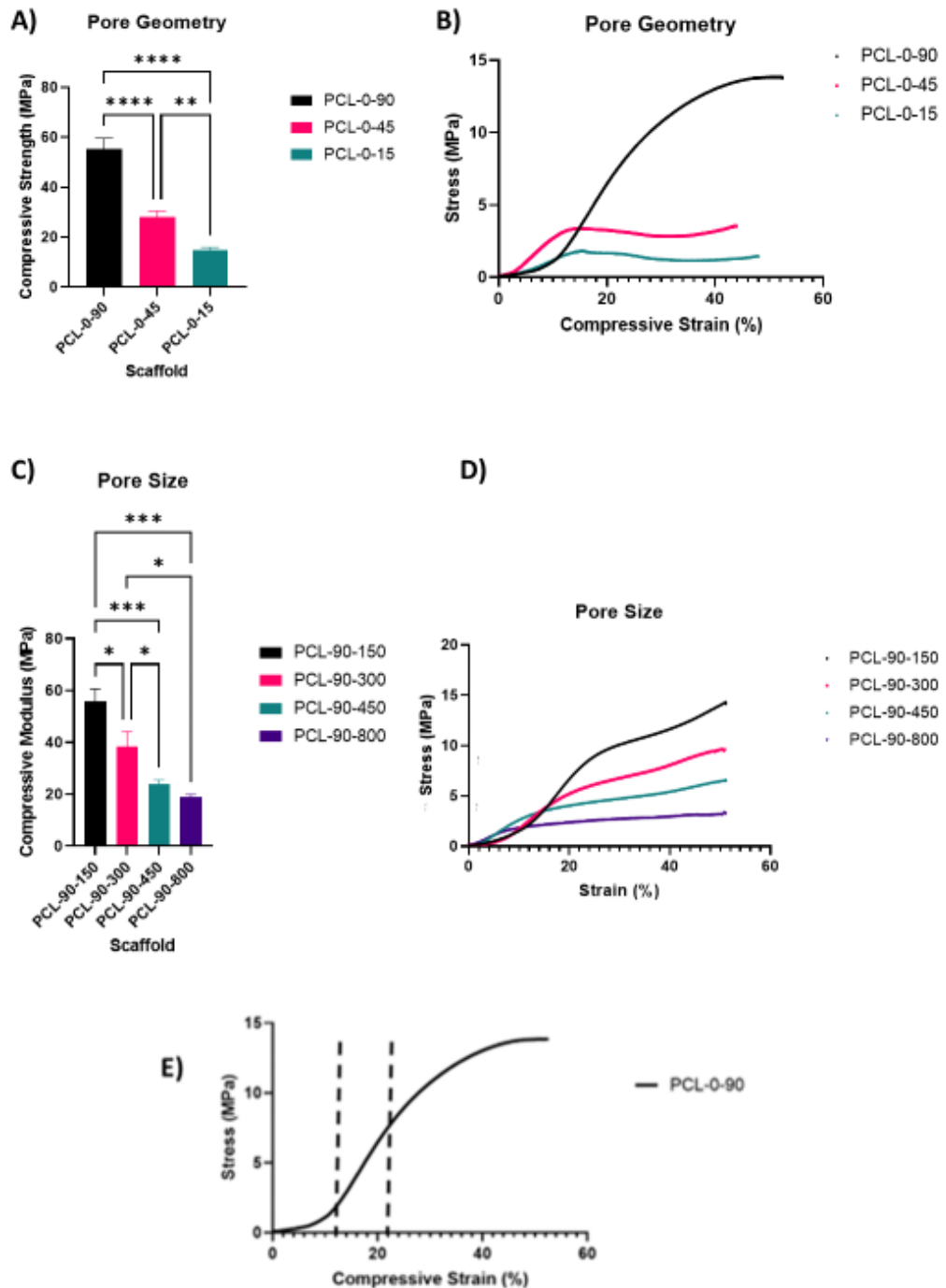


Figure 4-7 A) Compressive modulus mean values with \pm standard deviation of scaffolds with varied geometry ($n=3$) and B) the representative associated stress-strain curves. C) Compressive moduli mean values with \pm standard deviation of scaffolds with different pore sizes ($n=3$) and D) their representative stress-strain curves E) Stress-strain curve for PCL-0-90 indicating 10% linear region from which the modulus was calculated. * $P < 0.026$ ** $P < 0.09$ *** $P < 0.001$

Mechanical characterisation as seen in Figure 4-7 using compressive testing quantifies how changes in pore size and shape change the mechanical properties of scaffolds. Often a balance has to be struck between optimising internal pore architecture for suitable mechanical properties, that of human articular cartilage are recorded as between 0.44-20.4 MPa [94], but also a structure that provides appropriate surface area for cell attachment but also a large enough pore size to facilitate cell migration and nutrient diffusion in order to induce desirable cellular responses. It is therefore important to consider both elements when assessing scaffold properties. Changes in pore geometry, away from the most commonly seen 0/90° lattice architecture saw a decrease in the overall compressive modulus of the structures. Given the similar porosity exhibited by the scaffolds, differences in mechanical properties can largely be attributed to the orientation of struts and the resulting pore shape. Decreasing the deposition angle between struts for scaffolds with the same external geometry results in a decrease of the number of pores per axial single layer (pores per cross section approximately; PCL-0-90 = 324, PCL-0-45 = 216, PCL-0-15 = 90), and in turn less points of interconnection of struts between adjacent layers as they are deposited on top of one another. This will contribute to the scaffolds inability to resist compressive forces and similar trends have been seen elsewhere with FDM PCL scaffolds [183, 234]. In addition to this due to the low angle between struts the connections formed were not as strong as PCL-0-90 in which struts are deposited tangentially onto the struts below and fuse together much more easily. Printing patterns were much more prone to error when the angle of deposition was decreased as low as 15°. During compression PCL-0-45 and PCL-0-15 which exhibited lower compressive modulus appeared to visually exhibit shearing, in which the connections between layers sheared and came apart, a behaviour not evident in 0/90° samples. Therefore, it may be that the difference of the shape of the fibre connections. The connections are formed between printing adjacent layers on top of one another, and changing the angle between struts that is influencing the shape of these connections. Moving from a square connection formed between the right angle fibres in 0/90° to the more rhombic shaped connections in 0/45° and 0/15° there becomes a

decreased contact surface area between struts of adjacent layers, which would explain the shearing that causes struts to slip away from each other and deform under compression [9, 233].

Increasing pore size saw a significant decrease in the modulus of scaffolds under compression. The decreased volume of pore space and increased volume of material in 150 μm pore size scaffolds allowed it to withstand compression better than the other pore size groups. Scaffolds with a smaller pore size offer more surface area which has been shown to improve initial cell attachment but over longer periods of cell culture limits the migration of cells [132]. Scaffolds with a pore size above 300 μm were able to overcome this effect and were less susceptible to cell aggregations developing at the periphery of the structures [132]. Adequate tissue ingrowth and ECM production is vital for the maintenance of scaffolds mechanical properties *in vivo* as the polymer struts start to degrade [240]. Above 300 μm the modulus of the scaffolds significantly declined, although there was no statistically significant difference between scaffold pore size groups 450 μm and 800 μm . All pore size groups, fabricated with the same 0/90° strut arrangement displayed similar behaviour on the stress-strain curve, with an initial short linear region which is taken as the point in which the probe meets the scaffold, followed by a larger region of linear elasticity and finally a plateau indicating plastic deformation, which fits with previous literature [70]. The increased steepness of the smaller pore groups (150 μm and 300 μm) in the second larger linear elastic region can be attributed to the increased number of joints between struts and the decreased volume of pore space. This allows the scaffold to withstand compression forces for a more sustained period before entering plastic deformation than those groups with a larger pore size (450 μm and 800 μm).

4.3.4 Fluid Velocity Measurements

Flow experiments were performed by applying a flow rate of 5 mL/min based on flow regimes used in other literature [211] to cell free porous scaffolds which are mentioned

above. Experiments were performed using a custom-built flow chamber and a proton imaging probe for MRI scanning. This method allowed the visualisation of velocity profiles within a variety of porous architectures. NMR and MRI velocimetry measurements produce flow velocity maps using velocity information from each voxel over the entire scaffold. Velocities were recorded as the maximum velocity from within each individual pore (Figure 4-8), as flow within pores was laminar and velocity increased from wall to the centre of pore (Figure 4-18). Initially, experiments were performed using inserts that had a 3 mm inner diameter channel for fluid flow (Figure 4-9). From the outset created problems with large pockets of air becoming trapped between the scaffold and the inserts, seemingly too large to be perfused out of the scaffold through the channel of the insert. The effects of this can be seen in Figure 4-10 and Figure 4-11, in which a number of smaller bubbles and one very large bubble have formed, making it impossible to get an accurate representation of fluid flow through pores that is not influenced by the effects of bubble formation.

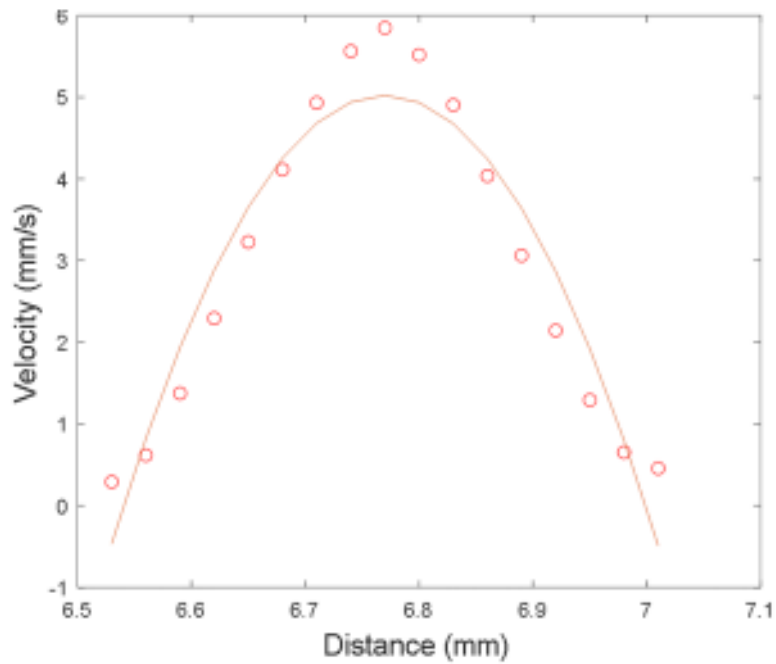
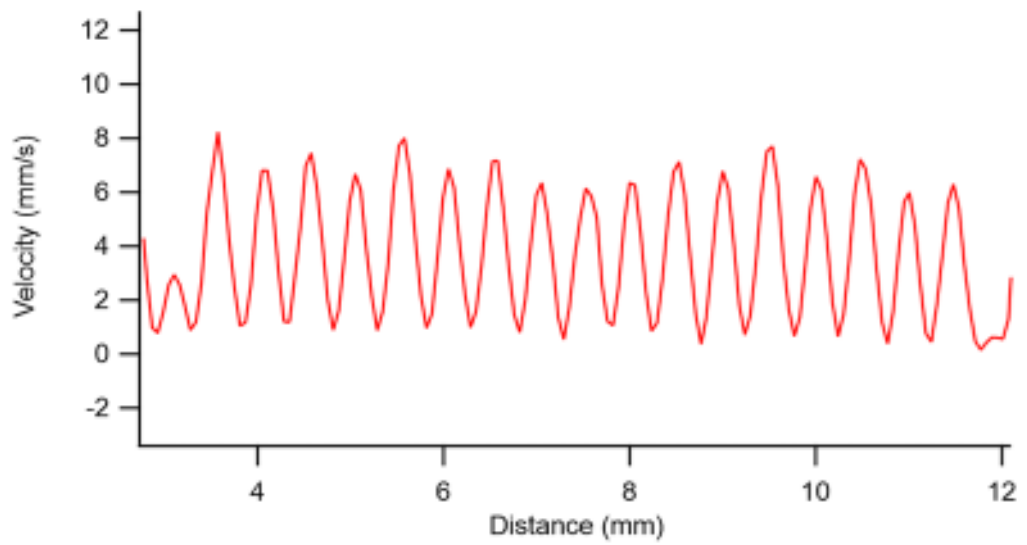


Figure 4-8 Example of pore velocity profiles, taken across a group of pores (above) and the profile of one single pore (below). Distance indicates location across the axial slice of a scaffold.

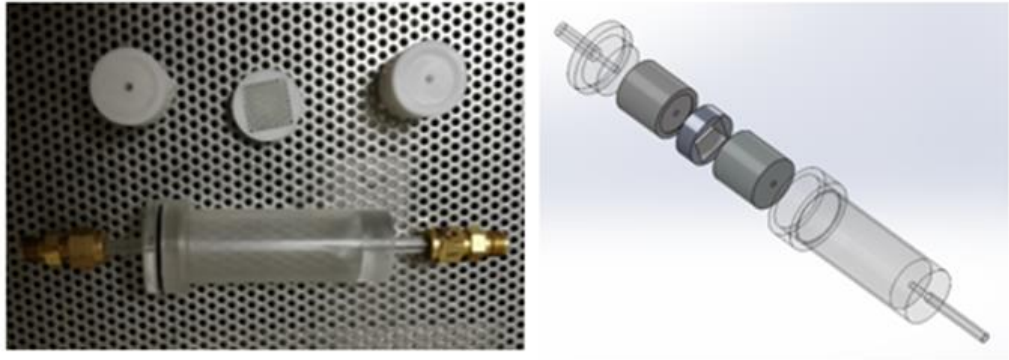


Figure 4-9 Flow chamber design before alterations, consisting of inlets that were not tapered that resulted in a high degree of bubble formation. Image of individual parts that make up chamber (left) and schematic of how parts fit together [241].

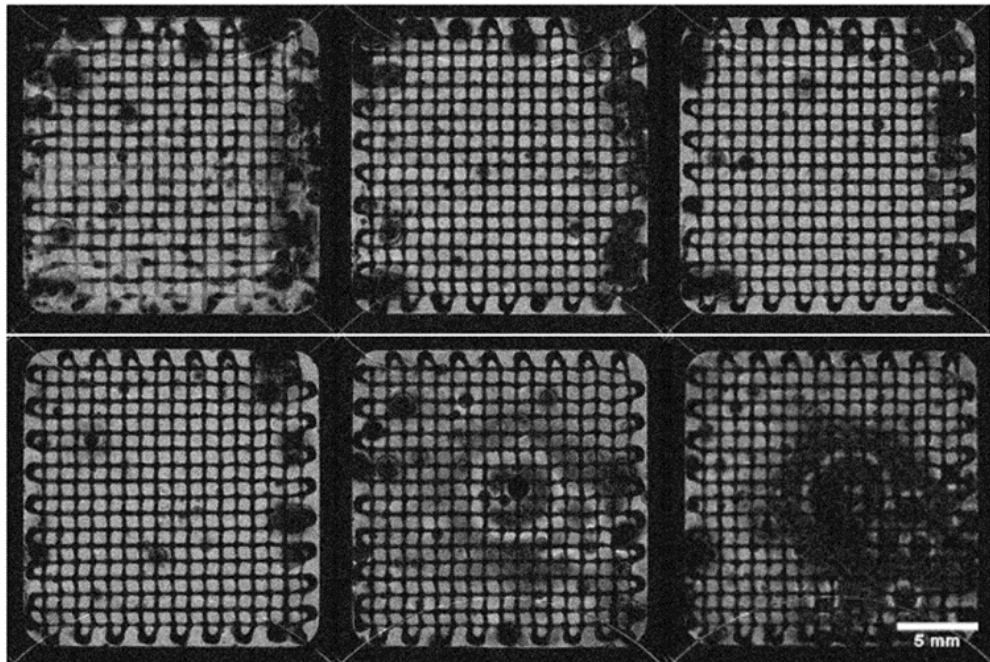


Figure 4-10 MSME imaging used to show how bubble formation in scaffolds, which appear as dark areas void of signal. Images taken as axial slices from top to bottom of scaffold.

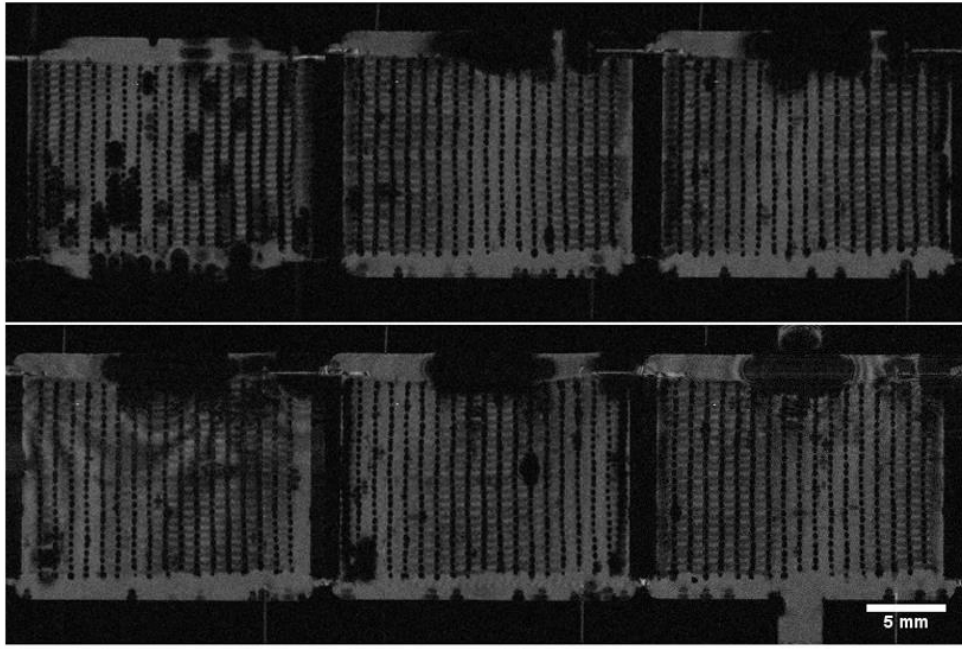


Figure 4-11 Sagittal projections slicing from left to right in the scaffold showing the formation of bubbles, appearing as larger round dark areas, particularly at the top region of the scaffold closest to the outlet.

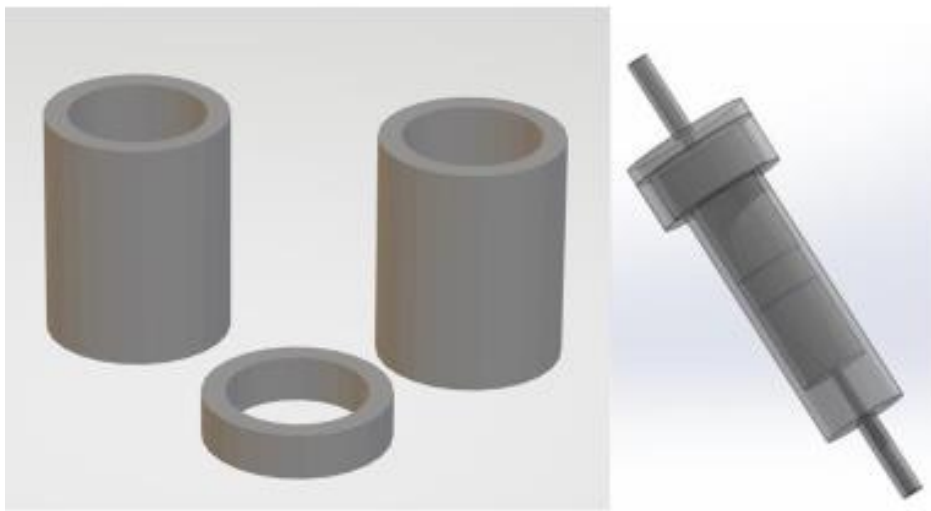


Figure 4-12 Redesigned flow chamber with inlets that sit either side of scaffold holder, the internal diameter of inlets has been greatly increased to avoid bubble formation. Image of individual components (top) and schematic of parts assembled (below).

To try to alleviate bubble formation, the inserts were redesigned so the inner diameter was increased to 16 mm (Figure 4-12). The much wider opening above and below the scaffold did successfully allow for the removal of bubbles, and scaffolds produced homogeneous fluid filled pores. However, when measuring velocity there was an unexpected result, in that an irregular velocity map was produced (Figure 4-13). Velocity varied across the scaffold from left to right, velocity was lower in the middle of but faster at both edges of the scaffold. Turbulence is known to be associated with high velocity flow and large orifice inlets. The chamber in this experiment had been

designed with space above and below the scaffold that could be easily and freely filled with fluid under the expectation this would reduce the formation of bubbles from pockets of trapped air. However, the chamber still had small inlets and outlets (3 mm) at the points of connection with tubing. This means there is a sudden transition from a small channel to a much larger channel. The combination of fluid flowing at a relatively fast velocity, and moving from a small inlet to a widening orifice and then back to small micro-channels in the porous scaffold could therefore result in turbulence and in turn heterogeneous velocity patterns. Turbulence is a random and stochastic process in which molecules become disorganised and begin to swirl with the formation of eddy currents. Reynolds number, the ratio between inertial forces and viscous forces, can be used to characterise flow, flow becomes turbulent when Reynolds number >3000 . The formation of these eddy currents can cause circular flow which may explain the flow velocity pattern seen in Figure 4-13. To circumvent these issues, the insert design was altered to a tapered design (described in 4.2.2) to create a more gradual transition from one size channel to another and maintain laminar flow. This provided a balance between the avoidance of bubble formation, but did not produce irregular velocity patterns within scaffolds. Such that the remaining experiments in this thesis use flow chamber design.

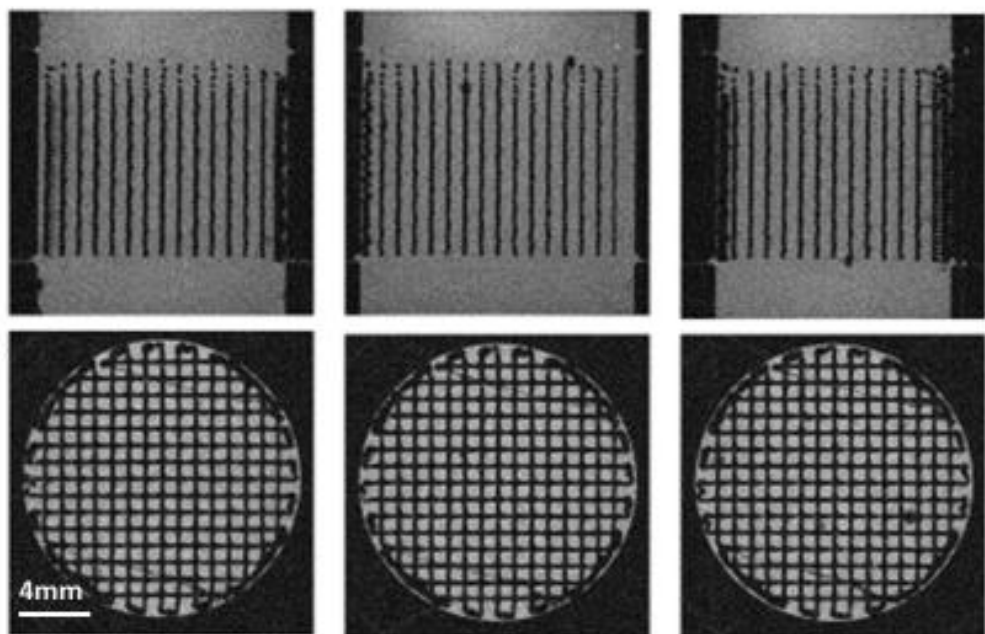
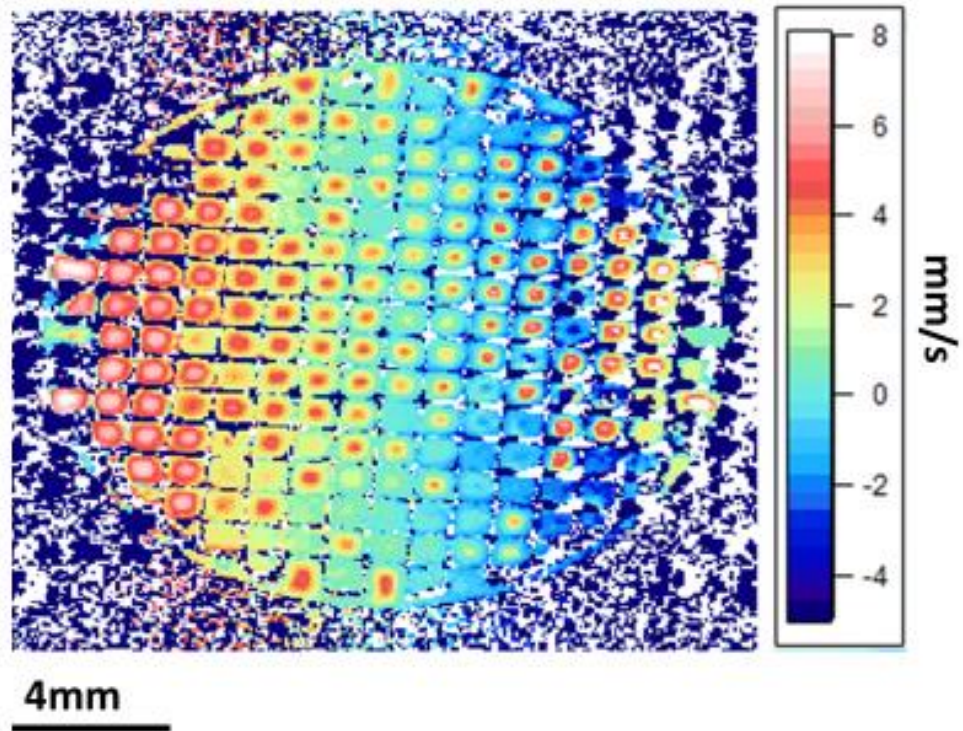


Figure 4-13 Resultant velocity map (top) in which colour scale indicates recorded velocities as mm/s. MSME images (bottom) from changing the design of flow chamber inserts to avoid bubble formation Images taken from 3 sliced locations in the axial and sagittal directions.. Velocity map shows a inhomogeneous pattern of velocity. MR imaging shows bubbles were successfully removed.

4.3.4.1 Pore Size

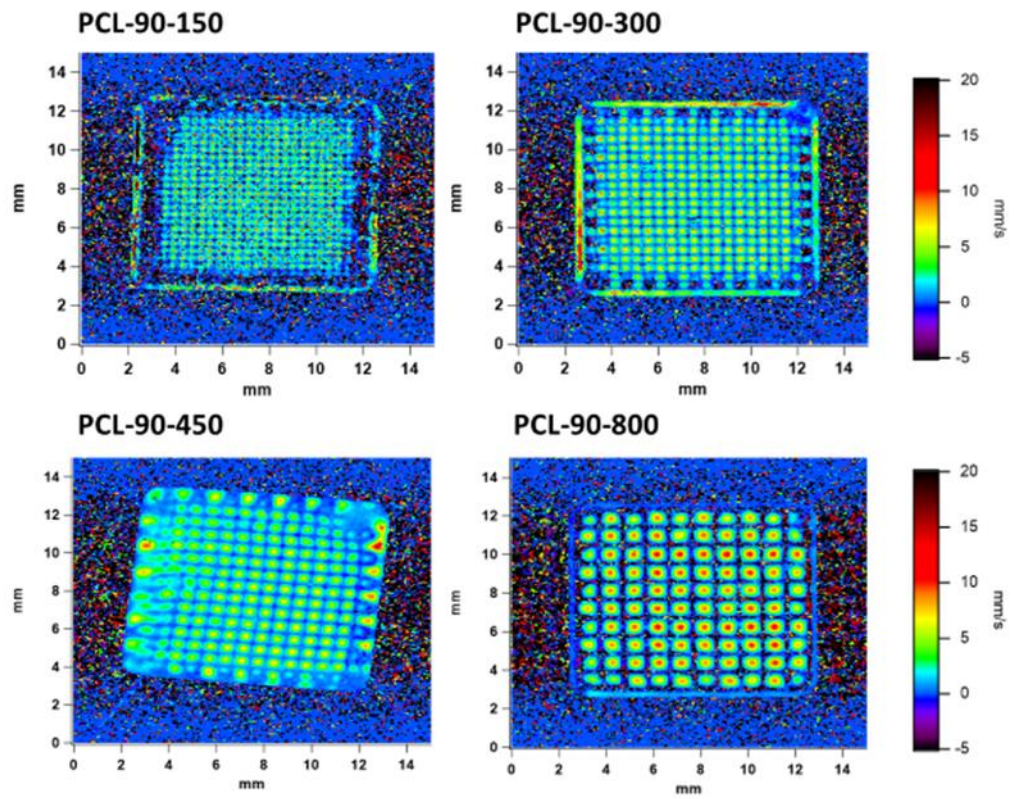


Figure 4-14 Mapped velocity in porous scaffolds using NMR and MRI. Signal is recorded from proton dense fluid water in individual pores travelling in the z direction. Areas around the scaffold made up of plastic represent areas of noise.

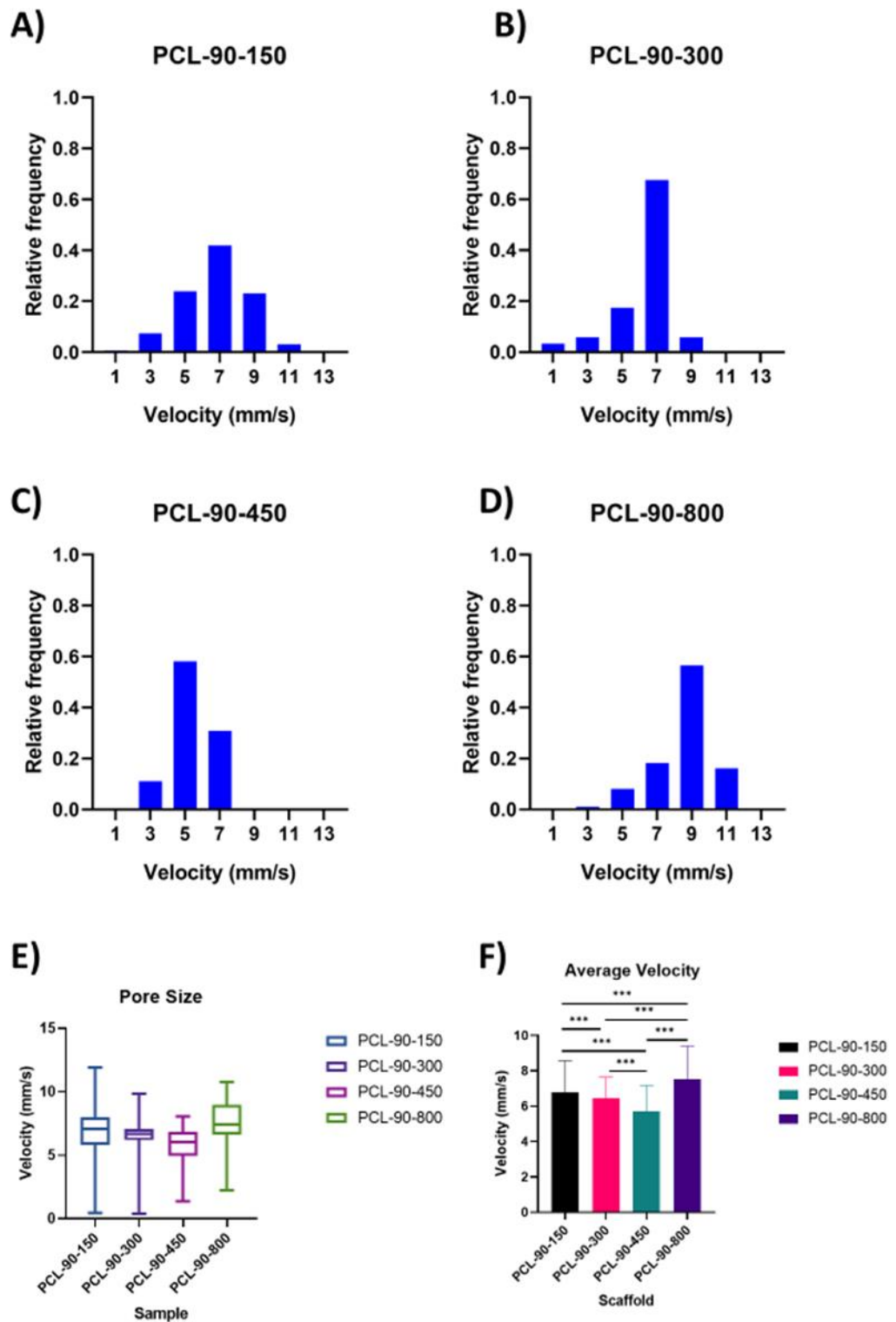


Figure 4-15 (A-D) Relative frequency of velocities measured in scaffolds with varied pore sizes shown in histograms. E) Box Plots showing distribution and amount of variation of velocity and F) comparison of average velocity of flow through scaffolds with varying pore sizes. Significance difference (***) $p < 0.001$ between all group comparisons for mean velocity measurements for pore size groups ($n = 3$).

The effect of pore size in scaffolds grown under perfusion bioreactor conditions has been modelled to show that pore size strongly influences the predicted shear stress magnitudes, with lower pore sizes resulting in higher shear stress [242]. In our study fluid perfused through scaffolds, varied by their pore size from 150µm up to as large as 800µm, was recorded and translated to corresponding velocity maps (Figure 4-14). Scaffolds printed with the smallest pore size had the largest spread of velocities recorded within individual pores ranging from 0.44 mm/s minimum recorded up to a maximum of 11.88 mm/s (Figure 4-15). The reduced size of pores seemingly made the scaffold more prone to having pores within which velocity significantly decreased compared to the average velocity. Similarly, other pores in predominantly the PCL-90-150 samples and in some cases in PCL-90-300, saw some individual pores with a greatly increased velocity. This could be directly related to the pores with zero or low velocity not being entirely permeable and therefore not as easily allowing fluid to pass through, resulting in a build-up of localised pressure, forcing the fluid through other pores at a much greater velocity. Similar results have been shown in studies to visualise the clogging process in a homogeneous porous medium, which resulted in increasing pressures and incidences of higher velocity particles as the number of clogged pores increased [243].

For all scaffolds, there was notably regions at the periphery of high velocity where the seal between scaffold and chamber was not tight enough to prevent gaps, such that this larger area of space compared to pores induced preferential flow through these regions at a greater velocity. Although the velocity in this region was not included in the results (Figure 4-15) the effects of this to the porous regions in the scaffold need to be elucidated. The gaps themselves could be attributed to variations in flow patterns recorded across the scaffold pores as it essentially creates a very large pore that would cause preferential less restricted flow through the gap as opposed to the surrounding actual scaffold pores in the same vicinity, which are much smaller. This replicates results from another CFD simulation of perfusion in 3D printed scaffolds [244].

Larger pore sizes have been simulated with CFD to show that the increased pore space allows a linearly increasing fluid velocity [245]. Although in our study that the largest pore size 800 μm is associated with the largest mean velocity of 7.5 mm/s (Figure 4-15) the trend in fluid velocity from smallest to largest pore is certainly not linear. In fact, from 150 μm pore size upwards to 450 μm the trend appears to be a decrease in the mean velocity across all pores. However, amongst these groups and the PCL-90-800, none displayed a homogeneous distribution of velocity across the scaffold. The degree of variation in velocity can be visualised in the boxplot figure (Figure 4-15) shows the smaller pore groups PCL-90-150 and PCL-90-300, had the largest overall spread of data, consistent with the associated histograms (Figure 4-15) and with the visible mapping of velocities showing a range of low velocity and high velocity pores across the scaffold. This variability will influence the overall mean velocity and can explain why a linear trend between increasing pore size and increasing velocity is not seen in this study.

Above all else flow maps produced using NMR and MRI measurements validate this technique as an alternative to current CFD and Optical methods as a non-destructive experimental method. Accurately quantifying velocities and the associated forces in bioreactors for dynamic culture currently remains a challenge but is vital for understanding the roles those forces, and the design of the bioreactor and scaffold play in the differentiation and proliferation of cells. Numerical models, whilst providing a fast and cost-effective way to simulate the fluidic environment within scaffolds, can be limited by the computational capacity and the assumptions about the flow conditions required. For instance, some studies have incorporated scaffolds with geometry idealised to regular geometry due to the computational difficulties of meshing real geometry [12, 246]. A study [244] compared modelling of scaffolds with meshed real geometry and found a great degree of variation between scaffolds despite them being commercially produced using rapid prototyping methods, with stress levels as much as two times higher from sample to sample. Therefore, this demonstrates the importance of thorough analysis in order to quantify the real forces

applied to cell seeded scaffolds which may be better achieved through experimental data.

Inhomogeneous flow patterns could impact a number of variables in the 3D culture of cells under dynamic conditions. It is firstly important to consider how the inhomogeneous velocity patterns will be reflected with inhomogeneous stress exposure for cells. For a Newtonian fluid, shear stresses are linearly proportional to the velocity gradient, such that increased velocity results in increased shear stresses. Wall shear stress levels for MSC's can be used to invoke different responses. Studies varying perfusion and in turn shear stress levels have been able to show that lower shear stress level in low velocity or static culture conditions support a greater increase in proliferation, compared to higher levels of shear stresses which were associated with increased osteogenic differentiation [172, 173]. Other studies using MCT3T3 have similarly shown low fluid induced shear stresses encouraged a higher degree of cell proliferation compared to higher shear stresses which resulted in the expression of osteogenic markers. However, in the aforementioned studies higher velocities were associated with either increased cell death [8] or inhibiting the expression of osteogenic markers [247]. Therefore, it is evident the importance of shear stresses and the mechano-response of cells. Inhomogeneous velocity patterns that induce inhomogeneous shear stress patterns would ultimately result in a varied response by cells depending on their location within the scaffold, and this in turn reduces the capabilities to successfully regenerate tissues.

It is also important to consider how far the variability of velocities could influence cell seeding and initial cell distributions. The volume of available surface area and the preferred path of travel for cell suspensions are the two biggest factors to consider. MSC's have been shown to more successfully infiltrate scaffolds compared to static culture and migrate through scaffolds in the direction of flow compared to seemingly random migration under static conditions [248, 249]. However increasing pore size is also negatively correlated with levels of cell attachment [122]. Therefore, in our study

although the larger pore sizes were prone to relatively fewer variable velocities the porous structure itself may not at all be suitable for a good degree of cell attachment. Furthermore to this flow rate is also proportional to cell detachment [7] so a reduced flow rate in conjunction with a reduced pore size could also improve cell attachment. Increasing pore size even without the introduction of fluid shear stresses also increases cell infiltration and avoids cell aggregation at the scaffold periphery, although in that reported study the largest pore size was 325 μm and later in culture the smallest pores (85 μm) did form cell aggregates at the periphery [131]. It is therefore difficult to predict the suitability of each scaffold in this study in terms of cell adhesion and migration but it is clear from the literature that pore size plays an influential role in the outcome.

4.3.4.2 Pore Geometry

Another factor in porous architecture design which has garnered interest is the shape or geometry of pores, and its potential in influencing the overall outcome for tissue regeneration strategies. In this study, laydown angles were varied between groups whilst keeping all other variables constant to create pores differing in shape. The geometry of scaffold pores effects the biological performance in terms of cell seeding and cell proliferation under static cell culture conditions. There is evidence that decreasing deposition angles can provide more pore space, which improves hMSC's accessibility and colonisation of the inner part of scaffolds over 21 days [233], in addition to other studies in which changes in pore architecture using offsets provided a greater surface area for attachment which resulted in significantly higher levels of cell proliferation [250]

CFD simulations have been utilised to map fluid flow through porous scaffolds with a focus on the geometry of pore, with many prioritising scaffolds with irregular scaffold geometries [178, 251, 252]. However, these studies, restricted by computational requirements were only able to model subsections of scaffolds. Other studies have

progressed to model the entirety to avoid influence of boundary conditions but come at an increased computational cost [182, 253]. In this study, NMR and MRI velocimetry measurements were taken in scaffolds with three pore shapes 0/90° 0/45°, 0/15°. A slice selective method was employed which can be used to measure velocity at specific locations at a selected slice thickness. The results from this study only include measurements taken from the central region of the scaffold as to compare the effects of scaffold pore geometry as when comparing velocity information from different regions of the scaffold there was no significant differences between velocity profile irrespective of position (Figure 4-16).

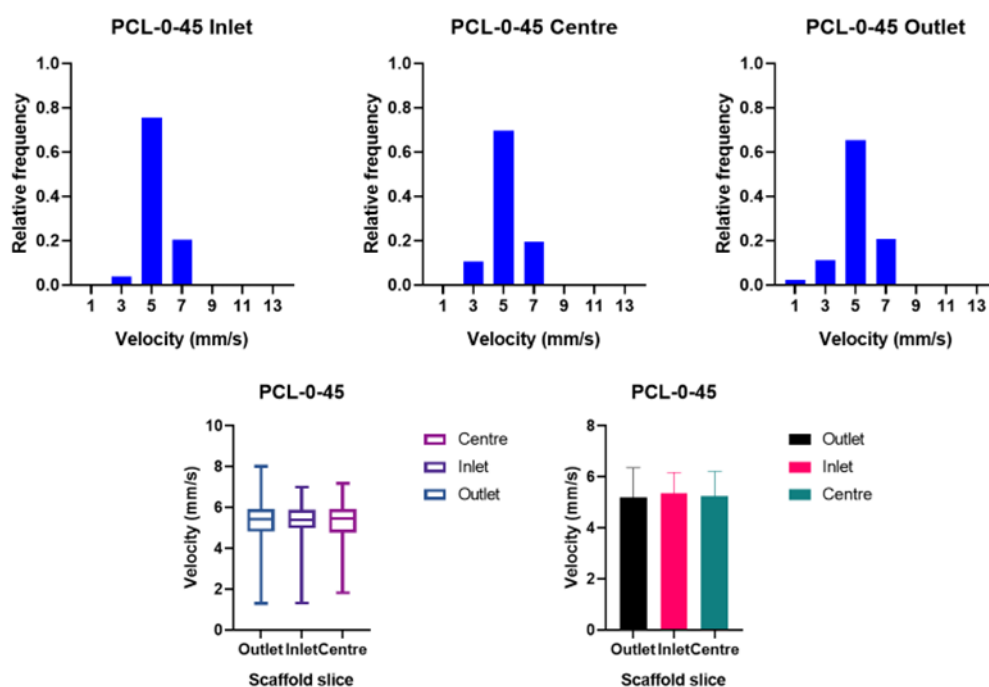


Figure 4-16 Relative frequency distribution of three sliced images taken from different locations within the same scaffold. Boxplot to visualise how the spread of data compares and a bar chart to show the average velocity and standard deviation of each slice (n=3).

Each pore group was perfused with fluid at 5 mL/min, and each possessed interconnected pore channels and similar degrees of porosity. However, decreasing the angle between struts to 0/15° seemed to largely effect the homogeneity of fluid flow through the scaffold. Relative frequency distributions (Figure 4-17) for this group

showed that there was a much greater spread of velocities recorded at pore level across the scaffold resulting in a much more heterogeneous flow pattern. In contrast to this the 0/90° and 0/45° angles both displayed a relatively similar distribution of velocity and a comparatively more homogeneous flow pattern. PCL-0-15 scaffolds had large variations between measurements of pore length (Table 4-2) which could explain this. The standard deviation for pore length measurements was more than $\pm 200 \mu\text{m}$ for PCL-0-15, compared to $\pm 28 \mu\text{m}$ for PCL-0-90 and $\pm 45 \mu\text{m}$ for PCL-0-45 respectively. The pore sizes in PCL-0-15 scaffolds are inhomogeneous, made up of some very large pores and some much smaller. This is reflected in the inhomogeneity of velocities which was much quicker in the larger and less restrictive pores, where flow is preferential. However, in the smaller more restrictive pores there was a lower velocity of flow measured. This greater degree of variation in pore measurements is likely to be a result of limitations associated with dimensional accuracy between CAD designs and actual scaffolds of 3D printing FDM techniques. Optimisation studies of FDM parameters have highlighted that deposition angles and orientation of printed struts affect the dimensional accuracy of printed structures compared to original CAD designs [72, 254, 255].

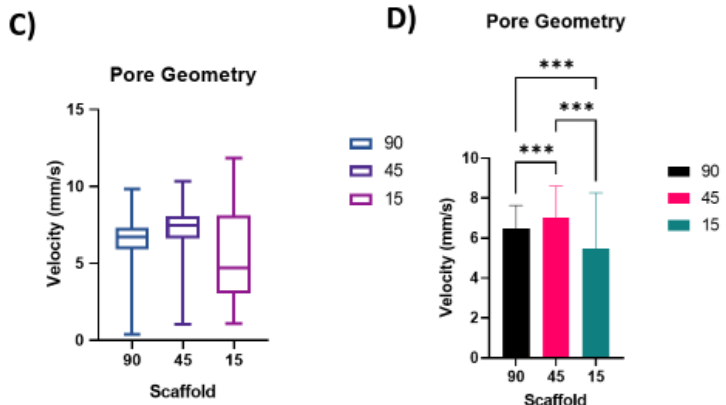
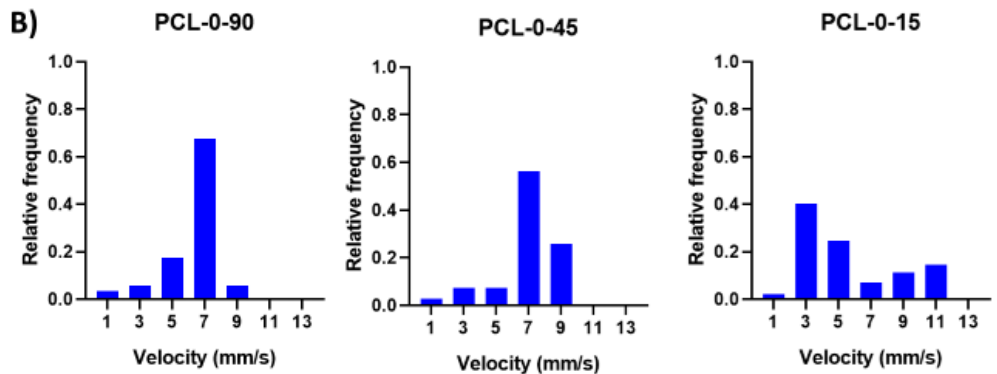
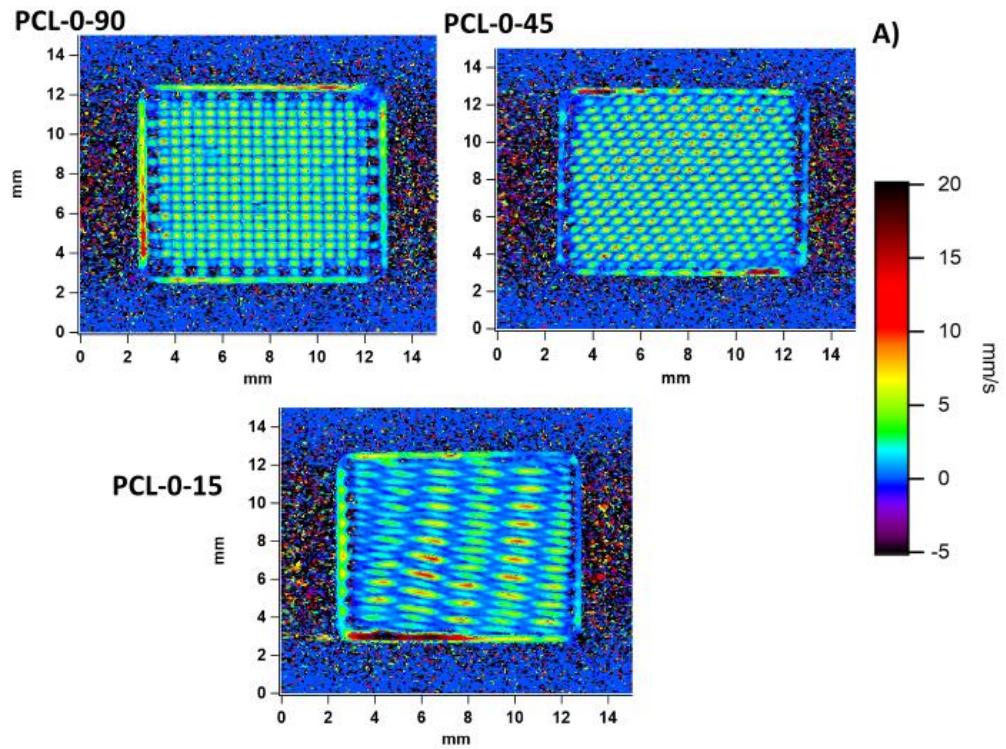


Figure 4-17 A) Mapped velocity in porous scaffold using NMR and MRI displaying the flow distribution in different pore geometries. B) Histograms displaying relative frequency of velocity within each geometry.

C-D) Distribution box plots and average velocity measure \pm standard deviation in porous scaffold with distinct pore geometry ***P <0.001 (n=3).

Furthermore, printing with a small angle of 15° between deposited struts reduces the possibility of good layer to layer adhesion because this relies on good overlapping of struts in consecutive layers, however due to constraints of the printing technique low angles instead resulted in struts having a limited contact area due to the angle causing in some instances struts to be printed alongside each other instead of fusing together on top of one another. In addition to this, there were less points of connection between struts within a layer due to less pores per layer and another study has characterised strut deposition angles of 15° causing irregular layer connections [234]. Fused deposition modelling printing relies on good connection between layers of molten material and reducing this could create a less controlled homogeneous pore architecture. Contrary to this, PCL-0-90 and PCL-0-45 both exhibited uniform geometry with much less variation in pore dimensions which was reflected in the more even distribution of flow velocities.

The absence of laminar flow could also be proposed as a reason for inhomogeneous flow regimes in a perfusion system. Turbulence is a random and stochastic process in which molecules become disorganised, and swirl to produce eddy currents, altering the subsequent velocity profile. Visualising flow profiles can identify which flow regime is present. Velocity flow profiles which indicate laminar flow form a parabolic curve with peak velocities at the centre of the channel in question, as opposed to turbulent flow in which a fairly flat distribution of velocity would be expected over the cross section of the pore channel. Second order polynomial curve fitting shows that the behaviour of flow in channels for each scaffold geometry (Figure 4-18) produced a near parabolic curve, regardless of the peak velocity or pore shape. This therefore indicates that differences in flow homogeneity is not likely to have been the result of turbulent flow within pores.

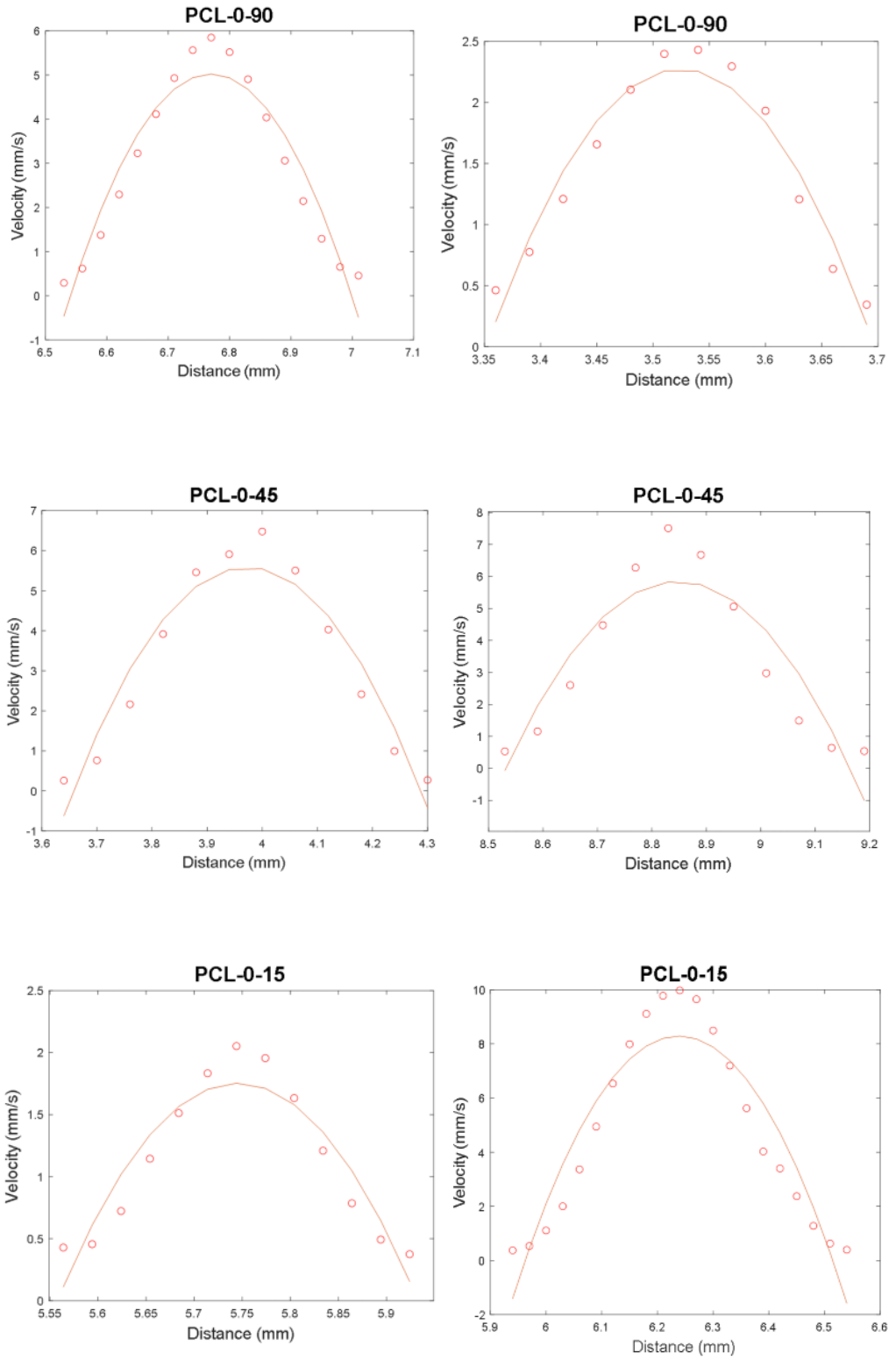


Figure 4-18 Examples of curve fitting of velocity profiles for individual pores for each scaffold geometry.

4.3.4.3 Leak Area

Velocities from each sample were only recorded within the porous channels. Comparison of repeats of each pore design showed for PCL-0-90 and PCL-045 samples were largely consistent with each other. Whilst PCL-0-15 had more variation between samples it continued with a trend of a wide spread of different velocities (Figure 4-20 and Figure 4-21). However, one thing that became apparent, when comparing replicates was that some scaffolds did not achieve as good a seal with the periphery of the flow chamber as others, this was mostly prevalent for PCL-0-15. This is evident in the mapped flow diagrams where large areas of high velocity fluid are passing through at the edges of scaffolds. In sample 3 of PCL-0-90 (Figure 4-20) appears to be fully flush to the edges of the chamber with no visible leak area, which corresponds to the smallest relative distribution of velocities measure within pores. This compared to all three repeats of the PCL-0-15 scaffolds and PCL-0-45 (Figure 4-20) which tended to be compressed in the direction of the 15° and 45° strands (Figure 4-19), but not in the struts at 0°. Thus, creating gaps at the periphery perpendicular to the strands in the 0° direction of the scaffold to form a visible leak area increased the degree of variation in velocity.

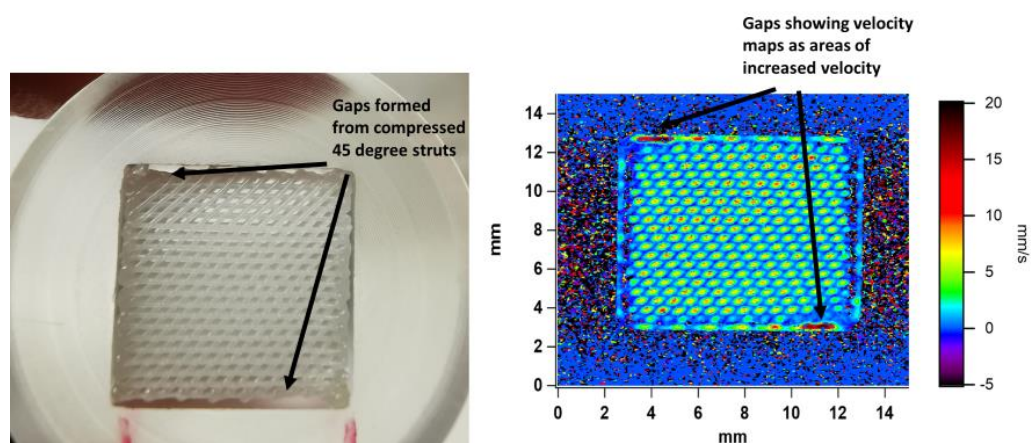


Figure 4-19 Image showing a scaffold within flow chamber insert that encases it during flow experiments compared with the flow map produced from this. Highlighted are the gaps formed when the scaffold is enclosed in the chamber and the corresponding effects in velocity mapping.

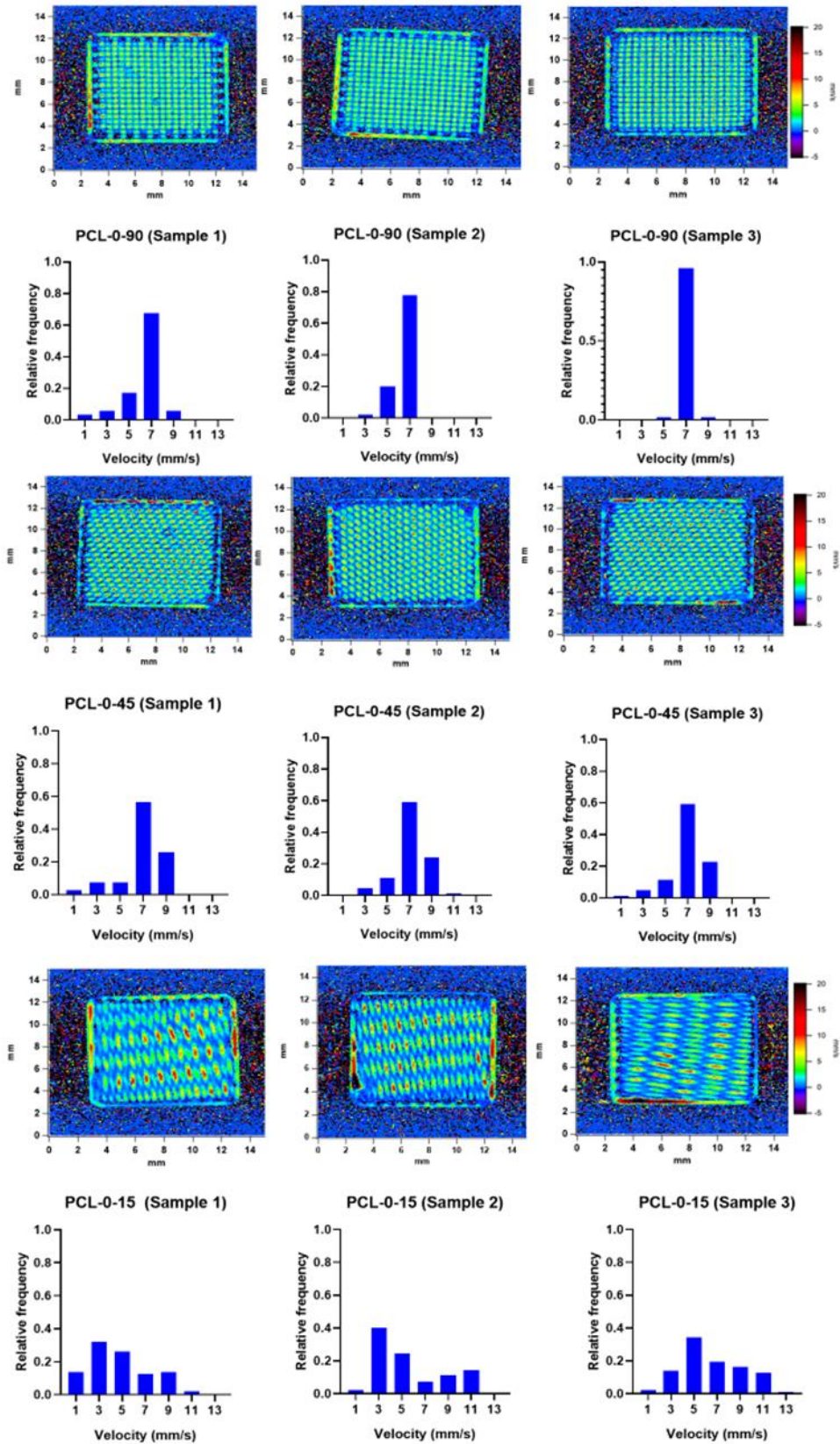


Figure 4-20 Velocity profiles of PCL-0-90, PCL -0-45 and PCL-0-15 geometry porous scaffolds repeated three times on separate scaffolds

under the same flow conditions and relative frequency distribution graphs for each sample

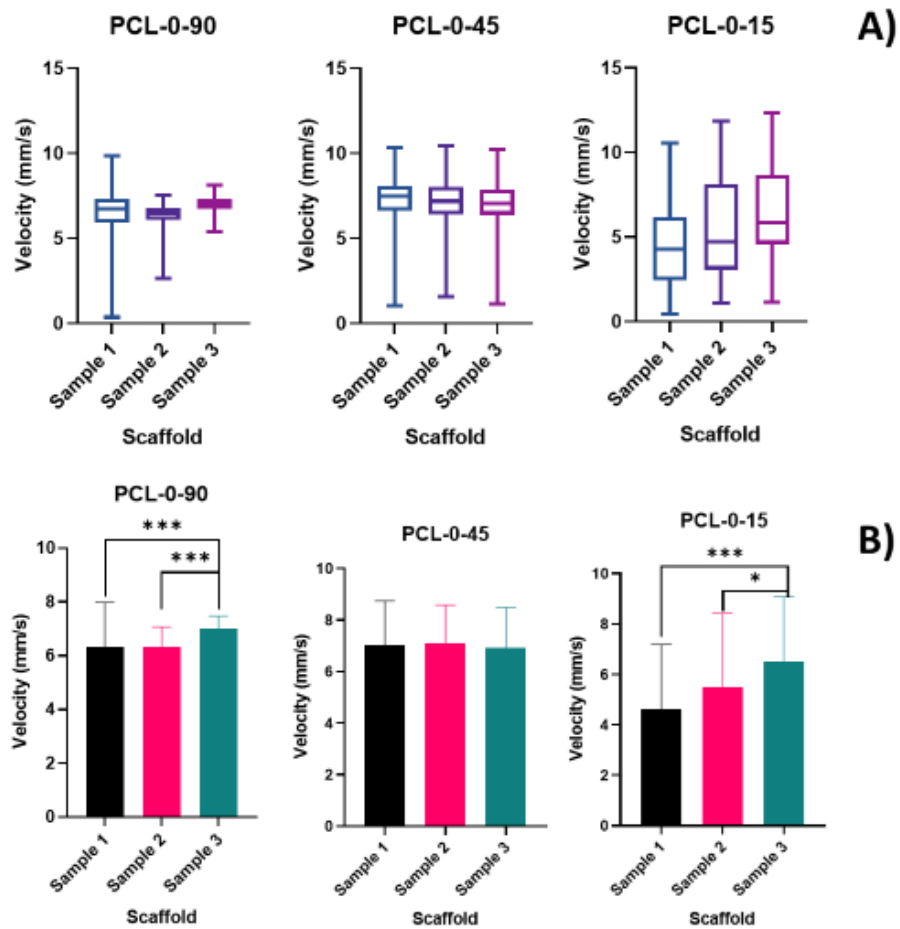


Figure 4-21 A) Box plot diagrams displaying the distribution of velocities recorded for each scaffold with in pore geometry groups. B) Average velocities \pm standard deviation for each sample within each geometry group *P 0.03 ***P <0.001 (n=3).

The effect of this leak area in relation to homogeneity of flow patterns across the scaffold was quantified. The total area (mm^2), defined as the area between the sidewall of the scaffold, and the chamber wall within which fluid was flowing, was compared with the average velocity recorded across all pores within the associated scaffold and the standard deviation of said average velocity. A Pearson correlation test (Figure 4-22) between leak area and average velocity returned an r value, defined as the coefficient of correlation and measured between -1 and +1, of -0.4722 which indicated a negative correlation between increased velocity and decreased leak area,

although was not a significant statistical correlation ($P=.199$). Likewise, there was a slight positive correlation between increasing leak area and increasing standard deviation, with an r value of 0.5102, but again not statistically significant ($P=.161$). Pearson correlation is a linear correlation coefficient to indicate the extent to which points will lie on a straight line, in which -1 represents a strong negative correlation, +1 indicates a strong positive correlation and zero indicates no correlation at all. The R squared values indicate the fraction of variance between the two variables, such that 26% of the variation in the measurements of velocity standard deviation can be explained by the leak area, and likewise 22% of variation in average velocity measurement are accounted for by the leak area. All of this indicates there is no obvious connection between velocity fluctuations and the leak are, at least statistically. However, the effect of something like a large leak area that vary between scaffolds, would make it more difficult to standardise the culture process for cells.

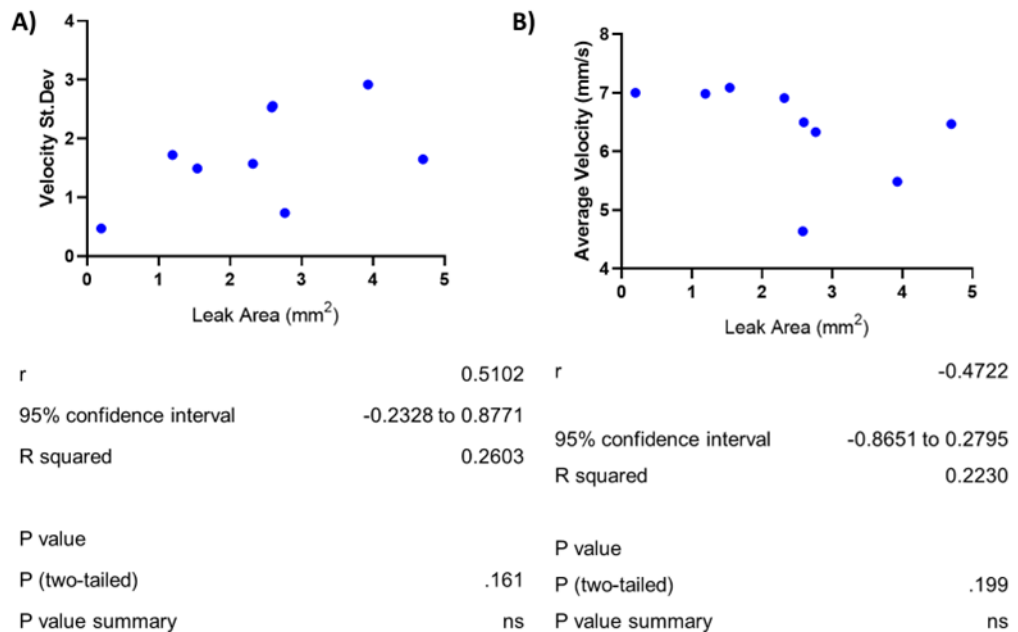


Figure 4-22 A) The total area of the leak area (scaffold where the seal to bioreactor is not flush and allows to flow through) plotted against the standard deviation of velocity within a scaffold where R^2 value shows 26% of standard deviation is accounted for by the Leak area. B) The overall average velocity plotted against the leak area, where R^2 value shows 22% of Average velocity is accounted for by the leak area.

Despite no statistically significant correlation between the variables, it is fair to say that scaffolds without a flush fit between scaffold periphery and bioreactor walls, presenting gaps for fluid to move through outside of the porous architecture is an undesirable characteristic for dynamic cell culture. When all efforts are directed towards achieving homogeneous distribution on flow, large gaps in a perfusion system will only create a viable diversion for fluid flow, seeking the least resistive path. The large leak area has inadvertently created an additional large pore on the periphery of the system essentially increasing the porosity. Tortuosity factor is a quantitative method to measure the reduction in flow through an area over a unit of time imposed by obstacles to flow. In this case the obstacle to flow is the 3D printed struts, such that tortuosity is increased in the presence of struts compared to the straightest path in an unrestricted medium [256]. Tortuosity underpins the relationship between porous geometry and the transport process. It depends upon the connectivity and constriction of pores [257], such that increased porosity from the large less constrictive leak area causes flow paths to become less tortuous and as a result increased velocity [258]. This data does bring to light questions about bioreactor design, and how much consideration is given to how bioreactors facilitate scaffolds. There is consideration in other research for how dead zones can be avoided in scaffold through effective bioreactor design [259] i.e. ensuring maximum effective flow of media that reaches all area of scaffolds. Less consideration however has been given to how flow could be bypassing parts of the scaffold due to poor fits for scaffolds in bioreactors although it has been highlighted elsewhere as an issue that arises [244]. This data also provides an insight into how future bioreactor design may need to be more adaptable to the increased ability of 3D printing to produce more complex and irregular scaffolds, whilst maintaining an efficient flow regime. Traditionally bioreactor design incorporates rigid press fit scaffold housing [112, 170] similar to what is used in this study, but as results here show there is a danger such rigid components are not suitable for scaffolds susceptible to compression when confined. Deformable scaffold holders have been employed in bioreactor design to facilitate easier housing of scaffolds regardless of shape, however despite this, the holder did still require a good level of rigidity in

scaffolds to prevent compression of the construct so may be better suited to metallic or ceramic scaffolds, or more stiff polymer scaffolds [260].

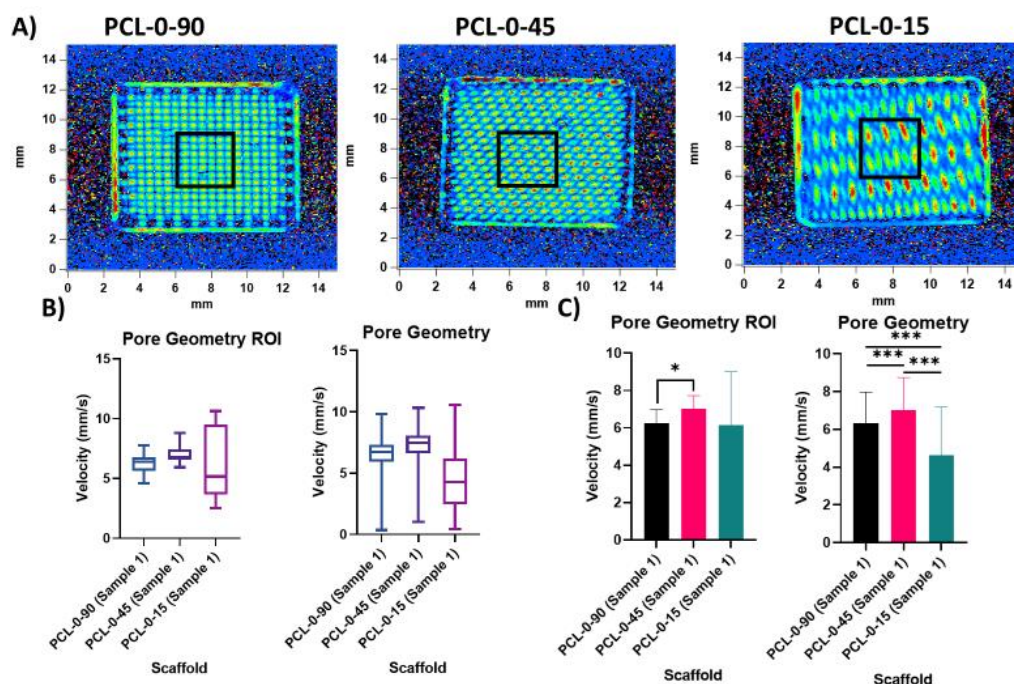


Figure 4-23 A) Velocity maps for each pore architecture highlighting a region of interest from which velocities were extracted B) Boxplots comparing the degree of variation between velocities recorded for a whole scaffold area and an area of ROI C) Average velocities for each measurements \pm standard deviation ($n=3$).

Given that the leak area is restricted to small portions of the flow map relative to the entire scaffold geometry then it is reasonable to assume any effects of the leak area on velocity within pore channels will be limited to areas close to the area without a tight seal between scaffold and chamber wall. Such that, taking a region of interest (ROI) away from the leak areas should provide a more accurate representation of the flow pattern within the porous regions. In Figure 4-23 PCL-0-90 and PCL-0-45 boxplots when a ROI is taken indicate that compared to the whole scaffold slice, both have a comparatively short interquartile range of data and are largely in agreement with each other. Velocity data over the whole scaffold in PCL-0-90 and PCL-0-45 displays however much longer whiskers indicating a much larger maximum and much lower minimum peak velocity. The less variable results of within the region of interest

for PCL-0-90 and PCL-0-45 indicate that much of the variation is likely to be due to the imperfect outer geometry of scaffolds creating scaffold-chamber distance that varies between samples and in turn a source of variability in velocities. Away from these defects the velocities (shown in ROI) in the more uniform structured pores for PCL-090 and PCL-0-45 velocities became much more homogenous. PCL-0-15 in both the ROI and over the entire scaffold still displayed a higher degree of variation but as previously discussed in addition to the scaffold-chamber variation at the periphery, PCL-0-15 had a much greater degree of variation between individual pore sizes, which is seemingly reflected in the variation of velocities regardless of location measured.

This initial proof of concept study shows the potential of NMR and MRI velocimetry methods to acquire experimental data within a dynamic cell culture system. This data can be used to validate CFD assumptions or used to further understanding for *in vitro* dynamic culture. This method can be applied to evaluate the significance of changes to scaffold and bioreactor designs also in relation to the expected velocity flow patterns, which may be used to optimise designs. In the remaining chapters of this thesis, the techniques here are further built upon to incorporate cell culture and MR imaging techniques. Characterising the effect of cell attachment and proliferation on fluid velocity distribution is important for understanding and predicting effects of dynamic culture. Relating areas of cell deposition after seeding, and subsequent tissue formation using MR imaging methods, and then comparing to measured flow maps at various extended time points in cell culture would provide more information for how far flow variability effects the mechanical environment for cells.

4.4 Conclusion

Variability in scaffold porous architecture can strongly affect the fluid velocity variability in 3D perfusion culture systems. An NMR and MRI velocimetry method was utilised to characterise the effect of local porous architecture variations on the fluid dynamics. This method was successful in displaying how far fluid velocity variability occurred as

a result to changes in the porous architecture, mainly the pore size and the pore geometry. This level of variability could potentially be a source of heterogeneous cell distributions and mechanical environment affecting the subsequent tissue formation, and in turn the viability of the scaffold for the purposes of tissue regeneration. A lack of experimental alternatives to computational models of fluid dynamics could be overcome with the methodology proposed. However further *in vitro* testing would be required to fully validate the effectiveness of this technique in informing conclusions for cell culture experiments.

5 Magnetic Nanoparticle Cell labelling Study for Locating Cells in 3D Porous Scaffolds

5.1 Introduction

Beyond scaffold and bioreactor design and the need to optimise both for achieving heterogeneous flow throughout a porous scaffold, there also needs to be an understanding of cell behaviour. Tissue engineering strategies using stem cells often involve combining cells with biomaterial scaffolds to create a three dimensional microenvironment in which tissues are regenerated. Cartilage tissue engineering using this combination of stem cells and biomaterial scaffolds has shown great promise [261-263]. The inherent inability of cartilage to regenerate itself following damage and the increasing prevalence of osteoarthritis [264] has created a real need to transfer tissue engineering based repair strategies into clinical practice. Evidence *in vitro* has shown that Mesenchymal Stem Cells (MSC's) are able to differentiate into chondrocytes when provided with a suitable 3D environment [123], mechanical stimulus [265], mass transport of nutrients [165], and the delivery of growth factors [266]. In addition to this compared to chondrocytes, MSC's are more easily isolated from a variety of sources in the human body including bone marrow, adipose tissue, and umbilical cord tissue [267, 268]. Therefore, multipotent differentiation capability and increased availability mean MSC's are a popular choice for seeding tissue engineering scaffolds.

Assessment of cell-seeded constructs to quantify and characterise tissue regeneration is important to improve and optimise tissue regeneration strategies. Magnetic resonance imaging [192] has been used for non-destructive evaluation of cartilage matrix components [192, 269], but with the addition of contrast agents MRI can also be used to evaluate tissue engineering systems at a cellular level. MRI contrast can

be attributed to differences in proton density, or to the time it takes protons to relax back to equilibrium. In MRI protons are aligned with the magnetic field, and a radio frequency (RF) pulse is introduced to disrupt this alignment. The nuclei return to their alignment through relaxation processes known as spin-lattice relaxation (T1) and spin-spin relaxation (T2). T1 is the time constant for the return of longitudinal magnetisation to equilibrium in the z-axis after an RF pulse [270]. T2 is the time taken for protons to lose phase coherence among the nuclei spinning perpendicular to the magnetic field, causing exponential decay in the transverse magnetisation following an RF pulse. This dephasing of protons occurs as a result of intrinsic or extrinsic static magnetic field inhomogeneities. When both intrinsic molecular interactions and extrinsic magnetic field inhomogeneities account for dephasing, then T2* weighted images are produced [270].

Super Paramagnetic Iron Oxide Nanoparticles (SPIONs) can be effectively added to cells during culture to be internalised by the cells, labelling them magnetic to provide a negative contrast in T2* weighted MRI [217, 271, 272]. SPIONs are able to increase the cell magnetic susceptibility and in turn reduce MRI signal intensities by decreasing the transverse relaxation component T2*, leading to signal loss and thus they appear darker in MR images [273, 274]. MRI combined with magnetic cell labelling has been successfully used in combination with stem cells *in vivo*, allowing non-invasive detection up to six weeks after implantation [275]. *In vitro* models using tissue engineering scaffolds have also been used in conjunction with magnetic iron oxide labelled stem cells to show cell can be imaged using MRI which opens the possibility to track the migration and visualise MSC's weeks after seeding onto scaffolds using MR imaging methods [273, 276].

Cell seeding on to porous biomaterial scaffolds presents in itself the challenge of achieving a homogeneous distribution of cells throughout the 3D construct to allow homogeneous tissue formation. A common characteristic of static seeding is low seeding efficiencies and inhomogeneous cell distributions [241, 277]. Seeding

efficiencies and homogeneous distributions are imperative for interactions between cells which may only be overcome in static seeding by increasing the amount of cells required for seeding [278]. An alternative to this is the use of dynamic seeding and bioreactors. A number of bioreactors have been designed to improve 3D culture and differentiation of MSC's including spinner flask [279], rotating wall [280], and perfusion [173]. Spinner flask and rotating wall bioreactors are able to effectively increase mass transport, but may not always be the most effective at reaching cells in the centre of scaffolds. Perfusion bioreactors are known to improve the homogeneous cell distribution [223] and improve cell-seeding efficiency [281, 282] through the cell suspensions being perfused through the entirety of the porous structure to provide more adequate cell penetration compared to static seeding.

In a perfusion bioreactor system cell adhesion, cell seeding efficiency and cell migration are all likely to be affected by not only the porous architectures of the scaffold, including the size, shape and interconnectivity of pores, but also the chosen flow rate. The desire to enhance mass transport can result in high shear stresses imparted onto cells, to the detriment of cell-scaffold adhesion [283]. Computation models have been developed to simulate dynamic cell seeding conditions and investigate the roles of flow and the scaffold. Pore size was identified to be a factor by Olivares [284] who simulated cell attachment in a gradient scaffold (100 μm – 400 μm pore size) in which a larger number of cells was identified within the larger pore region. However, in this study, the smaller pores were located at the periphery of the scaffold, and it is unclear if this may also have been a limiting factor in a perfusion system. Such that mass transport may have been considerably better at the centre of the scaffold, where larger pores would have provided greater permeability and perhaps a preferred route for fluid flow. Campos Marin [285] found through modelling and *in vitro* experiments that static seeding produced heterogeneous distribution of cells, with a higher number of cells near the seeding surface. In dynamic seeding cells followed the fluid stream without great interaction with the scaffold resulting in a poor seeding efficiency despite the increased mass transport properties. The computational

models in this study predicted a much greater seeding efficiency than the *in vitro* experimental results from post seeding analysis. Conclusions about experimental data are drawn from relating inlet velocities to the final seeding efficiency. Cell imaging using a method that can probe opaque scaffold materials during the seeding process or during culture without the need to pause or stop experiments, would provide more of an insight into how cells migrate through and interact with the scaffold. Assessment of *in vitro* cell migration is more popularly assessed with microscopy techniques including scanning electron microscopy and confocal microscopy. Light microscopy methods are dependent on light penetration so assessing full depth of scaffolds without scaffold destruction remains difficult. Histological methods of construct slices and 3D visualisation using Micro-CT can also be successfully used, but both methods require sample fixation and in the case of the latter the addition of heavy metal labelling of cells using toxic osmium tetroxide [286]. Therefore, the non-invasive and non-destructive ability of MRI to acquire real time images of cell seeded constructs could prove beneficial.

The aim of this study is to use magnetic nanoparticles to image labelled stem cells seeded onto porous polymer scaffolds using MRI. In the previous chapter, MR imaging and NMR methods were successfully applied with respect to velocity fields in tissue engineering scaffolds. In this chapter MR imaging is applied to image cells within porous polymer scaffolds. To further knowledge of perfusion systems, particularly once cells have been included within scaffolds, then it is vital to acquire information on cell location and cell density. The understanding of cell transport during seeding and subsequent migration during culture is important for the optimisation of bioreactor and scaffold design to enhance homogeneous distributions and efficiency. Thermally extruded 3D printed scaffolds were selected with a permeable interconnected porous architecture to allow adequate migration and growth of cells inside the scaffold. MRI and NMR techniques are used to visualise cells labelled with magnetic nanoparticles within the scaffold. Providing an alternative method for cell visualisation in an entire scaffold using a non-invasive and non-destructive technique

could provide a key insight for how cell-scaffold interactions are affected by many factors to improve overall experiment design, and *in vitro* tissue maturation.

5.2 Methodology

5.2.1 Scaffold Design and Fabrication

Scaffolds were designed with the software BioCAD which generates code to be used by a thermal extrusion based 3D printer (RegenHU, Switzerland) to fabricate a scaffold of the dimensions 10 mm x 10 mm x 5 mm (length x width x height).

Polycaprolactone (PCL) pellets ($M_n=45,000 \text{ g mol}^{-1}$ Sigma Aldrich UK) were extruded through a 330 μm nozzle at a temperature of 74°C and a pressure of 4 bar, whilst the air temperature was maintained at 26°C using a hood to enclose the printer. Within the enclosed environment a fan set to 1000 rpm was used to aid the cooling of the struts upon deposition to the platform. Print head speed was set to 30 mm s^{-1} and the extrusion rate of the material was set to 15 revolutions per metre travelled by the print head. The height of each printed layer was set to 0.15 mm for the scaffold.

5.2.2 Cell Culture and Scaffold Seeding

5.2.2.1 Cell labelling

Commercially available Nanomag-D (Micromod, Germany) 250 nm particles with COOH surface functionality were used to label cells. Immortalised human MSCs were seeded in a T75 flask were allowed to reach 80% confluency in FBS containing expansion media before the expansion media was replaced with an appropriate volume magnetic nanoparticles diluted in expansion media. Cells were incubated

overnight (24hrs) at 37°C and 5% CO₂ giving time for the particles to be internalised by the cells. Cells were then washed (3x) to remove any non-internalised particles ready for seeding or fixation and Prussian blue staining.

5.2.2.2 *Static culture*

Immortalised human mesenchymal stem cells (MSCs) were cultured in expansion medium (Dulbecco's modified eagle's medium with 10% FBS, 1% L-Glutamine and 1% antibiotic/antimycotic solution). PCL scaffolds were manually seeded with 1×10^6 cells per 100 μ l droplet pipetted directly onto the scaffold. Scaffolds were then incubated for three hours to allow cells to attach before growth media was added to each well to fully immerse the scaffolds.

5.2.2.3 *Dynamic Culture*

For dynamic culture scaffolds were sterilised using 3x cycles of 30-minute immersion in IMS followed by 30-minute immersion in PBS, before being incubated overnight in FBS containing media. Following this the scaffolds were seeded with 1×10^6 immortalised human MSC's, suspended in 40 μ L of expansion media (Dulbecco's modified eagle's medium with 10% FBS, 1% L-Glutamine and 1% antibiotic/antimycotic solution). Scaffolds were seeded using the same static method, allowing 3 hours to attach before being loaded into the flow chambers described in 6.2.3. Following this an additional 25 ml of fresh expansion media (Dulbecco's modified eagle's medium with 10% FBS, 1% L-Glutamine and 1% antibiotic/antimycotic solution) was added to each chamber system. This was perfused at a rate of 1 mL/min, for up to 14 day time points, with media changed every 2-3 days.

5.2.3 Cell Culture Analysis

At Days 0, 1, 7 and 14 the MSC seeded scaffolds were harvested, washed sufficiently with PBS, sectioned into 6-8 smaller pieces before each being digested at 37°C over 3 days in 800 µl of papain solution (280 µg/ml papain, 5 mM L-cysteine, 50 mM EDTA in Duplecco's PBS with a pH of 6.5). Assays were used to quantify the DNA content from the supernatant of the digested samples. DNA quantification was carried out using a Quant-iT Picogreen kit (Invitrogen) and the assays were performed in triplicate.

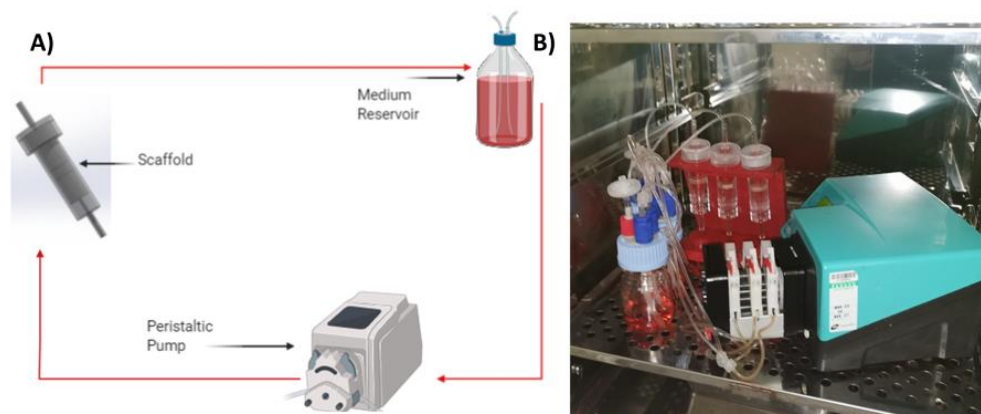


Figure 5-1 Schematic diagram of components of dynamic culture experiments (left), and image of set up in cell culture incubator [241]

5.2.4 Prussian Blue Staining

Prussian blue is an iron based stain that can be used to identify the presence of Magnetic Nanoparticles. Monolayers of cells fixed in well plate with 4%PFA for 15-20 minutes at room temperature before equal volumes of 20% Hydrochloric Acid solution and 10% Potassium Ferrocyanide were added immediately to the cells. In order to

effectively stain cells this mixture was applied to the monolayer culture for 5 minutes at room temperature. Images were taken using a Nikon Eclipse TS100 with blue regions indicating the presence of MNP's.

5.2.5 Scaffold preparation for MR imaging

Preparing the scaffold for imaging required having the pores filled with water to provide a proton density suitable for acquiring enough signal to image the internal structure. Iron containing nanoparticles act as a negative contrast, and appear as dark spots void of signal, however any pockets of air or bubbles will also appear as low signal intensity voids. Therefore, the scaffold needs to be homogeneously filled with water and free from air bubbles to confidently identify the presence of labelled cells. To achieve this the scaffolds were filled with 20 w/v% Pluronic F-127 gels, which provided a similar proton density as imaging with water filled pores. However compared to filling with water, Pluronic F-127 gel was a more stable structure as the gel could be maintained in place at room temperature, was less prone to bubble formation and the gel could be isolated to the scaffold only rather than needing to fill the entire chamber with water. This was advantageous to achieve a much smaller field of view, avoiding any folding in effects, which resulted in higher resolution imaging.

5.2.6 Gel Formation

Kappa-carrageenan gel (K-CG) formation was prepared using a 2 w/v% mix of water and K-CG powder (Sigma-Aldrich, UK) to form an aqueous solution at 80°C by continuous stirring. The aqueous solution was transferred to a petri dish, and cell free scaffolds were immersed in the solution, and allowed to cool to form a gel encapsulation around scaffolds.

Pluronic F-127 (Sigma Aldrich, UK) at a concentration of 20 w/v% was prepared by dissolving the polymer into water at a temperature below 4°C, leaving it to fully

dissolve over 24 hours before pipetting into cell-seeded scaffolds which had also been cooled to 4°C.

5.2.7 MR Imaging for Cell Seeded Scaffolds

Two imaging protocols were used to confirm the presence of labelled cells, a gradient echo imaging method FLASH (Fast Angle Low Shot) and a spin echo MSME (Multi-Slice Multi-spin) method. Gradient echo imaging is much more sensitive to magnetic field inhomogeneity caused by both air bubbles and ferromagnetic materials including iron based nanoparticles, such that surrounding areas of water tend to be distorted, as MRI relies on homogenous static magnetic fields to accurately reflect the locations and dimensions. However, spin echo imaging can be used to eliminate field inhomogeneity due to a refocusing pulse and show the exact location and dimension of magnetic susceptibility artefacts without the surrounding distortion [287]. Therefore, both methods were used to image cell seeded scaffolds, gradient to show the magnetic susceptibility effects of the SPIONs and then spin echo to recover that lost signal to reflect the actual dimensions of the SPIONs, such that bubbles would still be easily visible but cells containing nanoparticles would not.

MR imaging parameters of the cell seeded scaffolds using a slice thickness of 0.5mm were obtained with an NMR system consisting of a 9.4T 400 MHz Bruker instrument and a 25mm imaging probe. A gradient echo imaging method FLASH (ParaVision 6.0, Bruker BioSpin MRI GmbH, Germany) was used to obtain axial, sagittal and coronal slice images with an echo time (TE) = 3 ms and a repetition time (TR) = 1000 ms, a 12 mm x 12 mm field of view (FOV), matrix size = 256x256 and a resolution = 0.046 mm. Multi-Slice Multi-Spin echo (MSME) images were also performed with TR = 1000 ms, TE = 14 ms, a matrix size = 256 x 256, FOV = 12 mm x 12 mm and a resolution of 0.046 mm.

5.3 Results and Discussion

5.3.1 Prussian Blue

Prussian blue staining of iron content within cells to demonstrate uptake of Nanomag-D-COOH iron containing magnetic nanoparticles was successful in showing cell uptake (Figure 5-2). Regions of blue in internal cell structure clearly visible at all concentrations (B-25 $\mu\text{g/ml}$, C – 50 $\mu\text{g/ml}$ and D – 100 $\mu\text{g/ml}$) compared to 0 $\mu\text{g/ml}$ with no visible affect to cell morphology. Despite increasing concentration there was no distinctive difference in the visual uptake of Nanomag and intensity of blue regions. Prussian blue staining of cell seeded scaffolds showed again good uptake of nanoparticles by the MSC's which could be visualised as adherent to the 3D scaffold structure three hours post seeding in Figure 5-3

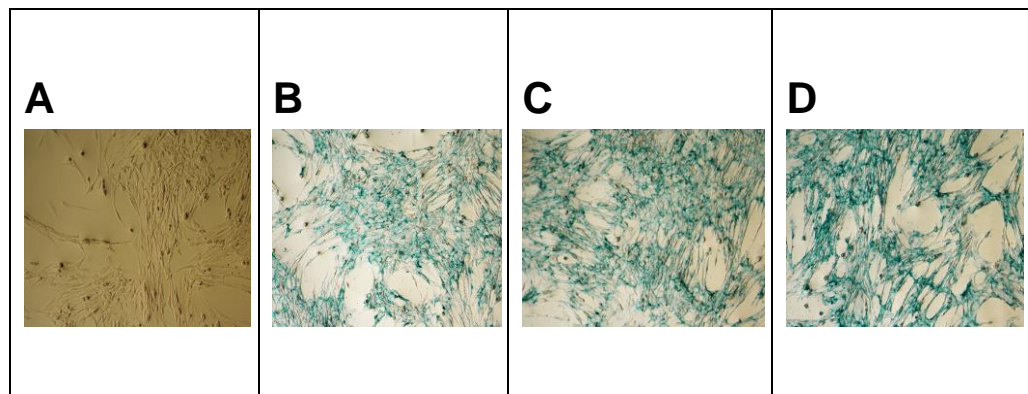


Figure 5-2 Prussian blue staining of ihMSC's fed with A) 0 $\mu\text{g/ml}$ B) 25 $\mu\text{g/ml}$ C) 50 $\mu\text{g/ml}$ D) 100 $\mu\text{g/ml}$ of magnetic nanoparticles. Monolayer of PFA fixed culture was stained with Prussian blue after being left overnight in media containing nanoparticles.

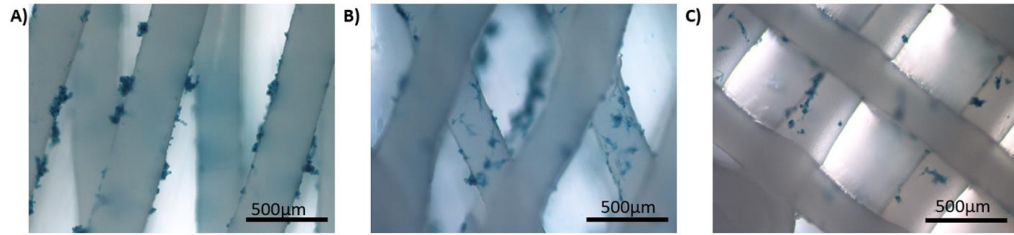


Figure 5-3 Prussian Blue staining of cells seeded on 3D PCL scaffolds using static seeding with different pore geometry 3 hours after seeding scaffolds with labelled cells using a concentration of 50 µg/ml. Scaffold geometry used were laydown patterns 0/15(A) 0/45(B) and 0/90(C). Prior to staining scaffolds were fixed using PFA. For imaging scaffolds were sectioned and images taken from internal regions of scaffold.

5.3.2 Cell Viability

The viability of cells post MNP feeding in culture over 7 days was not adversely effected when compared to cells seeded without the addition of MNP's (Figure 5 4). Cells were seeded at different concentrations (25 µg/ml, 50 µg/ml and 100 µg/ml), and compared against unlabelled controls. An Alamar blue reduction assay showed that metabolic activity increased in all four groups at a largely very similar rate in 7 days of culture as expected, indicating MNP's did not limit the proliferation or viability of cells. DNA quantification over the same period for the same concentrations supported this(Figure 5 4), also displaying an increase in DNA content over the course of seven days in culture with no significant difference in DNA content by Day 7 for any group. This supports results from another study using the same Nanomag particles, labelling MSC's with Nanomag alone did not result in diminished viability or ability of cells to proliferate [209].

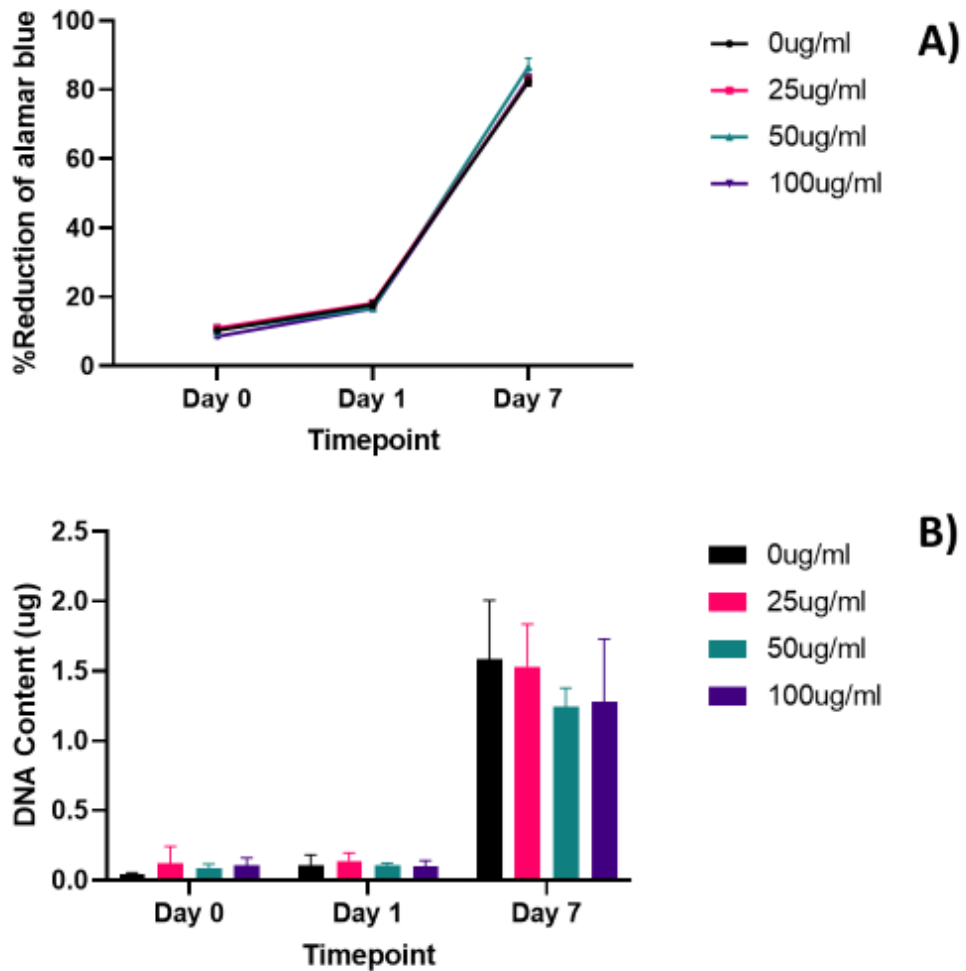


Figure 5-4 Alamar blue reduction (A) and DNA quantification (B) of ihMSC cells cultured with MNP's for seven days using 6 well culture plates. Cells were labelled with magnetic nanoparticles, seeded using static seeding and then cultured in growth media for up to 7 days under static conditions (n=3).

5.3.3 Static cell culture

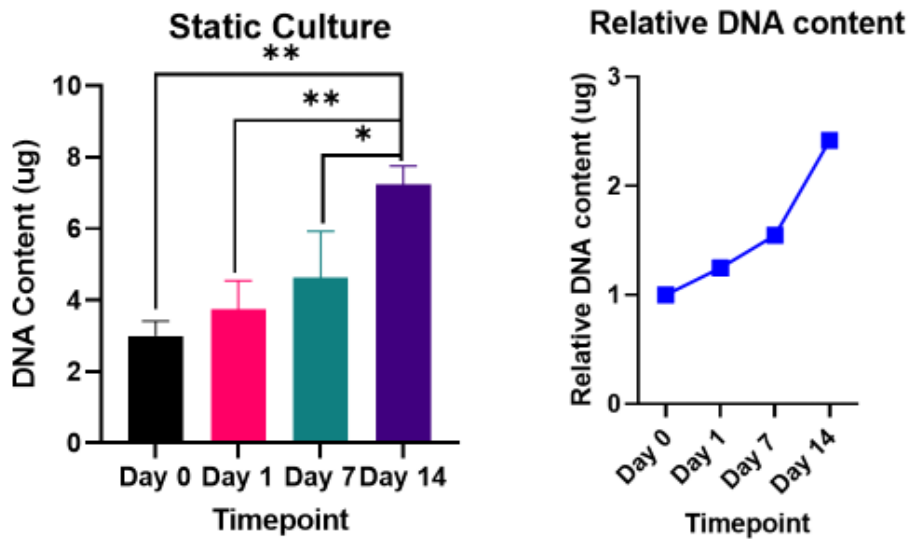


Figure 5-5 DNA content of scaffolds grown with labelled cells in static conditions, and DNA relative to Day 0. Scaffolds used had 0-90 strut orientation and pore size of approximately 270 μ m. 1×10^6 ihMSC cells were seeded per scaffold, $n=3$ for each time point. * $p < 0.0332$ ** $p < 0.0021$

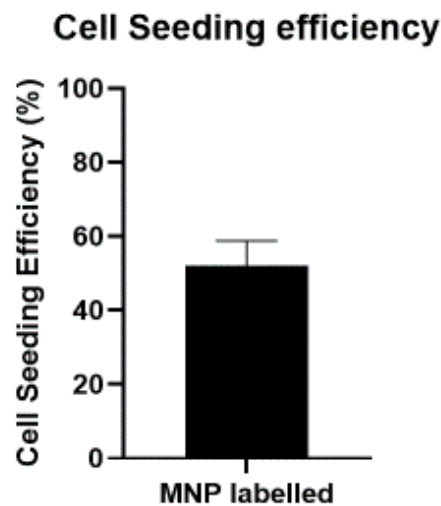


Figure 5-6 Cell seeding efficiency measured using DNA content of cell suspension of 1×10^6 ihMSCs compared to DNA content of scaffold after initial seeding and attachment ($n=3$) presented as a percentage.

Scaffolds were seeded using a cell suspension of 1×10^6 using a manual droplet method, to drop the cell suspension droplet directly onto the upper surface of the scaffold. Scaffolds were then given 3 hours to attach before being immersed in culture media and grown for up to 14 days in static growth conditions. Cell scaffolds were harvested, and analysed for the total DNA content following cell lysis. Results showed that there was an increase in DNA content over time post labelling cells with 50ug/ml concentration of magnetic nanoparticles (Figure 5-5).

Labelling of MSC's prior to seeding with magnetic nanoparticles was carried out to allow the detection of cells within a 3D system using MRI to facilitate non-invasive assessments of the distribution of cells. This could be used for long-term assessment of cell distribution or the initial effects of cell seeding methods. One of the challenges in working with 3D cell seeded constructs is achieving an equal density of cells throughout the interior of the scaffold, beyond just seeding on exterior surface layers.

In this study, for static culture 1×10^6 labelled MSC cells were deposited in a 100 μ l droplet suspension directly on to the upper surface of the scaffolds. Assessment of static cell culture experiments by quantifying absolute DNA content showed seeding was successful at incorporating cells into the scaffold, and that over a 14 day period cells continued to proliferate within the scaffold. Scaffolds were immersed in expansion media for up to 14 days, and at day 14 scaffolds exhibited a significantly higher cell compared to day 0. DNA content increased linearly for each time point indicating a relatively constant rate of proliferation in 3D PCL scaffolds.

Scaffolds fabricated via 3D printing are able to produce characteristics like controlled homogeneous architecture, high porosity and 100% interconnectivity. However, pore sizes tend to be much larger than cell size; the scaffolds have an open architecture and also poor cell-material adhesion limit the potential to achieve a high cell seeding efficiencies. Low cell seeding efficiency and a heterogeneous distribution of cells is linked to low rates of tissue formation, an overall lower density of tissue formation and

differences in cell differentiation behaviour [112, 288, 289]. Static cell seeding in this study achieved a high seeding efficiency (Figure 5-6) indicating that the levels of porosity and pore size in this scaffold did not greatly diminish the potential for cell adhesion. However, good cell seeding efficiency does not ultimately mean the distribution of cells in this 3D environment will be homogeneous, this therefore is assessed later in this chapter using MR imaging.

The scaffold environment also influences cell infiltration into scaffolds. Pore size, matrix stiffness, and strut orientation all play a role in influencing cell behaviour. For instance, electrospun scaffolds have provided structures to mimic natural ECM environments, directing the alignment of cells and subsequent deposition of extracellular components, but due to a relatively small pore size many cells are limited to more growth on the scaffold periphery [290]. Alternatively, 3D printed scaffolds, which also provide control over strut orientation and thickness, but produce scaffolds with larger and controlled pore sizes is a viable option for increasing cell infiltration. However, even with optimised porous architectures, the influence of seeding techniques on overall seeding efficiency has to be considered as well. In this study cells were manually seeded, using 100 μl droplets containing approximately 1×10^6 cells directly onto the upper surface of the scaffold and grown in static culture. Cell seeding efficiency results showed that static cell seeding achieved a high efficiency of 52% (Figure 5-6). Therefore, it is clear that cell seeding in this way was capable of incorporating a high number of cells within the scaffold, and would in theory lead to good tissue formation. However, the homogeneous distribution of these cells still needs to be assessed using MR imaging techniques to visualise cells as this impacts the subsequent level of homogeneous tissue formation during *in vitro* maturation.

Further to this, homogeneous cell distribution, initial cell seeding techniques, and the chosen design characteristics for scaffolds are not the only factors upon which a successful culture experiment depend on. Static culture can still be limited by inadequate delivery of nutrients and removal of waste via diffusion to the centre of the

scaffold. Therefore, even if cells are able to effectively penetrate the central regions through effective seeding or infiltration they still may not be able to survive if the scaffold depth exceeds the diffusive limits. Cell seeded scaffolds have been shown to have a much higher growth rate at the periphery compared to central regions, because cells closer to the nutrient source compared to the much lower concentration of diffused nutrients inside the scaffold have a greater rate of proliferation [188]. The same study equated decreasing oxygen concentrations from top to bottom of the scaffold with decreasing cell density further into the scaffold supporting evidence from other studies that diffusion alone is unable to support full tissue growth across three-dimensional scaffolds [119, 291].

5.3.4 Dynamic Cell Culture

Static culture in conjunction with 3D printed scaffolds can be used to provide an appropriate porous environment that theoretically does not inhibit cell infiltration into the centre of the scaffold but static cell seeding techniques can still inhibit overall distribution of cells initially, and then the subsequent migration of cells into the scaffold during culture. Dynamic culture using perfusion offers an alternative, and has been compared to static culture controls in a number of studies. Similarly to in this thesis, Theodoridis et al. used 3D printed PCL scaffold in perfusion culture that had been pre-seeded using the static droplet methods and then grown in dynamic culture, and compared to static controls. Results showed that from perfusion culture there was an improved overall cell population achieved, and a cell scaffold penetration depth that was more homogeneous in distribution compared to its static counterparts [107].

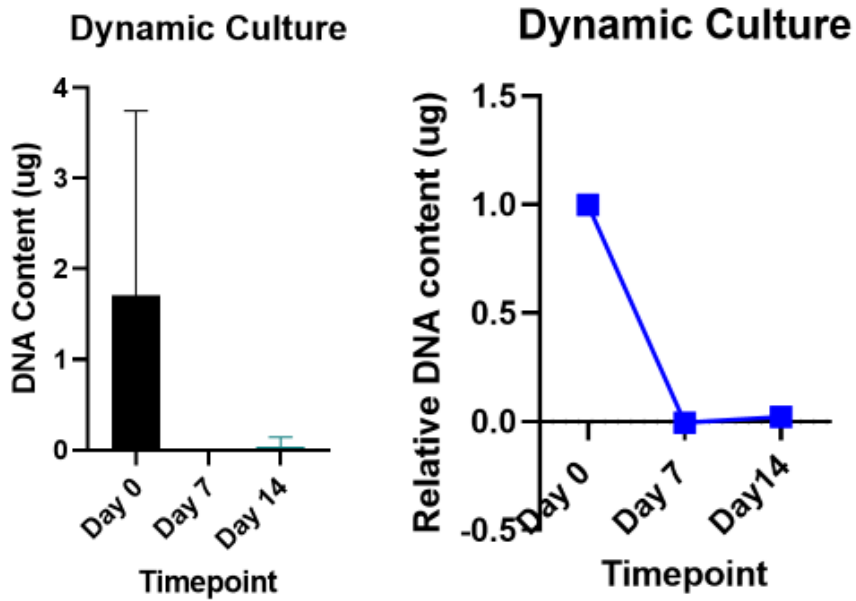


Figure 5-7 DNA content of scaffolds grown with labelled cells in dynamic perfusion conditions, and DNA relative to Day 0. Scaffolds were pre seeded with 1×10^6 ihMSCs before being grown under perfusion flow of 1mL/min for up to 14 Days.

In this current study labelled cells were pre-seeded using manual static methods and then cultured on scaffolds using a perfusion bioreactor system. Cells were labelled prior to seeding with iron containing magnetic nanoparticles for visualisation using MRI, and then seeded using the identical method described for static culture, left to attach for 3 hours before being loaded into perfusion system and cultured for up to 14 days. Results from this experiment showed that despite the good initial cell seeding, at subsequent time points there was little or no DNA content that could be quantified (Figure 5-7). This clearly demonstrates that the flow rate chosen in this experiment was too high to create an environment that was conducive for cell growth and proliferation. Whilst static experiments do not always produce homogeneous cell seeding distributions or encourage cell migration away from scaffold periphery, applying a perfusion rate that is too high has been associated with cell detachment and cell death [7, 227]. The potential negative effects of perfusion culture are demonstrated here, one of the main challenges with establishing dynamic culture experimental procedures is establishing the external flow rate to be applied to cells

within the porous space of scaffolds. Although the lack of retained living cells in the scaffolds for dynamic culture make them inappropriate to proceed with MR imaging on them, it does still highlight the potential role non-invasive imaging could play in establishing the root cause of problems, for example if it was largely cell detachment then over what time period did cell detachment occur.

5.3.5 MR Imaging

5.3.5.1 Sample Preparation

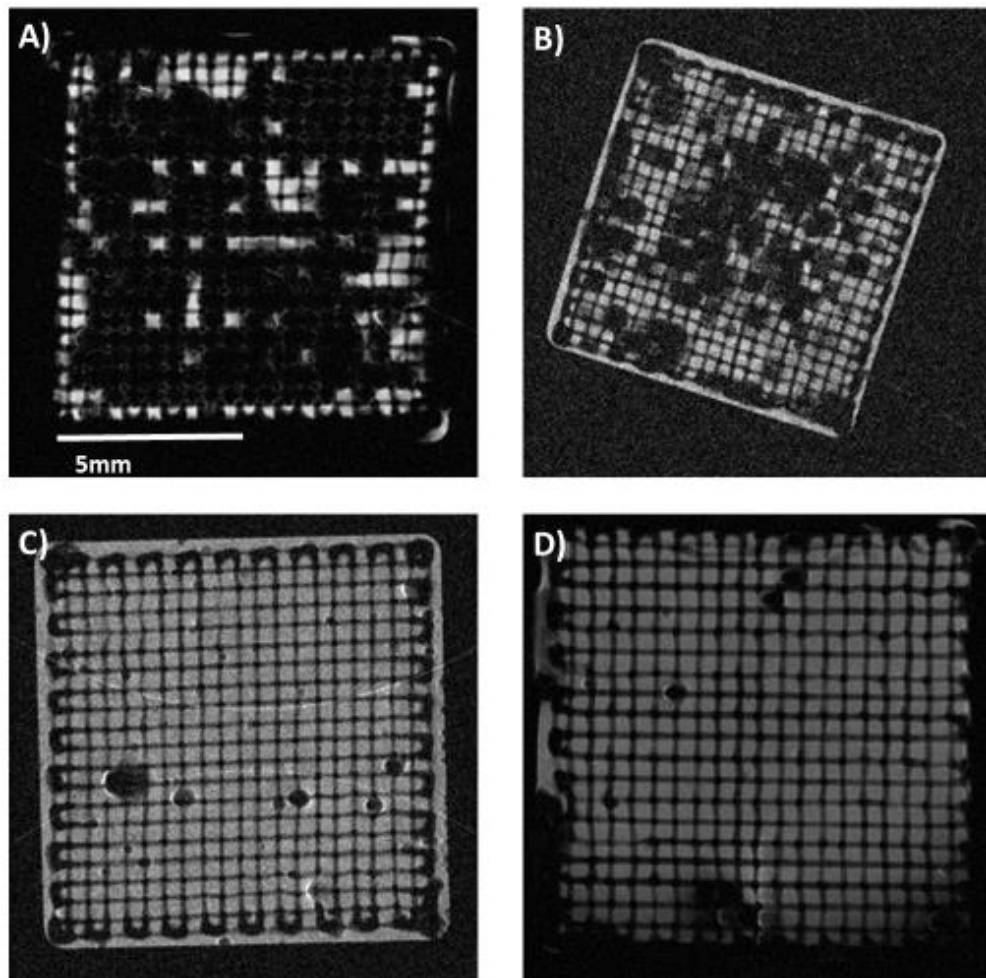


Figure 5-8 MR Images showing different methods of sample preparation for unseeded cell free scaffolds, in an attempt to remove artefacts caused by bubble formation; A) No preparation to keep porous structure filled with water B) Scaffold manually filled by immersing in fluid C) Scaffold placed

under vacuum and then immersed D) Pores were vacuumed, filled with degassed water and then entire scaffold encapsulated in kappa carrageenan gel.

To achieve good image resolution for cell visualisation using MRI it is important to limit the field of view to the cell-seeded scaffold alone, as much as possible. In order to do this, high signal from proton dense liquids must be isolated to the scaffold alone, as any fluid outside the scaffold will cause large amounts of signal outside of the field of view and this signal will not be correctly phase encoded in relation to its location. This will create folding artefacts at the periphery of the image resulting from signal outside of the field of view being folded over on the centre of the image, which can only be avoided by increasing the field of view at the expense of image resolution. The simplest way to fill the void regions of the porous scaffold would be to flow fluid through the scaffold using the flow chamber, as this has been an effective way to stop the emergence of bubbles. However, for the aforementioned reasons, flowing water either side of the scaffold to fill its pores is not conducive for high-resolution imaging. Figure 5-8 shows in images A) and B) respectively the difference between moving a scaffold straight from the PBS it had been immersed in to the imaging probe, or manually filling scaffold pores by assembling the scaffold in the flow chamber submerged in fluid. Submerging the scaffold does improve the number of filled porous channels but it is clearly very heterogeneous and there is a high proclivity for bubble formation.

In Figure 5-8 C) the scaffold had been placed under a vacuum for a short amount of time to remove air from the porous space before filling those voids with fluid via submersion. This was achieved by removing the scaffold from the vacuum chamber and immediately submerging in water, before the scaffold was loaded into an already fluid filled chamber. This was largely successful with regard to homogeneous distribution of fluid and limiting bubble formation, but practically difficult to achieve as a repeatable result due to fluid escaping the scaffold during loading into the chamber and the magnet, largely just due to the natural effects of gravity, creating pore channels void of fluid, and in turn signal. To negate this issue, following the same

procedure of vacuuming the scaffold and submerging to fill pores with degassed water, the next step taken was to encapsulate the fluid filled scaffold in a 2wt% kappa carrageenan gel (Figure 5-9). Kappa carrageenan is a natural polysaccharide compatible with MRI that undergoes sol-gel transition when cooled to room temperature. As shown in Figure 5-8 D) pore filling is like C) again primarily homogeneously filled with water, but the use of gel to seal the water filled scaffold allowed a much more stable transfer to probe, and allowed repeated and more sustained imaging of samples without loss of fluid. Kappa carrageenan gel around the scaffold did not interfere with the signal within the scaffold or limit the field of view as was the case with volumes of water above and below the scaffold. Although using gel was successful for imaging scaffolds, the steps involved in heating and vacuuming for preparing a cell seeded scaffold for imaging would not be appropriate for maintaining cell viability, such that other gel forming materials may be more applicable. In this case, Pluronic F-127, a polymeric gel which undergoes sol-gel transition at approximately 23°C for a gel of 20 w/v% concentration [292] was used to better facilitate cell-scaffold imaging.

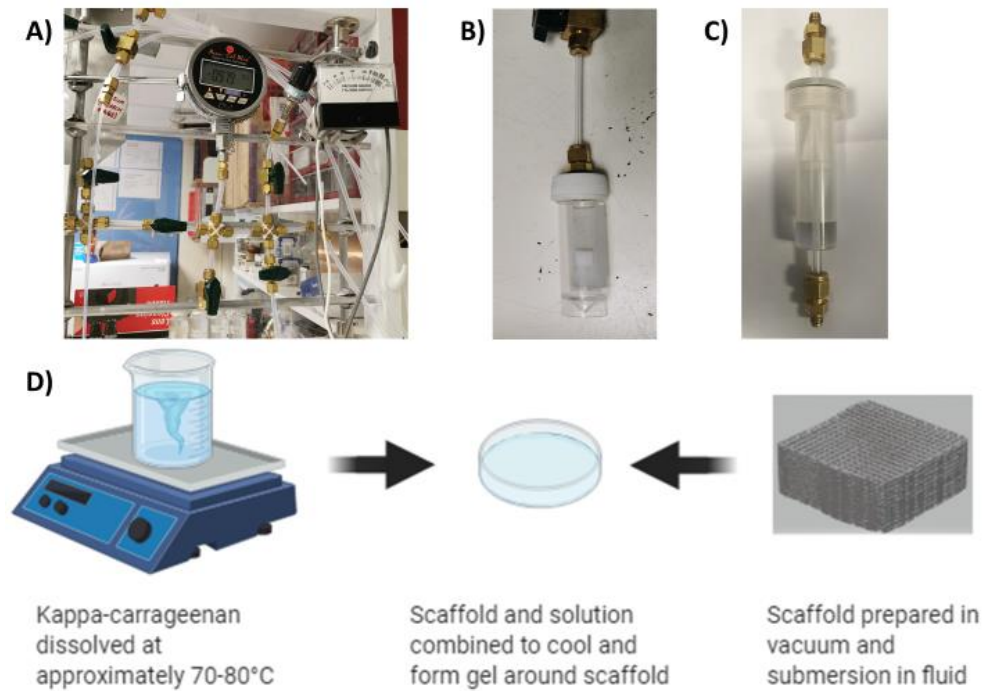


Figure 5-9 A) and B) Showing parts of system to vacuum air out of pores of blank cell free scaffolds C) Chamber used to house scaffold for imaging D) Schematic of process to encapsulate scaffold in kappa carrageenan gel after scaffold had been removed from vacuum.

5.3.5.2 Imaging labelled cells

Before assessing labelled cells within a PCL scaffold, to ensure visualisation of seeded cells, Pluronic F-127 hydrogel containing labelled cells was prepared. Pluronic F-127 is a synthetic polymer, it is thermo-responsive, forming gels at room temperature or above and capable of reversible gelation. It has non-toxic and biocompatibility properties that are ideal for cell encapsulation. Cells containing iron within a hydrogel were imaged, to validate that the introduction of iron containing nanoparticles to label cells would successfully act as a negative contrast at this concentration. Using a hydrogel which constitutes typically of a 3D polymeric matrix capable of holding large amounts of water, therefore giving rise to a high proton density, ideal to be used in conjunction with negative contrast agents. Indeed, labelled mesenchymal stem cells within hydrogels have been successfully imaged using T2 relaxation imaging to clearly visualise cells as areas of signal voids and corroborated

with histology and Prussian blue staining [271, 272]. Comparisons between Hydrogels containing labelled cells in Figure 5-10 and cell free hydrogels in Figure 5-11 clearly show the presence of signal void regions when imaged using gradient echo sequences, these areas of lower signal intensity are correlated with areas of labelled cells (Figure 5-10). On the other hand, when the NMR tube contained only Pluronic F-127 gel, the high water content gave rise to a homogeneous region of high signal intensity (Figure 5-11), that did not decrease in signal to the same degree after the same number of echo images as when the gel contained labelled cell. This gives good confidence that labelled cells can be visualised using a 50ug/ml concentration of Nanomag-D particles and at this cell density.

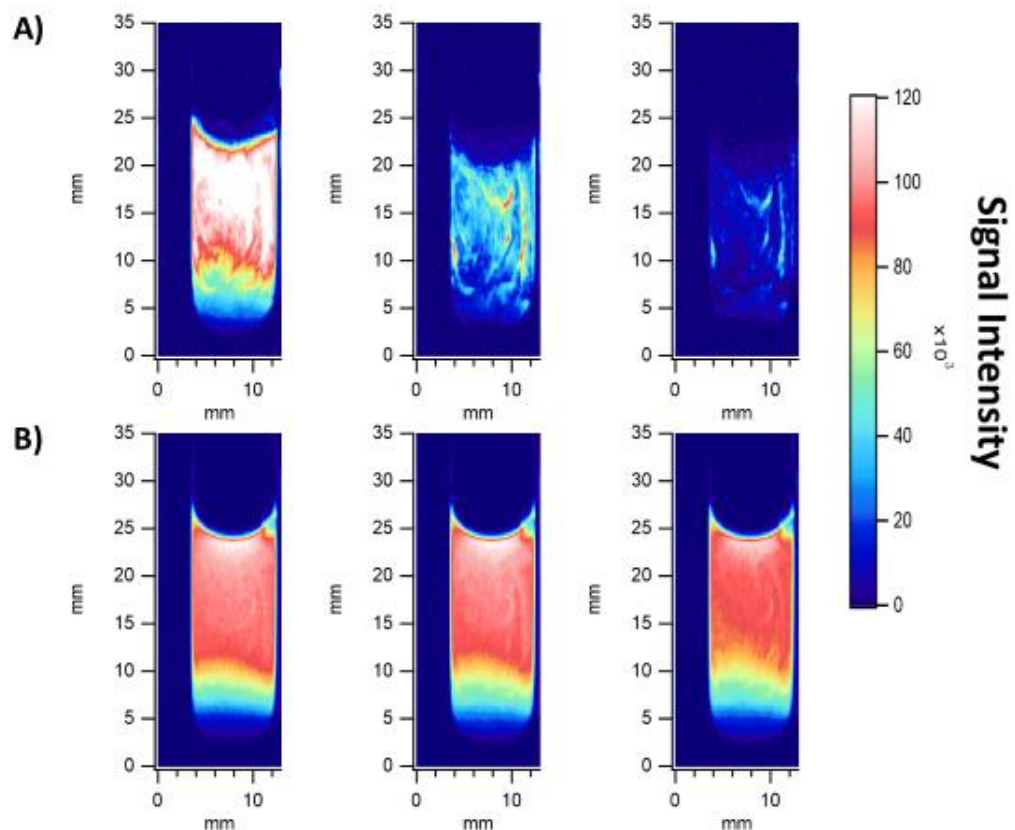


Figure 5-10 Signal intensity images of labelled cells dispersed through 2ml of Pluronic F-127 gel in a 10mm NMR tube imaged. A) Gradient echo imaging acquisition method. Images left to right are acquired in series with 4ms echo time between each image. Images were acquired as a 2 mm thick sagittal slice in a 128x128 pixel array. TE 4 ms, TR 1000 ms. B) Spin echo of same slice of gel. Images acquired every echo, using parameter TE 5.1 ms and TR 1000 ms.

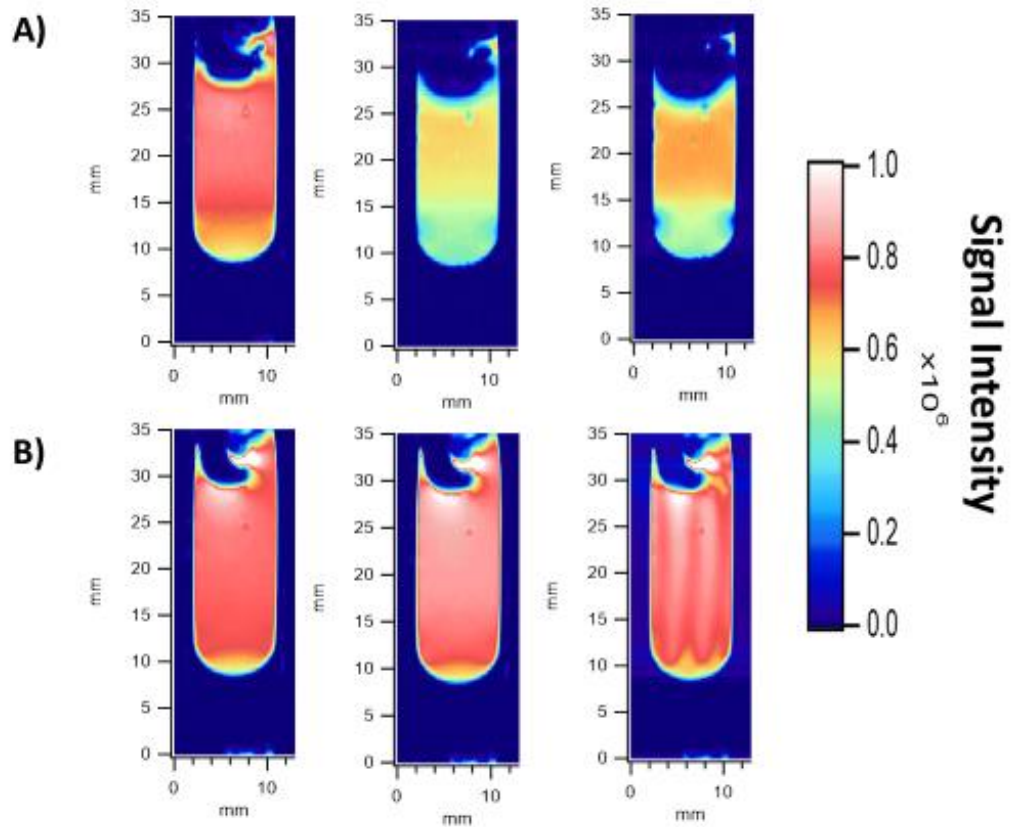


Figure 5-11 A) Blank gel not containing cells in 10 mm NMR tube. Signal intensity images acquired in 2 mm slices using gradient echo pulse sequence to give images with increasing echo time from left to right by 4 ms with each echo image B) Spin echo images of identical slices of blank gel using MR imaging parameters TE 5.1 ms and TR 1000 ms.

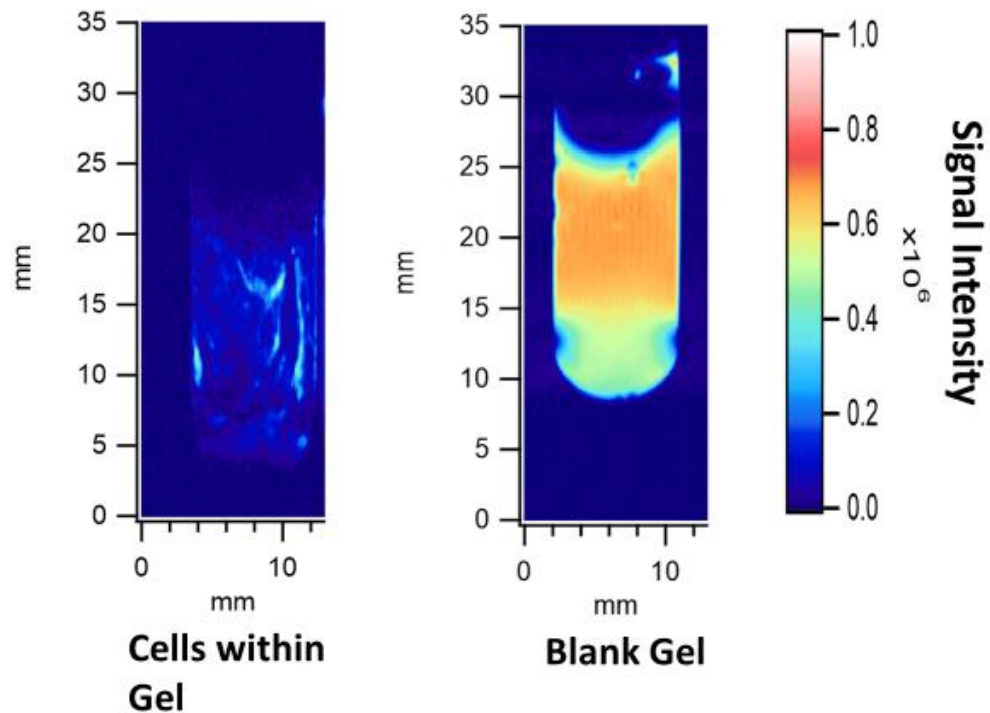


Figure 5-12 Images of gel containing cells dispersed throughout the gel compared to a blank gel. Both images represent the third echo image, in which signal has had 12 ms to decay. The presence of iron oxide nanoparticles causes the gel containing cells to lose signal at a much quicker rate confirming they can be detected within Pluronic F-127 gel using this MR imaging method.

Figure 5-10 and Figure 5-11 show the difference between a blank gel, and gel dispersed with labelled cells. Figure 5-12 shows the difference in signal intensity between both gels after three echo images. Gradient echo images clearly show signal intensity in the presence of labelled cells deteriorates much quicker compared to the blank gel, and by the time the third echo is acquired the gel containing cells signal has almost completely waned (Figure 5-12). As time elapses between each echo image that is acquired, relaxation of magnetisation in the transverse plane due to protons going out of phase is reflected in a decrease in signal intensity in images. The rate at which transverse relaxation is affected by the magnetic field inhomogeneities the presence of iron causes, such that relaxation times are much quicker and signal intensity decreases quicker. This effect can be quantified using T2* weighted images that depicts the differences in T2* relaxation times. To confirm that there would be sufficient contrast between locations containing labelled cells and those voids of cells

both types of gel were loaded into an NMR tube, one upon top of the other and imaged (Figure 5-14). Mixing both types of gel in one NMR tube in Figure 5-13 and Figure 5-14, further shows the contrast in the effect on signal intensity between the upper blank gel and where the cells are present. The cell free gel in the upper section of the tube maintains much more of its signal intensity as each image is acquired with every echo. In the lower region of the tube, by the time the sixth echo image is acquired the signal has almost completely depleted. In order to pipette Pluronic F-127 in liquid form it has to be cooled to around 4°C, so when one cooled gel in liquid form was added upon the room temperature gel, there was some cooling on the surface of this gel which caused mixing at the boundary. This effect can be seen in Figure 5-15 and Figure 5-16, in which axial sliced images taken at the boundary between both types of gel show that there has been some mixing, and particularly at the edges, the blank gel has encroached into the layer of gel containing cells. There is however still a good degree of contrast between the two materials, and the extent of the gels mixing did not impede the visible contrast between the gels.

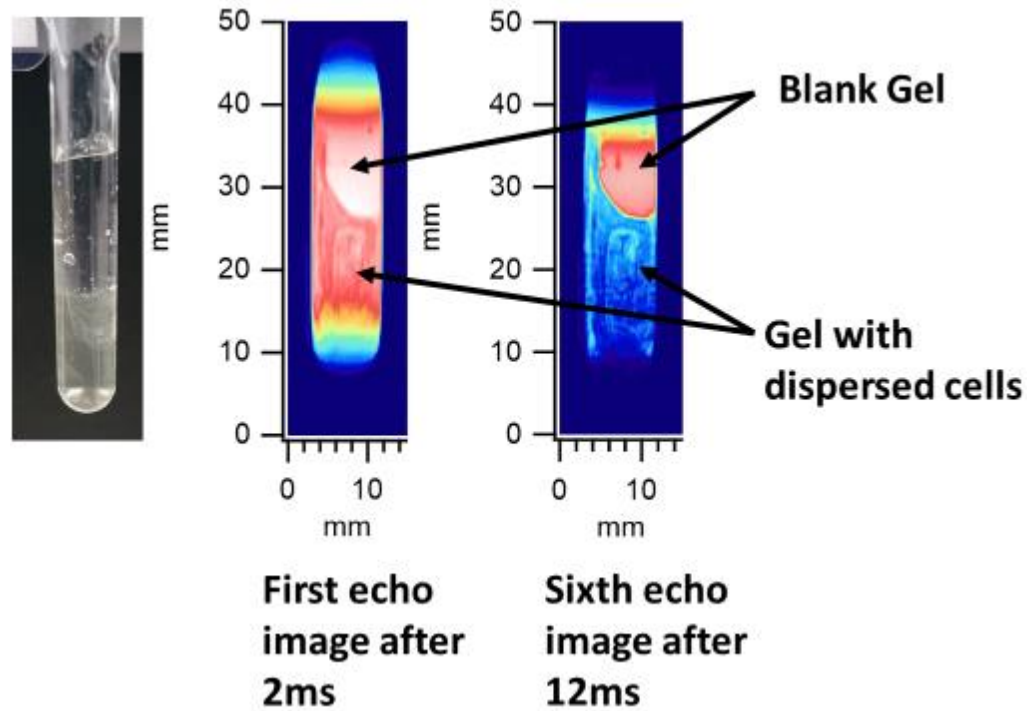


Figure 5-13 Images showing NMR tube containing a mix of blank gel and Pluronic gel that has labelled cell dispersed throughout. First and last echo images show over time the amount of signal present in the gel containing cells decreases much quicker. The blank gel maintains similar levels of signal intensity between images.

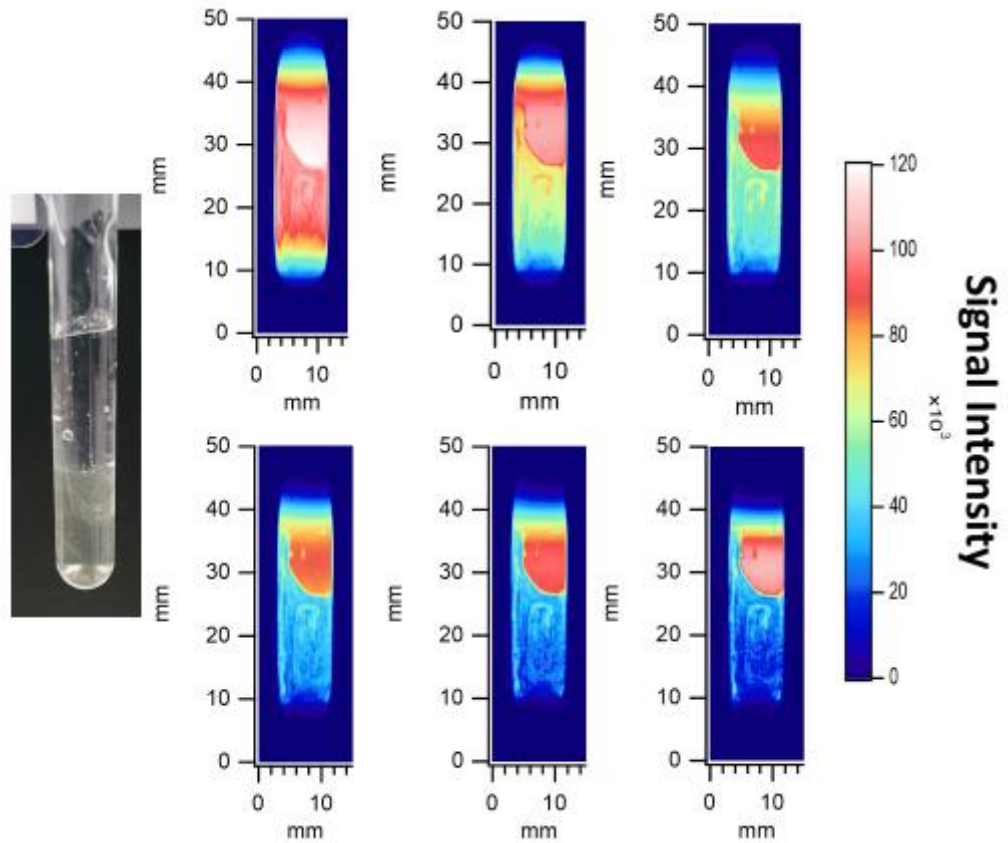


Figure 5-14 MR images showing signal intensity. 10 mm NMR tube (left) containing both Plurionic F-127 gel dispersed with 1×10^6 cells (bottom section of gel in tube) and gel only (top section of gel in tube). Gradient echo images acquired every 2 ms from a 2 mm thick sagittal orientated slice. Six Echoes are acquired with a 128×128 pixel array. Each echo image shows decay in signal over time, quicker decay indicates the presence of iron labelled cells.

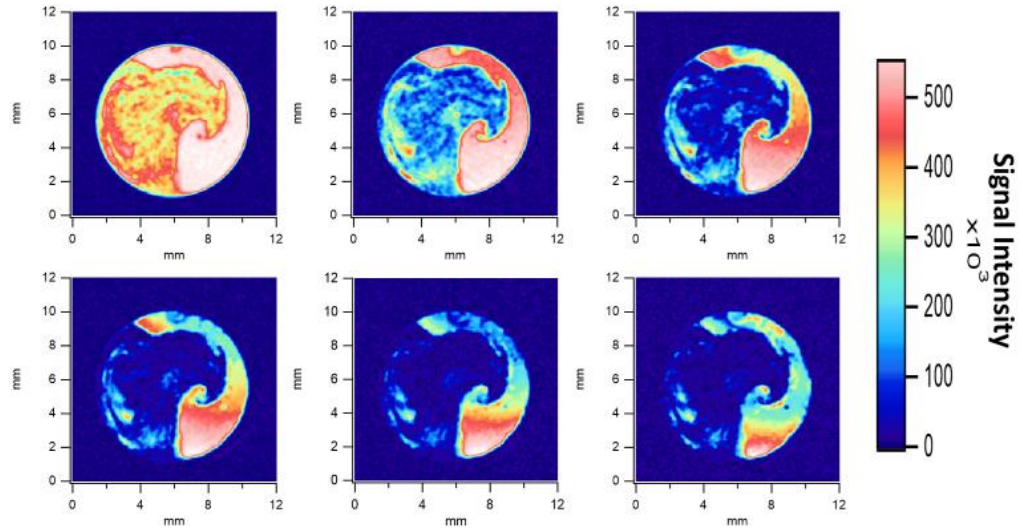


Figure 5-15 Two gel types imaged in 10mm NMR tube. One gel free of cells, the other containing iron oxide labelled cells. Axial 2 mm slice echo images every 5 ms showing differences in signal intensity between blank gel and gel containing iron oxide labelled cells. 128x128 pixel images acquired using gradient echo pulse sequences, and imaging parameters TE 5 ms, TR 1000 ms.

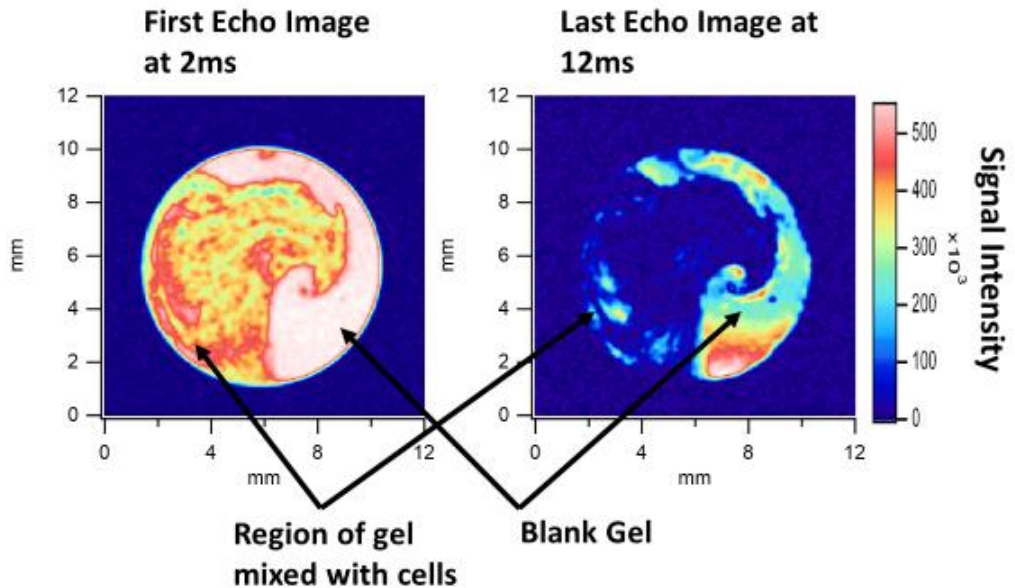


Figure 5-16 Axial projection of NMR tube containing both types of gel. In the time between the first and last echo image the signal in the gel containing iron labelled cell decreases a great deal more than the contrasting blank gel.

To further examine and confirm the effects of cells after labelling with 50 $\mu\text{g/ml}$ of Nanomag-D nanoparticles, T_2^* relaxation mapping can quantify and provide contrast in images in terms of relaxation times. In Figure 5-17 T_2^* relaxation maps are split into two regions of interest, based on each gel. T_2^* relaxation times can be extracted from signal intensity MR images on a pixel by pixel basis using curve fitting methods to express the pixel signal intensity as a function of time, that result in an image of T_2^* times displayed pixel by pixel. In Figure 5-17, histograms taken to show the distribution of T_2^* times show a much greater spread of relaxation times, and a greater amount of longer relaxation times for the blank gel, compared to relaxation times in the cell labelled gel. This supports results shown in a study also using iron oxide labelled cells, encapsulated within a polymer hydrogel. Increasing density of labelled cells had the effect of reducing the overall average T_2^* relaxation times compared to an unlabelled cell control [274].

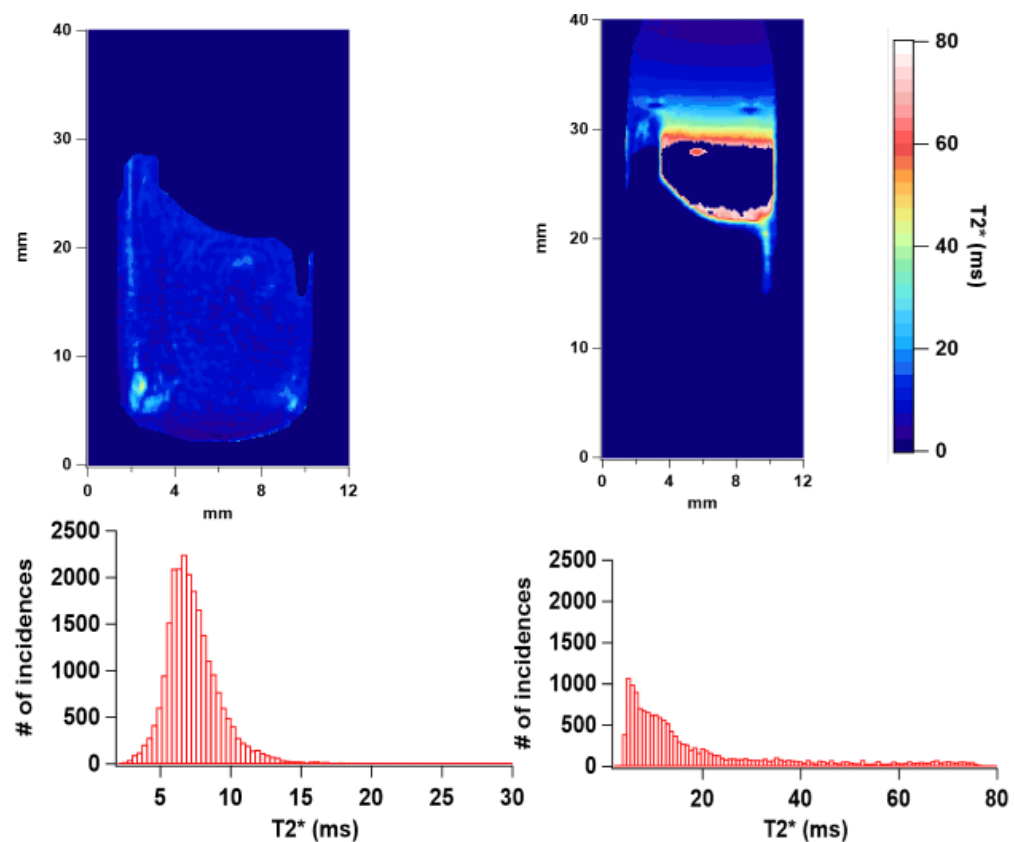


Figure 5-17 T_2^* relaxation map, separated into two regions of interest, of an NMR tube containing two parts corresponding with each region of

interest; a gel mixed with iron labelled cells (left) and a blank gel [241]. Associated histograms show the distribution of $T2^*$ relaxation times for both material types.

Imaging cells labelled with iron oxide nanoparticles in porous polymer scaffolds can be challenging because the labelled cell provide negative contrast, but polymer also appears as dark areas of low signal. Therefore, to validate that cells could be visualised within a scaffold, and to optimise image acquisition parameters a scaffold with larger 600 μm pores was filled with gel that had labelled cells dispersed throughout. A control scaffold filled with a blank gel was included to ensure cell visualisation. The scaffolds were placed one on top of the other, and wrapped in Teflon tape to keep them secure in place during imaging (Figure 5-18). As before, images were acquired using gradient echo and spin echo pulse sequences. In Figure 5-19 and Figure 5-20, sagittal and axial projections show the contrast between scaffolds filled with blank Pluronic F-127 gel and gel containing labelled cells. With an echo time of 2 ms, each gradient echo image shows the declining signal intensity over time in both scaffolds. In the sagittal orientation (Figure 5-19) slices from two locations show that the cell filled scaffold positioned on top, had a quicker decline in signal intensity. Likewise, axial slices taken as one from the top scaffold and one from the bottom, again clearly indicate the cell containing scaffold has a greater loss of signal intensity with every image (Figure 5-20 and Figure 5-21).

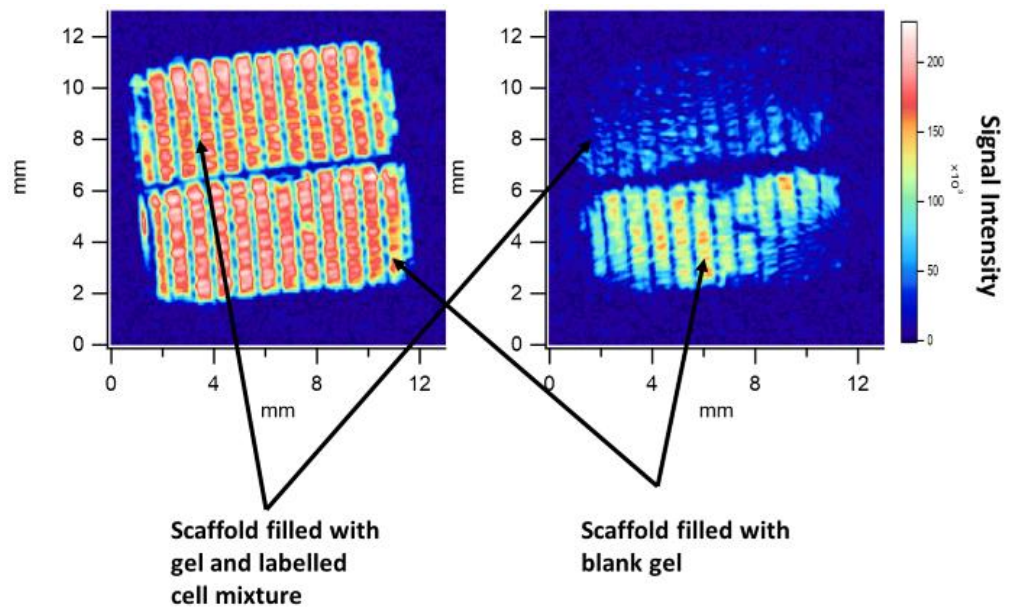


Figure 5-18 First and last echo image acquired with 8 ms between each image, showing how over time the scaffold containing iron labelled cells loses signal at a much more substantial rate than the scaffold containing gel only.

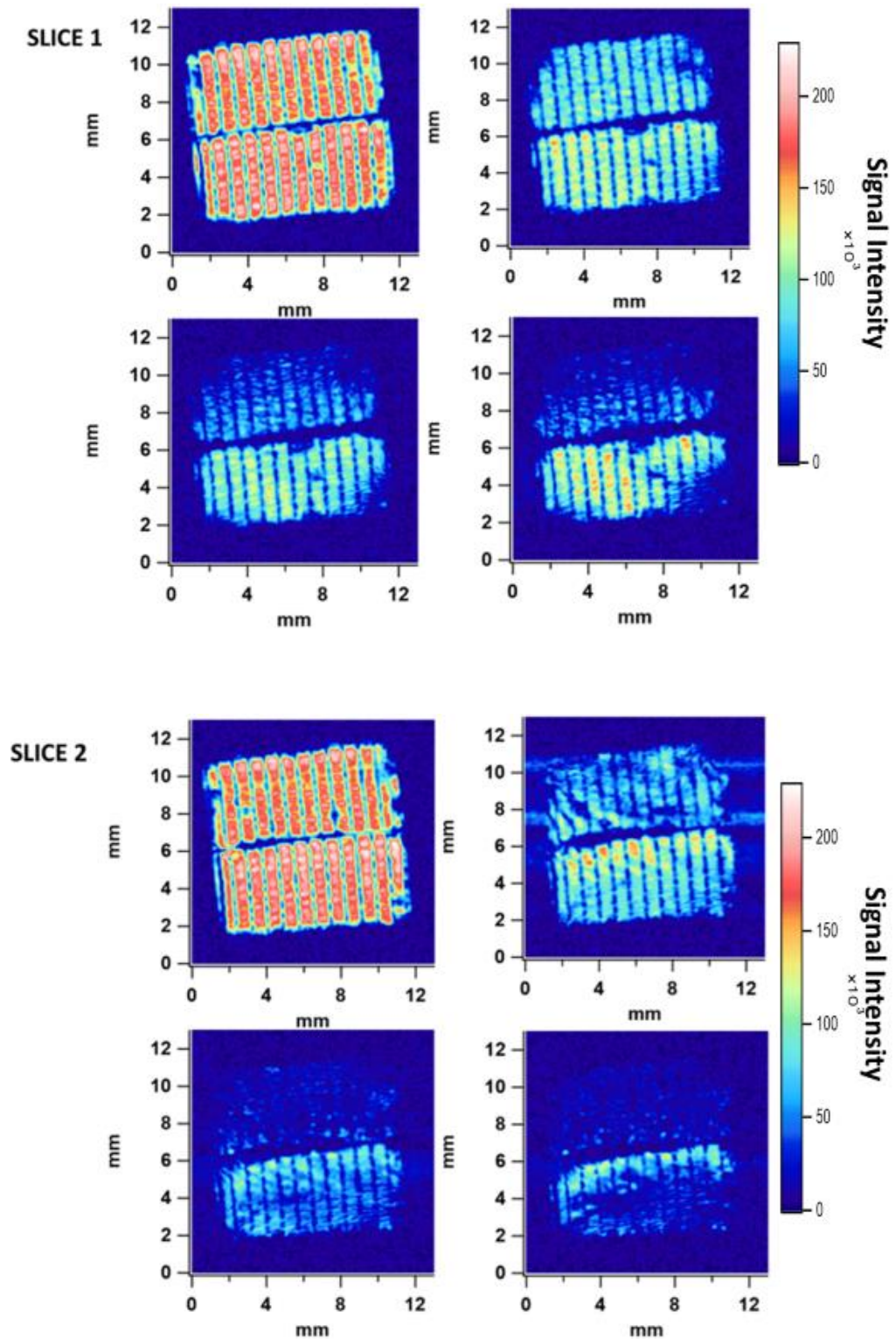


Figure 5-19 Two Scaffolds with 600 μm pores, stacked upon one another and imaged using MRI. One scaffold is filled with gel containing labelled cells (top) and one filled with a blank gel (bottom), to visualise cells within a polymer network. Gradient Echo imaging of two sagittal 0.5 mm sliced locations, 4 echo images acquired per slice, each 2ms apart.

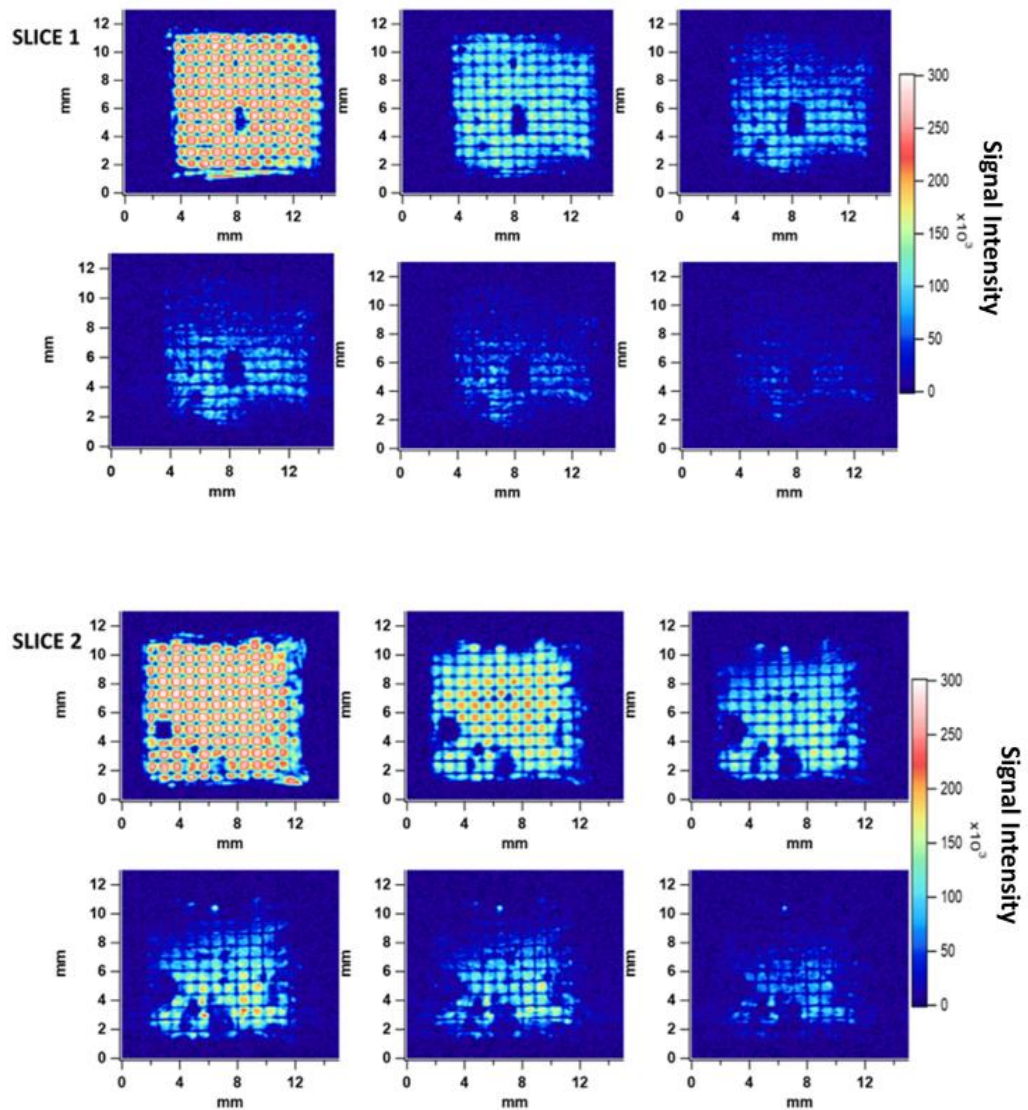


Figure 5-20 MR signal intensity images. Axial slices of stacked scaffolds, containing either gel with dispersed labelled cells or blank gels. Images acquired as a 0.5 mm slice every 2 ms. Slice 1 and slice 2 are axial 0.5 mm slices taken from different locations in stacked scaffolds, one from scaffold with gel/cells mixture (Slice 1) and one from scaffold with blank gel (slice 2).

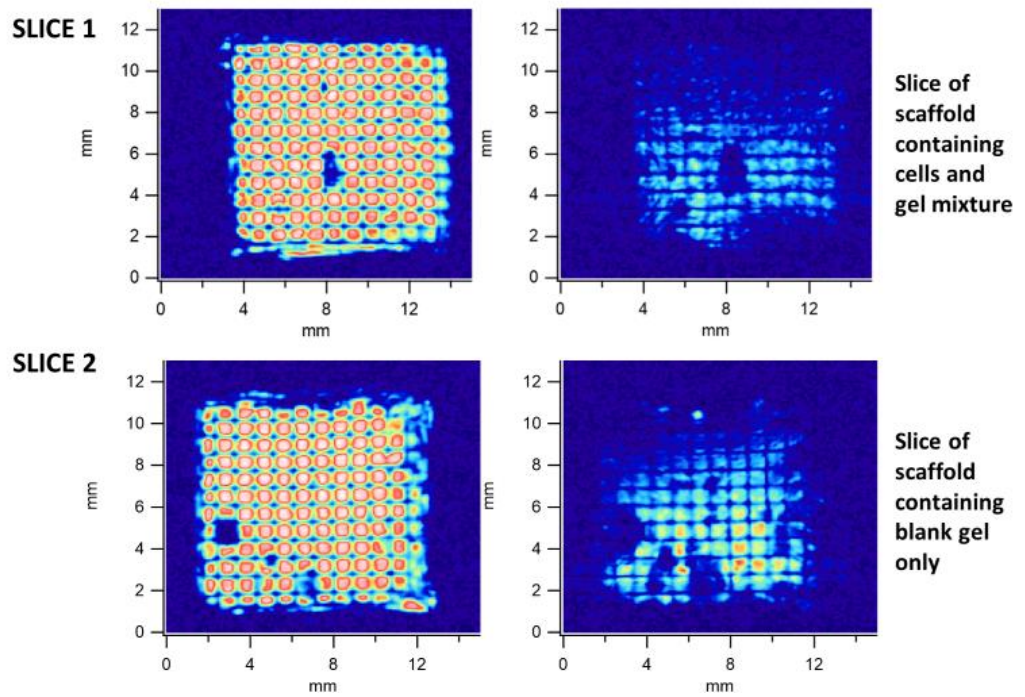


Figure 5-21 Slice of each scaffold acquired as gradient echo images. First echo at 2ms (left) and Fourth echo image [241] after 8 ms shows that in the scaffold containing cells there is a greater degree of reduction in signal intensity over the same time period compared to the scaffold containing the blank gel only.

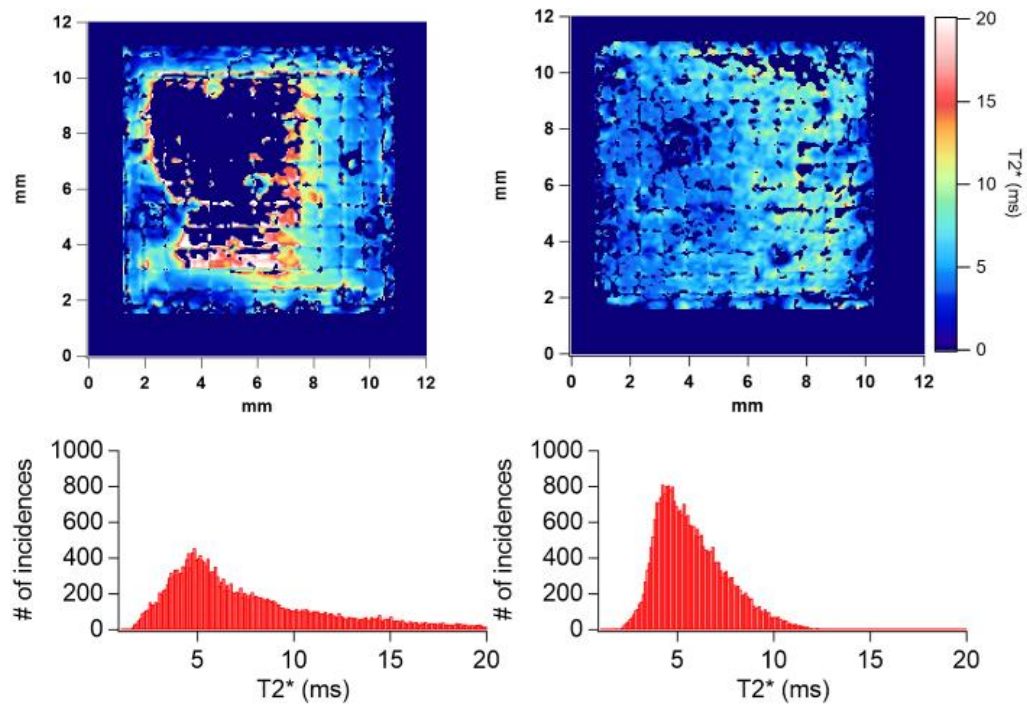


Figure 5-22 Regions of interest bounding each gel filled scaffold, cell free (left) and with labelled cells [241] taken from axial T2* relaxation maps. Corresponding histograms show the frequency and distribution of T2* relaxation times. Cell free scaffolds filled with 20 w/v% Pluronic F-127 gel. Scaffold containing cells, has pores filled with Pluronic F-127 gel that has been seeded with 1×10^6 magnetic labelled ihMSCs. Axial images of stacked scaffolds were used to generate T2* maps.

To quantify this, T2*relaxation maps were produced of both axial (Figure 5-22) and sagittal (Figure 5-23) projections. Isolating relaxation times by using regions of interest to bound both types of scaffold and compare the distribution of relaxation times showed a greater tendency for shorter times as expected in the presence of gels containing labelled cells. Scaffolds filled with blank gels displayed a much wider distribution of relaxation times, with a greater incidence of higher transverse relaxation times. Further to this, spin echo imaging was again employed to confirm that any signal lost due to the iron oxide labelled cells could be recovered (Figure 5-24 and Figure 5-25). Spin echo images, which include a refocusing pulse to acquire signal, are unaffected by the artefacts caused by inhomogeneities in the magnetic field, and to magnetic susceptibility effects of ion containing nanoparticles due to them being refocused. Therefore, using spin echo imaging techniques on the same samples,

validates that the signal loss seen in the series of gradient echo images, but that is acquired with a spin echo refocusing pulse, is due to the susceptibility artefacts as a result of magnetic nanoparticles.

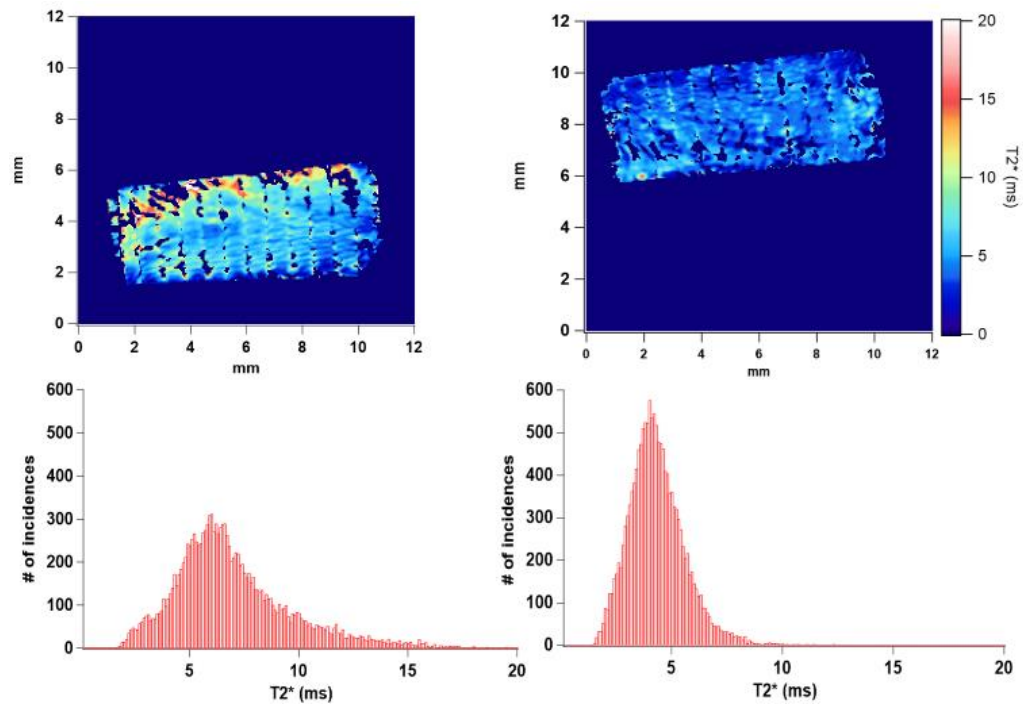


Figure 5-23 Regions of interest bounding each gel filled scaffold, cell free (left) and with labelled cells [241] taken from sagittal T2* relaxation maps. Corresponding histograms show the frequency and distribution of T2* relaxation times. . Cell free scaffolds filled with 20 w/v% Pluronic F-127 gel. Scaffold containing cells, has pores filled with Pluronic F-127 gel that has been seeded with 1×10^6 magnetic labelled ihMSCs. Sagittal projection of stacked scaffolds.

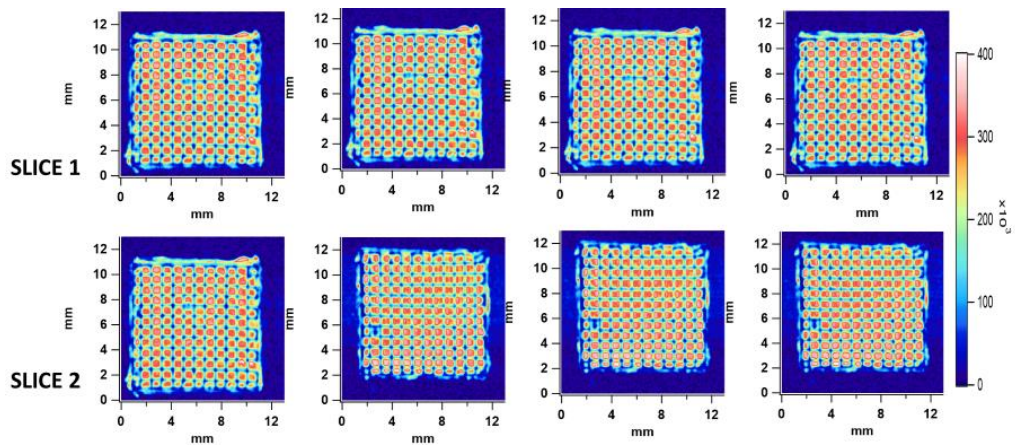


Figure 5-24 Axial images acquired using spin echo pulse sequence. Slice 1 shows scaffold filled with cell seeded gel, cells having been labelled with iron containing nanoparticles. Slice 2 shows porous scaffold filled with gel only. Images were acquired using parameters TE 5.1 ms, TR 1000 ms to produce 128x128 pixel images.

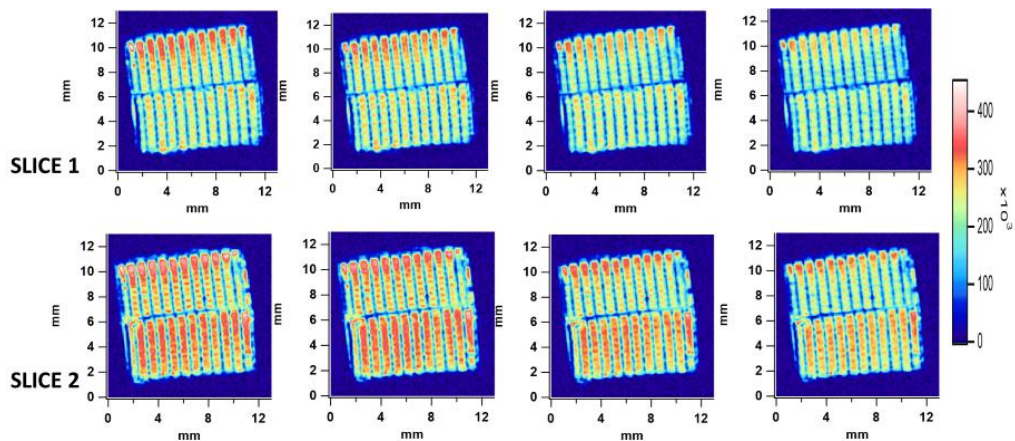
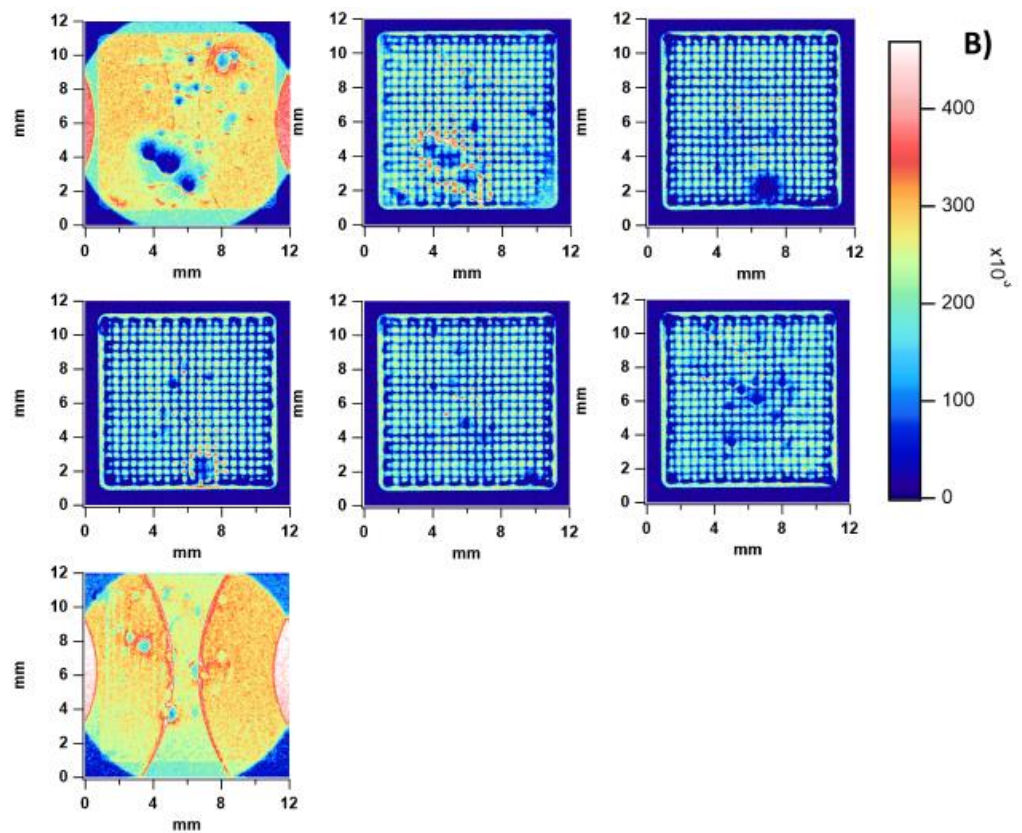
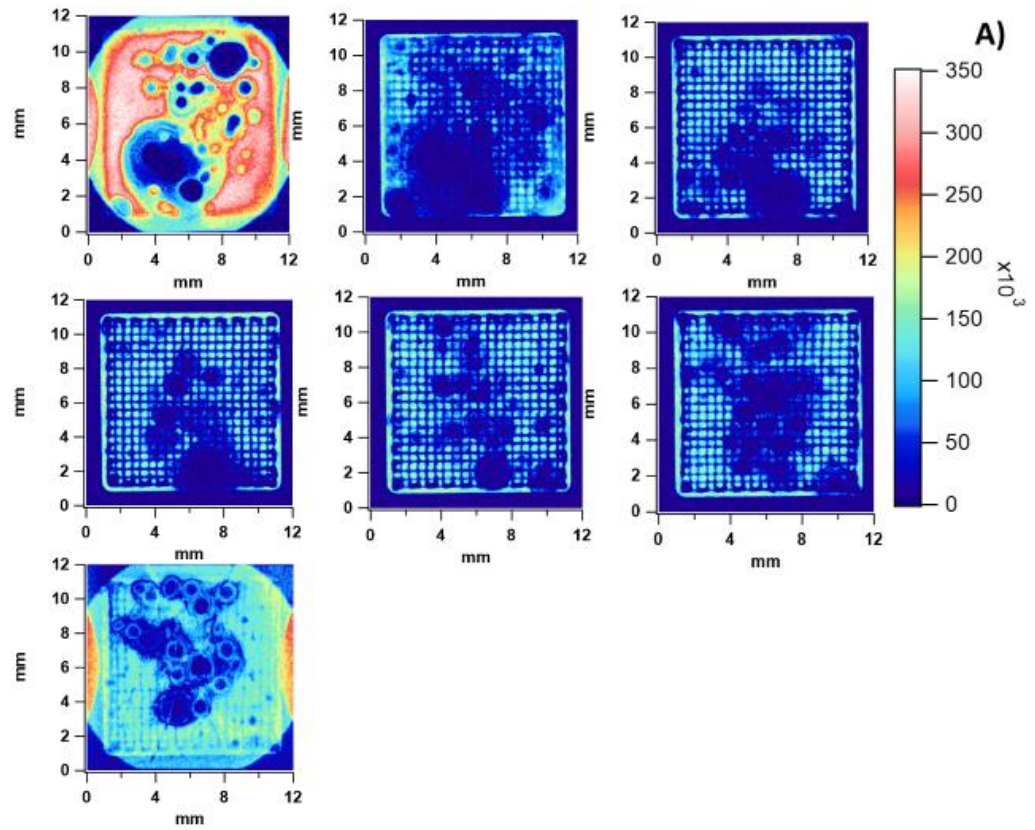


Figure 5-25 Spin echo images of sagittal 0.5 mm slices showing spin echo images acquired every 5.1 ms of stacked scaffolds with labelled and blank gels. Lower scaffold contains gel only, and upper scaffold contains labelled cells dispersed throughout gel. Slices acquired from two different sagittal planar locations. Imaging acquisition parameters TE 5.1 ms, TR 1000 ms, 128x128 pixels.

5.3.5.3 Imaging cell seeded scaffolds

Superparamagnetic iron oxide nanoparticles offer high signal contrast in T2 and T2*-weighted sequences in a non-toxic and biodegradable format, that can be efficiently taken up by cells following surface coatings with functional ligands or the introduction

of transfection agents [271]. Transfection agents are often used for labelling MSC's as they do not possess the same phagocytic capacity as other cells. However transfection agents used in too high concentrations are toxic [293, 294], limiting future use and approval in human studies. Dextran coatings of SPIONs and surface functional groups including carboxyl groups can be used for effective nanoparticle take up by cells without the use of a transfection agent. Mailänder et al. [295] reported that increasing COOH groups on commercially available dextran coated nanoparticles increased the spontaneous uptake of magnetic nanoparticles by MSC's, located mainly inside the endosomal and lysosomal compartments without any introduction of transfection agents. Therefore, throughout this thesis commercially available nanoparticle Nanomag-D-COOH were selected, consisting of an iron core and dextran shell and functional COOH groups and was used in conjunction with MSC's for magnetic resonance imaging, and have been successfully visualised in other MRI research [218, 296]. In this study, following cell labelling and seeding into scaffolds, the scaffolds were in culture, either static or dynamic, for a further 14 days. With every division of cells, the magnetic endosome is shared between two daughter cells, such that the concentration of iron reduces by a factor of two with every division [297]. Given that in this study, static seeding had shown to have a much higher rate of proliferation and cell retention within the scaffold compared to dynamic experiments, the scaffold which had been cultured for 14 days in growth medium post MNP labelling was chosen for imaging. Now cells are attached, unlike previously where the cells were dispersed within a gel and filled pores, cells will have formed attachments to the polymer strands which also show as areas of low signal and without a reasonable density of cells, they may be much more difficult to locate or differentiate between cells and struts. However, using gradient echo pulse sequences to visualise labelled cells, the cells will appear as voids in signal much larger than actual cell size.



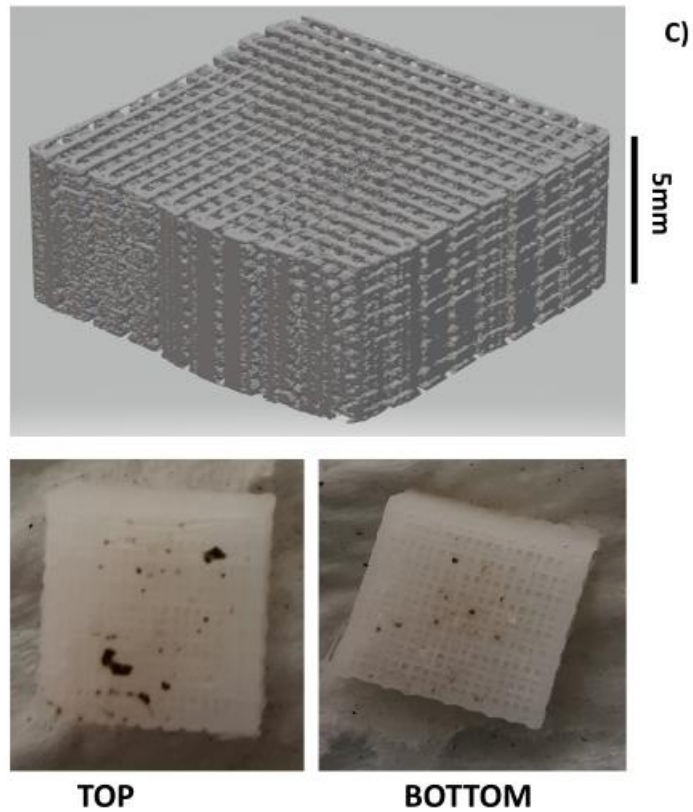


Figure 5-26 A) MR signal intensity images of Gradient echo pulse sequence to acquire 1mm axial slices throughout 300um pore scaffold seeded with ihMSCs labelled prior to seeding. Scaffold had been seeded using manual droplet of 1×10^6 cells suspended in 100 μ l of media and cultured for a subsequent 14 days in expansion media. B) Spin echo images of identical slices from the same scaffold. C) Micro CT reconstruction of scaffold, and images of cell seeded scaffold showing clustering of labelled cells on surfaces.

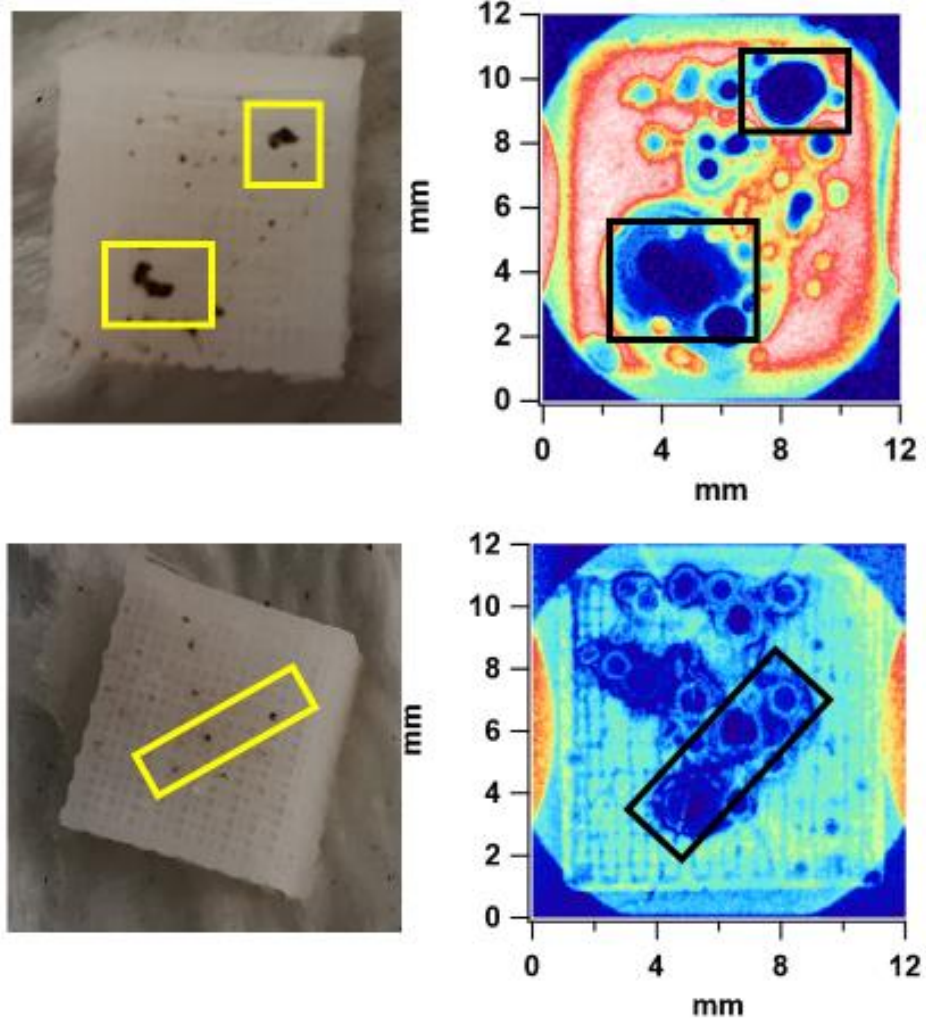


Figure 5-27 Images of cell seeded scaffold, after 14 days in culture, seeded with labelled cells (left) compared against MR gradient echo sequenced images of the corresponding scaffold surface [241]. Highlighted are examples of some corresponding areas of cells between actual and MR imaged scaffold surface.

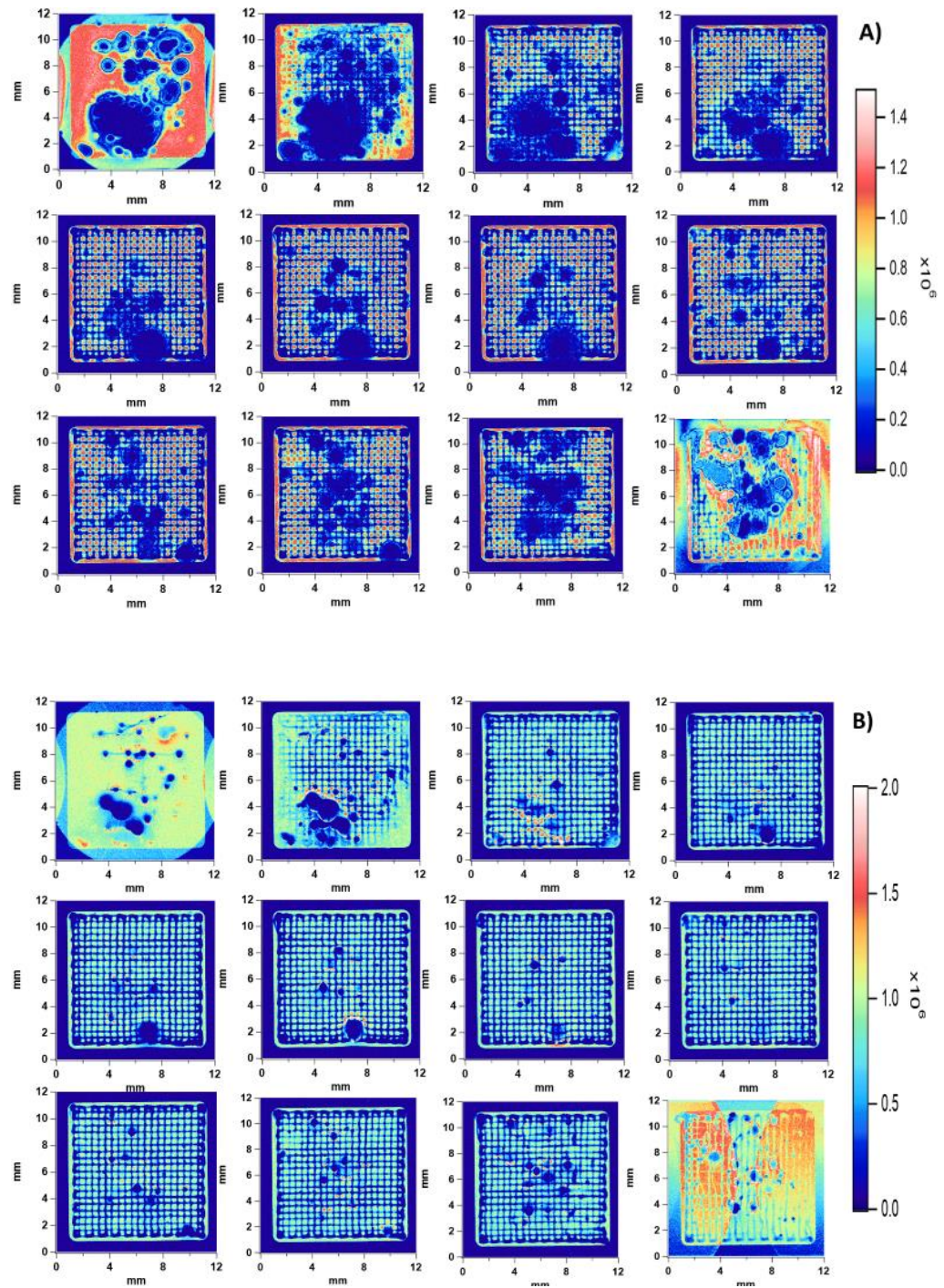
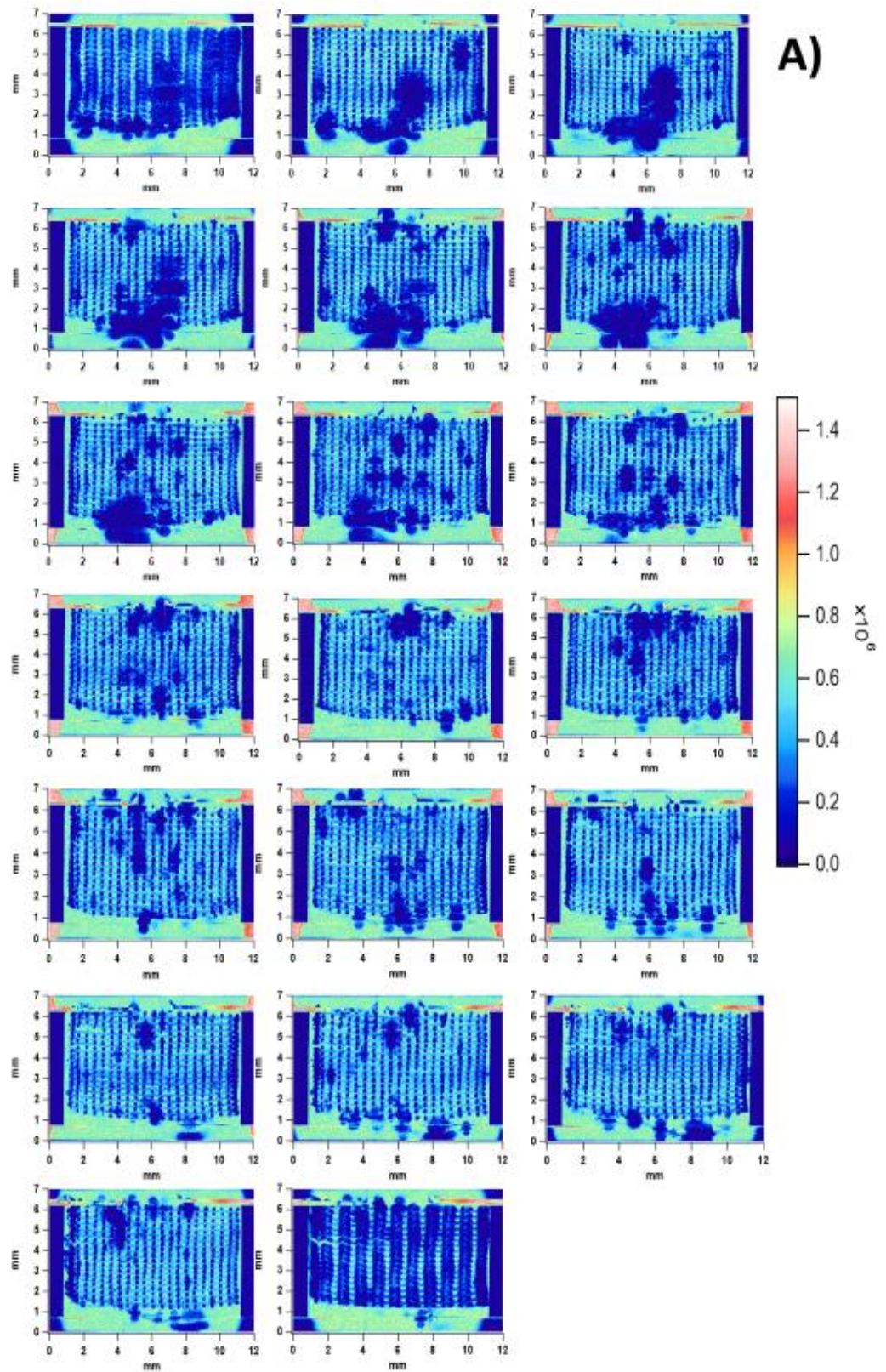


Figure 5-28 MR signal intensity images acquiring twelve 0.5mm axial slices of A) gradient echo sequenced images and B) spin echo sequenced images of a scaffold seeded with labelled cells and grown under static conditions for 14 days. Both MR acquisition sequences were used to produce 512x512 pixel images. Showing 12 slices from second echo for both image sets.

This is evident in Figure 5-26, gradient echo images of scaffold surfaces can be directly compared to visible clusters of labelled cells that grew on the outer surfaces of

the scaffold. In addition to this Figure 5-27 shows a direct comparison between the outer surfaces of the scaffold, which had cell aggregates visible by eye can be directly corresponded with the location of large signal voids on the first and last sliced images acquired using the gradient echo pulse sequence. This demonstrates the ability of MR imaging to locate cells within porous matrix.

Gradient echo images taken from multiple slices show clearly the effects of labelled cells throughout the depth of the scaffold. Spin echo images of the same slices recover most of the signal lost to the magnetisation susceptibility artefacts caused by cells. Regions of cell clusters are still visible in spin echo images, but the size is much more reflective of the actual cell sizes or clusters of cells due to the elimination of those signal artefacts that surround cells in the gradient echo images. Higher resolution axial and sagittal images taken from a higher number of slices, slicing from left to right in the sagittal plane in Figure 5-28 and Figure 5-29 give good visual representation of how far cell growth has penetrated the scaffold depth. Figure 5-30 shows comparisons between two slices taken from the same locations, comparing gradient echo with spin echo images of cells. Upper and lower regions of the scaffold have a higher density of cells, this is likely due to the static seeding technique which consists of dispensing a concentrated droplet directly on top of the scaffold. With a pore size of approximately 300 μm and a strut diameter of approximately 200 μm it is likely that most cells that do not get deposited on the top surface of struts, will fall through the porous space and be deposited at the bottom surface of the scaffold. The central regions of the scaffold are not completely devoid of cells, although it is not clear if this is a result of cell migration or the initial deposition of cells. In seeding labelled cells, there was a tendency for cells to form clusters in high concentration suspensions which could have contributed to cells being more likely to be retained in the porous matrix due to the increased size compared to a single cell.



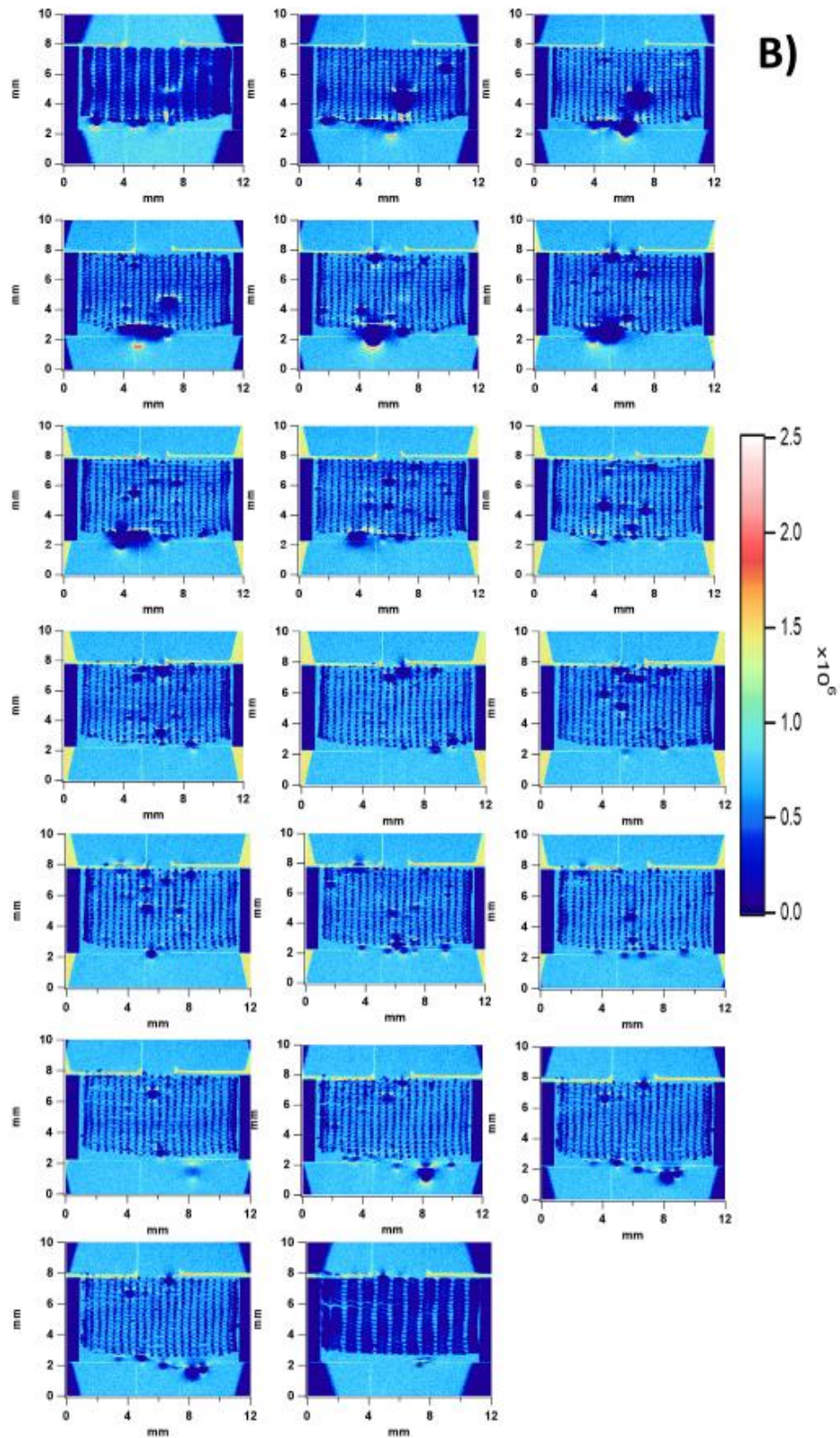


Figure 5-29 MR signal intensity images of twenty 0.5 mm sagittal sliced A) gradient echo images acquired every 2ms and B) spin echo images acquired every 5.1 ms in a pixel of 256x256. Scaffold seeded with magnetic nanoparticle labelled cells and grown in static conditions for 14 days. Large areas of signal voids in both image sets correspond with location of cells.

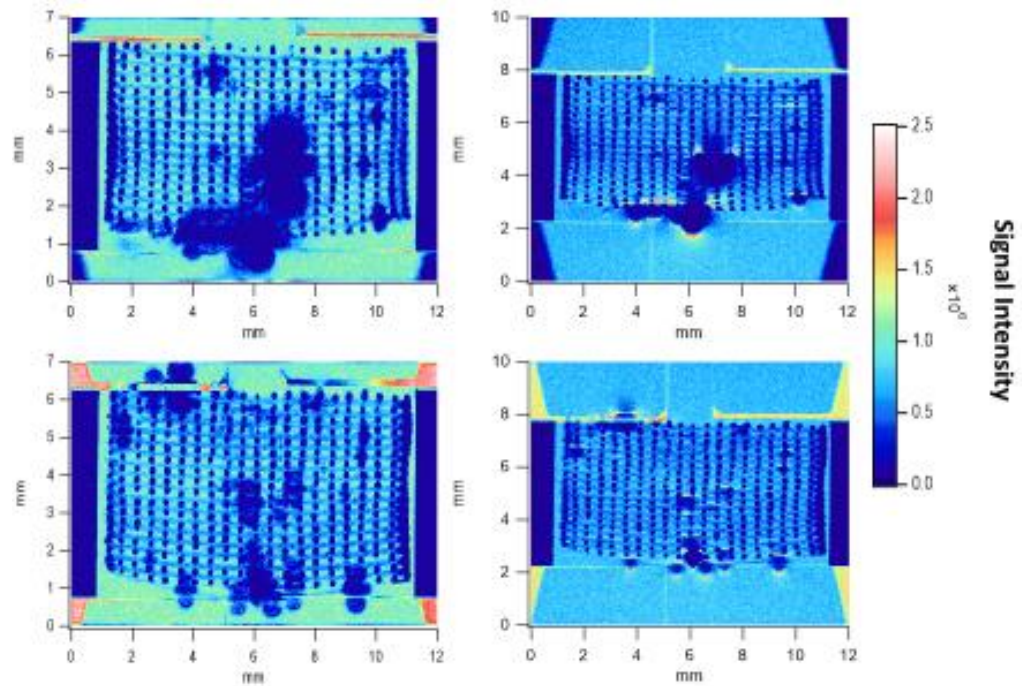


Figure 5-30 Comparison between gradient echo (left) and spin echo [241] of identical sagittal sliced images taken from a scaffold seeded with cells post labelling with iron oxide nanoparticles. Areas of signal void show location of cells, spin echo sequenced images more accurately portray the size of cells or groups of cells.

Figure 5-31 shows the difference between a cell labelled and blank scaffold. Both scaffolds were imaged using the same acquisition parameters to acquire seven slices through the depth of the scaffold. The effect of the labelled cell concentration after two weeks of proliferation in culture media is evident. Large areas of signal of loss correspond with cell location that do not exist in the cell free scaffold (Figure 5-32) can be directly compared, further demonstrating the ability of MR imaging to locate cells within a porous polymer scaffold.

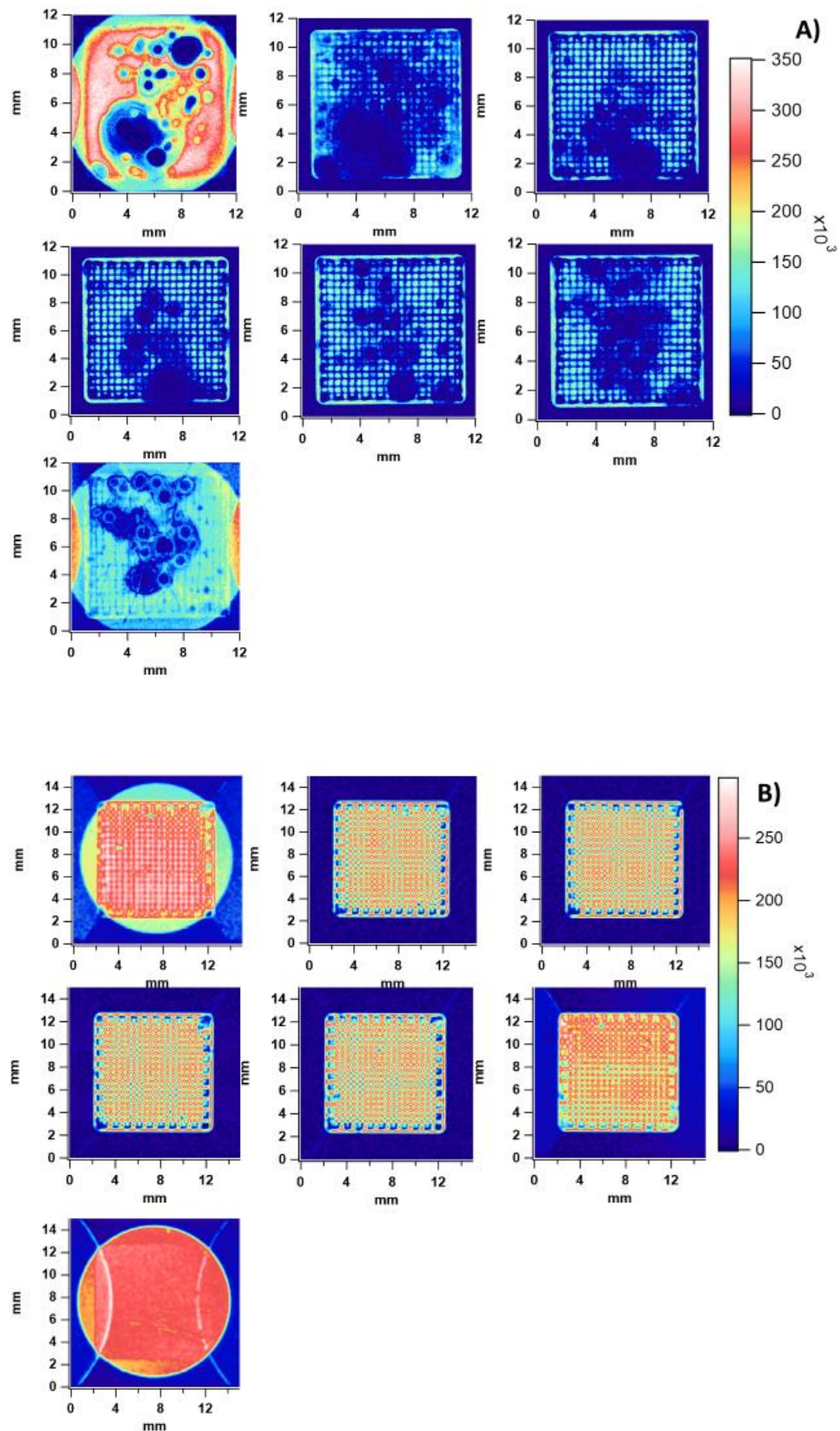


Figure 5-31 Comparison of (A) scaffold seeded with labelled cells and static cultured for 14 days against a completely cell free scaffold (B) both filled with Pluronic F-127 gel. Both sets of images were acquired using a gradient

echo pulse sequence using parameters TE 2 ms and TR 1000 ms to produce 256x256 pixel array images. Large areas void of signal indicate presence and location of cells that are not present in the blank scaffold.

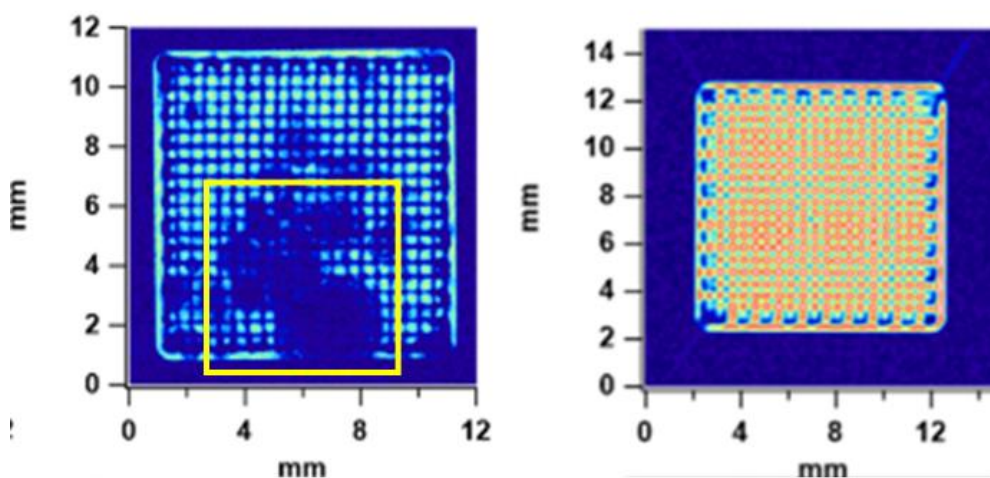


Figure 5-32 Slice from same axial location in a cell seeded scaffold (left) and a blank scaffold [241]. Highlighted area shows large loss of signal, indicating the presence of cells, labelled with iron oxide nanoparticles to act as a negative contrast agent.

MR imaging offers a real alternative for cell imaging for *in vitro* after seeding in porous polymer structures, without the requirement for invasive methods. In this study three-dimensional PCL scaffolds printed and seeded with immortalised MSC's and used to evaluate the non-invasive imaging capabilities of MRI in tissue engineering. Prior to seeding, cells were labelled magnetic nanoparticles at 50 $\mu\text{g/ml}$ concentration, to act as a contrast agent for MR imaging to effectively capture cell location and infiltration into the porous structure of the scaffold. MRI detection of MNP labelled cells *in vitro* and *in vivo* has been previously successfully proven using hydrogel systems. High resolution gradient-echo imaging with 9.4T MRI was able to detect labelled cells at a singular level when prepared in an agarose gel [298]. Further to this *in-vivo* non invasive cell localisation has been achieved using T2*-weighted gradient echo, successfully detecting the presence of iron nanoparticles in animal studies using cell injected rats [299]. Cells labelled with magnetic nanoparticles act as a local magnetic perturbation that results in a loss of signal around the cell, such that magnetic cells appear as areas of void signal, which the size of often exceeds the actual size of the

cell [300]. Gradient echo imaging of cell seeded scaffolds (Figure 5-28) showed exactly this effect when compared to spin echo images taken from the same axial positions, in which the signal voids appeared much larger. Gradient echo imaging is used because it does not involve refocusing pulses such that it is sensitive to the relaxation process of the decreased transverse relaxation component $T2^*$ induced by strongly magnetised perturbation [298]. $T2^*$ is the dephasing time what accounts for both intrinsic molecular interactions and extrinsic magnetic field inhomogeneity unlike $T2$ which only accounts for molecular interactions. Spin echo sequences employ two RF pulses with flip angles of 90° and a second refocusing 180° pulse which serves to cancel dephasing effects caused by inhomogeneity in the local magnetic field to, generate $T1$ or $T2$ weighted images [270]. The signal intensity loss from field inhomogeneity is therefore minimised using Spin echo sequences and as a result of this spin echo images are more effective for visualising the location of MNP labelled cells. Spin echo images acquired in this study can therefore be more effectively used as qualitative analysis of cell location and density in that location. Gradient echo images are more or less sensitive to $T2^*$ decay depending on user defined parameters. Parameters include echo time (TE) which is the time between the beginning of the RF excitation pulse and the acquisition of signal, repetition time (TR) which is defined as the time between successive pulse sequences and finally the flip angle which is the amount of rotation the net magnetisation experiences upon application of the RF pulse. $T2^*$ decay due to nuclei dephasing starts when the excitation pulse is applied, therefore the longer the TE the greater the signal because there is more dephasing. Low flip angles and long TR reduces $T1$ relaxation effects, allowing $T2^*$ effects to become dominant [301].

Tracking cell distribution and cells ability to populate biomaterial scaffolds is difficult to do whilst preserving the scaffold and not disrupting cellular behaviour. Traditionally, methods have been limited to 2D techniques of sectioning and staining to assess post culture [302, 303]. Micro-CT offers an alternative for post culture analysis that can preserve the scaffold structure and limit disruption to cells, to produce three-

dimensional reconstructions and analysis of cell-seeded scaffolds. However this often requires the use of toxic fixatives like osmium tetroxide [304] or complex post processing methods to visualise cells [305]. Pre-culture labelling of cells with barium sulphate to visualise with Micro-CT has been successful to provide contrast between cells and scaffold [306] but this could only be achieved with a number of post culture steps to prepare the scaffold for imaging including fixation and freeze-drying. Furthermore, this study only analysed a static seeding method, although Micro-CT has been used to assess dynamic seeding with magnetic iron oxide particles [307]. This research concluded that compared to static seeding the use of fluid flow or syringe injected seeding the distribution of cells in three-dimensional PCL scaffolds was greatly improved when imaged with Micro-CT at day 3. However the cell number compared to static was lower at day 3, suggesting the seeding efficiency was reduced, potentially due to the need to use more dilute cell suspension for dynamic seeding, such that some cells will be washed away during seeding.

Although cell localisation and visualisation was successfully shown in this current experiment using MR imaging, the results are limited as it only provides a snap shot of cell proliferation at one point in culture. To properly highlight the advantages of MRI over methods like the μ -CT studies mentioned previously, it is important to evaluate a scaffold at multiple time points to show cell migration within the same scaffold without invasive methods of fixation ceasing cell proliferation. This information would provide a more true picture of cell behaviour under different culture conditions, rather than comparing different scaffolds at different time points. Direct comparisons in the latter situation are difficult as cell seeding distributions, efficiencies and growth will differ to some degree between scaffolds.

Magnetic resonance imaging of cells containing magnetic iron oxide nanoparticles seeded onto scaffolds have been used to investigate cell distribution, primarily using hydrogel scaffolds [272-274]. Polymeric biomaterial scaffolds have reported on using MRI methods to observe cellular distribution [308, 309] using a method to detect

differences in signal intensities between culture medium and cells, and using diffusion weighted gradients to enhance image contrast with no additional cell labelling for detection. Labelled cells seeded within porous polymer scaffolds present a different challenge compared to using hydrogels because the scaffold material itself is similar to MNP's with a decreased signal intensity in imaging [300, 310]. However, in this current study, fused deposition modelling produces scaffolds in which the porous architecture is highly organised and well defined, so it is easier to distinguish between the scaffold material and labelled cells than it is in randomly orientated heterogeneous pores. A further benefit of using MRI for cell tracking over other aforementioned methods is the scope to image live cells without fixation, as it is possible to maintain certain culture conditions like temperature and image scaffolds in culture media in some cases [308].

Irrespective of method to assess cell migration and distribution under perfusion, predominantly research has shown that distribution of cells is much more homogeneous when compared to static culture [107, 168, 249, 311]. However, given how many variables there are between experiments, including bioreactor design, scaffold pore shapes and sizes, and flow conditions chosen and inputted into different studies, it can be difficult to make direct comparisons between studies, and establish optimal conditions. Therefore, efforts to increasingly understand what drives cell behaviour and responses, the limiting factors inhibiting infiltration and their ability to populate scaffolds using non-invasive imaging techniques can help to direct scaffold design to more optimal structures.

5.4 Conclusion

Visualisation of cells within three-dimensional porous scaffolds is an important method of characterisation for assessing the overall success of 3D culture. The location and distribution of cells throughout a scaffold can strongly influence subsequent tissue formation and the quality of said formation. Understanding how changes in scaffold

design, culture methods, and bioreactor design influence the overall infiltration of cells into scaffolds and monitoring changes in cell location over time could be aided with the use of non-invasive MR imaging for cell visualisation. In this study, cells were labelled iron oxide magnetic nanoparticles to act as negative contrast agent for identification within a porous polymer matrix. Results showed that after successful uptake of magnetic nanoparticles and proliferation within the scaffold, cells could be located and imaged throughout the entire scaffold. For future experiments, it is important to further validate this method as capable for real time imaging by capturing images of cells live during culture experiments as opposed to fixing them as was done in this experiment. Scanning times and temperatures can be modified to accommodate such an experiment and maintain the viability of the culture experiment.

6 The Relationship between Cell Seeded 3D porous Scaffolds and Perfusion

6.1 Introduction

Imaging cell location provides an insight into how flow influences cell seeding distributions and cell migration in perfusion culture. However, it does not provide information on how cells influence flow patterns and visa versa. Effective nutrient supply, waste removal and a range of biomechanical cues in large 3D tissue engineering constructs are often highlighted as benefits of a dynamic culture environment and bioreactor systems [117]. Indeed, this is true for the application of shear stresses via a perfusion bioreactor to mesenchymal stem cells (MSC's), which has been shown to be effective in directing both chondrogenic [3, 180, 312] and osteogenic [5, 171, 172] differentiation. Fluid perfusion creates shear stresses that provide a source of mechanotransduction pathways by which MSC's respond to in a range of cellular biochemical and biological responses. Increased MSC proliferation has been linked to the application of low flow rates compared to static culture [172, 173]. In both of these studies, conversely, applying a higher flow rate upregulated osteogenic differentiation but appeared to inhibit the proliferation capabilities of the cells. Different magnitudes of shear stress resulting from perfusion cultures have been able to show distinct cartilage phenotype expression for experiments using MSC's [313, 314] whilst some magnitudes of flow impeded production of chondrogenic matrix components [6]. Differences indicate that dynamic culture for chondrogenic differentiation is not a standardised process and there are multiple interactions between cells, scaffolds, and fluid flow within systems that need to be understood. Often times in order to optimise perfusion culture conditions, computational modelling of flow is first used to predict how such interactions will ultimately direct cell fate [13, 116, 186, 285].

In addition to fluid shear stresses, increased mass transport for sufficient nutrient delivery and removal of waste products ensures good cell metabolism is aided with perfusion culture.

Limited mass transport into 3D scaffolds is often a limitation associated with static culture that results in tissue formation restricted to the peripheral regions [315]. Polymer scaffolds can be considered as a two-phase system made up of a solid phase containing polymer matrix and cellular material, and a void phase made up of the culture medium. A volume averaging method can be applied to calculate diffusion coefficients as a function of cell volume fraction and time [316] to indicate levels of mass transport. Overtime, this degree of diffusivity can be increased into the scaffold due to the degradation, and swelling properties of scaffold materials. On the other hand, diffusion can be decreased by the synthesis of new ECM molecules occupying previous void space [317]. Therefore, mass transport of material into a scaffold is not just dependent on initial conditions like applied flow rate, and pore architecture, it is also dependent on how far the system changes throughout culture. Monitoring these changes would be ideal for leading optimisation of either scaffold or bioreactor design to facilitate culture conditions for ECM production and cell differentiation. The changes add a new level of complexity, that despite the effectiveness of modelling in many cases, it can still be very difficult to successfully predict the degree and rate of changes that are likely to occur.

Computational fluid dynamics (CFD) models have been used to attempt to effectively take into account ECM growth and neo-tissue formation, and how far this reduces pore size, overall scaffold permeability and ultimately increases fluid velocity. One such study showed that pore volume filling from 10% of the scaffold up to 60% filled increased wall shear stresses from 0.0034 to 0.005 Pa and 0.004 to 0.008 Pa for two distinct pore geometry [13]. This indicated changes in internal pore structure could expose cells to much higher than desired shear stresses. Further models in bone tissue engineering have sought to assess how much applied flow rate would need to be reduced over time to ensure shear stress levels don't exceed values that promote ECM mineralisation [116]. Results showed that compared with a constant flow rate, decreasing flow rate linearly could be used to keep shear stresses consistently within what is considered an optimal region for ECM mineralisation. Ideally, to increase the validity of findings like in these studies, experimental data would be very informative to show just how much flow rate over time is affected by cell

ingrowth, and how this relates to subsequent ECM formation. Further to this CFD models have also been used to predict that small changes to cell culture systems will result in subsequent changes in models predictions which measured outputs including pressure and shear stress. One study into cell culture media viscosity and density highlighted that the concentration of serum in culture media, and changes in culture media over time due to cell excretions changed the viscosity of culture media and in turn increased viscosity of the fluids. The addition of 5%, 10% and 20% FBS in Phoons study increased fluid viscosity compared to the deionised water control by 30%, 48% and 107% respectively, although the fluid remained in a Newtonian state, there was evidence of shear thinning particularly in the presence of high concentrations of FBS. Further to this, after culture with cells the media containing 5% concentration FBS increased in viscosity up to 40% after 3 days [318]. This is significant when considering the effects for cells because increased viscosity has been linked to increased mineralised matrix deposition in bone tissue engineering [5], such that a consequence of these changes in media viscosity could be beneficial if properly utilised. However, this also highlights some key issues with modelling, given that assumptions about culture media behaving as a Newtonian fluid in which viscosity remains constant independent of stress continuously over long culture periods. In CFD models, not accounting for changes in viscosity and how that would affect the velocity of the media perfusion could be limiting the accuracy of predictions about cellular conditions experienced.

Monitoring changes in scaffold permeability and changes in fluid velocity over an extended period of culturing with cell-seeded scaffolds is challenging without the introduction of tracers or necessitating non opaque materials and is the focus of this chapter. NMR and MRI velocimetry has the ability to probe opaque materials and measure steady state flow conditions using the spin properties of nuclei, in this case hydrogen nuclei, which are exhibited when nuclei are in the presence of an applied magnetic field. These properties can be used to resolve spatial information, and distinguish nuclei of atoms with different physical properties including atoms experiencing different amounts of translational diffusion [193], key for studying flow in porous medium. MRI velocimetry utilises the signal produced by the precession of spins to encode for position by introducing magnetic field gradients. This

means that the frequency of precession depends on the location of the nuclei. Velocity encoding requires the application of bipolar gradient pulse pairs, in which motion of nuclei causes dephasing of the signal, hence velocities recorded are proportional to net phase shift.

The purpose of this study was to evaluate firstly the differences in growth of cells into pores when cultured in either chondrogenic media and expansion media. From this fluid velocity maps were taken at time points during culture to assess how far cell proliferation and ECM production effect the velocity profiles. This velocity mapping will allow to eventually linking biological responses of cells to physical changes in cell culture. Linking these outcomes could aid decisions on bioreactor parameters and design, or optimise scaffold porous scaffold design based on the information on the velocity and in turn shear stresses cells experience during culture.

6.2 Methodology

6.2.1 Scaffold Design and Fabrication

Scaffolds were designed with the software BioCAD which generates code to be used by a thermal extrusion based 3D printer (RegenHU, Switzerland) to fabricate a scaffold of the dimensions 10 mm x 10 mm x 5 mm (length x width x height). Polycaprolactone (PCL) pellets ($M_n=45,000 \text{ g mol}^{-1}$ Sigma Aldrich UK) were extruded through a 330 μm nozzle at a temperature of 74°C and a pressure of 4 bar, whilst the air temperature was maintained at 26°C using a hood to enclose the printer. Within the enclosed environment a fan set to 1000 rpm was used to aid the cooling of the struts upon deposition to the platform. Print head speed was set to 30 mm s⁻¹ and the extrusion rate of the material was set to 15 revolutions per metre travelled by the print head. The height of each printed layer was set to 0.15 mm for the scaffold.

6.2.2 Cell culture and scaffold seeding

6.2.2.1 *Static Culture*

Pre-seeding scaffolds were sterilised using washes of 70% IMS and PBS for upto 3 hours before being incubated in FBS containing media overnight for fibronectin adsorption to improve cell attachment to PCL. Immortalised human mesenchymal stem cells (MSCs) were cultured in expansion medium (Dulbecco's modified eagle's medium with 10% FBS, 1% L-Glutamine and 1% antibiotic/antimycotic solution). PCL scaffolds were manually seeded with 1×10^6 cells per 100 μ l droplet pipetted directly onto the scaffold. Scaffolds were then incubated for three hours to allow cells to attach before growth media was added to each well to fully immerse the scaffolds.

6.2.2.2 *Dynamic Culture*

For dynamic culture, sterile scaffolds that had been incubated overnight in FBS containing media were seeded with 1×10^6 immortalised human MSC's, suspended in 40 μ L of expansion media (Dulbecco's modified eagle's medium with 10% FBS, 1% L-Glutamine and 1% antibiotic/antimycotic solution). Scaffolds were seeded using the same static method, allowing 3 hours to attach before being loaded into the flow chambers described in 6.2.3. Following this, an additional 25 ml of fresh chondrogenic media (serum free expansion medium supplemented with 50 μ g/ml L-ascorbic acid phosphate, 40 μ g/ml L-proline, 1% ITS+ premix, 1% Non-essential amino acids and 10 ng/ml TGF- β) was added to each chamber system, and perfused at a rate of 1 mL/min, for up to 28 day time points, with media changed every 2-3 days, or for 14 day samples 25 ml of expansion media (Dulbecco's modified eagle's medium with 10% FBS, 1% L-Glutamine and 1% antibiotic/antimycotic solution) was added instead.

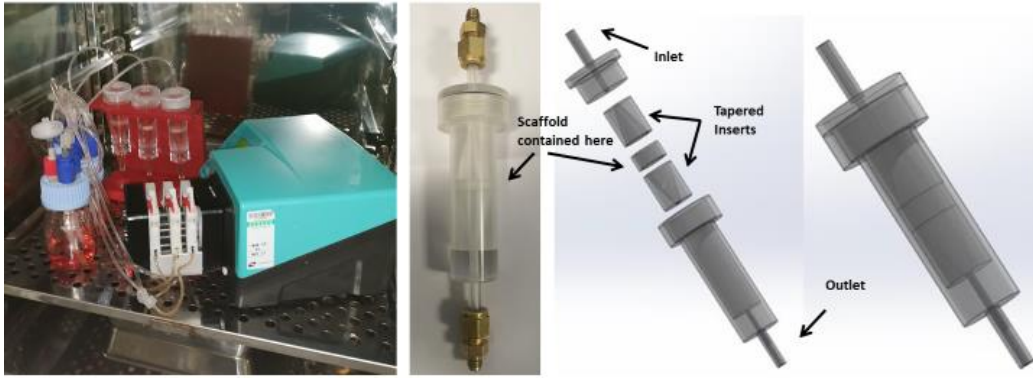


Figure 6-1 Dynamic perfusion culture set-up in incubator, cell culture chamber image and schematic images showing chamber design.

6.2.3 Flow chamber and System

The flow chamber was designed to fit a 25mm proton clear bore volume resonator of 9.4T Bruker Avance III vertical bore MRI scanner. The chamber body was manufactured out of acrylic, containing a further three acrylic inserts. One to hold scaffolds with the dimensions of 10 mm x 10 mm x 5 mm (L x W x H) in the central region of the chamber and then two further Teflon inserts of 27.5 mm length, tapered at an angle of 7.25° on both walls to sit either side of the central scaffold containing insert. The tapered inserts created a channel that started at 3 mm diameter at the inlet and outlet, and had a 10 mm diameter nearest the scaffold, to allow fluid flow through the chamber without sudden changes in pressure. Brass inlet and outlets were fixed to either ends of the acrylic chamber, with a channel diameter of 3mm also, allowing the chamber to be fixed (Swagelok) to silicone tubing ensuring a tight leak free system. A peristaltic pump (Watson Marlow) circulated continuous flow. The pump used silicone manifold (Elkay labs) tubing with an inner diameter of 2.29 mm which connected to Masterflex Tygon E-food (B-44-4x) tubing with an inner diameter 1.6 mm and made up the tubing network outside of the peristaltic pump. The circular flow system was completed with a reservoir to provide and collect water for the flow system. The pump flow rate was set to 10rpm, which was calculated to be a mass flow rate of 1 mL/min.

6.2.4 NMR and MRI velocity Measurements

The flow set up described in 6.2.3 was used to acquire flow measurements, using Bruker Topspin 3.5. Slice selective velocity measurements of flow in the Z-direction through the porous architecture of the scaffolds with a single slice thickness of mm were obtained with an NMR system consisting of a 9.4T Bruker instrument and a 25mm imaging probe within which the flow chamber was placed vertically. 3D acquisition is required for this method, where by spatial encoding is performed in two planes and in the third plane the flow encoding gradient is applied. In this experiment the flow encoding gradient was applied in the Z direction, to produce image sizes of 256x256 pixels. Imaging slice thickness was set at 2.8 mm and positioned in the centre of the scaffold. Imaging parameters were TE=18 ms, TR=1000 ms, FOV=15 mmx15 mm. Data processing and velocity calculations were carried out using Prospa V3.12 software (Magritek, Wellington), whilst subsequent analysis was done using IGOR pro 8.04 (Wavemetrics, USA).

6.2.5 MR Imaging of Cell seeded scaffolds

Each scaffold was loaded into the flow chamber described in 6.2.3 and the porous regions were filled with water. The flow chamber was loaded vertically into 25mm ¹H probe, and measurements were acquired using Bruker Avance III 400MHz spectrometer at 9.4 Tesla, controlled using Paravision 6.0.1 software. Gradient images were acquired using a TR of 4000 ms, TE of 5 ms, number of averages was 4, a 12 mm x 12 mm FOV for a matrix size of 512x512. The resolution of the images acquires was 23 x 23 μm using a 0.5 mm slice thickness. The total scanning time to acquire these images was 2h and 16m.

Spin echo sequence was also used to acquire images using the following parameters, TR of 4000 ms, TE of 14 ms, a 12 x 12 mm FOV, and acquisition pixel array of 512 x 512. Slice thickness was set to 0.5 mm, and a resolution of 23 x 23 μm was achieved. Total scanning

time for this image acquisition was 2 hours and 16 minutes. The acquired data sets for both imaging methods were zero filled to achieve a matrix reconstruction size of 1024 x 1024. The data sets were reconstructed using Prospa V3.12 (Magritek, Wellington) before image processing using Igor Pro 8.04 (WaveMetrics, USA).

6.2.6 Cell viability and Chondrogenic differentiation analysis

At Days 1, 14 and 28 the MSC seeded scaffolds were harvested, washed sufficiently with PBS, sectioned into 6-8 smaller pieces before each being digested at 37°C over 3 days in 800 µl of papain solution (280 µg/ml papain, 5 mM L-cysteine, 50 mM EDTA in Duplecco's PBS with a pH of 6.5). Assays were used to quantify the DNA content and sulphated glycosaminoglycan (sGAG) from the supernatant of the digested samples. DNA quantification was carried out using a Quant-iT Picogreen kit (Invitrogen) while the sGAG content was quantified using 1,9-dimethylmethylene blue (DMMB, Sigma-Aldrich). Assays were performed in triplicate.

6.2.7 Osmium Tetroxide staining

Cell seeded scaffold were also fixed for image analysis using 2.5% glutaraldehyde overnight before being washed with PBS. Fixed scaffold were prepared for SEM and micro-CT scanning by further fixation with 1% osmium tetroxide. Before being imaged the scaffold must be completely dry, so samples are left to dry for one to two days in a fume hood.

6.2.8 Micro-computed Tomography

For characterisation, scaffolds were analysed using an x-ray µ-CT scanner (Skyscanner 1174) with a voxel resolution of 7.7 µm, x-ray source current 800 µA and voltage 50 kV. X-ray images were obtained every 0.4° rotation in/ a full 360° revolution of the stage which

samples were mounted to. N-Recon software reconstructs the obtained transmission images to 2-dimensional slices. CTAn software uses the reconstructed slices to create 3D models to visualise pore interconnectivity and carry out morphometric analysis of the scaffolds including calculating overall bulk porosity. Cell seeded scaffolds that have been fixed using osmium tetroxide staining can be imaged using this method to show the distribution of cells. Distribution of cells can be segmented from the structure of the scaffold by using threshold values of upper grey 255 lower 103 for cells and upper grey 81 lower grey 16 for the scaffold.

6.3 Results and Discussion

6.3.1 Static cell culture

6.3.1.1 Cell Seeding efficiency and proliferation

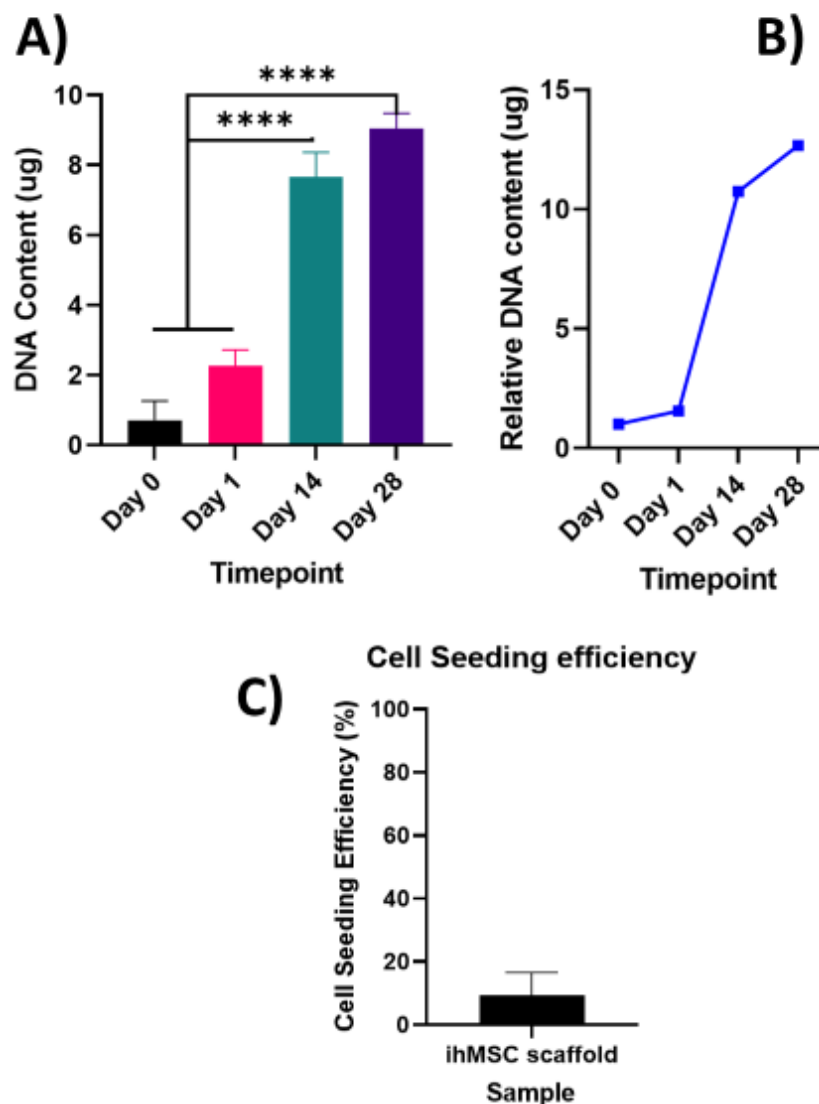


Figure 6-2 DNA content measured over 28 days for 3D cell seeded PCL scaffolds, seeded and grown under static conditions in chondrogenic media containing TGF- β . A) DNA content average content \pm standard deviation (n=3) and B) Relative DNA content normalised to day 0. C) cell seeding efficiency measured using DNA content of cell suspension compared to scaffold after initial seeding and attachment (n=3). ****p<0.0001

Figure 6-2 shows DNA content measured from cell seeded scaffolds, that had been digested using Papain to release DNA, and the resultant supernatant was assayed at each timepoint. Cells were manually seeded onto scaffolds and cultured for up to 28 days, in chondrogenic media, containing TGF- β to support growth and differentiation. The initial cell seeding efficiency using manual static seeding was low (Figure 6-2), with around 10% of cell suspension being retained on the scaffold after 3 hours allowed for cells to attach. Unfortunately, scaffolds with high pore interconnectivity and large pores, although beneficial for cellular activity including migration and proliferation into the centre of the scaffold, do not necessarily promote a high seeding efficiency. This is why a high density of cells are pipetted onto the scaffold during seeding to try and mitigate for this issue as much as possible. Other studies have looked to alter the characteristics of scaffolds to overcome this, including creating porous surface topography [319] to enhance cell adhesion and retention, or in some cases creating a pore size gradient [10] to enhance seeding efficiency. However, given this study was focusing on changes in flow due to cellular activity focus was kept on homogenous porous environments to avoid other variables effecting flow patterns. Prior to seeding, sterilised scaffolds were immersed overnight in serum containing media to provide a source of cell-adhesion proteins to increase the likelihood of cell-surface interactions.

Cell proliferation in scaffolds was measured using DNA quantification (Figure 6-2). DNA content and relative DNA content showed a marked increase from day 1 through to day 28. This supports that PCL porous scaffolds can be used to create a 3D environment in which MSC's freely proliferate [106, 320]. Cell scaffolds were stained using osmium tetroxide for μ -CT imaging. Micro CT imaging can be used in conjunction with cells stained with a heavy metal, to be visualised through the use of threshold parameters to separate the cells from the polymer scaffold [319, 321]. Micro CT 2D image slices were reconstructed into a 3D model of cells and the scaffold respectively to illustrate the location and density of cells throughout the scaffold (Figure 6-3). The 3D reconstructions supported that cell growth increased across the scaffold during culture. The 3D reconstructions can also be used to visualise cell locations (Figure 6-3). Initially, on day 0 after seeding, a large density of cells can be seen on the upper surface of the scaffold, corresponding with the location of the

droplet cell suspension is pipetted during seeding. As culture time progresses, day 14 and day 28 both display similar characteristics in terms of a higher density of cells being located at the periphery of the scaffold, featuring on the sides and top surface. This is consistent with other studies that have shown polymer scaffolds seeded with cells [315, 322]. Factors including pore size and architecture can affect cell distribution throughout scaffolds, particularly smaller pore sizes limiting cell migration [131]. Given the relatively larger pore size used in this study, outer cell aggregation is likely due to lack of diffusion of nutrients and oxygen to the centre of scaffolds, causing cells to stay closest to where this the most availability of fresh medium.

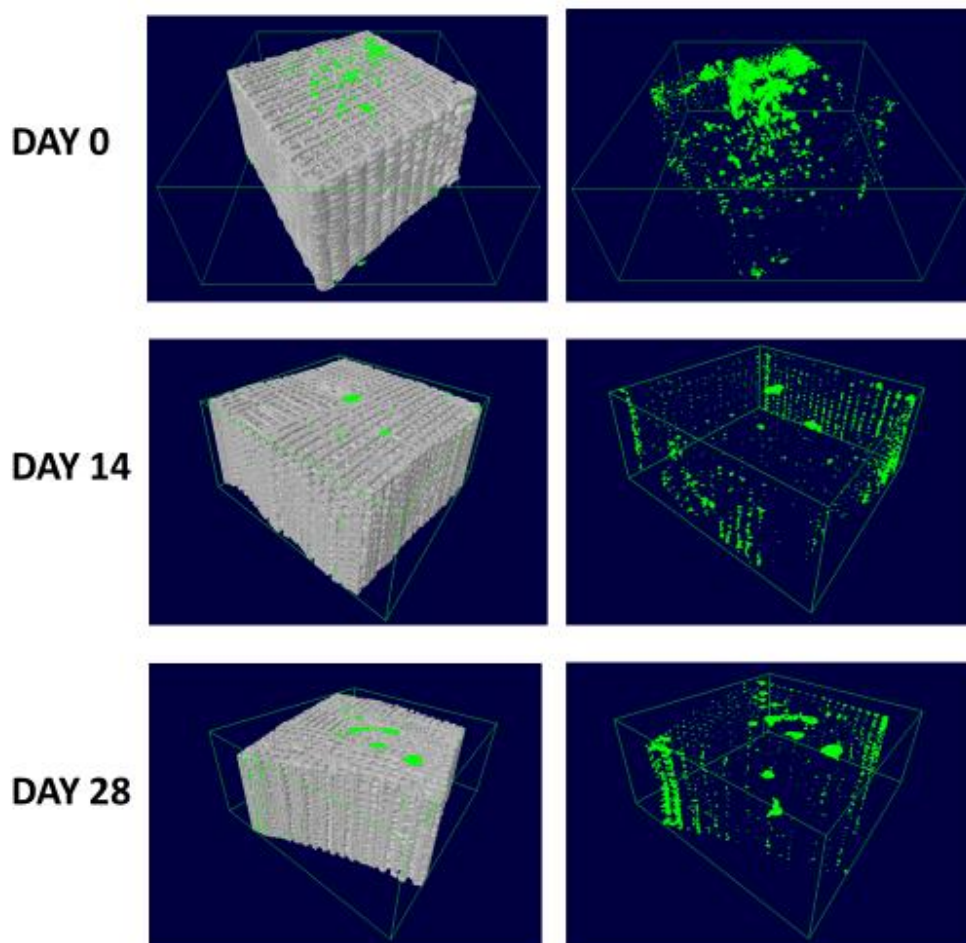


Figure 6-3 Micro-CT reconstructions of cell seeded scaffolds and grown under static conditions in chondrogenic growth media at Day 0, 14 and 28 post staining with osmium tetroxide.

6.3.1.2 MSC Chondrogenic differentiation

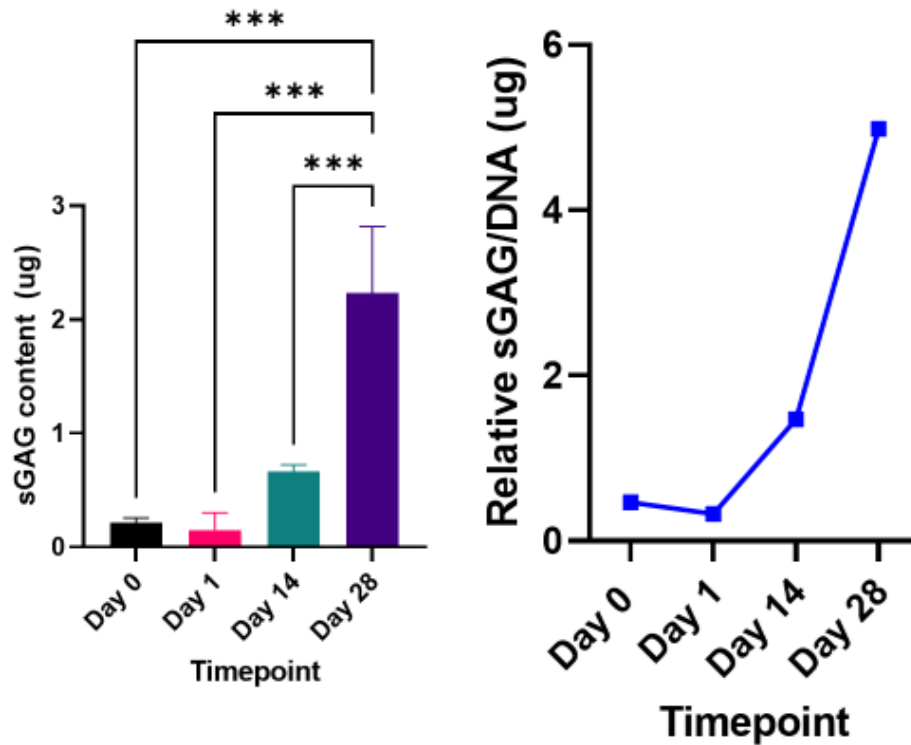


Figure 6-4 Chondrogenic differentiation of MSCs in 3D printed scaffolds quantified using DMMB assay (to measure sGAG content), and measured over 28 days in static culture (n=3) (left). sGAG content relative to total DNA content normalised to day 0 (n=3) [241]. ***p<0.0002

In order to quantify chondrogenic differentiation, results in Figure 6-4 show the quantity of sulphated glycosaminoglycan, measured using a DMMB assay on the supernatant of digested samples. Cell seeded scaffolds were grown under static culture conditions for up to 28 days in chondrogenic media supplemented with TGF- β 1 growth factor. Cell number increased within the constructs over the 28 days, although the cell number between days 14 and day 28 were largely similar, with no statistically significant difference between them (Figure 6-2). This cell proliferation also corresponds with an increase in sGAG content produced within the scaffolds. However, the increase in sGAG is much lower in terms of absolute value when compared with the amount of DNA content after 28 days. This is also

the case when compared with other studies using PCL scaffolds seeded with MSC's for chondrogenesis [323] the sGAG production is comparably lower. This lower level of GAG production after 28 days compared to the absolute levels of DNA content would suggest that in static conditions cells preferred to proliferate as opposed to differentiate, something that is supported by the results seen in Raimondi study [176]. However, given sGAG production does not occur instantly, MSC's have been shown differentiate and begin to accumulating GAGs after approximately 12 days [324] .

6.3.2 Dynamic Cell Culture

6.3.2.1 Cell seeding efficiency and growth

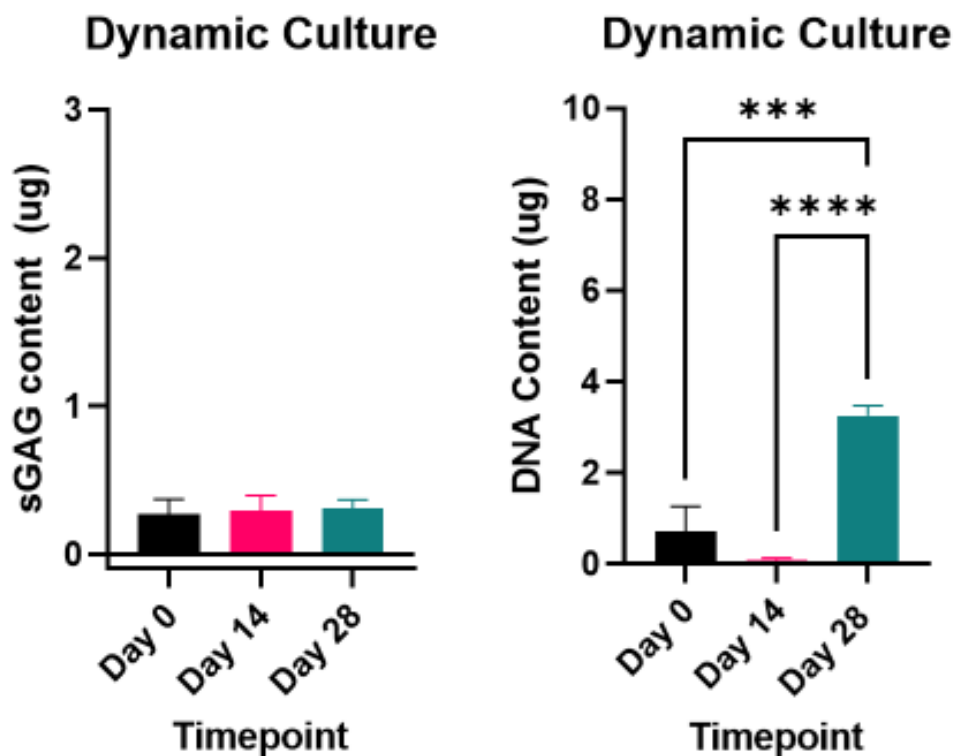


Figure 6-5 Results for cell seeded scaffolds grown under perfusion dynamic culture at 1mL/min for up to 28 days in chondrogenic media, showing DNA content [241] quantified using Pico Green Assay (n=3), and sGAG content (left) measured using DMMB assay (n=3). ***p<0.0002

For dynamic culture experiments cells were seeded directly onto PCL scaffolds using the same manual seeding method as scaffolds in the static culture experiments. Cells were allowed to attach for 3 hours before they were loaded into individual flow chambers and perfused with culture media for 14 days and 28 days. As with in static experiments, culture media used contained TGF- β 1, which acts to regulate chondrogenic differentiation and promote cartilage synthesis [325]. Perfusion of media provided cell seeded scaffolds with increased mass transport of culture media, in addition to inducing levels of hydrodynamic forces not present for static culture. Results showed for dynamic culture experiments (Figure 6-5) that there was minimal cell proliferation or evidence of MSC chondrogenic differentiation. Given that cell-seeding techniques used were identical, differences in cell number after one day in culture were minimal. Over the subsequent culture period cells perfused with culture media showed an inconsistent trend in DNA content. For samples cultured for 14 days showed close to zero levels of DNA content, and although at day 28 there was an increase (3.25 μ g) indicating some proliferation however this is still significantly lower than compared to day 28 in static conditions (9.04 μ g) which was almost 3 times higher. A significant decrease in proliferation compared to static conditions would suggest the dynamic conditions were not favourable for cell growth. Increasing levels of fluid flow and shear rates has been associated with both cell detachment and apoptosis [326]. Cell detachment is likely the reason for such low DNA content at day 14 as seen in Figure 6-5. After 14 days under perfusion any cells weakly attached to the scaffold surface would likely be detached due to the forces involved in perfusion. A low density of cells in scaffolds limits cell-cell communication. Studies have shown that a high density of cells led to increased cell proliferation, particularly in the first seven days of culture, which was attributed to an increased amount of cell-cell communication via gap junctions [327]. Given that increase in DNA content was not seen until 28 days, it is likely that the very low number of attached cells and cell communication in the scaffold limited the rate of proliferation, and it wasn't until 4 weeks in culture cell density had achieved more suitable levels for increased cell proliferation.

Fluid flow and the induced shear stresses in relation to gene expression has shown that high induced shear stresses are linked to apoptosis through three pathways; cytoskeleton reorganisation, extrinsic signalling pathways and endoplasmic reticulum stress by linking the expression of genes associated with these pathways to increasing shear stress [328]. Cell detachment has been shown to be proportional to increasing flow rates [7, 329], McCoy identified that a flow velocity of over 235 $\mu\text{m/s}$ was linked to increased detachment of cells which had bridged between struts. However, this bridging of cells was linked to smaller pores, whereas pore sizes of more than 300 μm , like those used in this study, were more likely to contain cells with a flat morphology with greater adhesion strengths. Other literature has presented cell detachment values of more than 60% for flow rates of 0.5 mL/min and 1.0 mL/min for scaffolds that had been statically seeded and then exposed to flow [278]. This is supported by other literature, in which cell washout and apoptosis has been linked to a similar flow rate values [8, 175]. Although some studies have presented successful results in terms of cell proliferation and differentiation with flow rates close to 1 mL/min used in this study in PCL printed scaffolds [107] the same study did also record high cell death and shear induced hypotrophy under dynamic conditions. Evidently, even if studies are similar in many respects, results can still be largely dependent on a number of factors which play a role in flow characteristics, and each study is individual, meaning flow characteristics need to be properly understood from study to study to produce effective outcomes.

Further to this, cell adhesion to polycaprolactone is known to be poor, the high hydrophobicity of PCL leads to reduced cell affinity [330], and given the additional forces applied in dynamic systems, and potential for cell detachment, high cell affinity is imperative for scaffold success. PCL scaffolds are often surface modified to decrease the hydrophobic properties and increase cell adhesion. This has been achieved using a number of methods, including NaOH treatments to reduce the water contact angle [331], surface plasma treatments [332] and blending PCL with a more hydrophilic material [330]. In this study, to improve cell adhesion scaffolds were submerged into culture medium prior to seeding, which allows proteins to be absorbed onto the PCL strut surfaces and provide binding sites for cells increasing cell adhesion. However, the proteins attach themselves to the surface using only

weak attraction forces like Van der Waal forces [333], such that cells may be more easily removed from the surface of the scaffold, particularly in the presence of fluid flow. Therefore, it may be more appropriate to seek alternative methods of surface modification to make PCL scaffolds a more viable option for use in dynamic culture environments, and allow better cell retention than was achieved in these experiments.

Studies using PCL scaffolds have incorporated a number of methods to improve cell attachment by reducing the hydrophobicity of the biomaterial. Methods to achieve this include protein coating, plasma, laser and chemical treatment [48, 334-336]. Using collagen to improve cell adhesion to PCL has shown as a major protein found in the ECM collagen is able to improve cell anchorage, such that it has been shown to successfully improve the adhesion of fibroblast cells compared to PCL alone [48]. Further methods to improve cell adhesion to PCL has included the addition of small concentrations of pristine graphene in combination with NaOH treatments was able to show a significant increase in cell attachment and proliferation [337]. Given there are a number of proven ways to increase how readily cells can attach to PCL it should be considered that any future work would include a step to reduce the hydrophobic properties of PCL so that it is no longer a limiting factor in dynamic cell culture.

6.3.2.2 MSC Chondrogenic Differentiation

Results for measuring the content of sulphated glycosaminoglycan in cell seeded scaffolds showed that dynamic perfusion did not increase levels (Figure 6-5) compared to static experiments, this is contrary to many other studies. Compared to static culture, it has been well documented that creating a dynamic environment for MSC's grown on PCL scaffolds is associated with increased chondrogenic differentiation including significantly higher sulphated glycosaminoglycan production [338, 339]. MSC differentiation potential is dependent on mechanical cues in biology, and often externally applied mechanical loads *in vitro* are used including tension, compression, shear stress and hydrostatic pressure can all affect the lineage of MSC's [3, 265, 340-342]. In the case of fluid flow induced shear

stresses, MSC responses in 3D tissue engineering are understood to be driven by two key events, mechanosensing and mechanotransduction. The prior referring to the ability to sense physical cues from the surrounding microenvironment, and the latter is the ability to transduce external forces into biochemical signals that in turn elicit a cell function [343]. Results however from quantifying sulphated glycosaminoglycan's showed no increase over the 28 days culture time indicating that MSCs did not differentiate and begin to laydown extracellular matrix. Compared to static results which in line with cell increasing cell proliferation over the 28 day period, there was not the same trend or level of increase in cell number in the cells grown under perfusion. This is reflected in the accumulation of sGAG or the lack thereof, indicating the low number of cells limits the quantity of ECM constituents that can be measured.

6.3.3 Fluid Velocity Measurements

In order to assess changes in culture media velocity across porous scaffolds, cells were cultured either in expansion media or chondrogenic media and then fixed. In this study investigated was a scaffold that had been grown for 28 days under static conditions in chondrogenic media and evidenced ECM production, and a scaffold cultured for 14 days in expansion media under static condition which showed to have 3 fold increase in cell number. Scaffolds following fixation at the relevant time point were assessed by measuring flow conditions using MRI velocimetry techniques. Although in these experiments it was more practical to fix scaffolds due to logistical constraints, there is scope within this technique to continue cell growth and characterise the movement of fluid through pores, owing to MRI velocimetry suitability to non-invasively measure steady flow in opaque materials. In order to correlate flow patterns with specific pore in growth of cells scaffolds post MRI velocity encoding cells were imaged using MRI to show location of cells. For the 28 day chondrogenic scaffold, cells were unlabelled pre seeding and imaged using contrast in diffusion of free water against diffusion of water constrained in cells. These scaffolds were stained with osmium tetroxide for Micro-CT imaging to validate cell location post fixation. This heavy metal staining of cell membranes acts as a contrast agent and allows scaffold

materials to be distinguished from cellular material due to the much higher x-ray attenuation, through post scan threshold settings. In the case of the scaffold grown in expansion media for 14 days, cells were pre labelled with magnetic nanoparticles as we had shown labelling did not inhibit cell proliferation but had not investigated the effects of differentiation, hence the 28 day chondrogenic cultured sample was unlabelled. The iron labelled cells are used to provide negative contrast between cell location and surrounding free water (as seen in previous chapter). The aim of these flow experiments was to evaluate the effect of cell growth, and in some cases differentiation leading to ECM deposition, would have on the flow of liquid through the porous scaffold environment. An identical blank scaffold was also assessed using the same MRI velocimetry methods to allow proper assessment of cell effects.

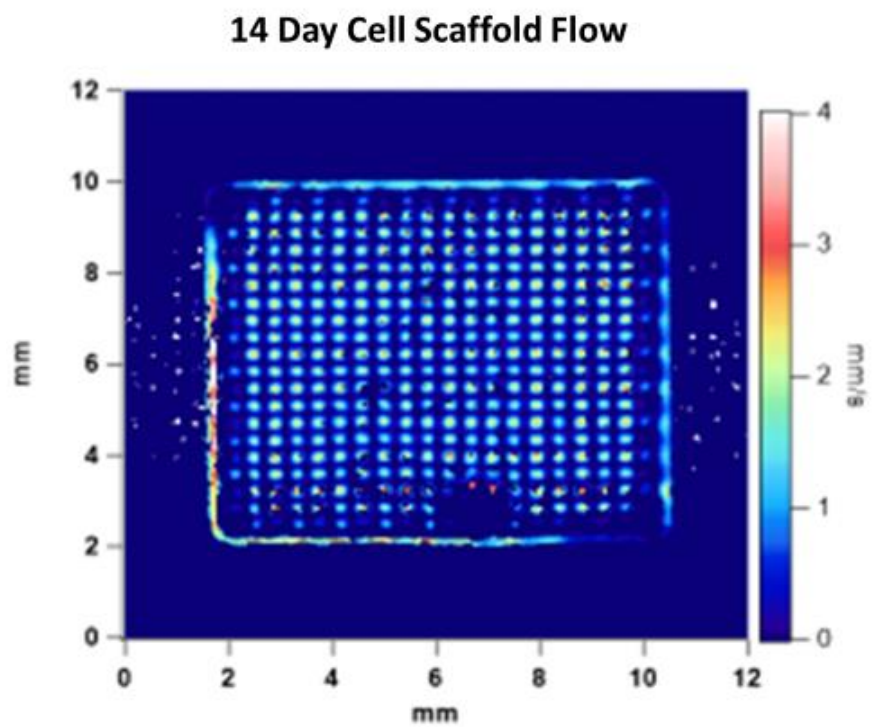
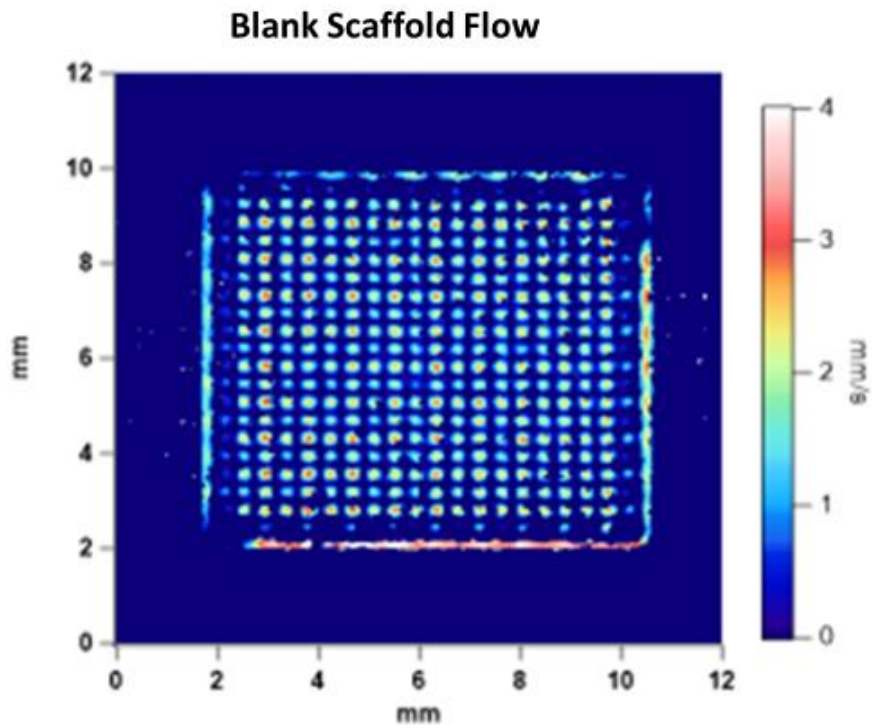


Figure 6-6 Velocity bulk measurements mapped as velocimetry images of scaffolds, showing a cell free blank scaffold (top) and a cell seeded scaffold that has been cultured in growth media for 14 days under static conditions (bottom).

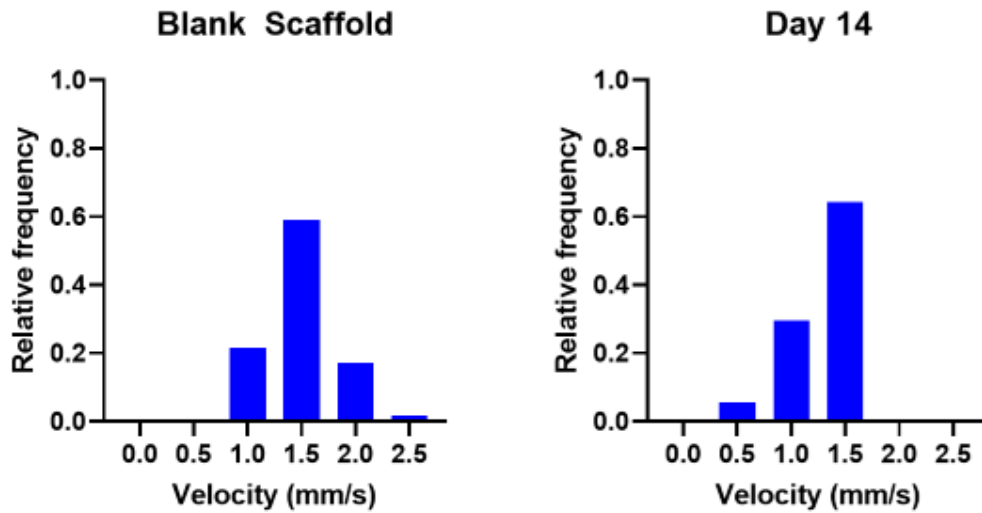


Figure 6-7 Histograms showing the relative frequency distributions recorded from peak velocity values within each pore for a blank cell free scaffold (left) and for a scaffold that has been cell seeded and cultured in static conditions for 14 days.

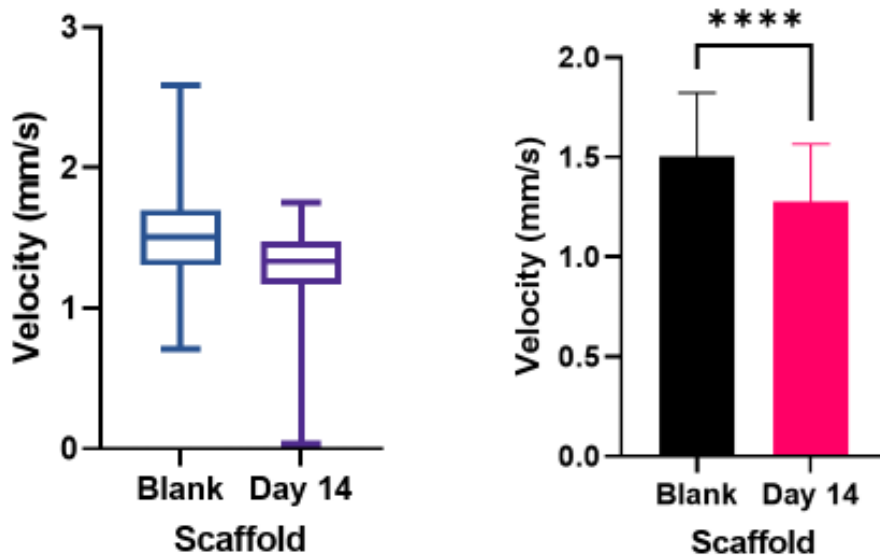


Figure 6-8 Box Plots showing distribution of velocity and average velocity of flow through scaffolds without cells, and cultured with cells for up to 14 days under static conditions in growth media. **** $p < 0.0001$ ($n=1$).

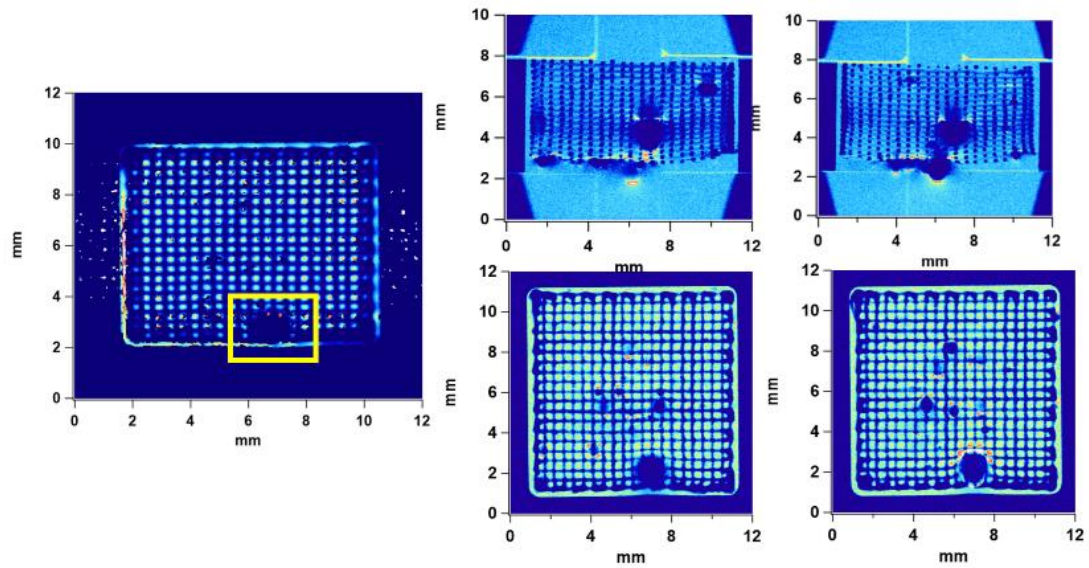
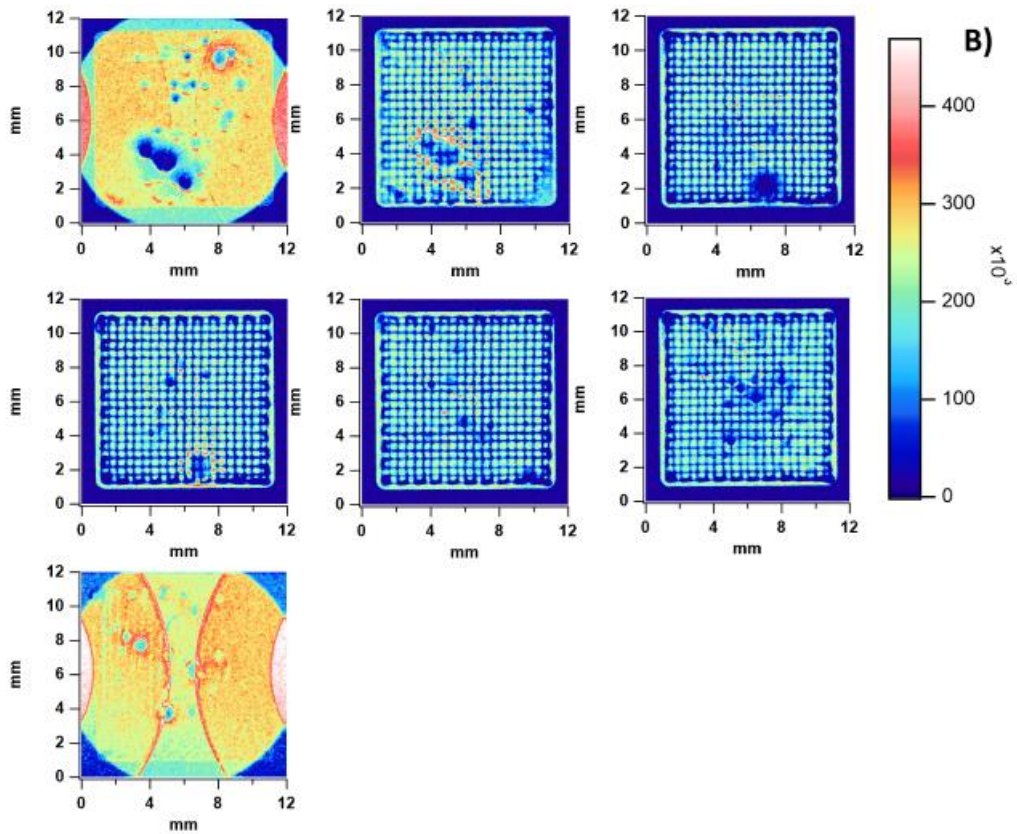
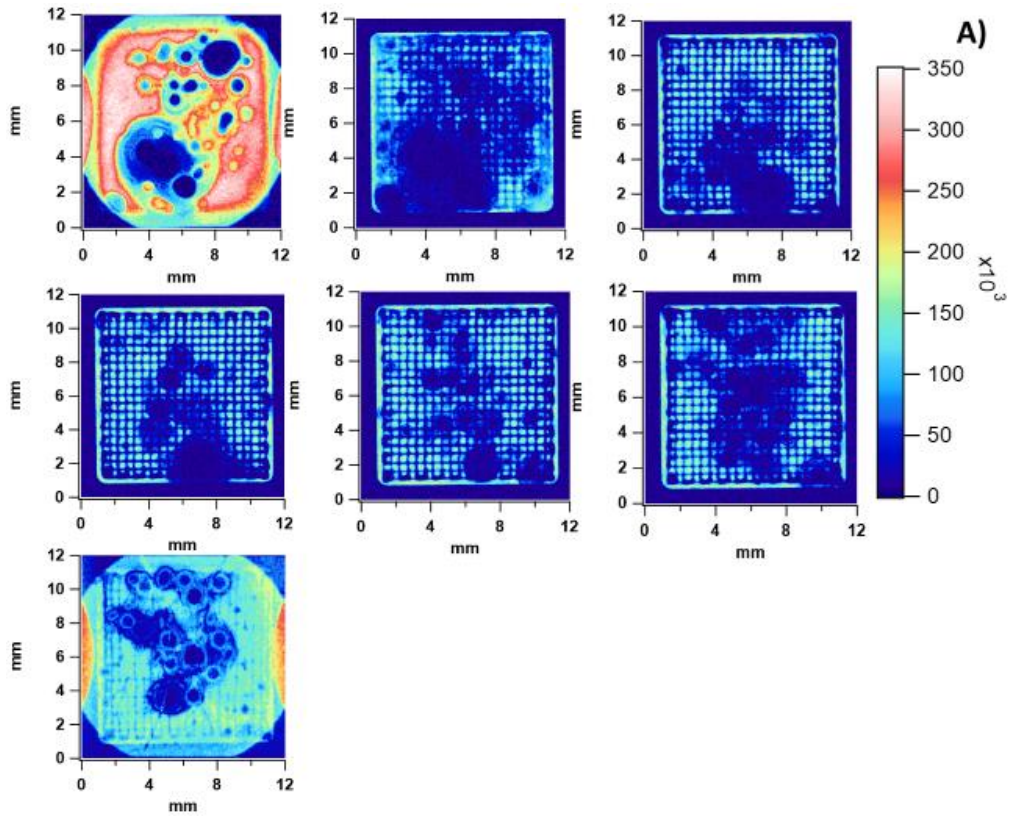


Figure 6-9 Velocimetry map of cell seeded scaffold grown in static culture for 14 days, and MR images of the same scaffold. Highlighted on the velocimetry map (left) is the largest impediment of flow, represented as a large area where velocity is 0 mm/s. MR images [241] acquired with a spin echo pulse sequence show the sagittal and axial projections of slices that show dense areas of cells that correspond with the location of the area of no flow.

NMR and MRI velocimetry mapping was used as a method to evaluate the differences in flow between a blank porous scaffold, and scaffolds that have been cell seeded and cultured for an extended period. Results comparing a blank scaffold with a 14 day cultured scaffold, the first most evident difference is the presence of a zone of no flow visible on the upper edge of the scaffold (Figure 6-6) as well as some smaller but still visible areas that have zero flow. MR images taken from the same scaffold using a spin echo pulse sequence (Figure 6-9) to identify cell location show that the blank voids of flow in velocity mapping can be correlated to sliced images taken from the same location, in which iron oxide labelled cells also show as large blank areas, in this case void of signal.

In Figure 6-7 and Figure 6-8 velocities measured as a peak velocity from within each individual pore and collated to show the distribution of recorded flow velocities and the overall average compared to a blank cell free scaffold. Histograms (Figure 6-7) show there is a tendency for higher moving flow in the blank scaffold, whereas the cell seeded scaffold has a distribution skewed left slightly, more toward to the lower velocity measurements. This is

reflected in the average velocity of each scaffold (Figure 6-8) in which the 14 day cultured scaffold recorded a significantly lower average velocity across all pores. In the cell seeded scaffold the average velocity was lower than that of the blank scaffold (Figure 6-8), to a level that was statistically significant, and values never surpassed 2 mm/s unlike in the blank scaffold, which tended to record higher peak velocity values. This indicates that the presence of cellular material within pores is restricting the freedom of flow and thus slowing it. Around the large area of no flow there are one or two pores which exhibit a much higher velocity which is expected as an area of blocked pores will increase pressure in surrounding areas. However, in other pores where it is known from imaging that there is the presence of cells, but the channel is not blocked entirely, this seems to have the effect of just restricting and slowing fluid flow.



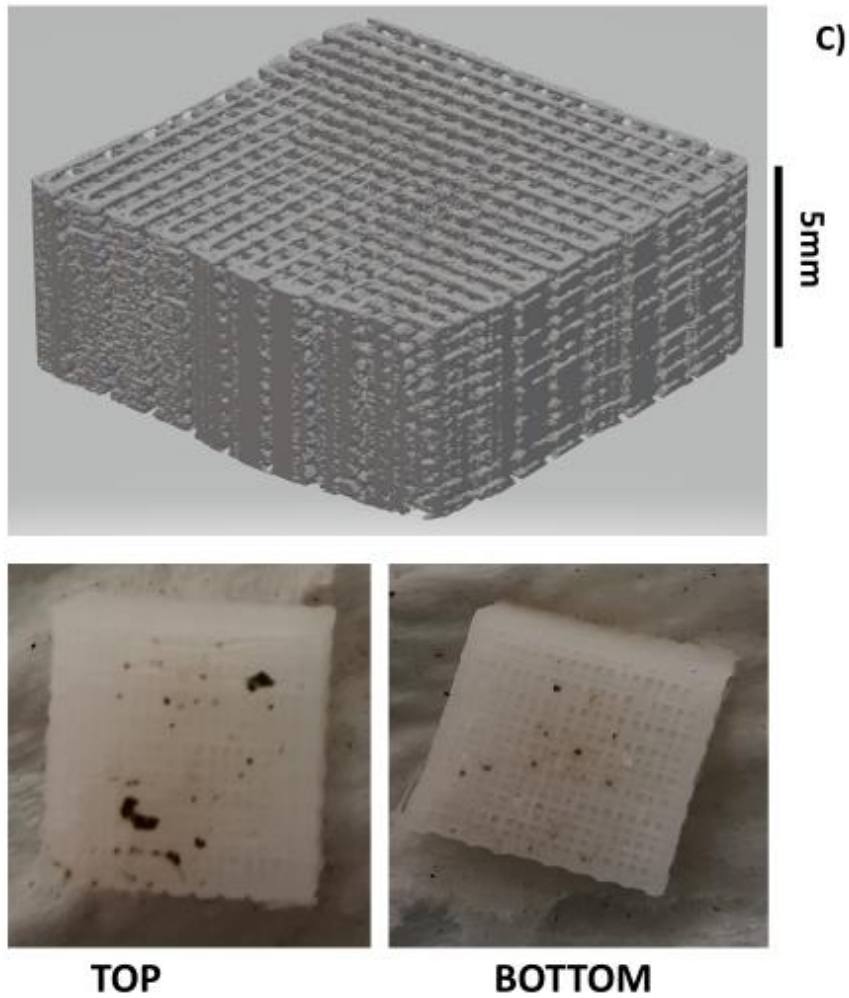
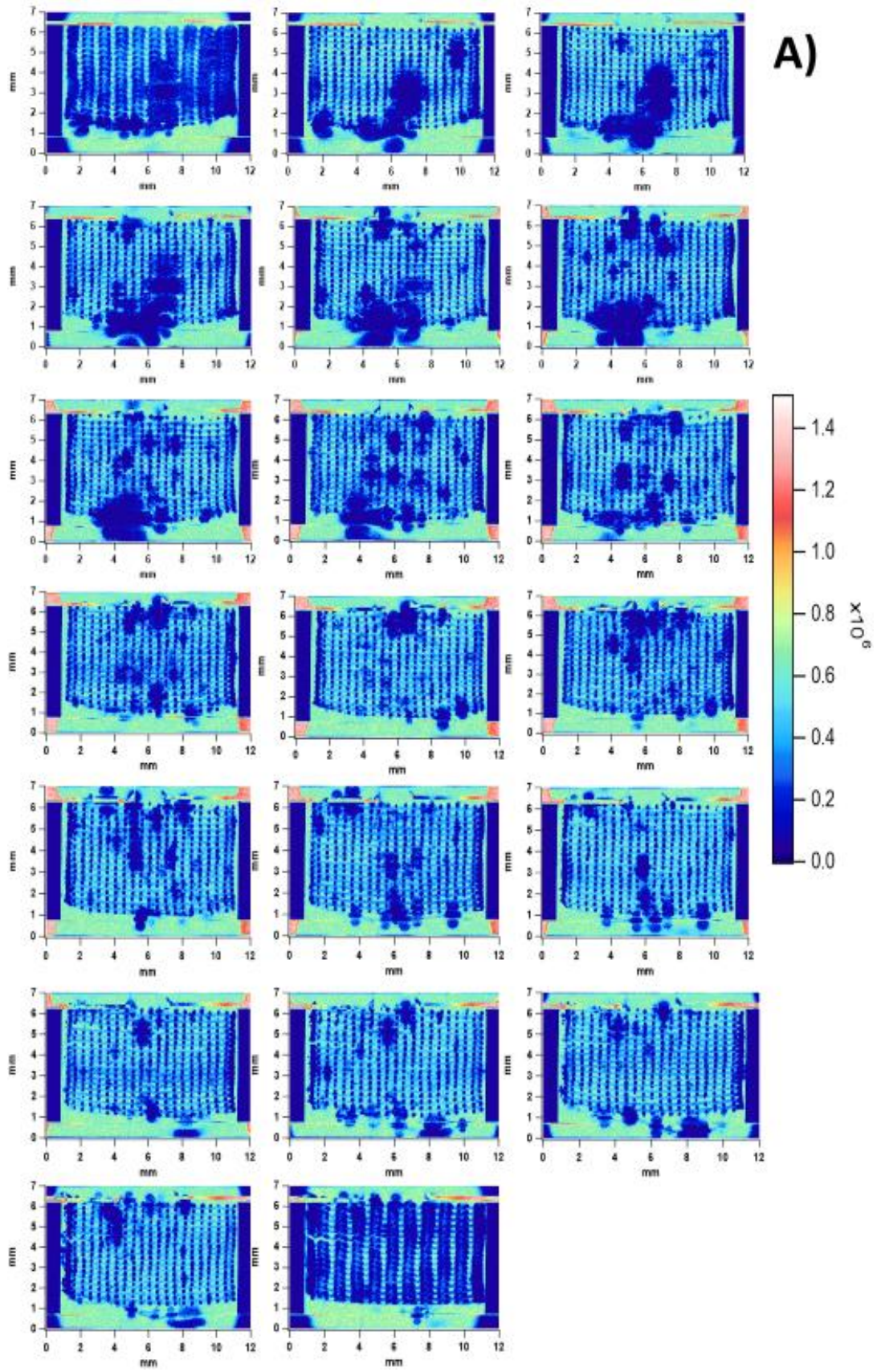


Figure 6-10 As displayed in the previous chapter, cell seeded scaffold that cells have been pre labelled with magnetic nanoparticles, seeded at 1×10^6 per scaffold and then cultured for 14 days in static conditions. A) Gradient echo 1mm sliced images and B) spin echo 1 mm sliced images to visualise labelled cell location within scaffolds. C) Schematic of scaffold and images showing clustering of labelled cells on outer surfaces of scaffold.



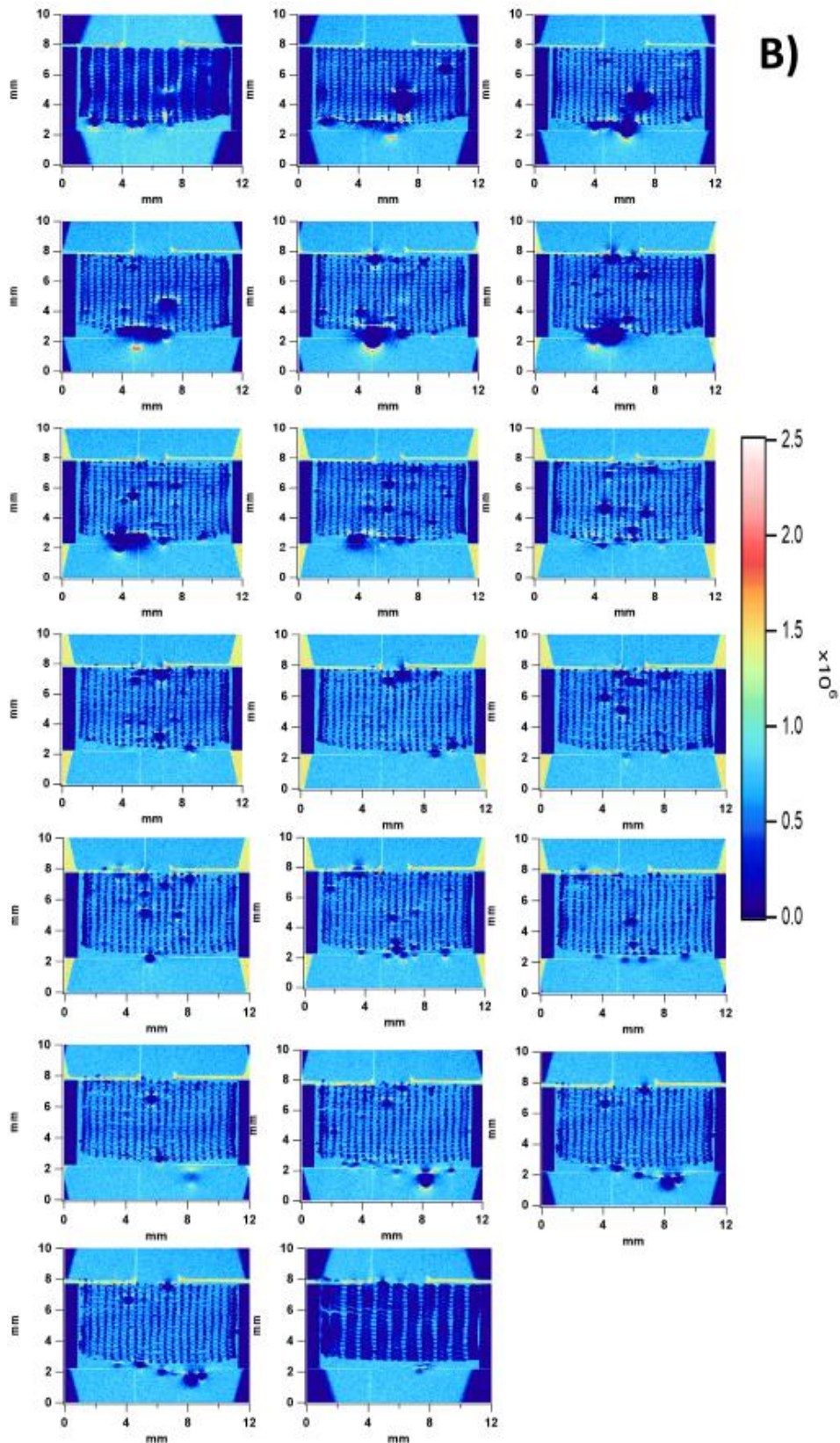


Figure 6-11 Signal intensity MR images from cell seeded scaffold cultured for 14 days in growth media under static conditions imaged using different MR image acquisition methods A) Gradient echo image acquisition and B) spin echo image

acquisition of sagittal slices showing locations of labelled cells on scaffold from which velocity was mapped.

MR images of the same cell laden scaffold show sliced in axial (Figure 6-10) and sagittal (Figure 6-11) directions, using spin echo and gradient echo images, clearly display the presence of iron labelled cells. Labelled cells using superparamagnetic iron oxide nanoparticles cause cells to act as a negative contrast by reducing MRI signal intensities such that they appear as areas of no signal in a scaffold, which has been filled with a high signal intensity proton dense fluid like water [273, 274]. Figure 6-10 and Figure 6-11 show clearly that cells occupy large portions of the scaffold in both gradient echo and spin echo images. Gradient echo imaging is much more sensitive to magnetic field inhomogeneity caused by iron containing nanoparticles, such that surrounding areas of water are distorted, as MRI relies on a homogenous static magnetic field to accurately reflect the locations and dimensions. However, spin echo imaging can be used to eliminate these field inhomogeneity due to a refocusing pulse and show a more accurate location and dimension of magnetic susceptibility artefacts without the surrounding distortion [287]. Therefore, both methods were used to image cell-seeded scaffolds, gradient echo to show the magnetic susceptibility effects of the labelled cells and then spin echo to recover that lost signal to reflect the actual dimensions of locations of labelled cells. Cell location and variations in flow, certainly for the largest visible area of zero flow within the pore matrix can be corresponded with the largest area of cells. The largest cell cluster shown in Figure 6-9, present in both axial and sagittal MR image projections. For this scaffold, it appears cell are in large clusters as opposed to dispersed evenly throughout the structure. It has been found that magnetic nanoparticles, that use a dextran coating, as is the case in this can result in an increased rate of aggregation of MNP's when cultured with FBS which is attributed to agglutination by serum components [344]. Large clusters of labelled cells are visible in this system, they can be seen on the surfaces of scaffolds in Figure 6-10 C. Clustering of cells increased the number of cells retained in the scaffold during seeding as evidenced by the much higher seeding efficiency (Figure 6-12). Cells appeared to preferentially attach to the upper surface they were deposited onto and given there increased size compared to single cells were less likely to be washed straight through large scaffold pores. This clustering, although does not

aid a homogeneous distribution of cells, resulted in a higher cell seeding efficiency. It is well established that high seeding densities in 3D porous structures for tissue engineering is beneficial for cell-cell interaction, cell differentiation behaviour and overall tissue formation [345, 346]. At this time in culture, 14 days post seeding, it does not appear that in static culture the cells have achieved migration to the most central regions of the scaffold in a great degree so it is unlikely that this seeding method, despite increased efficiency would be beneficial for homogeneous tissue formation.

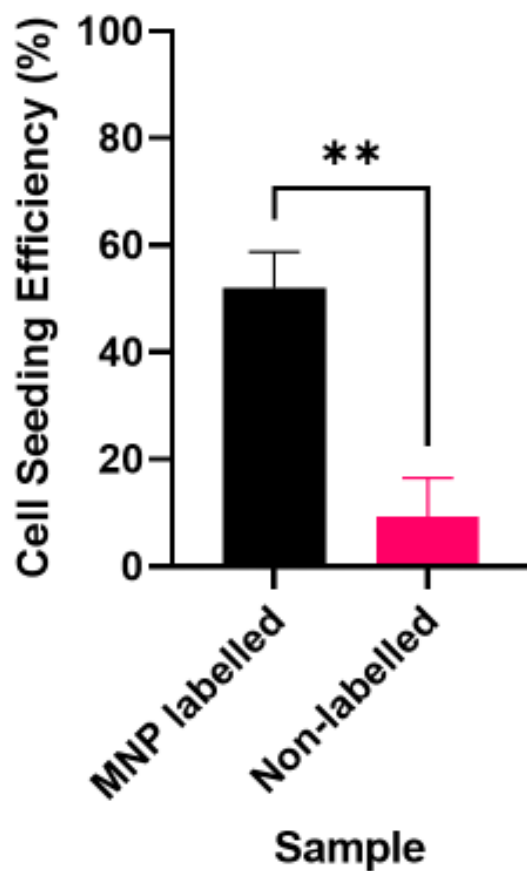


Figure 6-12 Cell seeding efficiency of cells labelled with magnetic nanoparticles compared to unlabelled cells seeded with the same seeding method onto identical scaffolds. Scaffolds were seeded and left for 3 hours to attach before cells were harvested, and DNA was quantified and compared with DNA content of total cell suspension. ** $p < 0.002$ (n=3)

In the case of this experiment however, a scaffold with a high cell seeding efficiency that has been cultured for 14 days does provide a scaffold with obvious cell growth occupying pore space, even if not homogeneous. Quantifying the overall effects of this on peak pore velocities using MRI velocimetry shows that, outside of the areas of complete no flow, there is a general tendency for flow velocities to be lower than the values recorded in a blank scaffold. Under these conditions, the scaffold was cultured in growth media, which facilitates good levels of MSC proliferation [347]. The addition of growth factors to culture media, including TGF- β 1 has been investigated and shown to enhance chondrogenesis [266]. Differentiation of MSCs and enhanced deposition of extra cellular material, made up of different molecules including sulphated glycosaminoglycan's, collagen fibres and proteoglycans will present a different flow environment within the scaffold. Therefore, to investigate this, 3D porous scaffolds that had been grown in static culture using TGF- β 1 containing media for 28 days was used in the same NMR and MRI velocimetry experiments.

Results of mapping the velocity across pores in a scaffold after 28 days in culture with chondrogenic media compared against a blank scaffold free of cells (Figure 6-13) show no obvious areas of blocked pores or restricted flow due to cell activity. However, quantifying velocity values shows that the average velocity in the cell seeded scaffold was significantly lower than in the blank scaffold (Figure 6-14), with the maximum velocity recorded never exceeding 1.6mm/s, unlike the blank scaffold which recorded velocities as high as 2.6 mm/s. The histograms of each data set shown in Figure 6-15 show a skew in the data towards the left for the cell seeded scaffold, indicating more slow moving flow in the pore channels compared to the blank scaffold.

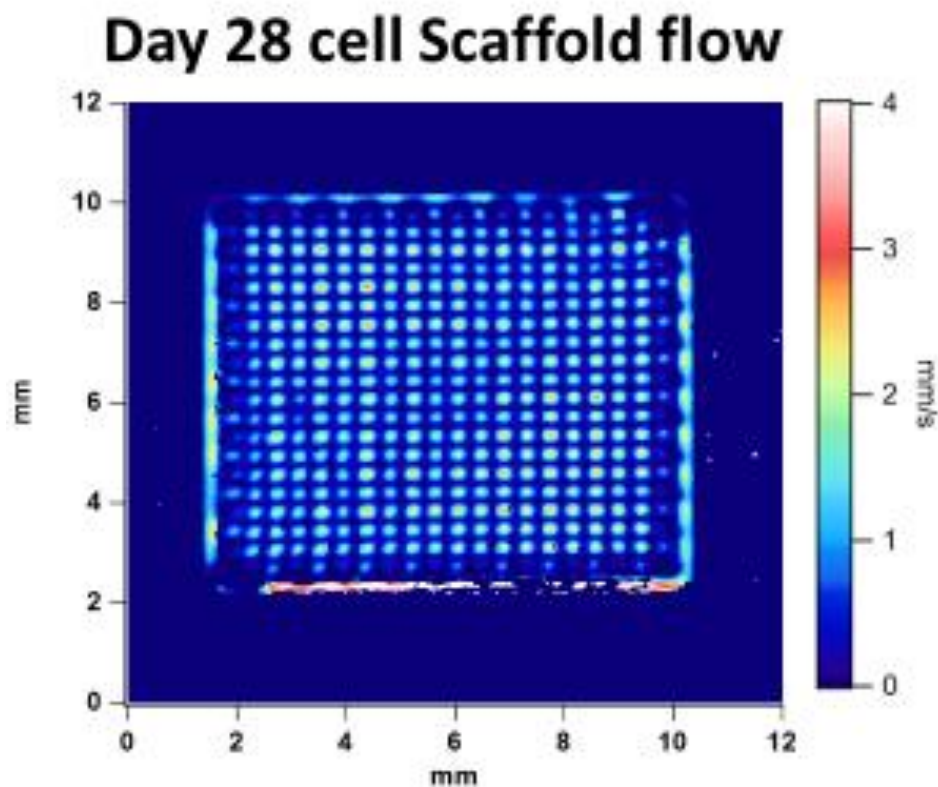
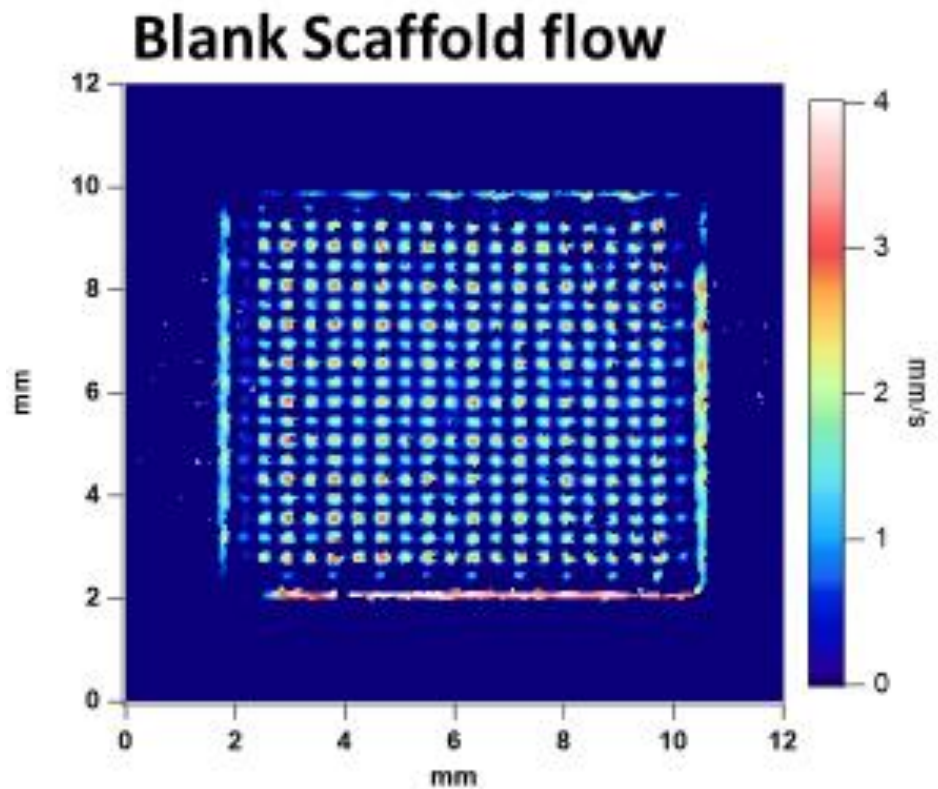


Figure 6-13 Bulk measurements of velocity to produce velocimetry maps showing distribution of flow velocity through scaffolds without cells (top), and cultured with cells for up to 28 days with chondrogenic media (bottom). Velocity was measured using NMR and MRI velocimetry methodology.

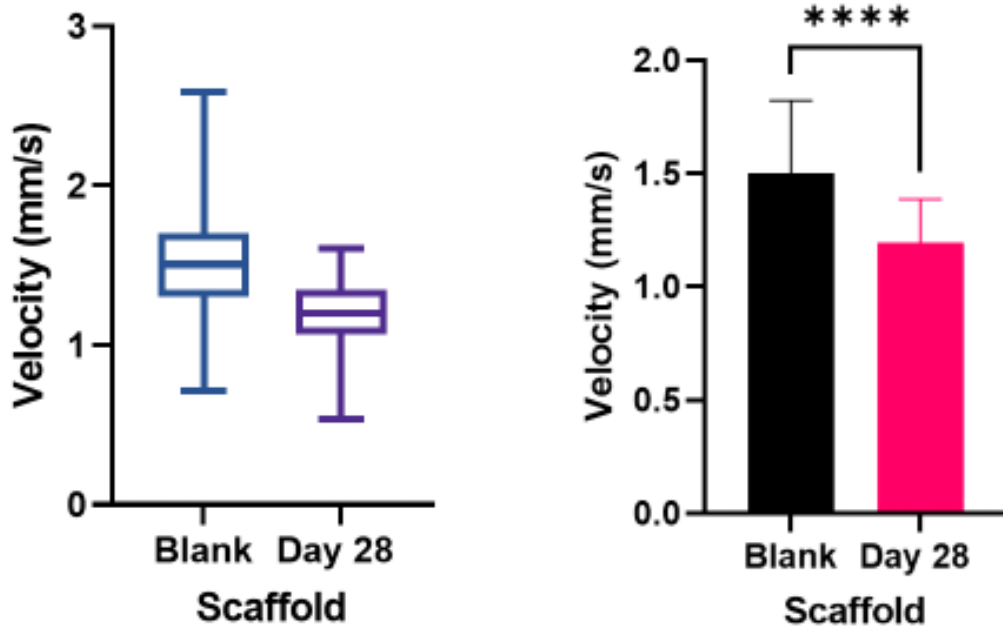


Figure 6-14 Box Plots showing distribution of velocity and average velocity \pm standard deviation of flow through scaffolds without cells, and cultured with cells for 28 days with chondrogenic media. **** $p < 0.0001$ ($n=3$).

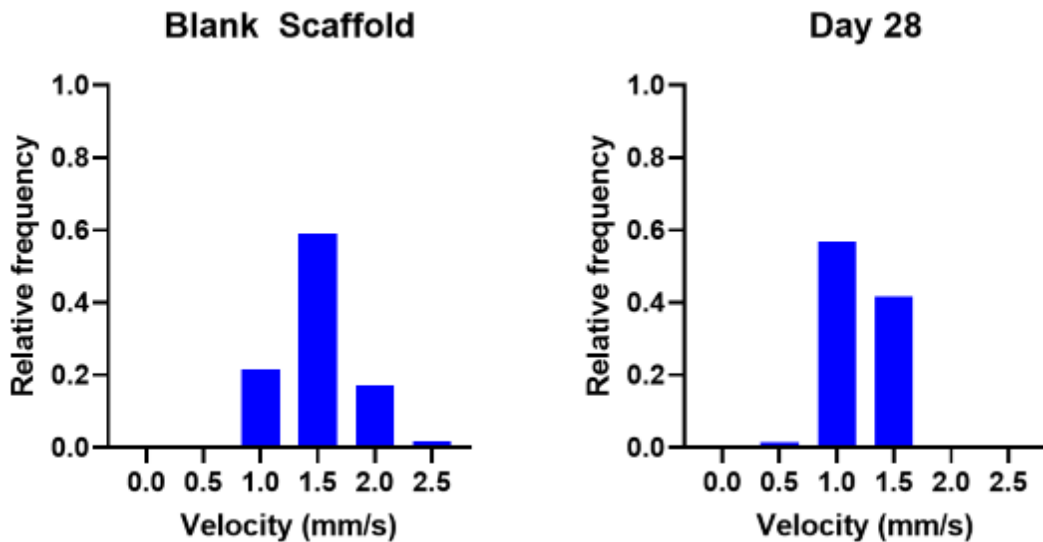


Figure 6-15 Relative frequency of peak pore velocities measured in scaffolds. The blank scaffold shows peak recorded velocities for a cell free scaffold. Day 28 shows peak recorded velocities for a scaffold that has been cultured under static conditions for 28 days in chondrogenic media.

In the case of this scaffold, assays had shown there was good evidence of cell proliferation (Figure 6-2) and sGAG deposition (Figure 6-4) indicating the differentiation of MSCs and subsequent ECM formation. It is expected that formation of tissue in scaffolds as they mature *in vitro* will reduce permeability as cells and ECM begin to occupy the pore space which will decrease the pore size. A decrease in a channel or pore size is associated with increased pressure drop and fluid velocity which is not the case here. However, in this scenario it is not as straight forward as a decrease in pore size, the presence of cellular material on struts changes the boundary conditions between the fluid and the solid matrix. When fluid flows through a channel, energy is spent maintaining the flow, but internal friction and changes to boundary conditions can cause energy loss. Sudden or gradual change of boundaries results in changes in magnitude, direction or distribution of the velocity of the flow [348]. This loss is termed head loss, which is the sum of elevation head, velocity head and pressure head, and is proportion to the length of the channel, the square of the velocity and the friction factor. Given cell channels were not blocked, and fluid still moved through but at a slower rate compared into a blank scaffold, it could be the presence of cells along struts effecting fluid flow in this manner. This effect is also seen when in incidences of biofilm growth, when growing on the interior of pipe walls, biofilm replaces the solid interface of the pipe wall with a pliable biofilm, which result in energy losses from flow fields [349].

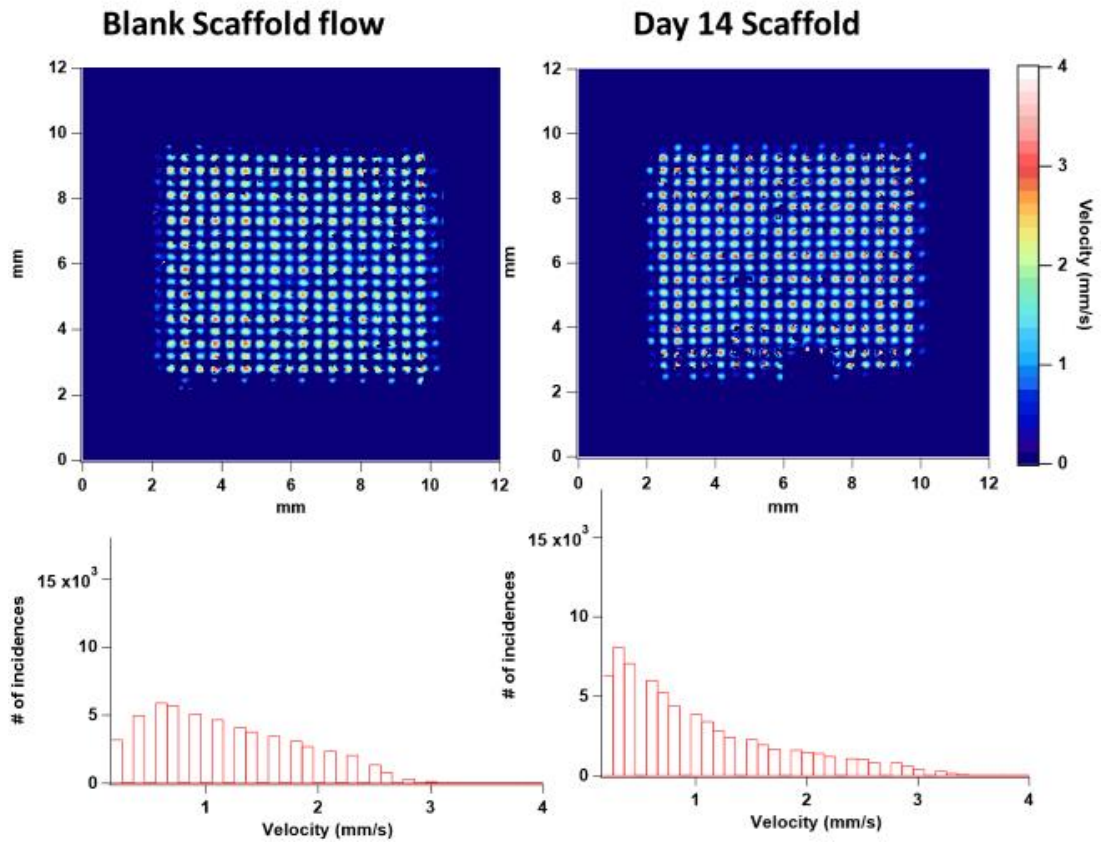


Figure 6-16 Blank scaffold and scaffold cultured for 14 days in static conditions using growth media. Histograms show the distribution of velocities taken from all pixel in velocity map, including peak pore velocities and velocities at pore walls.

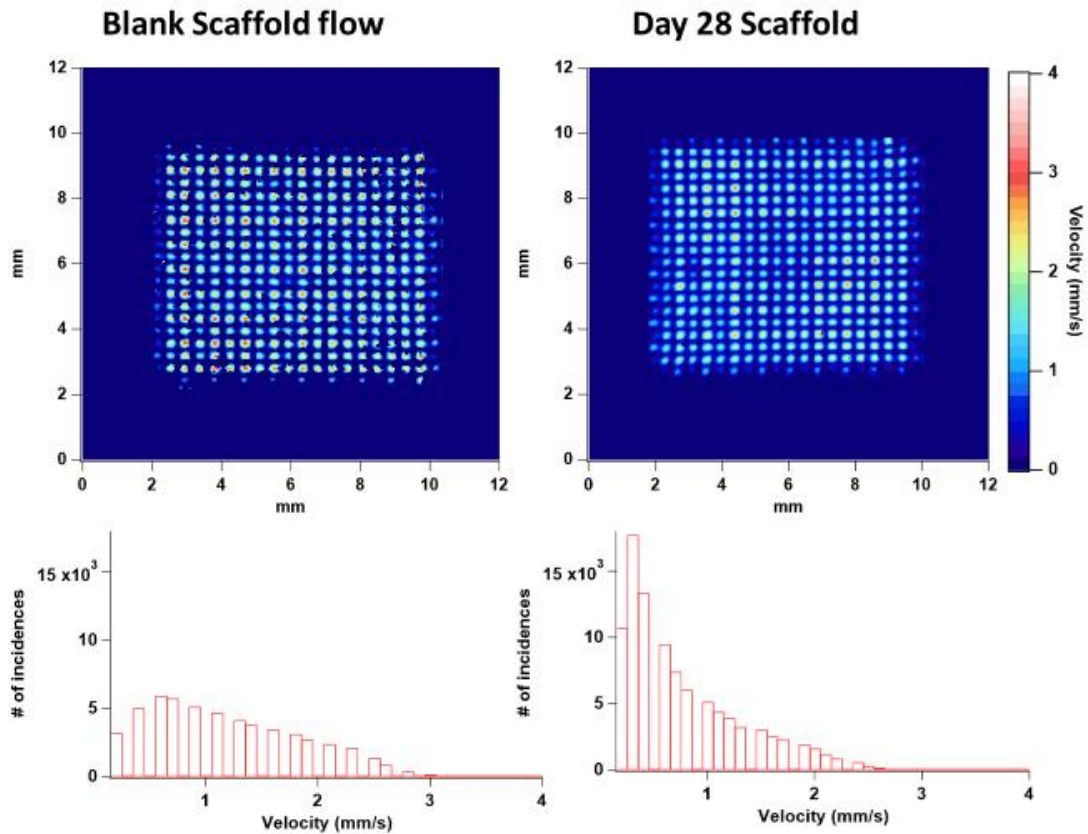


Figure 6-17 Blank scaffold and scaffold cultured for 28 days in static conditions using chondrogenic media including TGF- β 1 growth factors. Histograms show the distribution of velocities taken from all pixel in velocity map, including peak pore velocities and velocities at pore walls.

In Figure 6-16 and Figure 6-17 velocities over the entirety of the scaffold were recorded, as opposed to just the velocity at which flow peaked within pores, instead including all recorded values, such as the values at pore wall interfaces between the scaffold structure and the perfused fluid. Similar to peak values of velocity, there is a skew left towards lower velocities in both scaffolds that have been cultured with cells compare to the blank scaffold. This skew is much more prominent in the scaffold that had been cultured for 28 days in chondrogenic media (Figure 6-17). However, unlike the day 14 scaffold, this scaffold did not have appear to have any blocked pores, or areas of zero flow, which in the case of the other scaffold caused surrounding pores to have much higher velocities of flow.

It could also be argued, that given there is gaps between the edges of scaffold and the flow chamber wall, this could allow velocity to be diverted through this gap to alleviate increased

pressure as a result of constricting pores. However, this gap is also present for the blank scaffold, and there is no distinctive differences in velocity between them, both recording values between 3 and 4 mm/s. If there is no increase in velocity in this area between the two types of scaffold then it is unlikely this area has become a more preferential area for fluid to flow through to alleviate an increase in pressure and shear forces as a result of cells blocking pores. Taking only the velocities from these regions of faster flowing gaps, in both blank and cell seeded scaffolds show that the cells within scaffolds don't cause faster velocities to flow through the gaps, indicating the similar over distribution of flow in both types of scaffolds (Figure 6-18 and Figure 6-19). This indicates these areas do not play a significantly different role in the flow velocity patterns recorded between blank scaffolds and scaffolds where cells are present.

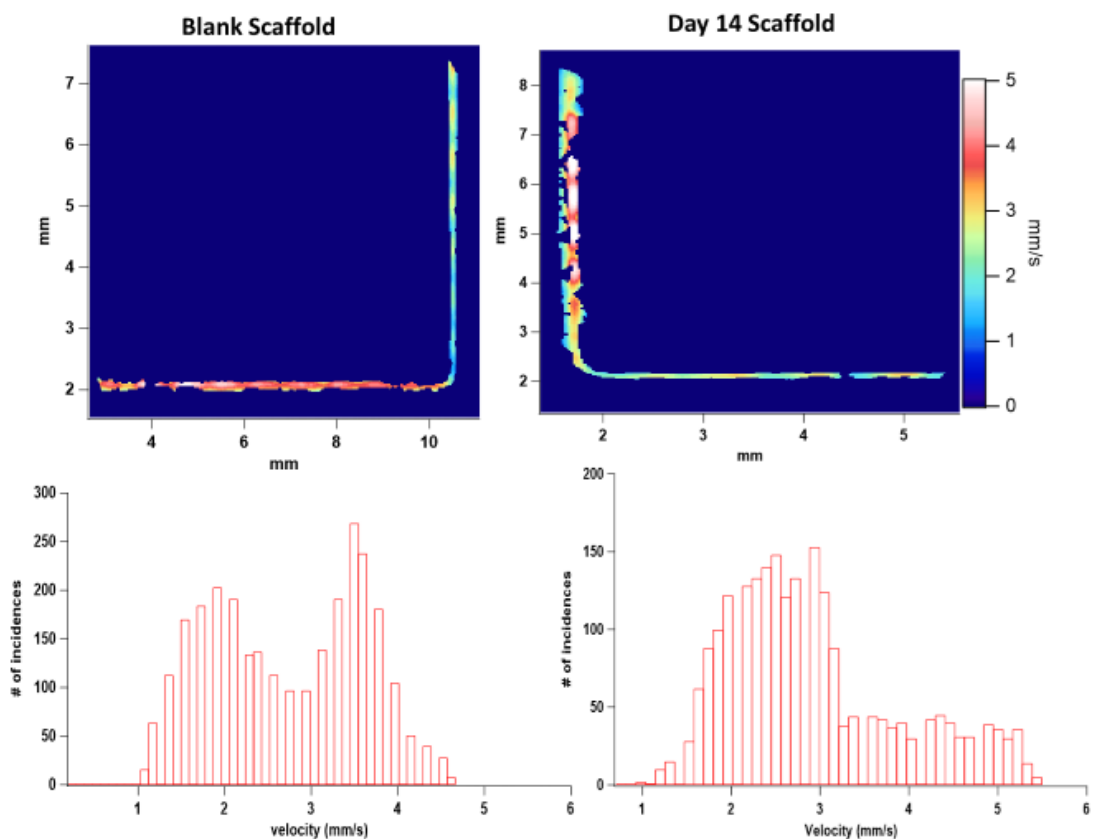


Figure 6-18 Velocities extracted from each pixel in gap regions between scaffold wall and chamber wall, comparing range of velocities between blank scaffold and 14 day cell seeded scaffold cultured under static conditions in growth media.

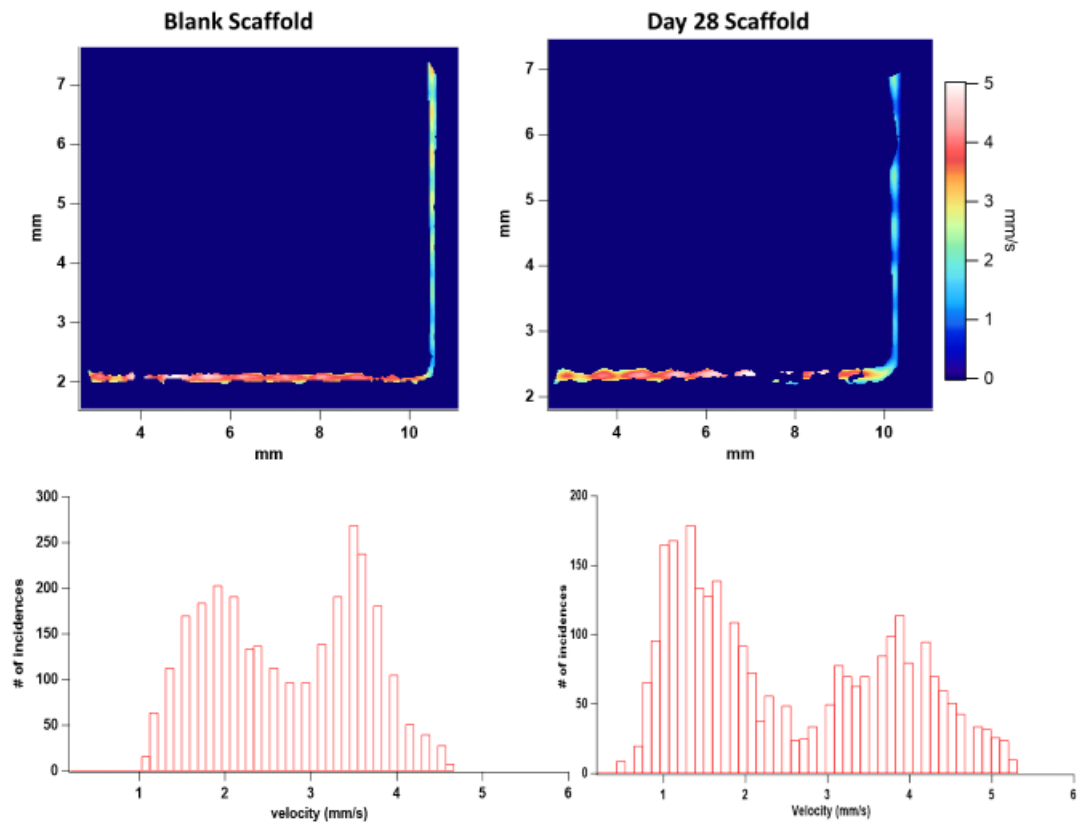


Figure 6-19 Velocities extracted from each pixel in gap regions between scaffold wall and chamber wall, comparing range of velocities between blank scaffold and 28 day cell seeded scaffold grown under static conditions in chondrogenic media.

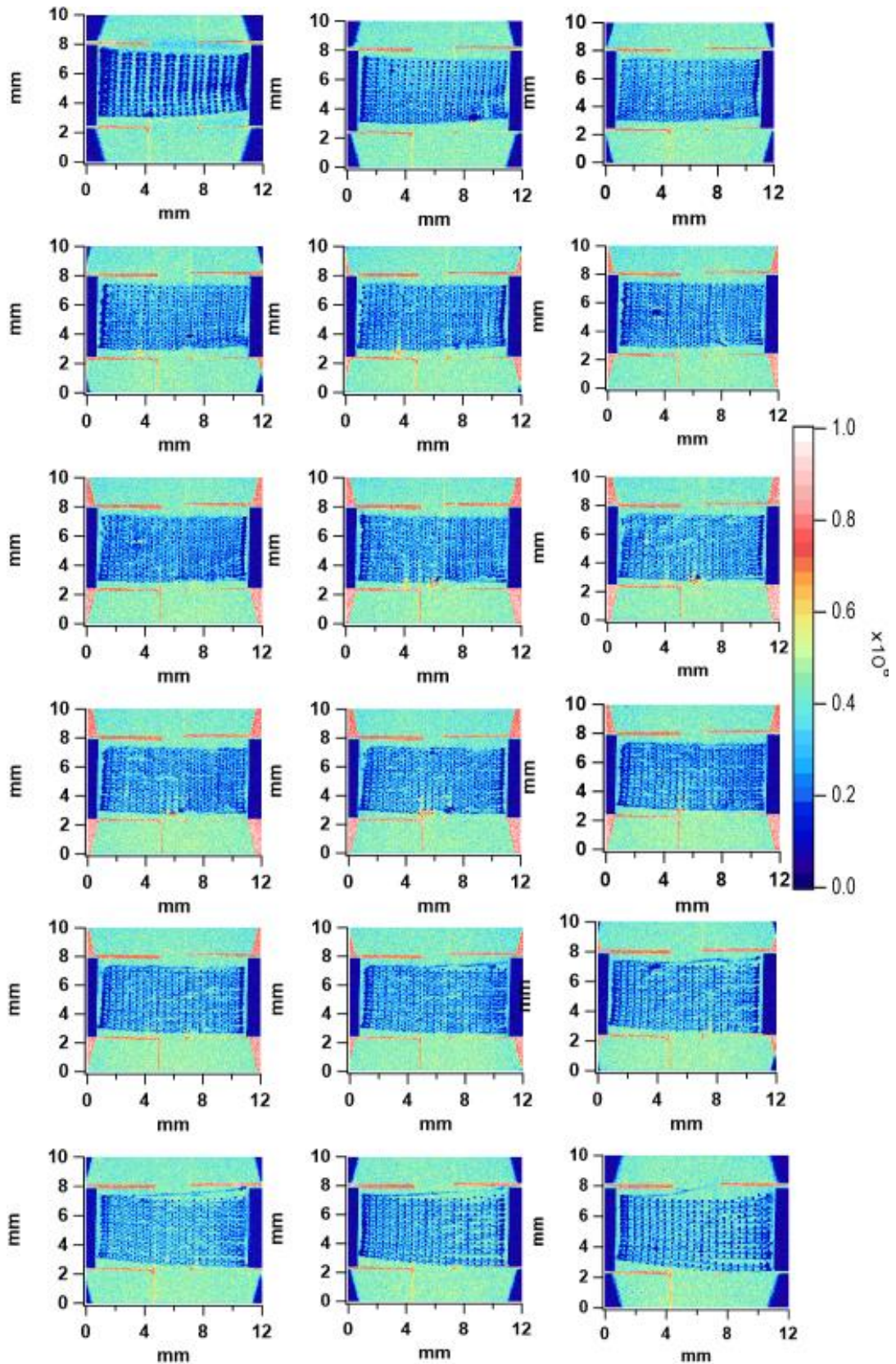


Figure 6-20 Sagittal sliced spin echo images acquired from cell seeded scaffold, cultured for 28 days in chondrogenic media. Images acquired every 0.5 mm as slices with a 14 ms echo time and 512x512 pixel array.

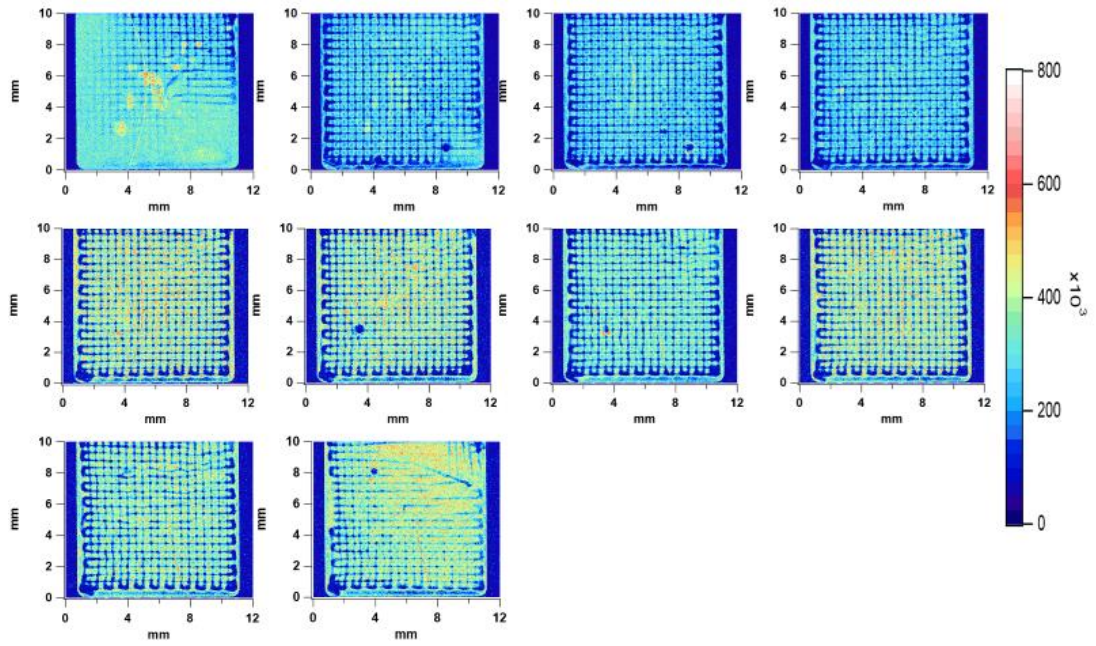


Figure 6-21 Axial sliced spin echo images acquired from cell seeded scaffold, cultured for 28 days in chondrogenic media. Images acquired every 0.5 mm as slices with a 14 ms echo time and 512x512 pixel array.

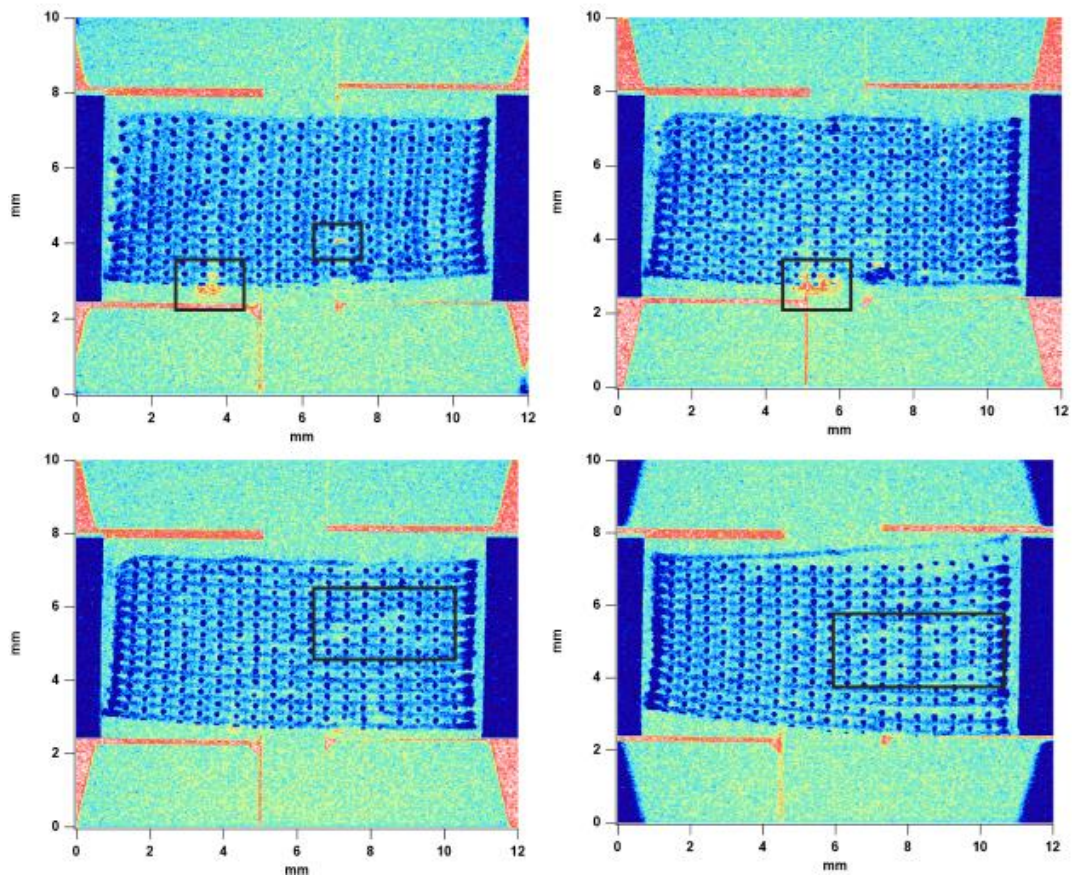


Figure 6-22 Sagittal slices selected from Figure 6-20 to more clearly show brighter areas in highlighted regions which indicate the presence of cellular material. Images acquired using spin echo method to produce 0.5 mm slices with a 14 ms echo time.

In the 28 day cultured chondrogenic scaffold, the cells had not been labelled, but could still be imaged by utilising the effects of diffusion of water in the system. Diffusion driven displacement of water can be encoded in the MRI signal by spatial and temporal variations of the magnetic field. This means in areas of faster diffusion, MRI signal attenuation is more pronounced when gradient pulses are applied [350]. In this scaffold there is free water filling the channels of the scaffold and water contained within the cell membranes, which gives rise to differences in displacement of water molecules, and in turn a signal contrast between cells containing water and free water, in which the cells will appear brighter due to less signal attenuation. The contrast is not as great as seen with the labelled cells, but areas of cells are still visible using this methodology (Figure 6-23) and cells benefit from no cell manipulation for labelling being required. In addition to this, given polymer also appears as dark regions of

signal void when imaged, like magnetic nanoparticles, imaging cells without labelling would be beneficial for providing areas of brightness to contrast polymer networks, particularly for scaffolds with smaller pore sizes. This can be seen in Figure 6-24 which highlights that only do cells appear brighter, but these areas can be quantified in terms of signal intensity. Using MRI to image unlabelled cells has been performed on hydrogels using diffusion weighted, T2 and Magnetisation Transfer NMR signals to quantify cell density [351]. Results showed that cell density within hydrogels could be imaged using all three methods of signal acquisition, with increasing cell concentration either reducing or increasing signal depending on experiment time. However, these methods were applied to hydrogels only, and not solid polymer networks, in which the polymer provides areas of void signal. Abarateigi [308] imaged cells in polymer porous scaffolds, and similar to results in this study observed higher signal intensity in cells compared to that of the fluid phase and the signal of the scaffold. This imaging method for this study validated that there is cell in growth into pores cells, and that the effects of this should be considered when looking at differences in velocity regimes. Cell location was also reconstructed using Micro-CT which shows the distribution after 28 days (Figure 6-3).

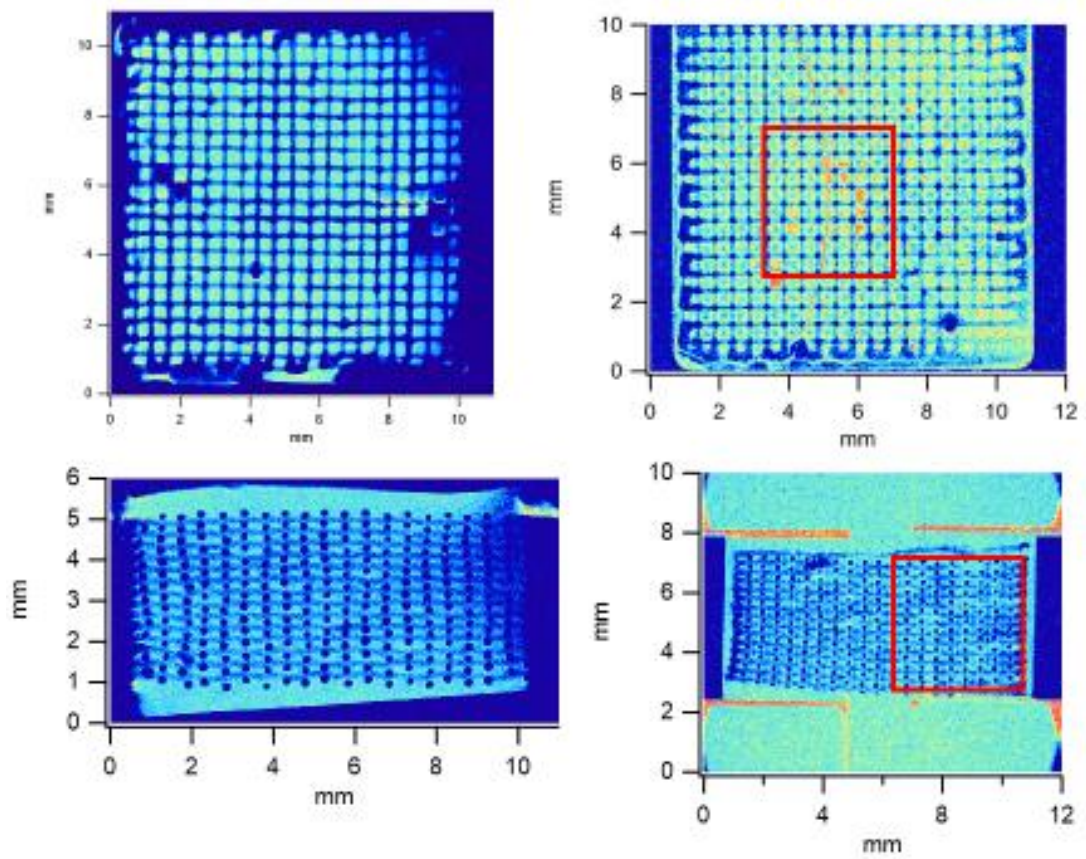


Figure 6-23 MSME images of both blank and cell seeded scaffolds grown for 28 under static conditions in chondrogenic media to compare regions of cells against those without.

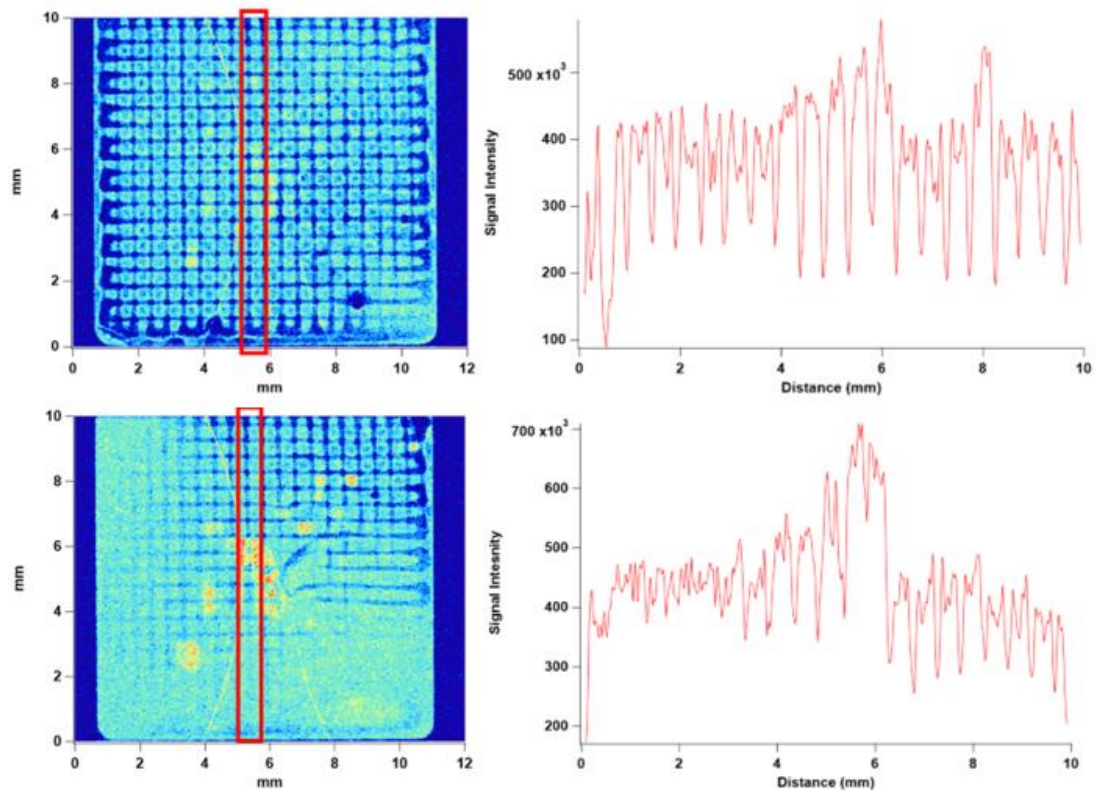


Figure 6-24 Individual MR images of axial slices taken from a scaffold cultured for 28 days in static conditions using chondrogenic media. Slices show profiles of highlighted pores in relation to signal intensity to demonstrate increased signal in presence of cells compared to other areas.

Imaging cell location is vital for understanding any relationship between cell behaviour and any resultant forces in a dynamic environment. The level of shear stresses applied to cells can influence the strongly the success of scaffolds *in vitro*. Different magnitudes of shear stress has successfully been applied to MSC based strategies for both cartilage and bone tissue engineering using perfusion bioreactors, and within cartilage tissue engineering alone different magnitudes have resulted in distinct different phenotypes. Differences between scaffold and bioreactor design in each study make it difficult to quantify exactly the underlying molecular signalling involved. Increased levels of sGAG levels indicate increased deposition of extra cellular matrix following MSC differentiation, but how far this is a result of mechanical loading is unclear. Although it has been shown that external mechanical forces are associated with increased sGAG accumulation, it has also been shown that TGF β alone can lead to a much greater increase of sGAG content [352]. In some cases flow perfusion has even been shown to be detrimental to the differentiation of MSC's, diminishing the

release of sGAG [6]. This study showed, that with flow perfusion rate of 1.22mL/min applied to MSC labelled 3D printed porous scaffolds, resulted in overall lower release of GAGs when compared to static samples after 28 days in culture. An increase of early hypertrophic markers and decrease in collagen type II was also detected. Therefore, establishing a system that optimises flow induced forces for cells is vital for cell survival and optimal tissue formation. However, there are a number of factors that influence the flow patterns.

Designing scaffolds for cell culture in perfusion bioreactors must take into consideration a number of factors including mechanical performance, surface area for cell attachment, and a pore size to allow effective perfusion of media. Computer models of flow have shown how far changes in some of these design considerations, including pore size, pore interconnectivity and geometry can alter flow regimes [7, 12, 182, 353]. Although CFD is an effective way to produce predictions that take into account a lot of complexities in bioreactor and scaffold design, it is more difficult to accurately however to take into account the complexities of cell behaviour over an extended period of dynamic culture. Proliferation and growth of cells, deposition of extra cellular matrix components, secretion of various metabolic by-products and proteins are all significant changes occurring in real time. The magnitude and rates at which these happen are much more difficult to reliably predict and will depend on a number of experimental factors including seeding density, flow conditions and length of culture time.

In velocity mapping for both types of scaffolds, there was visible and quantifiable differences in velocity compared to blank scaffolds, which experimentally at least proves that cell culture changed velocity profiles over time. Currently research to directly compare cell growth and fluid flow perturbation is almost entirely carried out computationally. Many CFD models that have included conditions to try and account for cell behaviour have been carried out using a number of methods. Volume averaging approaches, which consider the porosity and permeability of scaffolds to be time dependent, assuming that cell growth and shear forces are distributed homogeneously throughout the scaffold, and that there is a uniform increase in both over time [354, 355]. However, in culture cell growth rates and the distribution of cells and shear forces does not occur in perfect homogeneity, so this fails to accurately capture

the interactions between biological components and fluid regimes. As seen in both scaffolds used for velocity mapping in this experiment, neither provided a good homogeneity of cell growth. Both scaffolds differed in initial seeding densities and resultant distribution and number of cells, but a method to enable visualisation of this fact would better inform modelling parameters, or experimental design.

Moving boundary conditions, in which the boundary changes in line with predicted cell and tissue growth to better reflect the biophysical environment within reactors has been incorporated in to CFD models as another method to predict behaviour at the interface between biomass (made up of cells and ECM) and the culture medium. One study assumed the interface moved with a velocity calculated as a function of oxygen concentration and shear stress [356]. In this study, although considerations were made for the complex nature of changing boundary conditions, the study was still limited however for predicting behaviour in 3D scaffolds, as it only modelled a small subsection of the scaffold in culture for just 5 days. As evidenced in this current study, cell deposition tended to form closer to outer edges, and although this is likely due to poor mass transport of nutrients into the scaffold centre during static culture, it still showcases the importance of viewing the scaffold as a whole to get the truest picture of the successes and limitations of individual culture experiments.

For mapping velocity maps, scaffolds and MSCs were either cultured in growth media alone to promote primarily cell proliferation, or cultured with chondrogenic differentiation inducing media. After 14 days in culture with growth media, cells appeared to cause more pore channel blockages when it came to liquid perfusion. After 28 days in chondrogenic media, although the effect of overall slower velocity was recorded in both samples, it was to a higher degree in the chondrogenic sample. This could indicate that differentiation and ECM deposition had a bigger effect on the flow velocity. However, given each sample had very different seeding efficiencies and length of culture time it is difficult to directly compare the two results, and more experiments would need to be done to properly establish if this was the case. Models have gone far enough to incorporate pore filling with cells and ECM

formation at varying degrees until complete pore closure, going beyond cell growth in 2D along struts to predict behaviour when cells bridge across pores, termed 3D growth [13]. This resulted in a significant increases in shear stress predictions for cells located in the microporous neotissue compared to those in the macroporous scaffold, warranting the need to expand models to include this degree of pore filling. However, in this model the actual permeability of the newly formed porous tissue is unknown, limiting the applicability of estimates in shear rate increases. Similarly, Zhao [14] modelled pore filling with cells and ECM, in combination with a decreasing flow rate inversely proportional to culture time. The models used assumptions that cells only grew flat on the scaffold surface without bridging across the increasingly smaller pores, and that cell and ECM were homogenised as one material.

These models have taken into consideration changes in the porous medium, and are effective at showing how potential scenarios could be detrimental to achieving an ideal range of shear forces for *in vitro* tissue culture. Limitations however are clear when predicting cell behaviour to achieve the most precise modelling, and experimental data is required to further knowledge, as it has been shown with the results in this study, the overall velocity profiles did not align with any of the aforementioned model predictions. The models referenced here all predict the cell and ECM growth into scaffold porous regions would increase velocity due to restricted pores and in turn increase the shear stresses. Zhao [14] used a model that predicted to effectively mitigate the effects of this increase in shear stresses, the input velocity would need to be reduced linearly with culture time. Conversely, in this study the scaffolds cultured with cells compared to blank cell free scaffolds, velocity within pores decreased, such that if these model predictions of requirements to reduce input velocity were applied it is unlikely to continue to provide appropriate mechanical stimulus. This supports the need for experimental validation to truly reflect behaviours or results it is almost impossible for models to accurately predict without this prior experimental knowledge. Thus, modelling shouldn't be used as a unilateral approach to investigating dynamic tissue engineering experiments, and should be used alongside experimental validation.

Experimental measurements of flow for *in vitro* 3D tissue engineering models has proven difficult, researchers are keen to avoid invasive or destructive techniques that are limited to only post culture analysis, and avoid the addition of tracers that may not be transferrable to *in vivo* applications. MRI and NMR offer a real alternative to such invasive methods, in respect to both imaging and assessing velocity, particularly in when opaque porous structures are being used to facilitate tissue regeneration. Outside of regenerative medicine, MRI has been used extensively to characterise the properties of porous media, including fluid flow within a porous medium [236, 357-359]. Cell seeded constructs grown in bioreactors have been investigated in combination with MRI, to measure apparent diffusion coefficients (ADC) to show how cell growth in scaffold micro environments affects permeability. Initial seeding of gels did not impact the diffusion coefficient [360] but in a longer study, from day 20 to 40 a significant drop in ADC was correlated with increased MSC activity and ECM secretion [361]. MRI velocity encoding has successfully been applied in the context of tissue engineering scaffolds to cell free scaffolds to examine the heterogeneity of flow profiles in the porous architecture, and changes in internal hydrogel structure due to the application of flow [211].

Other disciplines have used MRI velocity encoding to examine the effects of random porous media, and like the scaffolds used in this current study, ordered porous media on fluid or gas flow. For example, 3D printed triply-periodic minimal surfaces (TPMS) structures, which incidentally have been considered for tissue engineering scaffold designs [362], have also been investigated by MRI and CFD to establish flow fields [363]. Ordered porous media was able to evenly distribute flow from the inlet through the channels for flow with a low Reynolds number, in which maximum velocities were at the centre of the channels which is a typical feature of laminar flow. An increase in volumetric flow rate and in turn Reynolds number led to more turbulent flow characteristics, highlighting the significance of input parameters on overall flow regimes. Results were compared to CFD experiments; the results were in good quantitative agreement, showing MRI experiments are a good tool for CFD validation. MRI velocity measurements in bioreactors to study the impact and structures of biofilms, showing that similar to cell growth within scaffolds, biofilm in a capillary bioreactor caused

perturbation effects to what was steady laminar flow in a clean bioreactor. Secondary flows emerged causing variation in the axial velocity which could be directly linked to the presence of large biofilm nodules [364]. Despite these examples, utilising velocity encoding for bioreactor and porous scaffold measurements in regenerative medicine has been largely under used. The ability to combine velocity measurements with imaging cell locations poses as a real benefit for increased understanding for bioreactor conditions and the biological response. As shown in this study, velocity with porous polymer structures, can be encoded, and the addition of cells can be accounted for through imaging and contrasting velocity maps.

6.4 Conclusion

Methods to evaluate conditions within dynamic culture environments, and in turn assess the effects these environments have on cells without destruction of scaffolds could vital for furthering understanding, and improving experimental procedures for maturing tissue engineering constructs. In this study MRI velocimetry is presented as a method to assess fluid velocity across porous scaffolds that have been cultured with cells, to make direct comparisons with unseeded scaffolds. Two scaffolds were assessed, one cultured only in expansion media, and another cultured in chondrogenic media to encourage differentiation and ECM production. Alongside this, the imaging capabilities of MRI was employed to locate cells within scaffolds prior to running flow experiments, to show the distribution of cells throughout the scaffold. Results showed cells could be successfully imaged within a porous network, both with and without cell labelling using iron nanoparticles. Velocity patterns in cell-laden scaffolds showed a trend of reducing peak velocity within pores. Predominantly, model predictions for cell growth in pores have resulted in pore constriction increasing fluid velocity, and in turn shear forces. The results of this study do not support these predictions, this is likely due to the imperfect seal between the periphery of the scaffold and the flow chamber, altering the expected flow pattern. This however still highlights the power of experimental studies alongside modelling to show how valid models are, and provide insight into less predictable behaviours systems. There is scope to carry out many more

investigations of cell seeded scaffolds grown in different conditions, and matured for longer time points to further assess effects of cells on flow fields.

7 Conclusions and Future Work

7.1 Conclusions

It is clear from the depth of research that perfusion bioreactors are a popular tool for *in vitro* culture and maturation of cartilage and bone tissues. Experimental methods to investigate the flow conditions, with the aim to understand the effect of flow on cell behaviours, have been limited. A key result of this thesis is validation of NMR and MRI velocimetry as a tool that can be successfully used to measure fluid velocity in porous biomaterial scaffolds for tissue engineering. Probing scaffolds in a way that permits non-invasive examination of the entire scaffold under perfusion and measure velocity within pore channels has previously proven difficult, and here NMR and MRI methods are presented as a valid alternative. In chapter 4, using 3D printing in conjunction with CAD allows for the fabrication of scaffolds with highly controlled pore architecture including pore size and pore geometry. By controlling the pore architecture, velocimetry mapping was successfully utilised to show how varying pore characteristics directly impact the localised distribution and range of velocities measured. This therefore showed the influence of scaffold design on resultant flow fields, and that NRM and MRI velocimetry can be used to resolve those flow fields and inform decisions of scaffold pore architecture design.

In chapter 5, MR imaging capabilities were used for the visualisation of cells within the porous polymer scaffolds. The non-invasive and non-destructive benefits of MRI present an opportunity to image the full depth of a cell laden scaffold without the need to destroy the scaffold, or in the cases of other imaging methods like Micro-CT stain the scaffold with heavy toxic metals like Osmium Tetroxide. In this study, cells were successfully imaged within the porous scaffold after 14 days of *in vitro* culture. This demonstrated the potential for

monitoring cell location and density using MRI, key to understanding cell behaviour, growth and migration in culture. The purpose of chapter 6 was to combine both of the aforementioned techniques, cell visualisation and encoding flow in porous biomaterials. Combining these two elements was proven to be key to understanding the relationship between perfused fluid, the forces it exerts and the resultant cellular behaviours. Cell location was successfully visualised, and in turn fluid velocity maps were produced, and compared to cell free structures, showing significant differences in overall velocity profiles. This presents the real potential of the use of NMR and MRI techniques to create a more comprehensive understanding of dynamic *in vitro* culture, and optimisation of tissue regeneration methodology.

7.2 Future Work

This thesis explored the role NMR and MRI methods could play in tissue engineering applications, focusing on the ability to probe scaffolds to establish local flow fields and to visualise cells cultured in the 3D polymer matrix. It has been shown that there are multiple benefits to culturing cells under perfusion when compared to static culture methods, but equally when the parameters are not optimised there is increased risks of undesired shear induced differentiation, cell detachment, or even cell death. It has been shown that there exists a need for more experimental methods to further understanding of the mechanisms in dynamic culture. However, in order to better demonstrate the benefits, and potential need for NMR velocimetry, future studies may benefit from modelling expected outcomes initially with CFD and comparing with experimental results. Prominent differences between models of culture over time under perfusion compared to experimental results would demonstrate the need for this type of analysis and may be used to further modelling capabilities. Likewise, closely matched velocity maps and modelled data, would be a powerful tool for exemplifying the accuracy of a given model. Therefore, there is good scope for the two methods to work together in unison to further improve tissue regeneration *in vitro*.

This study successfully combined cell cultured scaffolds with NMR and MRI, to not only identify cell location, but also measure the effects cell culture had on the flow fields within its pores. However, to examine the full potential of these the aforementioned techniques to monitor *in vitro* dynamic culture, it would be important to show that cell seeded scaffolds can be examined at multiple culture time points without terminating the culture experiment. In addition to this, the failed dynamic culture experiments in this thesis limited NMR and MRI examination to only static cultured scaffolds. Incorporating and applying the flow encoding and cell imaging experiments to cell-scaffolds that have been grown under perfusion would allow for more definitive links between to drawn between cell behaviour and the effects of flow.

Further to this, an important element that needs to be evaluated alongside velocity profiles is the exact shear stresses that are being exerted as a result, and in turn the relationship shear stresses have with chondrogenic differentiation. An in depth understanding of shear stress levels in cell seeded scaffolds, establishing a relationship if any between how changes in shear stresses and cellular response over the course of a dynamic culture experiment would significantly advance the optimisation of bioreactor and experiment design.

8 References

1. Murphy, C.M., et al., *Cell-scaffold interactions in the bone tissue engineering triad*. Eur Cell Mater, 2013. **26**: p. 120-32.
2. Zhao, F., et al., *Effects of Oxygen Transport on 3-D Human Mesenchymal Stem Cell Metabolic Activity in Perfusion and Static Cultures: Experiments and Mathematical Model*. Biotechnology Progress, 2005. **21**(4): p. 1269-1280.
3. Alves da Silva, M.L., et al., *Chondrogenic differentiation of human bone marrow mesenchymal stem cells in chitosan-based scaffolds using a flow-perfusion bioreactor*. J Tissue Eng Regen Med, 2011. **5**(9): p. 722-32.
4. Bancroft, G.N., et al., *Fluid flow increases mineralized matrix deposition in 3D perfusion culture of marrow stromal osteoblasts in a dose-dependent manner*. Proceedings of the National Academy of Sciences, 2002. **99**(20): p. 12600-12605.
5. Sikavitsas, V.I., et al., *Mineralized matrix deposition by marrow stromal osteoblasts in 3D perfusion culture increases with increasing fluid shear forces*. Proceedings of the National Academy of Sciences of the United States of America, 2003. **100**(25): p. 14683-14688.
6. Kock, L.M., et al., *Flow-perfusion interferes with chondrogenic and hypertrophic matrix production by mesenchymal stem cells*. Journal of Biomechanics, 2014. **47**(9): p. 2122-2129.
7. McCoy, R.J., C. Jungreuthmayer, and F.J. O'Brien, *Influence of flow rate and scaffold pore size on cell behavior during mechanical stimulation in a flow perfusion bioreactor*. Biotechnology and Bioengineering, 2012. **109**(6): p. 1583-1594.
8. Cartmell, S.H., et al., *Effects of medium perfusion rate on cell-seeded three-dimensional bone constructs in vitro*. Tissue Eng, 2003. **9**(6): p. 1197-203.
9. Hutmacher, D.W., et al., *Mechanical properties and cell cultural response of polycaprolactone scaffolds designed and fabricated via fused deposition modeling*. J Biomed Mater Res, 2001. **55**(2): p. 203-16.
10. Sobral, J.M., et al., *Three-dimensional plotted scaffolds with controlled pore size gradients: Effect of scaffold geometry on mechanical performance and cell seeding efficiency*. Acta Biomaterialia, 2011. **7**(3): p. 1009-1018.

11. Melchels, F.P.W., et al., *The influence of the scaffold design on the distribution of adhering cells after perfusion cell seeding*. *Biomaterials*, 2011. **32**(11): p. 2878-2884.
12. Zhao, F., et al., *Flow rates in perfusion bioreactors to maximise mineralisation in bone tissue engineering in vitro*. *Journal of Biomechanics*, 2018. **79**: p. 232-237.
13. Guyot, Y., et al., *A three-dimensional computational fluid dynamics model of shear stress distribution during neotissue growth in a perfusion bioreactor*. *Biotechnology and Bioengineering*, 2015. **112**(12): p. 2591-2600.
14. Zhao, F., et al., *Changes in scaffold porosity during bone tissue engineering in perfusion bioreactors considerably affect cellular mechanical stimulation for mineralization*. *Bone Reports*, 2020. **12**: p. 100265.
15. Ali, D., *Effect of scaffold architecture on cell seeding efficiency: A discrete phase model CFD analysis*. *Computers in Biology and Medicine*, 2019. **109**: p. 62-69.
16. Campos Marin, A., et al., *2D μ -Particle Image Velocimetry and Computational Fluid Dynamics Study Within a 3D Porous Scaffold*. *Annals of Biomedical Engineering*, 2017. **45**(5): p. 1341-1351.
17. Jia, Y., et al., *Doppler optical coherence tomography imaging of local fluid flow and shear stress within microporous scaffolds*. *Journal of biomedical optics*, 2009. **14**(3): p. 034014-034014.
18. Moutos, F.T. and F. Guilak, *Composite scaffolds for cartilage tissue engineering*. *Biorheology*, 2008. **45**(3-4): p. 501-12.
19. Getgood, A., et al., *Articular cartilage tissue engineering: today's research, tomorrow's practice?* *J Bone Joint Surg Br*, 2009. **91**(5): p. 565-76.
20. Cohen, N.P., R.J. Foster, and V.C. Mow, *Composition and dynamics of articular cartilage: structure, function, and maintaining healthy state*. *J Orthop Sports Phys Ther*, 1998. **28**(4): p. 203-15.
21. Buckwalter, J.A., H.J. Mankin, and A.J. Grodzinsky, *Articular cartilage and osteoarthritis*. *Instr Course Lect*, 2005. **54**: p. 465-80.

22. Sophia Fox, A.J., A. Bedi, and S.A. Rodeo, *The Basic Science of Articular Cartilage: Structure, Composition, and Function*. Sports Health, 2009. **1**(6): p. 461-468.
23. Bhosale, A.M. and J.B. Richardson, *Articular cartilage: structure, injuries and review of management*. British Medical Bulletin, 2008. **87**(1): p. 77-95.
24. Buckwalter, J.A., V.C. Mow, and A. Ratcliffe, *Restoration of Injured or Degenerated Articular Cartilage*. J Am Acad Orthop Surg, 1994. **2**(4): p. 192-201.
25. LU, X.L. and V.C. MOW, *Biomechanics of Articular Cartilage and Determination of Material Properties*. Medicine & Science in Sports & Exercise, 2008. **40**(2): p. 193-199.
26. Mow, V.C., et al., *Biphasic creep and stress relaxation of articular cartilage in compression? Theory and experiments*. J Biomech Eng, 1980. **102**(1): p. 73-84.
27. Vinatier, C., et al., *Cartilage tissue engineering: towards a biomaterial-assisted mesenchymal stem cell therapy*. Current Stem Cell Research & Therapy, 2009. **4**(4): p. 318-329.
28. Zhang, L., J. Hu, and K.A. Athanasiou, *The Role of Tissue Engineering in Articular Cartilage Repair and Regeneration*. Critical reviews in biomedical engineering, 2009. **37**(1-2): p. 1-57.
29. Khan, I.M., et al., *Clonal chondroprogenitors maintain telomerase activity and Sox9 expression during extended monolayer culture and retain chondrogenic potential*. Osteoarthritis and Cartilage, 2009. **17**(4): p. 518-528.
30. Reddi, A.H., *Role of morphogenetic proteins in skeletal tissue engineering and regeneration*. Nat Biotechnol, 1998. **16**(3): p. 247-52.
31. Benya, P.D. and J.D. Shaffer, *Dedifferentiated chondrocytes reexpress the differentiated collagen phenotype when cultured in agarose gels*. Cell, 1982. **30**(1): p. 215-24.
32. Caron, M.M.J., et al., *Redifferentiation of dedifferentiated human articular chondrocytes: comparison of 2D and 3D cultures*. Osteoarthritis and Cartilage, 2012. **20**(10): p. 1170-1178.

33. Phull, A.-R., et al., *Applications of Chondrocyte-Based Cartilage Engineering: An Overview*. BioMed Research International, 2016. **2016**: p. 17.
34. Havlas, V., et al., [*Comparison of chondrogenic differentiation of adipose tissue-derived mesenchymal stem cells with cultured chondrocytes and bone marrow mesenchymal stem cells*]. Acta Chir Orthop Traumatol Cech, 2011. **78**(2): p. 138-44.
35. Bai, X., et al., *BMP7 induces the differentiation of bone marrow-derived mesenchymal cells into chondrocytes*. Med Biol Eng Comput, 2011. **49**(6): p. 687-92.
36. An, C., et al., *IGF-1 and BMP-2 induces differentiation of adipose-derived mesenchymal stem cells into chondrocytes-like cells*. Ann Biomed Eng, 2010. **38**(4): p. 1647-54.
37. Somoza, R.A., et al., *Chondrogenic Differentiation of Mesenchymal Stem Cells: Challenges and Unfulfilled Expectations*. Tissue Engineering. Part B, Reviews, 2014. **20**(6): p. 596-608.
38. Mueller, M.B. and R.S. Tuan, *Functional characterization of hypertrophy in chondrogenesis of human mesenchymal stem cells*. Arthritis Rheum, 2008. **58**(5): p. 1377-88.
39. Athanasiou, K.A., et al., *Self-Organization and the Self-Assembling Process in Tissue Engineering*. Annual review of biomedical engineering, 2013. **15**: p. 115-136.
40. Sato, M., et al., *Articular Cartilage Regeneration Using Cell Sheet Technology*. The Anatomical Record, 2014. **297**(1): p. 36-43.
41. Gigout, A., M.D. Buschmann, and M. Jolicoeur, *Chondrocytes cultured in stirred suspension with serum-free medium containing pluronic-68 aggregate and proliferate while maintaining their differentiated phenotype*. Tissue Eng Part A, 2009. **15**(8): p. 2237-48.
42. DuRaine, G.D., et al., *Emergence of Scaffold-free Approaches for Tissue Engineering Musculoskeletal Cartilages*. Annals of biomedical engineering, 2015. **43**(3): p. 543-554.
43. Olubamiji, A.D., et al., *Modulating mechanical behaviour of 3D-printed cartilage-mimetic PCL scaffolds: influence of molecular weight and pore geometry*. Biofabrication, 2016. **8**(2): p. 025020.

44. Yeong, W.Y., et al., *Porous polycaprolactone scaffold for cardiac tissue engineering fabricated by selective laser sintering*. *Acta Biomaterialia*, 2010. **6**(6): p. 2028-2034.
45. Meng, Z., et al., *Design and additive manufacturing of flexible polycaprolactone scaffolds with highly-tunable mechanical properties for soft tissue engineering*. *Materials & Design*, 2020. **189**: p. 108508.
46. Park, S.A., et al., *Fabrication of 3D Printed PCL/PEG Polyblend Scaffold Using Rapid Prototyping System for Bone Tissue Engineering Application*. *Journal of Bionic Engineering*, 2018. **15**(3): p. 435-442.
47. Mei, N., et al., *Biocompatibility of Poly(epsilon-caprolactone) scaffold modified by chitosan--the fibroblasts proliferation in vitro*. *J Biomater Appl*, 2005. **19**(4): p. 323-39.
48. Sousa, I., et al., *Collagen surface modified poly(ε-caprolactone) scaffolds with improved hydrophilicity and cell adhesion properties*. *Materials Letters*, 2014. **134**: p. 263-267.
49. Nasiri, B. and S. Mashayekhan, *Fabrication of porous scaffolds with decellularized cartilage matrix for tissue engineering application*. *Biologicals*, 2017. **48**: p. 39-46.
50. El-Sherbiny, I.M. and M.H. Yacoub, *Hydrogel scaffolds for tissue engineering: Progress and challenges*. *Global Cardiology Science & Practice*, 2013. **2013**(3): p. 316-342.
51. Ahearne, M., et al., *Characterizing the viscoelastic properties of thin hydrogel-based constructs for tissue engineering applications*. *Journal of the Royal Society Interface*, 2005. **2**(5): p. 455-463.
52. Guo, Y., et al., *Mechanical reinforcement of hydrogels by nanofiber network undergoing biaxial deformation*. *Polymer Composites*, 2016. **37**(3): p. 709-717.
53. Visser, J., et al., *Biofabrication of multi-material anatomically shaped tissue constructs*. *Biofabrication*, 2013. **5**(3): p. 035007.
54. Jaiswal, M.K., et al., *Mechanically Stiff Nanocomposite Hydrogels at Ultralow Nanoparticle Content*. *ACS Nano*, 2016. **10**(1): p. 246-256.
55. Haycock, J.W., *3D Cell Culture: A Review of Current Approaches and Techniques*, in *3D Cell Culture: Methods and Protocols*, J.W. Haycock, Editor. 2011, Humana Press: Totowa, NJ. p. 1-15.

56. Lee, J., M.J. Cuddihy, and N.A. Kotov, *Three-dimensional cell culture matrices: state of the art*. *Tissue Eng Part B Rev*, 2008. **14**(1): p. 61-86.
57. Liu, C., Z. Xia, and J.T. Czernuszka, *Design and Development of Three-Dimensional Scaffolds for Tissue Engineering*. *Chemical Engineering Research and Design*, 2007. **85**(7): p. 1051-1064.
58. Leong, K.F., C.M. Cheah, and C.K. Chua, *Solid freeform fabrication of three-dimensional scaffolds for engineering replacement tissues and organs*. *Biomaterials*, 2003. **24**(13): p. 2363-2378.
59. Dehghani, F. and N. Annabi, *Engineering porous scaffolds using gas-based techniques*. *Current Opinion in Biotechnology*, 2011. **22**(5): p. 661-666.
60. Janik, H. and M. Marzec, *A review: Fabrication of porous polyurethane scaffolds*. *Materials Science and Engineering: C*, 2015. **48**: p. 586-591.
61. Sachlos, E. and J.T. Czernuszka, *Making tissue engineering scaffolds work. Review: the application of solid freeform fabrication technology to the production of tissue engineering scaffolds*. *Eur Cell Mater*, 2003. **5**: p. 29-39; discussion 39-40.
62. Wu, G.-H. and S.-h. Hsu, *Review: Polymeric-Based 3D Printing for Tissue Engineering*. *Journal of Medical and Biological Engineering*, 2015. **35**(3): p. 285-292.
63. Williams, J.M., et al., *Bone tissue engineering using polycaprolactone scaffolds fabricated via selective laser sintering*. *Biomaterials*, 2005. **26**(23): p. 4817-27.
64. Stevens, B., et al., *A review of materials, fabrication methods, and strategies used to enhance bone regeneration in engineered bone tissues*. *Journal of Biomedical Materials Research Part B: Applied Biomaterials*, 2008. **85B**(2): p. 573-582.
65. Do, A.-V., et al., *3D Printing of Scaffolds for Tissue Regeneration Applications*. *Advanced healthcare materials*, 2015. **4**(12): p. 1742-1762.
66. Duan, B., et al., *Three-dimensional nanocomposite scaffolds fabricated via selective laser sintering for bone tissue engineering*. *Acta Biomaterialia*, 2010. **6**(12): p. 4495-4505.
67. Liulan, L., et al., *Design and Fabrication of Bone Tissue Engineering Scaffolds via Rapid Prototyping and CAD*. *Journal of Rare Earths*, 2007. **25**: p. 379-383.

68. Kolan, K.C., et al., *Effect of material, process parameters, and simulated body fluids on mechanical properties of 13-93 bioactive glass porous constructs made by selective laser sintering*. J Mech Behav Biomed Mater, 2012. **13**: p. 14-24.
69. Savalani, M.M., et al., *The effects and interactions of fabrication parameters on the properties of selective laser sintered hydroxyapatite polyamide composite biomaterials*. Rapid Prototyping Journal, 2012. **18**(1): p. 16-27.
70. Zein, I., et al., *Fused deposition modeling of novel scaffold architectures for tissue engineering applications*. Biomaterials, 2002. **23**(4): p. 1169-1185.
71. Domingos, M., et al., *Polycaprolactone Scaffolds Fabricated via Bioextrusion for Tissue Engineering Applications*. International Journal of Biomaterials, 2009. **2009**: p. 9.
72. Mohamed, O.A., S.H. Masood, and J.L. Bhowmik, *Optimization of fused deposition modeling process parameters: a review of current research and future prospects*. Advances in Manufacturing, 2015. **3**(1): p. 42-53.
73. Bracaglia, L.G., et al., *3D printing for the design and fabrication of polymer-based gradient scaffolds*. Acta Biomaterialia, 2017. **56**: p. 3-13.
74. Nowicki, M.A., et al., *3D printing of novel osteochondral scaffolds with graded microstructure*. Nanotechnology, 2016. **27**(41): p. 414001.
75. Gungor-Ozkerim, P.S., et al., *Bioinks for 3D bioprinting: an overview*. Biomaterials Science, 2018. **6**(5): p. 915-946.
76. Melchels, F.P.W., J. Feijen, and D.W. Grijpma, *A review on stereolithography and its applications in biomedical engineering*. Biomaterials, 2010. **31**(24): p. 6121-6130.
77. Zakeri, S., M. Vippola, and E. Levänen, *A comprehensive review of the photopolymerization of ceramic resins used in stereolithography*. Additive Manufacturing, 2020. **35**: p. 101177.
78. Lee, J.W., et al., *3D scaffold fabrication with PPF/DEF using micro-stereolithography*. Microelectronic Engineering, 2007. **84**(5): p. 1702-1705.
79. Elomaa, L., et al., *Preparation of poly(ϵ -caprolactone)-based tissue engineering scaffolds by stereolithography*. Acta Biomaterialia, 2011. **7**(11): p. 3850-3856.

80. Melchels, F.P.W., J. Feijen, and D.W. Grijpma, *A poly(d,l-lactide) resin for the preparation of tissue engineering scaffolds by stereolithography*. *Biomaterials*, 2009. **30**(23): p. 3801-3809.
81. Zhang, X., X.N. Jiang, and C. Sun, *Micro-stereolithography of polymeric and ceramic microstructures*. *Sensors and Actuators A: Physical*, 1999. **77**(2): p. 149-156.
82. Guvendiren, M., et al., *Designing Biomaterials for 3D Printing*. *ACS Biomaterials Science & Engineering*, 2016. **2**(10): p. 1679-1693.
83. Ratheesh, G., et al., *3D Fabrication of Polymeric Scaffolds for Regenerative Therapy*. *ACS Biomaterials Science & Engineering*, 2017. **3**(7): p. 1175-1194.
84. Collins, M.N. and C. Birkinshaw, *Hyaluronic acid based scaffolds for tissue engineering—A review*. *Carbohydrate Polymers*, 2013. **92**(2): p. 1262-1279.
85. Suri, S., et al., *Solid freeform fabrication of designer scaffolds of hyaluronic acid for nerve tissue engineering*. *Biomed Microdevices*, 2011. **13**(6): p. 983-93.
86. Poldervaart, M.T., et al., *3D bioprinting of methacrylated hyaluronic acid (MeHA) hydrogel with intrinsic osteogenicity*. *PLoS ONE*, 2017. **12**(6): p. e0177628.
87. Echave, M.C., et al., *Gelatin as Biomaterial for Tissue Engineering*. *Curr Pharm Des*, 2017. **23**(24): p. 3567-3584.
88. Shi, W., R. He, and Y. Liu, *3D printing scaffolds with hydrogel materials for biomedical applications*. *European Journal of BioMedical Research; Vol 1, No 3 (2015): Novel biomaterials and biotechnology for nanomedicine*, 2015.
89. Landers, R., et al., *Rapid prototyping of scaffolds derived from thermoreversible hydrogels and tailored for applications in tissue engineering*. *Biomaterials*, 2002. **23**(23): p. 4437-4447.
90. Fedorovich, N.E., et al., *Biofabrication of osteochondral tissue equivalents by printing topologically defined, cell-laden hydrogel scaffolds*. *Tissue Eng Part C Methods*, 2012. **18**(1): p. 33-44.
91. Zorlutuna, P., et al., *Stereolithography-Based Hydrogel Microenvironments to Examine Cellular Interactions*. *Advanced Functional Materials*, 2011. **21**(19): p. 3642-3651.

92. Ren, X., et al., *Engineering zonal cartilage through bioprinting collagen type II hydrogel constructs with biomimetic chondrocyte density gradient*. BMC musculoskeletal disorders, 2016. **17**: p. 301-301.
93. Rhee, S., et al., *3D Bioprinting of Spatially Heterogeneous Collagen Constructs for Cartilage Tissue Engineering*. ACS Biomaterials Science & Engineering, 2016. **2**(10): p. 1800-1805.
94. Shepherd, D.E. and B.B. Seedhom, *The 'instantaneous' compressive modulus of human articular cartilage in joints of the lower limb*. Rheumatology (Oxford), 1999. **38**(2): p. 124-32.
95. Daly, A.C., et al., *A comparison of different bioinks for 3D bioprinting of fibrocartilage and hyaline cartilage*. Biofabrication, 2016. **8**(4): p. 045002.
96. Drury, J.L. and D.J. Mooney, *Hydrogels for tissue engineering: scaffold design variables and applications*. Biomaterials, 2003. **24**(24): p. 4337-4351.
97. Greene, G.W., et al., *Anisotropic dynamic changes in the pore network structure, fluid diffusion and fluid flow in articular cartilage under compression*. Biomaterials, 2010. **31**(12): p. 3117-3128.
98. Serra, T., J.A. Planell, and M. Navarro, *High-resolution PLA-based composite scaffolds via 3-D printing technology*. Acta Biomaterialia, 2013. **9**(3): p. 5521-5530.
99. Garlotta, D., *A Literature Review of Poly(Lactic Acid)*. Journal of Polymers and the Environment, 2001. **9**(2): p. 63-84.
100. Senatov, F.S., et al., *Mechanical properties and shape memory effect of 3D-printed PLA-based porous scaffolds*. Journal of the Mechanical Behavior of Biomedical Materials, 2016. **57**: p. 139-148.
101. Fisher, J.P., D. Dean, and A.G. Mikos, *Photocrosslinking characteristics and mechanical properties of diethyl fumarate/poly(propylene fumarate) biomaterials*. Biomaterials, 2002. **23**(22): p. 4333-4343.
102. Lee, K.-W., et al., *Poly(propylene fumarate) Bone Tissue Engineering Scaffold Fabrication Using Stereolithography: Effects of Resin Formulations and Laser Parameters*. Biomacromolecules, 2007. **8**(4): p. 1077-1084.
103. He, S., et al., *Synthesis of biodegradable poly(propylene fumarate) networks with poly(propylene fumarate)-diacrylate macromers as*

crosslinking agents and characterization of their degradation products. Polymer, 2001. **42**(3): p. 1251-1260.

104. Fisher, J.P., et al., *Soft and hard tissue response to photocrosslinked poly(propylene fumarate) scaffolds in a rabbit model.* Journal of Biomedical Materials Research, 2002. **59**(3): p. 547-556.
105. Woodruff, M.A. and D.W. Hutmacher, *The return of a forgotten polymer—Polycaprolactone in the 21st century.* Progress in Polymer Science, 2010. **35**(10): p. 1217-1256.
106. Daniela, S., et al., *3D-Printed PCL Scaffolds for the Cultivation of Mesenchymal Stem Cells.* Journal of Applied Biomaterials & Functional Materials, 2016. **14**(1): p. 19-25.
107. Theodoridis, K., et al., *Assessment of cartilage regeneration on 3D collagen-polycaprolactone scaffolds: Evaluation of growth media in static and in perfusion bioreactor dynamic culture.* Colloids and Surfaces B: Biointerfaces, 2019. **183**: p. 110403.
108. Yoon, H.H., et al., *Enhanced cartilage formation via three-dimensional cell engineering of human adipose-derived stem cells.* Tissue Eng Part A, 2012. **18**(19-20): p. 1949-56.
109. Zhu, Y., et al., *Numerical Simulation of Mass Transfer and Three-Dimensional Fabrication of Tissue-Engineered Cartilages Based on Chitosan/Gelatin Hybrid Hydrogel Scaffold in a Rotating Bioreactor.* Applied Biochemistry and Biotechnology, 2017. **181**(1): p. 250-266.
110. Selden, C. and B. Fuller, *Role of Bioreactor Technology in Tissue Engineering for Clinical Use and Therapeutic Target Design.* Bioengineering (Basel, Switzerland), 2018. **5**(2): p. 32.
111. Godara, P., C.D. McFarland, and R.E. Nordon, *Design of bioreactors for mesenchymal stem cell tissue engineering.* Journal of Chemical Technology & Biotechnology, 2008. **83**(4): p. 408-420.
112. Grayson, W.L., et al., *Effects of initial seeding density and fluid perfusion rate on formation of tissue-engineered bone.* Tissue Eng Part A, 2008. **14**(11): p. 1809-20.
113. Yeatts, A.B. and J.P. Fisher, *Tubular perfusion system for the long-term dynamic culture of human mesenchymal stem cells.* Tissue Eng Part C Methods, 2011. **17**(3): p. 337-48.

114. Daly, A.C., B.N. Sathy, and D.J. Kelly, *Engineering large cartilage tissues using dynamic bioreactor culture at defined oxygen conditions*. Journal of tissue engineering, 2018. **9**: p. 2041731417753718-2041731417753718.
115. Koch, M.A., et al., *Perfusion cell seeding on large porous PLA/calcium phosphate composite scaffolds in a perfusion bioreactor system under varying perfusion parameters*. Journal of Biomedical Materials Research Part A, 2010. **95A**(4): p. 1011-1018.
116. Zhang, Z., et al., *A 3D computational model of perfusion seeding for investigating cell transport and adhesion within a porous scaffold*. Biomechanics and Modeling in Mechanobiology, 2020.
117. Martin, I., D. Wendt, and M. Heberer, *The role of bioreactors in tissue engineering*. Trends in Biotechnology, 2004. **22**(2): p. 80-86.
118. Reinwald, Y., et al., *Interconnectivity and permeability of supercritical fluid-foamed scaffolds and the effect of their structural properties on cell distribution*. Polymer, 2014. **55**(1): p. 435-444.
119. Malda, J., et al., *The effect of PEGT/PBT scaffold architecture on oxygen gradients in tissue engineered cartilaginous constructs*. Biomaterials, 2004. **25**(26): p. 5773-5780.
120. Ishaug, S.L., et al., *Bone formation by three-dimensional stromal osteoblast culture in biodegradable polymer scaffolds*. J Biomed Mater Res, 1997. **36**(1): p. 17-28.
121. O'Brien, F.J., *Biomaterials & scaffolds for tissue engineering*. Materials Today, 2011. **14**(3): p. 88-95.
122. O'Brien, F.J., et al., *The effect of pore size on cell adhesion in collagen-GAG scaffolds*. Biomaterials, 2005. **26**(4): p. 433-41.
123. Matsiko, A., J.P. Gleeson, and F.J. O'Brien, *Scaffold mean pore size influences mesenchymal stem cell chondrogenic differentiation and matrix deposition*. Tissue Eng Part A, 2015. **21**(3-4): p. 486-97.
124. Ferlin, K.M., et al., *Influence of 3D printed porous architecture on mesenchymal stem cell enrichment and differentiation*. Acta Biomater, 2016. **32**: p. 161-169.
125. Perez, R.A. and G. Mestres, *Role of pore size and morphology in musculo-skeletal tissue regeneration*. Mater Sci Eng C Mater Biol Appl, 2016. **61**: p. 922-39.

126. Macchetta, A., I.G. Turner, and C.R. Bowen, *Fabrication of HA/TCP scaffolds with a graded and porous structure using a camphene-based freeze-casting method*. *Acta Biomaterialia*, 2009. **5**(4): p. 1319-1327.
127. Lee, J.-S., et al., *Effect of pore architecture and stacking direction on mechanical properties of solid freeform fabrication-based scaffold for bone tissue engineering*. *Journal of Biomedical Materials Research Part A*, 2012. **100A**(7): p. 1846-1853.
128. Moroni, L., J.R. de Wijn, and C.A. van Blitterswijk, *3D fiber-deposited scaffolds for tissue engineering: influence of pores geometry and architecture on dynamic mechanical properties*. *Biomaterials*, 2006. **27**(7): p. 974-85.
129. Bittner, S.M., et al., *Fabrication and mechanical characterization of 3D printed vertical uniform and gradient scaffolds for bone and osteochondral tissue engineering*. *Acta Biomaterialia*, 2019. **90**: p. 37-48.
130. Keogh, M.B., F.J. O'Brien, and J.S. Daly, *Substrate stiffness and contractile behaviour modulate the functional maturation of osteoblasts on a collagen-GAG scaffold*. *Acta Biomaterialia*, 2010. **6**(11): p. 4305-4313.
131. Murphy, C.M., M.G. Haugh, and F.J. O'Brien, *The effect of mean pore size on cell attachment, proliferation and migration in collagen-glycosaminoglycan scaffolds for bone tissue engineering*. *Biomaterials*, 2010. **31**(3): p. 461-6.
132. O'Brien, F.J., et al., *The effect of pore size on permeability and cell attachment in collagen scaffolds for tissue engineering*. *Technol Health Care*, 2007. **15**(1): p. 3-17.
133. Zhang, Q., et al., *Pore size effect of collagen scaffolds on cartilage regeneration*. *Acta Biomaterialia*, 2014. **10**(5): p. 2005-2013.
134. Han, K.-S., et al., *Effect of pore sizes of silk scaffolds for cartilage tissue engineering*. *Macromolecular Research*, 2015. **23**(12): p. 1091-1097.
135. Zhang, Z.Z., et al., *Role of scaffold mean pore size in meniscus regeneration*. *Acta Biomater*, 2016. **43**: p. 314-326.
136. Im, G.I., J.Y. Ko, and J.H. Lee, *Chondrogenesis of adipose stem cells in a porous polymer scaffold: influence of the pore size*. *Cell Transplant*, 2012. **21**(11): p. 2397-405.

137. Yamane, S., et al., *Effect of pore size on in vitro cartilage formation using chitosan-based hyaluronic acid hybrid polymer fibers*. J Biomed Mater Res A, 2007. **81**(3): p. 586-93.
138. Stenhamre, H., et al., *Influence of pore size on the redifferentiation potential of human articular chondrocytes in poly(urethane urea) scaffolds*. J Tissue Eng Regen Med, 2011. **5**(7): p. 578-88.
139. Lien, S.-M., L.-Y. Ko, and T.-J. Huang, *Effect of pore size on ECM secretion and cell growth in gelatin scaffold for articular cartilage tissue engineering*. Acta Biomaterialia, 2009. **5**(2): p. 670-679.
140. Oh, S.H., et al., *In vitro and in vivo characteristics of PCL scaffolds with pore size gradient fabricated by a centrifugation method*. Biomaterials, 2007. **28**(9): p. 1664-71.
141. Rodrigues, N., et al., *Manufacture and Characterisation of Porous PLA Scaffolds*. Procedia CIRP, 2016. **49**: p. 33-38.
142. Entezari, A., et al., *Architectural Design of 3D Printed Scaffolds Controls the Volume and Functionality of Newly Formed Bone*. Advanced Healthcare Materials, 2019. **8**(1): p. 1801353.
143. Sabree, I., J.E. Gough, and B. Derby, *Mechanical properties of porous ceramic scaffolds: Influence of internal dimensions*. Ceramics International, 2015. **41**(7): p. 8425-8432.
144. El-Ayoubi, R., et al., *Design and Dynamic Culture of 3D-Scaffolds for Cartilage Tissue Engineering*. Journal of Biomaterials Applications, 2009. **25**(5): p. 429-444.
145. Rouwkema, J., N.C. Rivron, and C.A. van Blitterswijk, *Vascularization in tissue engineering*. Trends in Biotechnology, 2008. **26**(8): p. 434-441.
146. Souness, A., et al., *Influence of scaffold design on 3D printed cell constructs*. J Biomed Mater Res B Appl Biomater, 2018. **106**(2): p. 533-545.
147. Woodfield, T.B.F., et al., *Design of porous scaffolds for cartilage tissue engineering using a three-dimensional fiber-deposition technique*. Biomaterials, 2004. **25**(18): p. 4149-4161.
148. Woodfield, T.B., et al., *Polymer scaffolds fabricated with pore-size gradients as a model for studying the zonal organization within tissue-engineered cartilage constructs*. Tissue Eng, 2005. **11**(9-10): p. 1297-311.

149. Alves da Silva, M.L., et al., *Chitosan/polyester-based scaffolds for cartilage tissue engineering: assessment of extracellular matrix formation*. *Acta Biomater*, 2010. **6**(3): p. 1149-57.
150. Park, S., et al., *3D polycaprolactone scaffolds with controlled pore structure using a rapid prototyping system*. *J Mater Sci Mater Med*, 2009. **20**(1): p. 229-34.
151. Melchels, F.P., et al., *Effects of the architecture of tissue engineering scaffolds on cell seeding and culturing*. *Acta Biomater*, 2010. **6**(11): p. 4208-17.
152. Somo, S.I., et al., *Pore Interconnectivity Influences Growth Factor-Mediated Vascularization in Sphere-Templated Hydrogels*. *Tissue engineering. Part C, Methods*, 2015. **21**(8): p. 773-785.
153. Miot, S., et al., *Effects of scaffold composition and architecture on human nasal chondrocyte redifferentiation and cartilaginous matrix deposition*. *Biomaterials*, 2005. **26**(15): p. 2479-89.
154. Malda, J., et al., *The effect of PEGT/PBT scaffold architecture on the composition of tissue engineered cartilage*. *Biomaterials*, 2005. **26**(1): p. 63-72.
155. Emans, P.J., et al., *Tissue-engineered constructs: the effect of scaffold architecture in osteochondral repair*. *Journal of Tissue Engineering and Regenerative Medicine*, 2013. **7**(9): p. 751-756.
156. Kemppainen, J.M. and S.J. Hollister, *Differential effects of designed scaffold permeability on chondrogenesis by chondrocytes and bone marrow stromal cells*. *Biomaterials*, 2010. **31**(2): p. 279-87.
157. Mao, C., et al., *Various approaches to modify biomaterial surfaces for improving hemocompatibility*. *Advances in Colloid and Interface Science*, 2004. **110**(1): p. 5-17.
158. Ruckenstein, E. and Z.F. Li, *Surface modification and functionalization through the self-assembled monolayer and graft polymerization*. *Advances in Colloid and Interface Science*, 2005. **113**(1): p. 43-63.
159. Recek, N., et al., *Cell Adhesion on Polycaprolactone Modified by Plasma Treatment*. *International Journal of Polymer Science*, 2016. **2016**: p. 7354396.
160. Honda, M.J., et al., *Shear stress facilitates tissue-engineered odontogenesis*. *Bone*, 2006. **39**(1): p. 125-33.

161. Yeatts, A.B. and J.P. Fisher, *Bone tissue engineering bioreactors: dynamic culture and the influence of shear stress*. Bone, 2011. **48**(2): p. 171-81.
162. Gharravi, A.M., M. Orazizadeh, and M. Hashemitabar, *Fluid-induced low shear stress improves cartilage like tissue fabrication by encapsulating chondrocytes*. Cell Tissue Bank, 2016. **17**(1): p. 117-22.
163. Pazzano, D., et al., *Comparison of chondrogenesis in static and perfused bioreactor culture*. Biotechnol Prog, 2000. **16**(5): p. 893-6.
164. Albro, M.B., et al., *Shearing of synovial fluid activates latent TGF-beta*. Osteoarthritis Cartilage, 2012. **20**(11): p. 1374-82.
165. Gemmiti, C.V. and R.E. Guldberg, *Fluid flow increases type II collagen deposition and tensile mechanical properties in bioreactor-grown tissue-engineered cartilage*. Tissue Eng, 2006. **12**(3): p. 469-79.
166. O'Connor, C.J., N. Case, and F. Guilak, *Mechanical regulation of chondrogenesis*. Stem Cell Research & Therapy, 2013. **4**(4): p. 61-61.
167. Novosel, E.C., C. Kleinhans, and P.J. Kluger, *Vascularization is the key challenge in tissue engineering*. Adv Drug Deliv Rev, 2011. **63**(4-5): p. 300-11.
168. Kleinhans, C., et al., *A perfusion bioreactor system efficiently generates cell-loaded bone substitute materials for addressing critical size bone defects*. Biotechnol J, 2015. **10**(11): p. 1727-38.
169. Kitagawa, T., et al., *Three-dimensional cell seeding and growth in radial-flow perfusion bioreactor for in vitro tissue reconstruction*. Biotechnol Bioeng, 2006. **93**(5): p. 947-54.
170. Bancroft, G.N., et al., *Fluid flow increases mineralized matrix deposition in 3D perfusion culture of marrow stromal osteoblasts in a dose-dependent manner*. Proceedings of the National Academy of Sciences of the United States of America, 2002. **99**(20): p. 12600-12605.
171. Li, D., et al., *Effects of flow shear stress and mass transport on the construction of a large-scale tissue-engineered bone in a perfusion bioreactor*. Tissue Eng Part A, 2009. **15**(10): p. 2773-83.
172. Vetsch, J.R., et al., *Flow velocity-driven differentiation of human mesenchymal stromal cells in silk fibroin scaffolds: A combined experimental and computational approach*. PLoS One, 2017. **12**(7): p. e0180781.

173. Zhao, F., R. Chella, and T. Ma, *Effects of shear stress on 3-D human mesenchymal stem cell construct development in a perfusion bioreactor system: Experiments and hydrodynamic modeling*. *Biotechnol Bioeng*, 2007. **96**(3): p. 584-95.
174. Porter, B.D., et al., *Noninvasive image analysis of 3D construct mineralization in a perfusion bioreactor*. *Biomaterials*, 2007. **28**(15): p. 2525-33.
175. Raimondi, M.T., et al., *The effect of hydrodynamic shear on 3D engineered chondrocyte systems subject to direct perfusion*. *Biorheology*, 2006. **43**(3,4): p. 215-22.
176. Raimondi, M.T., et al., *The effect of polyurethane scaffold surface treatments on the adhesion of chondrocytes subjected to interstitial perfusion culture*. *Tissue Engineering and Regenerative Medicine*, 2016. **13**(4): p. 364-374.
177. Zhu, G., et al., *Comparing effects of perfusion and hydrostatic pressure on gene profiles of human chondrocyte*. *Journal of Biotechnology*, 2015. **210**: p. 59-65.
178. Cioffi, M., et al., *Computational evaluation of oxygen and shear stress distributions in 3D perfusion culture systems: Macro-scale and micro-structured models*. *Journal of Biomechanics*, 2008. **41**(14): p. 2918-2925.
179. Gharravi, A.M., M. Orazizadeh, and M. Hashemitabar, *Direct expansion of chondrocytes in a dynamic three-dimensional culture system: overcoming dedifferentiation effects in monolayer culture*. *Artif Organs*, 2014. **38**(12): p. 1053-8.
180. Carmona-Moran, C.A. and T.M. Wick, *Transient Growth Factor Stimulation Improves Chondrogenesis in Static Culture and Under Dynamic Conditions in a Novel Shear and Perfusion Bioreactor*. *Cellular and Molecular Bioengineering*, 2015. **8**(2): p. 267-277.
181. Davisson, T., R.L. Sah, and A. Ratcliffe, *Perfusion increases cell content and matrix synthesis in chondrocyte three-dimensional cultures*. *Tissue Eng*, 2002. **8**(5): p. 807-16.
182. Zermatten, E., et al., *Micro-Computed Tomography Based Computational Fluid Dynamics for the Determination of Shear Stresses in Scaffolds Within a Perfusion Bioreactor*. *Annals of Biomedical Engineering*, 2014. **42**(5): p. 1085-1094.

183. Bartnikowski, M., et al., *Effects of scaffold architecture on mechanical characteristics and osteoblast response to static and perfusion bioreactor cultures*. *Biotechnology and Bioengineering*, 2014. **111**(7): p. 1440-1451.
184. Lesman, A., Y. Blinder, and S. Levenberg, *Modeling of flow-induced shear stress applied on 3D cellular scaffolds: Implications for vascular tissue engineering*. *Biotechnology and Bioengineering*, 2010. **105**(3): p. 645-654.
185. Cinbiz, M.N., et al., *Computational fluid dynamics modeling of momentum transport in rotating wall perfused bioreactor for cartilage tissue engineering*. *Journal of Biotechnology*, 2010. **150**(3): p. 389-395.
186. Hutmacher, D.W. and H. Singh, *Computational fluid dynamics for improved bioreactor design and 3D culture*. *Trends in Biotechnology*, 2008. **26**(4): p. 166-172.
187. Patrachari, A.R., J.T. Podichetty, and S.V. Madihally, *Application of computational fluid dynamics in tissue engineering*. *Journal of Bioscience and Bioengineering*, 2012. **114**(2): p. 123-132.
188. Mokhtari-Jafari, F., et al., *Mathematical modeling of cell growth in a 3D scaffold and validation of static and dynamic cultures*. *Engineering in Life Sciences*, 2016. **16**(3): p. 290-298.
189. Song, M.J., D. Dean, and M.L. Knothe Tate, *In Situ Spatiotemporal Mapping of Flow Fields around Seeded Stem Cells at the Subcellular Length Scale*. *PLoS ONE*, 2010. **5**(9): p. e12796.
190. Gao, Y.-B., et al., *A tracer liquid image velocimetry for multi-layer radial flow in bioreactors*. *BioMedical Engineering OnLine*, 2015. **14**: p. 10.
191. Bonn, D., et al., *Some Applications of Magnetic Resonance Imaging in Fluid Mechanics: Complex Flows and Complex Fluids*. *Annual Review of Fluid Mechanics*, 2008. **40**(1): p. 209-233.
192. Kotecha, M., D. Klatt, and R.L. Magin, *Monitoring cartilage tissue engineering using magnetic resonance spectroscopy, imaging, and elastography*. *Tissue engineering. Part B, Reviews*, 2013. **19**(6): p. 470-484.
193. Fukushima, E., *NUCLEAR MAGNETIC RESONANCE AS A TOOL TO STUDY FLOW*. *Annual Review of Fluid Mechanics*, 1999. **31**(1): p. 95-123.
194. Callaghan, P.T., *Principles of Nuclear Magnetic Resonance Microscopy*. 1993: Clarendon Press.

195. Lotz, J., et al., *Cardiovascular flow measurement with phase-contrast MR imaging: basic facts and implementation*. Radiographics, 2002. **22**(3): p. 651-71.
196. Gatehouse, P.D., et al., *Applications of phase-contrast flow and velocity imaging in cardiovascular MRI*. European Radiology, 2005. **15**(10): p. 2172-2184.
197. Stankovic, Z., et al., *4D flow imaging with MRI*. Cardiovascular Diagnosis and Therapy, 2014. **4**(2): p. 173-192.
198. Stankovic, Z., et al., *A feasibility study to evaluate splanchnic arterial and venous hemodynamics by flow-sensitive 4D MRI compared with Doppler ultrasound in patients with cirrhosis and controls*. Eur J Gastroenterol Hepatol, 2013. **25**(6): p. 669-75.
199. Barker, A.J., et al., *Bicuspid aortic valve is associated with altered wall shear stress in the ascending aorta*. Circ Cardiovasc Imaging, 2012. **5**(4): p. 457-66.
200. Bolger, A.F., et al., *Transit of blood flow through the human left ventricle mapped by cardiovascular magnetic resonance*. J Cardiovasc Magn Reson, 2007. **9**(5): p. 741-7.
201. Turney, M.A., et al., *Magnetic resonance imaging study of sedimenting suspensions of noncolloidal spheres*. Physics of Fluids, 1995. **7**(5): p. 904-911.
202. Britton, M.M. and P.T. Callaghan, *Nuclear magnetic resonance visualization of anomalous flow in cone-and-plate rheometry*. Journal of Rheology, 1997. **41**(6): p. 1365-1386.
203. McCarthy, K.L., et al., *VELOCITY PROFILES OF FLUID/PARTICULATE MIXTURES IN PIPE FLOW USING MRI*. Journal of Food Process Engineering, 1997. **20**(2): p. 165-177.
204. Jelinkova, V., et al., *Effects of entrapped residual air bubbles on tracer transport in heterogeneous soil: Magnetic resonance imaging study*. Organic Geochemistry, 2011. **42**(8): p. 991-998.
205. Li, M., et al., *Monitoring oil displacement processes with k-t accelerated spin echo SPI*. Magnetic Resonance in Chemistry, 2016. **54**(3): p. 197-204.

206. Pomerantz, A.E., E.E. Sigmund, and Y.Q. Song, *Spatial Heterogeneity Length Scales in Carbonate Rocks*. Applied Magnetic Resonance, 2007. **32**(1): p. 221.
207. Fridjonsson, E.O., et al., *Hydrodynamic dispersion in β - lactoglobulin gels measured by PGSE NMR*. The European Physical Journal E, 2011. **34**(2): p. 18.
208. Bernin, D., et al., *Microstructure of polymer hydrogels studied by pulsed field gradient NMR diffusion and TEM methods*. Soft Matter, 2011. **7**(12): p. 5711-5716.
209. Benjamini, D., et al., *Pore size distribution of bioresorbable films using a 3-D diffusion NMR method*. Acta Biomaterialia, 2014. **10**(6): p. 2762-2768.
210. Swider, P., et al., *Use of high-resolution MRI for investigation of fluid flow and global permeability in a material with interconnected porosity*. Journal of Biomechanics, 2007. **40**(9): p. 2112-2118.
211. Mack, J.J., et al., *Real-Time Maps of Fluid Flow Fields in Porous Biomaterials*. Biomaterials, 2013. **34**(8): p. 1980-1986.
212. Youssef, K., et al., *Macro-scale topology optimization for controlling internal shear stress in a porous scaffold bioreactor*. Biotechnology and Bioengineering, 2012. **109**(7): p. 1844-1854.
213. Youssef, K., et al., *4-D Flow Control in Porous Scaffolds: Toward a Next Generation of Bioreactors*. IEEE Trans Biomed Eng, 2017. **64**(1): p. 61-69.
214. Kurzyk, A., et al., *Characterization and Optimization of the Seeding Process of Adipose Stem Cells on the Polycaprolactone Scaffolds*. Stem Cells International, 2019. **2019**: p. 17.
215. Arbab, A.S., et al., *Efficient magnetic cell labeling with protamine sulfate complexed to ferumoxides for cellular MRI*. Blood, 2004. **104**(4): p. 1217-23.
216. Roeder, E., et al., *Dose-Response of Superparamagnetic Iron Oxide Labeling on Mesenchymal Stem Cells Chondrogenic Differentiation: A Multi-Scale In Vitro Study*. PLOS ONE, 2014. **9**(5): p. e98451.
217. Saldanha, K.J., et al., *Micrometer-sized iron oxide particle labeling of mesenchymal stem cells for magnetic resonance imaging-based*

monitoring of cartilage tissue engineering. Magn Reson Imaging, 2011. **29**(1): p. 40-9.

218. Markides, H., et al., *Ex vivo MRI cell tracking of autologous mesenchymal stromal cells in an ovine osteochondral defect model*. Stem Cell Research & Therapy, 2019. **10**(1): p. 25.
219. Okamoto, T., et al., *Clonal heterogeneity in differentiation potential of immortalized human mesenchymal stem cells*. Biochemical and Biophysical Research Communications, 2002. **295**(2): p. 354-361.
220. Buckley, C.T. and K.U. O'Kelly, *Maintaining cell depth viability: on the efficacy of a trimodal scaffold pore architecture and dynamic rotational culturing*. Journal of Materials Science: Materials in Medicine, 2010. **21**(5): p. 1731-1738.
221. Ishaug-Riley, S.L., et al., *Three-dimensional culture of rat calvarial osteoblasts in porous biodegradable polymers*. Biomaterials, 1998. **19**(15): p. 1405-1412.
222. Karande, T.S., J.L. Ong, and C.M. Agrawal, *Diffusion in Musculoskeletal Tissue Engineering Scaffolds: Design Issues Related to Porosity, Permeability, Architecture, and Nutrient Mixing*. Annals of Biomedical Engineering, 2004. **32**(12): p. 1728-1743.
223. Schmid, J., et al., *A Perfusion Bioreactor System for Cell Seeding and Oxygen-Controlled Cultivation of Three-Dimensional Cell Cultures*. Tissue Eng Part C Methods, 2018. **24**(10): p. 585-595.
224. Chan, W.Y. and C.K. Chong. *Perfusion Bioreactors Improve Oxygen Transport and Cell Distribution in Esophageal Smooth Muscle Construct*. in *13th International Conference on Biomedical Engineering*. 2009. Berlin, Heidelberg: Springer Berlin Heidelberg.
225. Rotenberg, M.Y., et al., *A multi-shear perfusion bioreactor for investigating shear stress effects in endothelial cell constructs*. Lab Chip, 2012. **12**(15): p. 2696-703.
226. Yu, W., et al., *A Microfluidic-Based Multi-Shear Device for Investigating the Effects of Low Fluid-Induced Stresses on Osteoblasts*. PLOS ONE, 2014. **9**(2): p. e89966.
227. Olivares, A.L., et al., *Finite element study of scaffold architecture design and culture conditions for tissue engineering*. Biomaterials, 2009. **30**(30): p. 6142-9.

228. Zhao, H., et al., *Effect of porous structure and pore size on mechanical strength of 3D-printed comby scaffolds*. Materials Letters, 2018. **223**: p. 21-24.
229. Di Luca, A., et al., *Influencing chondrogenic differentiation of human mesenchymal stromal cells in scaffolds displaying a structural gradient in pore size*. Acta Biomater, 2016. **36**: p. 210-9.
230. Di Luca, A., et al., *Gradients in pore size enhance the osteogenic differentiation of human mesenchymal stromal cells in three-dimensional scaffolds*. Scientific Reports, 2016. **6**(1): p. 22898.
231. Sanghani-Kerai, A., et al., *THE EFFECT OF PORE SIZE ON BONE MARROW MESENCHYMAL STEM CELL MORPHOLOGY, PROLIFERATION AND MINERALIZATION OF BONE IN VITRO*. Orthopaedic Proceedings, 2019. **101-B**(SUPP_2): p. 12-12.
232. Vissers, C.A.B., J.N. Harvestine, and J.K. Leach, *Pore size regulates mesenchymal stem cell response to Bioglass-loaded composite scaffolds*. Journal of Materials Chemistry B, 2015. **3**(44): p. 8650-8658.
233. Domingos, M., et al., *The first systematic analysis of 3D rapid prototyped poly(epsilon-caprolactone) scaffolds manufactured through BioCell printing: the effect of pore size and geometry on compressive mechanical behaviour and in vitro hMSC viability*. Biofabrication, 2013. **5**(4): p. 045004.
234. Ostrowska, B., et al., *Influence of internal pore architecture on biological and mechanical properties of three-dimensional fiber deposited scaffolds for bone regeneration*. J Biomed Mater Res A, 2016. **104**(4): p. 991-1001.
235. Scheven, U.M., et al., *Quantitative nuclear magnetic resonance measurements of preasymptotic dispersion in flow through porous media*. Physics of Fluids, 2005. **17**(11): p. 117107.
236. Sederman, A.J. and L.F. Gladden, *Magnetic resonance visualisation of single- and two-phase flow in porous media*. Magnetic Resonance Imaging, 2001. **19**(3): p. 339-343.
237. Hope, T.A., et al., *Comparison of flow patterns in ascending aortic aneurysms and volunteers using four-dimensional magnetic resonance velocity mapping*. J Magn Reson Imaging, 2007. **26**(6): p. 1471-9.
238. Markl, M., et al., *Time-resolved 3-dimensional velocity mapping in the thoracic aorta: visualization of 3-directional blood flow patterns in healthy*

- volunteers and patients*. J Comput Assist Tomogr, 2004. **28**(4): p. 459-68.
239. Amin, M.H.G., et al., *Study of flow and hydrodynamic dispersion in a porous medium using pulsed-field-gradient magnetic resonance*. Proceedings of the Royal Society of London. Series A: Mathematical, Physical and Engineering Sciences, 1997. **453**(1958): p. 489.
240. Zhang, Z.-Z., et al., *Scaffolds drive meniscus tissue engineering*. RSC Advances, 2015. **5**(95): p. 77851-77859.
241. Unsworth, J.M., et al., *Seeding cells into needled felt scaffolds for tissue engineering applications*. J Biomed Mater Res A, 2003. **66**(2): p. 425-31.
242. Boschetti, F., et al., *Prediction of the micro-fluid dynamic environment imposed to three-dimensional engineered cell systems in bioreactors*. Journal of Biomechanics, 2006. **39**(3): p. 418-425.
243. Shen, J. and R. Ni, *Experimental investigation of clogging dynamics in homogeneous porous medium*. Water Resources Research, 2017. **53**(3): p. 1879-1890.
244. Campos Marin, A. and D. Lacroix, *The inter-sample structural variability of regular tissue-engineered scaffolds significantly affects the micromechanical local cell environment*. Interface Focus, 2015. **5**(2): p. 20140097.
245. Ouyang, P., et al., *Hydromechanical mechanism behind the effect of pore size of porous titanium scaffolds on osteoblast response and bone ingrowth*. Materials & Design, 2019. **183**: p. 108151.
246. Papantoniou, I., et al., *Spatial optimization in perfusion bioreactors improves bone tissue-engineered construct quality attributes*. Biotechnol Bioeng, 2014. **111**(12): p. 2560-70.
247. Yu, W., et al., *A microfluidic-based multi-shear device for investigating the effects of low fluid-induced stresses on osteoblasts*. PloS one, 2014. **9**(2): p. e89966-e89966.
248. Kim, M.S., et al., *Enhancement of human mesenchymal stem cell infiltration into the electrospun poly(lactic-co-glycolic acid) scaffold by fluid shear stress*. Biochemical and Biophysical Research Communications, 2015. **463**(1): p. 137-142.

249. Nerurkar, N.L., et al., *Dynamic culture enhances stem cell infiltration and modulates extracellular matrix production on aligned electrospun nanofibrous scaffolds*. *Acta Biomaterialia*, 2011. **7**(2): p. 485-491.
250. Yilgor, P., et al., *3D Plotted PCL Scaffolds for Stem Cell Based Bone Tissue Engineering*. *Macromolecular Symposia*, 2008. **269**(1): p. 92-99.
251. Cioffi, M., et al., *Modeling evaluation of the fluid-dynamic microenvironment in tissue-engineered constructs: a micro-CT based model*. *Biotechnol Bioeng*, 2006. **93**(3): p. 500-10.
252. Jungreuthmayer, C., et al., *A comparative study of shear stresses in collagen-glycosaminoglycan and calcium phosphate scaffolds in bone tissue-engineering bioreactors*. *Tissue Eng Part A*, 2009. **15**(5): p. 1141-9.
253. Maes, F., et al., *Computational models for wall shear stress estimation in scaffolds: A comparative study of two complete geometries*. *Journal of Biomechanics*, 2012. **45**(9): p. 1586-1592.
254. Chung Wang, C., T.W. Lin, and S.S. Hu, *Optimizing the rapid prototyping process by integrating the Taguchi method with the Gray relational analysis*. *Rapid Prototyping Journal*, 2007. **13**(5): p. 304-315.
255. Sood, A.K., R.K. Ohdar, and S.S. Mahapatra, *Improving dimensional accuracy of Fused Deposition Modelling processed part using grey Taguchi method*. *Materials & Design*, 2009. **30**(10): p. 4243-4252.
256. Bini, F., et al., *A 3D Model of the Effect of Tortuosity and Constrictivity on the Diffusion in Mineralized Collagen Fibril*. *Scientific reports*, 2019. **9**(1): p. 2658-2658.
257. Barrande, M., R. Bouchet, and R. Denoyel, *Tortuosity of porous particles*. *Anal Chem*, 2007. **79**(23): p. 9115-21.
258. Shariati, V., M.H. Ahmadian, and E. Roohi, *Direct Simulation Monte Carlo investigation of fluid characteristics and gas transport in porous microchannels*. *Scientific reports*, 2019. **9**(1): p. 17183-17183.
259. Lawrence, B.J., M. Devarapalli, and S.V. Madihally, *Flow dynamics in bioreactors containing tissue engineering scaffolds*. *Biotechnology and Bioengineering*, 2009. **102**(3): p. 935-947.
260. Piola, M., et al., *Design and Functional Testing of a Multichamber Perfusion Platform for Three-Dimensional Scaffolds*. *The Scientific World Journal*, 2013. **2013**: p. 123974.

261. Li, W.-J., et al., *A three-dimensional nanofibrous scaffold for cartilage tissue engineering using human mesenchymal stem cells*. *Biomaterials*, 2005. **26**(6): p. 599-609.
262. Qi, Y., et al., *The restoration of full-thickness cartilage defects with mesenchymal stem cells (MSCs) loaded and cross-linked bilayer collagen scaffolds on rabbit model*. *Molecular Biology Reports*, 2012. **39**(2): p. 1231-1237.
263. Wang, Y., et al., *In vitro cartilage tissue engineering with 3D porous aqueous-derived silk scaffolds and mesenchymal stem cells*. *Biomaterials*, 2005. **26**(34): p. 7082-7094.
264. Hunter, D.J., D. Schofield, and E. Callander, *The individual and socioeconomic impact of osteoarthritis*. *Nat Rev Rheumatol*, 2014. **10**(7): p. 437-41.
265. Li, Z., et al., *Chondrogenesis of human bone marrow mesenchymal stem cells in fibrin-polyurethane composites is modulated by frequency and amplitude of dynamic compression and shear stress*. *Tissue Eng Part A*, 2010. **16**(2): p. 575-84.
266. Park, H., et al., *Effect of dual growth factor delivery on chondrogenic differentiation of rabbit marrow mesenchymal stem cells encapsulated in injectable hydrogel composites*. *Journal of Biomedical Materials Research Part A*, 2009. **88A**(4): p. 889-897.
267. Peng, L., et al., *Comparative analysis of mesenchymal stem cells from bone marrow, cartilage, and adipose tissue*. *Stem Cells Dev*, 2008. **17**(4): p. 761-73.
268. Stanko, P., et al., *Comparison of human mesenchymal stem cells derived from dental pulp, bone marrow, adipose tissue, and umbilical cord tissue by gene expression*. *Biomed Pap Med Fac Univ Palacky Olomouc Czech Repub*, 2014. **158**(3): p. 373-7.
269. Ramaswamy, S., et al., *Noninvasive assessment of glycosaminoglycan production in injectable tissue-engineered cartilage constructs using magnetic resonance imaging*. *Tissue Eng Part C Methods*, 2008. **14**(3): p. 243-9.
270. Stephen, Z.R., F.M. Kievit, and M. Zhang, *Magnetite Nanoparticles for Medical MR Imaging*. *Materials today (Kidlington, England)*, 2011. **14**(7-8): p. 330-338.

271. Andreas, K., et al., *Highly efficient magnetic stem cell labeling with citrate-coated superparamagnetic iron oxide nanoparticles for MRI tracking*. *Biomaterials*, 2012. **33**(18): p. 4515-4525.
272. Ramaswamy, S., et al., *Magnetic resonance imaging of chondrocytes labeled with superparamagnetic iron oxide nanoparticles in tissue-engineered cartilage*. *Tissue Eng Part A*, 2009. **15**(12): p. 3899-910.
273. Heymer, A., et al., *Iron oxide labelling of human mesenchymal stem cells in collagen hydrogels for articular cartilage repair*. *Biomaterials*, 2008. **29**(10): p. 1473-1483.
274. Saldanha, K.J., et al., *Magnetic resonance imaging of iron oxide labelled stem cells: applications to tissue engineering based regeneration of the intervertebral disc*. *Eur Cell Mater*, 2008. **16**: p. 17-25.
275. Bulte, J.W., et al., *Magnetodendrimers allow endosomal magnetic labeling and in vivo tracking of stem cells*. *Nat Biotechnol*, 2001. **19**(12): p. 1141-7.
276. Terrovitis, J.V., et al., *Magnetic resonance imaging of ferumoxide-labeled mesenchymal stem cells seeded on collagen scaffolds-relevance to tissue engineering*. *Tissue Eng*, 2006. **12**(10): p. 2765-75.
277. Burg, K.J., et al., *Comparative study of seeding methods for three-dimensional polymeric scaffolds*. *J Biomed Mater Res*, 2000. **51**(4): p. 642-9.
278. Alvarez-Barreto, J.F., et al., *Flow Perfusion Improves Seeding of Tissue Engineering Scaffolds with Different Architectures*. *Annals of Biomedical Engineering*, 2007. **35**(3): p. 429-442.
279. Teixeira, G.Q., et al., *A multicompartiment holder for spinner flasks improves expansion and osteogenic differentiation of mesenchymal stem cells in three-dimensional scaffolds*. *Tissue Eng Part C Methods*, 2014. **20**(12): p. 984-93.
280. Wang, T.W., et al., *Regulation of adult human mesenchymal stem cells into osteogenic and chondrogenic lineages by different bioreactor systems*. *J Biomed Mater Res A*, 2009. **88**(4): p. 935-46.
281. Wendt, D., et al., *Oscillating perfusion of cell suspensions through three-dimensional scaffolds enhances cell seeding efficiency and uniformity*. *Biotechnol Bioeng*, 2003. **84**(2): p. 205-14.

282. Zhao, F. and T. Ma, *Perfusion bioreactor system for human mesenchymal stem cell tissue engineering: dynamic cell seeding and construct development*. *Biotechnol Bioeng*, 2005. **91**(4): p. 482-93.
283. Lu, H., et al., *Microfluidic shear devices for quantitative analysis of cell adhesion*. *Anal Chem*, 2004. **76**(18): p. 5257-64.
284. Olivares, A.L. and D. Lacroix, *Simulation of cell seeding within a three-dimensional porous scaffold: a fluid-particle analysis*. *Tissue engineering. Part C, Methods*, 2012. **18**(8): p. 624-631.
285. Campos Marin, A., M. Brunelli, and D. Lacroix, *Flow perfusion rate modulates cell deposition onto scaffold substrate during cell seeding*. *Biomech Model Mechanobiol*, 2018. **17**(3): p. 675-687.
286. Hilldore, A., A. Wojtowicz, and A.W. Johnson, *Micro-CT based quantification of non-mineralized tissue on cultured hydroxyapatite scaffolds*. *J Biomed Mater Res A*, 2007. **82**(4): p. 1012-21.
287. Heese, F., P. Robson, and L.D. Hall, *Visualization of air bubbles by magnetic resonance imaging*. *IEEE Sensors Journal*, 2005. **5**(2): p. 277-280.
288. Mauck, R.L., et al., *The role of cell seeding density and nutrient supply for articular cartilage tissue engineering with deformational loading*. *Osteoarthritis and Cartilage*, 2003. **11**(12): p. 879-890.
289. Wang, L., et al., *Effect of Initial Seeding Density on Human Umbilical Cord Mesenchymal Stromal Cells for Fibrocartilage Tissue Engineering*. *Tissue Engineering Part A*, 2008. **15**(5): p. 1009-1017.
290. Baker, B.M. and R.L. Mauck, *The effect of nanofiber alignment on the maturation of engineered meniscus constructs*. *Biomaterials*, 2007. **28**(11): p. 1967-1977.
291. Wendt, D., et al., *Uniform tissues engineered by seeding and culturing cells in 3D scaffolds under perfusion at defined oxygen tensions*. *Biorheology*, 2006. **43**(3,4): p. 481-8.
292. Shriky, B., et al., *Pluronic F127 thermosensitive injectable smart hydrogels for controlled drug delivery system development*. *Journal of Colloid and Interface Science*, 2020. **565**: p. 119-130.
293. Arbab, A.S., et al., *Comparison of Transfection Agents in Forming Complexes with Ferumoxides, Cell Labeling Efficiency, and Cellular Viability*. *Molecular Imaging*, 2004. **3**(1): p. 15353500200403190.

294. Symonds, P., et al., *Low and high molecular weight poly(L-lysine)s/poly(L-lysine)-DNA complexes initiate mitochondrial-mediated apoptosis differently*. FEBS Lett, 2005. **579**(27): p. 6191-8.
295. Mailänder, V., et al., *Carboxylated Superparamagnetic Iron Oxide Particles Label Cells Intracellularly Without Transfection Agents*. Molecular Imaging and Biology, 2008. **10**(3): p. 138-146.
296. Kaggie, J.D., et al., *Ultra Short Echo Time MRI of Iron-Labelled Mesenchymal Stem Cells in an Ovine Osteochondral Defect Model*. Sci Rep, 2020. **10**(1): p. 8451.
297. Kolosnjaj-Tabi, J., et al., *Cell labeling with magnetic nanoparticles: Opportunity for magnetic cell imaging and cell manipulation*. Journal of Nanobiotechnology, 2013. **11**(1): p. S7.
298. Smirnov, P., et al., *Single-cell detection by gradient echo 9.4 T MRI: a parametric study*. Contrast Media & Molecular Imaging, 2006. **1**(4): p. 165-174.
299. Weis, C., et al., *In-Vivo Imaging of Cell Migration Using Contrast Enhanced MRI and SVM Based Post-Processing*. PLOS ONE, 2015. **10**(12): p. e0140548.
300. Poirier-Quinot, M., et al., *High-resolution 1.5-Tesla magnetic resonance imaging for tissue-engineered constructs: a noninvasive tool to assess three-dimensional scaffold architecture and cell seeding*. Tissue Eng Part C Methods, 2010. **16**(2): p. 185-200.
301. Chavhan, G.B., et al., *Principles, techniques, and applications of T2*-based MR imaging and its special applications*. Radiographics : a review publication of the Radiological Society of North America, Inc, 2009. **29**(5): p. 1433-1449.
302. Ashworth, J.C., et al., *Cell Invasion in Collagen Scaffold Architectures Characterized by Percolation Theory*. Advanced healthcare materials, 2015. **4**(9): p. 1317-1321.
303. Thevenot, P., et al., *Method to analyze three-dimensional cell distribution and infiltration in degradable scaffolds*. Tissue engineering. Part C, Methods, 2008. **14**(4): p. 319-331.
304. Dorsey, S.M., S. Lin-Gibson, and C.G. Simon, Jr., *X-ray microcomputed tomography for the measurement of cell adhesion and proliferation in polymer scaffolds*. Biomaterials, 2009. **30**(16): p. 2967-74.

305. Bradley, R.S., I.K. Robinson, and M. Yusuf, *3D X-Ray Nanotomography of Cells Grown on Electrospun Scaffolds*. *Macromolecular Bioscience*, 2017. **17**(2): p. 1600236.
306. Shepherd, D.V., et al., *3D imaging of cells in scaffolds: direct labelling for micro CT*. *Journal of materials science. Materials in medicine*, 2018. **29**(6): p. 86-86.
307. Palmroth, A., et al., *Evaluation of scaffold microstructure and comparison of cell seeding methods using micro-computed tomography-based tools*. *Journal of The Royal Society Interface*, 2020. **17**(165): p. 20200102.
308. Abarrategi, A., et al., *Label-free magnetic resonance imaging to locate live cells in three-dimensional porous scaffolds*. *Journal of the Royal Society, Interface*, 2012. **9**(74): p. 2321-2331.
309. Burg, K.J., et al., *Application of magnetic resonance microscopy to tissue engineering: a polylactide model*. *J Biomed Mater Res*, 2002. **61**(3): p. 380-90.
310. Lalande, C., et al., *Magnetic resonance imaging tracking of human adipose derived stromal cells within three-dimensional scaffolds for bone tissue engineering*. *Eur Cell Mater*, 2011. **21**: p. 341-54.
311. Pham, Q.P., U. Sharma, and A.G. Mikos, *Electrospun Poly(ϵ -caprolactone) Microfiber and Multilayer Nanofiber/Microfiber Scaffolds: Characterization of Scaffolds and Measurement of Cellular Infiltration*. *Biomacromolecules*, 2006. **7**(10): p. 2796-2805.
312. Gonçalves, A., et al., *Effect of flow perfusion conditions in the chondrogenic differentiation of bone marrow stromal cells cultured onto starch based biodegradable scaffolds*. *Acta Biomaterialia*, 2011. **7**(4): p. 1644-1652.
313. Alves da Silva, M.L., et al., *Cartilage Tissue Engineering Using Electrospun PCL Nanofiber Meshes and MSCs*. *Biomacromolecules*, 2010. **11**(12): p. 3228-3236.
314. Tıǧlı, R.S., et al., *Chondrogenesis in perfusion bioreactors using porous silk scaffolds and hESC-derived MSCs*. *Journal of Biomedical Materials Research Part A*, 2011. **96A**(1): p. 21-28.
315. Sailon, A.M., et al., *A novel flow-perfusion bioreactor supports 3D dynamic cell culture*. *Journal of biomedicine & biotechnology*, 2009. **2009**: p. 873816-873816.

316. Galban, C.J. and B.R. Locke, *Analysis of cell growth kinetics and substrate diffusion in a polymer scaffold*. Biotechnol Bioeng, 1999. **65**(2): p. 121-32.
317. Leddy, H.A., H.A. Awad, and F. Guilak, *Molecular diffusion in tissue-engineered cartilage constructs: effects of scaffold material, time, and culture conditions*. J Biomed Mater Res B Appl Biomater, 2004. **70**(2): p. 397-406.
318. Poon, C., *Measuring the density and viscosity of culture media for optimized computational fluid dynamics analysis of in vitro devices*. bioRxiv, 2020: p. 2020.08.25.266221.
319. Prasopthum, A., K.M. Shakesheff, and J. Yang, *Direct three-dimensional printing of polymeric scaffolds with nanofibrous topography*. Biofabrication, 2018. **10**(2): p. 025002.
320. Theodoridis, K., et al., *Hyaline cartilage next generation implants from adipose-tissue-derived mesenchymal stem cells: Comparative study on 3D-printed polycaprolactone scaffold patterns*. Journal of Tissue Engineering and Regenerative Medicine, 2019. **13**(2): p. 342-355.
321. Ruiz-Cantu, L., et al., *Characterisation of the surface structure of 3D printed scaffolds for cell infiltration and surgical suturing*. Biofabrication, 2016. **8**(1): p. 015016.
322. Declercq, H.A., et al., *The role of scaffold architecture and composition on the bone formation by adipose-derived stem cells*. Tissue engineering. Part A, 2014. **20**(1-2): p. 434-444.
323. Kim, H.-J., J.-H. Lee, and G.-I. Im, *Chondrogenesis using mesenchymal stem cells and PCL scaffolds*. Journal of Biomedical Materials Research Part A, 2010. **92A**(2): p. 659-666.
324. Xu, J., et al., *Chondrogenic differentiation of human mesenchymal stem cells in three-dimensional alginate gels*. Tissue Eng Part A, 2008. **14**(5): p. 667-80.
325. Wang, W., D. Rigueur, and K.M. Lyons, *TGF β signaling in cartilage development and maintenance*. Birth defects research. Part C, Embryo today : reviews, 2014. **102**(1): p. 37-51.
326. Macario, D.K., et al., *Inhibition of Apoptosis Prevents Shear-Induced Detachment of Endothelial Cells*. Journal of Surgical Research, 2008. **147**(2): p. 282-289.

327. Yassin, M.A., et al., *Cell seeding density is a critical determinant for copolymer scaffolds-induced bone regeneration*. Journal of Biomedical Materials Research Part A, 2015. **103**(11): p. 3649-3658.
328. Zhan, C., et al., *Low Shear Stress Increases Recombinant Protein Production and High Shear Stress Increases Apoptosis in Human Cells*. iScience, 2020. **23**(11): p. 101653.
329. Paim, A., et al., *Human dental pulp stem cell adhesion and detachment in polycaprolactone electrospun scaffolds under direct perfusion*. Braz J Med Biol Res, 2018. **51**(5): p. e6754.
330. Patrício, T., et al., *Characterisation of PCL and PCL/PLA Scaffolds for Tissue Engineering*. Procedia CIRP, 2013. **5**: p. 110-114.
331. Bosworth, L.A., et al., *Enhancing Biocompatibility without Compromising Material Properties: An Optimised NaOH Treatment for Electrospun Polycaprolactone Fibres*. Journal of Nanomaterials, 2019. **2019**: p. 4605092.
332. Jahani, H., et al., *Controlled surface morphology and hydrophilicity of polycaprolactone toward selective differentiation of mesenchymal stem cells to neural like cells*. Journal of Biomedical Materials Research Part A, 2015. **103**(5): p. 1875-1881.
333. Tallawi, M., et al., *Strategies for the chemical and biological functionalization of scaffolds for cardiac tissue engineering: a review*. Journal of the Royal Society, Interface, 2015. **12**(108): p. 20150254-20150254.
334. Domingos, M., et al., *Improved osteoblast cell affinity on plasma-modified 3-D extruded PCL scaffolds*. Acta Biomater, 2013. **9**(4): p. 5997-6005.
335. Poh, P.S.P., et al., *In vitro and in vivo bone formation potential of surface calcium phosphate-coated polycaprolactone and polycaprolactone/bioactive glass composite scaffolds*. Acta Biomater, 2016. **30**: p. 319-333.
336. Tiaw, K.S., et al., *Laser surface modification of poly(ϵ -caprolactone) (PCL) membrane for tissue engineering applications*. Biomaterials, 2005. **26**(7): p. 763-769.
337. Wang, W., et al., *Enhancing the Hydrophilicity and Cell Attachment of 3D Printed PCL/Graphene Scaffolds for Bone Tissue Engineering*. Materials (Basel, Switzerland), 2016. **9**(12): p. 992.

338. Silva, J.C., et al., *Extruded Bioreactor Perfusion Culture Supports the Chondrogenic Differentiation of Human Mesenchymal Stem/Stromal Cells in 3D Porous Poly(ϵ -Caprolactone) Scaffolds*. *Biotechnol J*, 2020. **15**(2): p. e1900078.
339. Zamanlui, S., et al., *Influence of hydrodynamic pressure on chondrogenic differentiation of human bone marrow mesenchymal stem cells cultured in perfusion system*. *Biologicals*, 2018. **56**: p. 1-8.
340. Liu, X., et al., *Mechanical Tension Promotes the Osteogenic Differentiation of Rat Tendon-derived Stem Cells Through the Wnt5a/Wnt5b/JNK Signaling Pathway*. *Cell Physiol Biochem*, 2015. **36**(2): p. 517-30.
341. Rui, Y.F., et al., *Mechanical loading increased BMP-2 expression which promoted osteogenic differentiation of tendon-derived stem cells*. *J Orthop Res*, 2011. **29**(3): p. 390-6.
342. Steward, A.J., D.R. Wagner, and D.J. Kelly, *The pericellular environment regulates cytoskeletal development and the differentiation of mesenchymal stem cells and determines their response to hydrostatic pressure*. *Eur Cell Mater*, 2013. **25**: p. 167-78.
343. Argentati, C., et al., *Insight into Mechanobiology: How Stem Cells Feel Mechanical Forces and Orchestrate Biological Functions*. *International journal of molecular sciences*, 2019. **20**(21): p. 5337.
344. Eberbeck, D., et al., *Quantification of the aggregation of magnetic nanoparticles with different polymeric coatings in cell culture medium*. *Journal of Physics D: Applied Physics*, 2010. **43**(40): p. 405002.
345. Holy, C.E., M.S. Shoichet, and J.E. Davies, *Engineering three-dimensional bone tissue in vitro using biodegradable scaffolds: investigating initial cell-seeding density and culture period*. *J Biomed Mater Res*, 2000. **51**(3): p. 376-82.
346. Li, Y., et al., *Effects of filtration seeding on cell density, spatial distribution, and proliferation in nonwoven fibrous matrices*. *Biotechnol Prog*, 2001. **17**(5): p. 935-44.
347. Hagmann, S., et al., *Different culture media affect growth characteristics, surface marker distribution and chondrogenic differentiation of human bone marrow-derived mesenchymal stromal cells*. *BMC Musculoskeletal Disorders*, 2013. **14**(1): p. 223.
348. Yasmina, L. and L. Rachid, *Evaluation of Energy Losses in Pipes*. *American Journal of Mechanical Engineering*, 2015. **3**(3A): p. 32-37.

349. Walker, J.M., J.E. Sargison, and A.D. Henderson, *Turbulent boundary-layer structure of flows over freshwater biofilms*. *Experiments in Fluids*, 2013. **54**(12): p. 1628.
350. Le Bihan, D. and M. Iima, *Diffusion Magnetic Resonance Imaging: What Water Tells Us about Biological Tissues*. *PLoS biology*, 2015. **13**(7): p. e1002203-e1002203.
351. Archer, B.J., et al., *Noninvasive Quantification of Cell Density in Three-Dimensional Gels by MRI*. *IEEE Trans Biomed Eng*, 2019. **66**(3): p. 821-830.
352. Kisiday, J.D., et al., *Dynamic compression stimulates proteoglycan synthesis by mesenchymal stem cells in the absence of chondrogenic cytokines*. *Tissue engineering. Part A*, 2009. **15**(10): p. 2817-2824.
353. Zhao, F., et al., *A multiscale computational fluid dynamics approach to simulate the micro-fluidic environment within a tissue engineering scaffold with highly irregular pore geometry*. *Biomechanics and Modeling in Mechanobiology*, 2019. **18**(6): p. 1965-1977.
354. Chung, C.A., et al., *Enhancement of cell growth in tissue-engineering constructs under direct perfusion: Modeling and simulation*. *Biotechnology and Bioengineering*, 2007. **97**(6): p. 1603-1616.
355. Sacco, R., et al., *A multiphysics/multiscale 2D numerical simulation of scaffold-based cartilage regeneration under interstitial perfusion in a bioreactor*. *Biomechanics and Modeling in Mechanobiology*, 2011. **10**(4): p. 577-589.
356. Nava, M.M., M.T. Raimondi, and R. Pietrabissa, *A multiphysics 3D model of tissue growth under interstitial perfusion in a tissue-engineering bioreactor*. *Biomechanics and Modeling in Mechanobiology*, 2013. **12**(6): p. 1169-1179.
357. Harel, E., et al., *Multiphase imaging of gas flow in a nanoporous material using remote-detection NMR*. *Nature Materials*, 2006. **5**(4): p. 321-327.
358. Sederman, A.J., et al., *Magnetic resonance imaging of liquid flow and pore structure within packed beds*. *Chemical Engineering Science*, 1997. **52**(14): p. 2239-2250.
359. Wu, A.-x., et al., *Pore structure and liquid flow velocity distribution in water-saturated porous media probed by MRI*. *Transactions of Nonferrous Metals Society of China*, 2016. **26**(5): p. 1403-1409.

360. Dubois, J., et al., *Flow dynamics within a bioreactor for tissue engineering by residence time distribution analysis combined with fluorescence and magnetic resonance imaging to investigate forced permeability and apparent diffusion coefficient in a perfusion cell culture chamber*. Biotechnology and Bioengineering, 2011. **108**(10): p. 2488-2498.
361. Crowe, J.J., et al., *A magnetic resonance-compatible perfusion bioreactor system for three-dimensional human mesenchymal stem cell construct development*. Chemical Engineering Science, 2011. **66**(18): p. 4138-4147.
362. Kapfer, S.C., et al., *Minimal surface scaffold designs for tissue engineering*. Biomaterials, 2011. **32**(29): p. 6875-6882.
363. Clarke, D.A., et al., *Investigation of flow through triply periodic minimal surface-structured porous media using MRI and CFD*. Chemical Engineering Science, 2021. **231**: p. 116264.
364. Seymour, J.D., et al., *Magnetic resonance microscopy of biofilm structure and impact on transport in a capillary bioreactor*. Journal of Magnetic Resonance, 2004. **167**(2): p. 322-327.